EES Catalysis

REVIEW ARTICLE

View Article Online
View Journal | View Issue

Check for updates

Cite this: *EES Catal.*, 2026, 4, 522

# Integrated $CO_2$ capture and conversion: dual-functional materials, mechanisms, and pathways to industrial decarbonization

Mohamed A. Elokl, Ahmed G. Ali, Abdelrahman M. Abdelmohsen, Ahmed A. Taha, Abdelrahman A. Ashour, Salma Elshabrawy and Nageh K. Allam *

Carbon dioxide ($CO_2$) is both the principal anthropogenic greenhouse gas and a valuable, non-toxic, and abundant $C_1$ feedstock for sustainable fuel and chemical production. Conventional approaches have typically addressed $CO_2$ capture and $CO_2$ conversion as independent processes; however, each remains energy-intensive and economically constrained when implemented in isolation. The emerging concept of integrated $CO_2$ capture and conversion (ICCC) offers a transformative strategy to simultaneously mitigate $CO_2$ emissions and synthesize value-added products within a unified system. Unlike the simple sequential coupling of capture and utilization, ICCC demands the synergistic integration of capture media, catalytic interfaces, and reaction environments, requiring interdisciplinary insight spanning materials chemistry, catalysis, and electrochemical engineering. This review critically surveys recent progress in ICCC with a focus on dual-functional materials (DFMs) that enable concurrent $CO_2$ capture and catalytic conversion. The discussion encompasses a broad range of DFMs, including porous organic polymers, covalent organic frameworks, zeolites, metal–organic frameworks, metal oxides, amines, ionic liquids, deep eutectic solvents, and molten salts. Mainstream $CO_2$ capture technologies, post-, pre-, and oxy-fuel combustion routes, and associated separation techniques such as absorption, adsorption, membrane filtration, cryogenics, and looping cycles are systematically analyzed through a SWOT framework (strengths, weaknesses, opportunities, and threats) across efficiency, energy, cost, and technology readiness dimensions. By coupling techno-economic evaluation with emerging mechanistic and computational insights, this review identifies viable strategies to bridge the gap between laboratory innovation and industrial deployment. Finally, we outline key research priorities, including the rational design of DFMs, optimization of catalytic interfaces, and integration of AI-driven process control, positioning ICCC as an emerging pathway toward industrial decarbonization and the global clean energy transition, while highlighting fundamental constraints from coupled $CO_2$ adsorption thermodynamics, transport, and catalytic kinetics that expose critical material-stability and system-integration challenges for large-scale deployment.

Received 8th November 2025,
Accepted 10th February 2026

DOI: 10.1039/d5ey00322a

rsc.li/eescatalysis

Open Access Article. Published on 12 fevral 2026. Downloaded on 01.06.2026 11:06:26.
This article is licensed under a Creative Commons Attribution-NonCommercial 3.0 Unported Licence.

## Broader context

Carbon dioxide ($CO_2$) emissions are the primary driver of global climate change, yet $CO_2$ also represents a vast, renewable carbon resource for producing sustainable fuels and chemicals. Conventional carbon capture and utilization approaches have advanced independently, but their separation limits overall efficiency, scalability, and economic viability. The emerging concept of integrated $CO_2$ capture and conversion (ICCC) provides a unified route to simultaneously mitigate $CO_2$ emissions and generate valuable products. By coupling $CO_2$ adsorption and catalytic transformation within a single system, ICCC redefines how we think about carbon management, from end-of-pipe mitigation to circular resource utilization. This review provides a comprehensive framework linking materials design, catalysis, and process engineering to establish ICCC as a cornerstone of carbon circularity and industrial decarbonization, accelerating the transition toward a net-zero energy future.

## Introduction

The rapid increase in atmospheric carbon dioxide ($CO_2$) concentrations, from less than 300 ppm in the pre-industrial era to

*Energy Materials Laboratory (EML), Physics Department, School of Sciences and Engineering, The American University in Cairo, New Cairo 11835, Egypt.*
*E-mail: nageh.allam@aucegypt.edu*



© 2026 The Author(s). Published by the Royal Society of Chemistry

Open Access Article. Published on 12 fevral 2026. Downloaded on 01.06.2026 11:06:26.
This article is licensed under a Creative Commons Attribution-NonCommercial 3.0 Unported Licence.

416.47 ppm in 2020 (Earth's $CO_2$), and further to 422.5 ppm in 2024 (IEA), has intensified the urgent need for engineered solutions to remove carbon from the atmosphere.[1–3] To align with the Paris Agreement's 1.5 °C pathway, the Intergovernmental Panel on Climate Change (IPCC) estimates that global greenhouse gas emissions must peak before 2025 and decline by 43% by 2030 and 84% by 2050.[4] And, as climate change accelerates, the challenges associated with $CO_2$, such as

**Mohamed A. Elokl**

*Mohamed A. Elokl received his BSc from the Department of Petroleum and Energy Engineering at The American University in Cairo with minors in Economics and Community Development. He is currently a graduate research assistant at the Energy Materials Laboratory (EML), where his research focuses on carbon capture and electrochemical conversion, emphasizing nanostructured catalysts, MOF-based and electrospun nanofiber materials, and biochar-derived composites. Beyond carbon utilization, he has contributed to green hydrogen research through anti-corrosive electrolyzers for seawater electrolysis and Africa's deployment feasibility, alongside carbon capture and storage (CCS) research using reservoir modeling and well placement design. His research integrates rational catalyst design and synthesis with advanced materials characterization, electrochemical interface analysis and modeling, and techno-economic assessment to advance sustainable energy and decarbonization technologies.*

**Ahmed G. Ali**

*Ahmed G. Ali is a research and teaching assistant at Ain Shams University and The American University in Cairo, Egypt. He obtained his MSc in Materials Science from the Skolkovo Institute of Science and Technology, Russia. His research focuses on the rational design of advanced materials for sustainable electrochemical energy conversion, including water electrolysis, HER, OER, $CO_2$ electroreduction, and the development of high-performance electrolyzer architectures and ion-conducting membranes.*

**Abdelrahman M. Abdelmohsen**

*Abdelrahman Abdelmohsen is a graduate research assistant at the Energy Materials Laboratory (EML), The American University in Cairo (AUC). His research interests span electrocatalysis, materials science, and electrochemical energy conversion, focusing on the development and electrochemical assessment of functional materials for $CO_2$ utilization, nitrogen-related electrochemical reactions, and sustainable chemical production. His work integrates materials engineering, advanced electrochemical characterization, and reaction engineering to develop efficient catalysts for energy and environmental applications.*

**Ahmed A. Taha**

*Ahmed A. Taha received his PhD in Environmental Science and Engineering from Tongji University, Shanghai, China. He began his career at the Soils, Water and Environment Research Institute (SWERI), Agricultural Research Center (ARC), Egypt, and later conducted research in China at Tongji University, Beijing University of Chemical Technology, and Beijing Forestry University, focusing on nanomaterials, membranes, and catalytic materials for environmental applications. From 2014 to 2017, he contributed to industry–academia collaborations in China on nanotechnology-based water treatment solutions. He returned to academia as an Associate Professor at SWERI, ARC, leading national and international projects. In 2023, he was awarded a Fulbright Postdoctoral Fellowship at the University of Cincinnati, USA, working with Prof. Dionysios D. Dionysiou and Dr Jingjie Wu on MOF- and nanofiber-based catalysts for $CO_2$ capture and conversion. After returning to Egypt, he cooperated with Prof. Nageh Allam's group at AUC on optimizing nanofiber catalysts for $CO_2$ electrochemical conversion. His research interests include MOFs, carbon nanomaterials, nanofiber membranes, heterogeneous catalysis for $CO_2$ mitigation, water treatment, and sustainable energy applications.*

Open Access Article. Published on 12 fevral 2026. Downloaded on 01.06.2026 11:06:26.
This article is licensed under a Creative Commons Attribution-NonCommercial 3.0 Unported Licence.

atmospheric $CO_2$ reduction, emissions mitigation, and conversion to carbon-based products, will remain persistent for decades.[5]

Carbon capture, utilization, and storage (CCUS) is widely regarded as a promising mitigation pathway.[6] Furthermore, the International Energy Agency (IEA) Net Zero Emissions scenario necessitates scaling Carbon Capture, Utilization, and Storage (CCUS) capacity from approximately 45 Mt $CO_2$ per year in 2022 to over 6.0 Gt $CO_2$ per year by 2050, a more than 100-fold increase required to address heavy industry, power generation, and transport.[7] However, conventional CCUS faces major hurdles: the processes of separation, compression, purification, and storage are highly energy-intensive, with prohibitive economic costs acting as a major barrier.[8,9] Additional concerns include limited geological storage capacity, high monitoring costs, and public resistance due to risks of potential leakage.[10]

Integrated carbon capture and utilization (ICCU), also known as integrated carbon capture and conversion (ICCC),[11] reactive capture of $CO_2$ (RCC),[12] and carbon capture and recycling (combined CCR),[13] has emerged as a compelling alternative. ICCC eliminates the need for desorption, compression, transportation, and long-term storage by enabling direct $CO_2$ conversion within absorbents, thereby reducing overall energy consumption and simultaneously lowering atmospheric $CO_2$ concentrations (Fig. 1).[14] These systems may take the form of integrated cascades or fully *in situ* single-pass processes.

In Aspen Plus–based syngas production TEA,[15] ICCU demonstrated higher energy efficiency (37.1%) compared to CCU (35.4%) for Ca-looping capture coupled with reverse water–gas shift (RWGS) syngas production, reflecting reduced energy consumption per unit product. Comparative syngas TEA shows the total annual cost of ICCU is $867.07 million, corresponding to a total cost of CO of $720.25 per tonne. In contrast, CCU has higher costs, with a total annual cost of $1027.61 million and a total cost of CO of $1004.53 per tonne. Analysis also shows that the ICCU process can produce more CO (1.20 Mt year$^{-1}$), less purge (0.21 Mt year$^{-1}$), and less consumption of CaCO3 (0.62 Mt year$^{-1}$). The Cost of $CO_2$ Avoided of ICCU (317.11 $ per ton) is much lower than that of CCU (1230.27 $ per ton). Furthermore, in methanation applications, the integrated route requires only one-third of the energy input consumed by the decoupled CCU process, which translates into a 13% reduction in production costs, lowering the price of methane from 962.86 € per ton in the conventional scheme to 837.1 € per ton with ICCU.[16]

Nevertheless, realizing the full extent of these efficiency gains requires a level of process-material integration that is not yet adequately reflected in most existing reviews, which focus on either capture materials or conversion technologies separately. As a result, the current ICCC literature remains fragmented, with limited comprehensive evaluations that bridge material design, process integration, techno-economic analysis, and industrial scalability. Furthermore, there is insufficient comparative assessment of dual-functional materials (DFMs) with respect to structural stability, product selectivity, and durability under realistic flue-gas conditions. Therefore, this review addresses existing gaps by presenting a

**Abdelrahman A. Ashour**

*Abdelrahman Ashour is a Graduate Research Assistant at the Energy Materials Laboratory, The American University in Cairo. His research focuses on developing and evaluating functional materials for electrocatalysis and sustainable energy conversion, with interests in $CO_2$ utilization, system design, and techno-economic analysis for renewable fuel production.*

**Salma Elshabrawy**

*Salma Elshabrawy received her BS (2021) and MS (2024) degrees in Chemical Engineering from Alexandria University, Egypt. She worked as a research assistant under the supervision of Prof. Nageh Allam, at the American University in Cairo, Egypt. The research focused on electrocatalytic $CO_2$ reduction, and integrated methods of capturing and conversion. She is currently pursuing her PhD in Chemical and Biomolecular Engineering at Rice University, USA, under the supervision of Dr Jason Adams, where her research focuses on kinetic modeling and computational simulation of electrocatalytic reactions.*

**Nageh K. Allam**

*Nageh Allam received his PhD in Materials Science and Engineering from Pennsylvania State University. He joined Georgia Institute of Technology as a postdoctoral fellow then Massachusetts Institute of Technology as a Research Scholar. After his postdoctoral tenure, he joined The American University in Cairo, where he is currently a professor of Materials Science and Engineering. His research focuses on the fabrication of well-designed nanostructured materials with composition, size, and shape control for use in energy conversion (Water electrolysis, $CO_2$ reduction, $NH_3$ synthesis, Biogas, etc.) and storage (Batteries & Supercapacitors), Capacitive deionization, Electrochemical sensors, Biomaterials, among others. The research comprises both experimental and theoretical activities.*


© 2026 The Author(s). Published by the Royal Society of Chemistry

Open Access Article. Published on 12 fevral 2026. Downloaded on 01.06.2026 11:06:26.
This article is licensed under a Creative Commons Attribution-NonCommercial 3.0 Unported Licence.

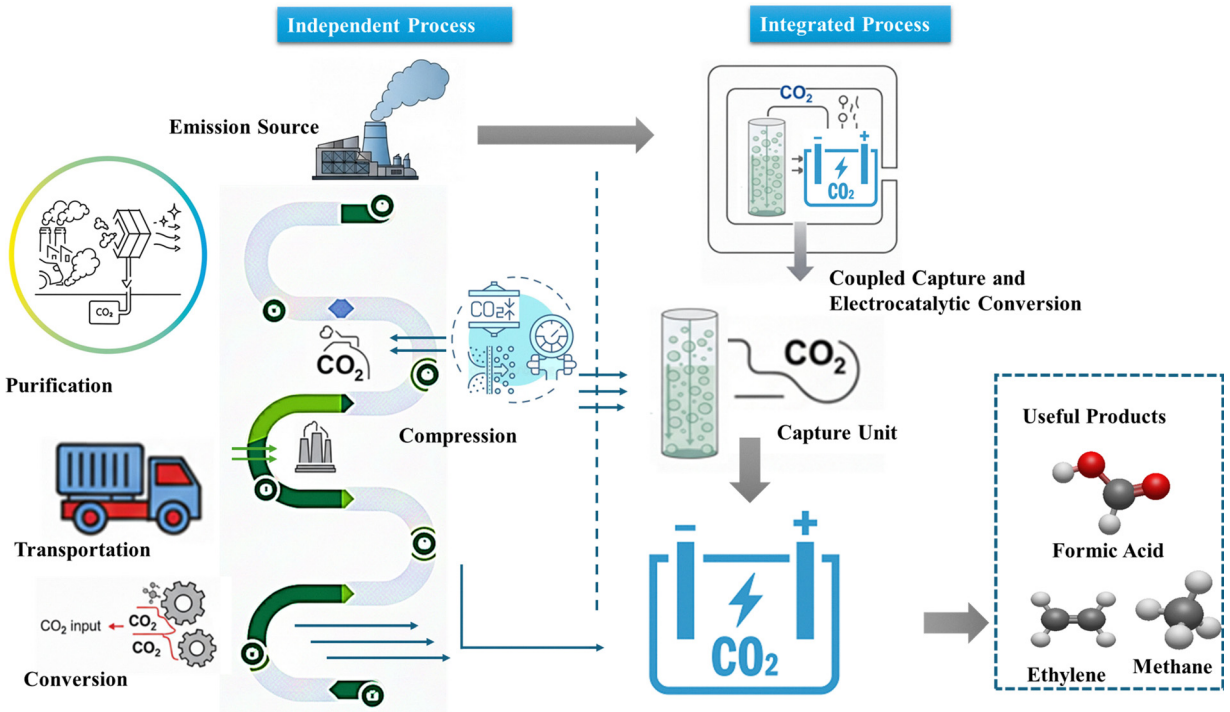


Fig. 1 A schematic comparing two pathways for $CO_2$ utilization: the conventional multi-step process (independent process) *versus* an integrated approach for direct capture and conversion (integrated process).

state-of-the-art analysis of the Integrated $CO_2$ Capture and Conversion (ICCC) field, spanning fundamental materials science to process-level techno-economics. Advances in dual-function materials (DFMs) are surveyed, including solid sorbents such as porous organic polymers (POPs), covalent organic frameworks (COFs), metal–organic frameworks (MOFs), zeolites, and metal oxides, as well as liquid solvents such as amines, ionic liquids (ILs), deep eutectic solvents (DESs), and molten salts. In addition, the performance and technology readiness levels (TRLs) of major capture and separation technologies are evaluated, along with the definition of critical performance indicators and the identification of outstanding challenges. As illustrated in (Fig. 2), the workflow of this review provides a structured pathway that connects materials development with carbon capture technologies and separation techniques and further extends to system-level performance indicators and techno-economic assessment, ensuring comprehensive coverage from fundamentals to applications. However, integrating capture and conversion within a single workflow imposes stringent kinetic and thermodynamic constraints: materials must bind $CO_2$ strongly enough for efficient capture yet release or activate it rapidly at catalytic sites, while mass transport and heat management must be compatible with high turnover frequencies under realistic flue-gas compositions. Therefore, this review places particular emphasis on how capture thermodynamics, diffusion limitations, reaction kinetics, and process synergies co-determine the performance window of integrated ICCC processes and dual-functional materials. Finally, a research roadmap is outlined to accelerate the transition of ICCC from laboratory-scale development to industrial deployment, complemented by a bibliometric analysis that maps development trends, research hotspots, and future directions.

## Bibliometric analysis of ICCC research

On July 1, 2025, the research status of ICCC was analyzed and discussed based on the core database of Web of Science, which is a multidisciplinary core journal citation index database for the most relevant academic journals and international conferences. To ensure comprehensive coverage, the following search terms were employed: integrated carbon capture and conversion, integrated $CO_2$ capture and utilization, ICCC, ICCU, carbon capture and *in situ* conversion, carbon capture and *in situ* utilization, and dual-functional materials. The bibliometric analysis was conducted with VOSviewer software to generate keyword clusters and visualize research trends.[17] Out of 2181 publications, 1336 were published between 2020 and 2025, reflecting the exponential growth in this field. After filtering repetitive terms, 51 keywords appeared more than 45 times among the 9081 retrieved, with dominant themes including flue gas, carbon dioxide capture, electrochemical reduction, absorption, adsorption, and dual-functional materials, all of which align with the primary scope of this review (Fig. 3). The author network revealed 9947 contributing researchers, of whom 30 authors have at least nine publications with one or more citations, underscoring the presence of a growing core community. Geographically, 97 countries have contributed to ICCC research. China leads publication output, mainly through the Chinese Academy of Sciences, followed by the United States, England, and South Korea, highlighting the global and competitive nature of this research domain.

Open Access Article. Published on 12 fevral 2026. Downloaded on 01.06.2026 11:06:26.
This article is licensed under a Creative Commons Attribution-NonCommercial 3.0 Unported Licence.

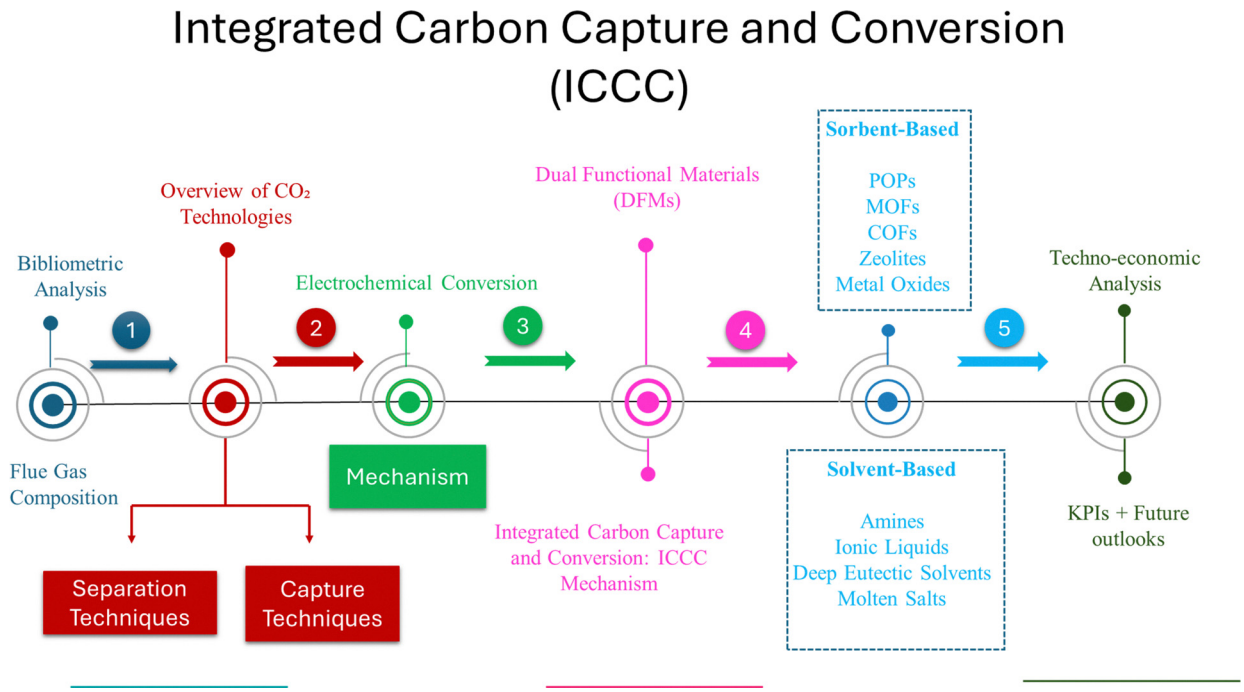


Fig. 2 Schematic overview of the review workflow: materials advances, capture technologies, performance indicators, and techno-economics.

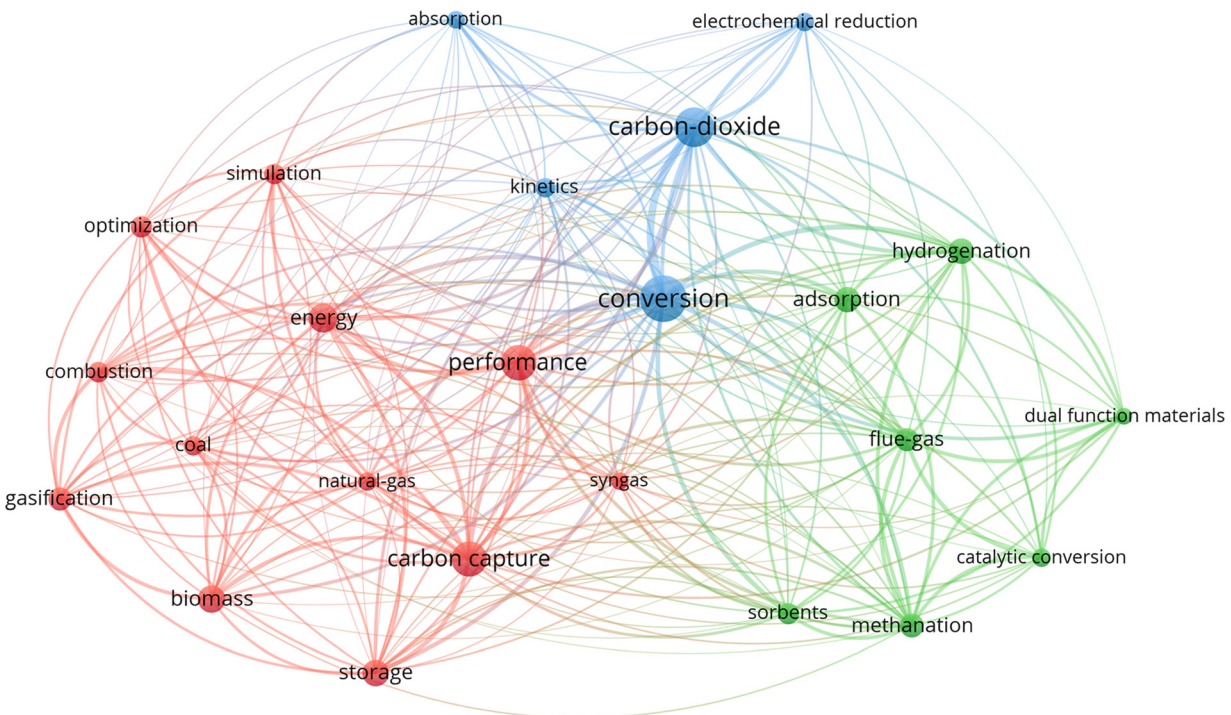


Fig. 3 Bibliometric analysis of keyword co-occurrence in research on integrated carbon capture and conversion. Each node represents a keyword, with its size corresponding to its frequency. The colored clusters group related terms, visually separating the main research sub-themes within the field.

## Insight

These bibliometric findings reveal not only the surging momentum of ICCC research but also a shift toward global collaboration, with strong leadership emerging in Asia alongside active contributions from North America and Europe. The clustering of keywords indicates a transition from fundamental $CO_2$ capture studies toward integrated electrochemical conversion and dual-functional material design. This trend underscores the urgency and relevance of ICCC as a multidisciplinary research frontier that bridges chemistry, materials science, and


© 2026 The Author(s). Published by the Royal Society of Chemistry

Open Access Article. Published on 12 fevral 2026. Downloaded on 01.06.2026 11:06:26.
This article is licensed under a Creative Commons Attribution-NonCommercial 3.0 Unported Licence.

engineering, and sets the stage for industrial translation in the coming decade. Beyond mapping existing trends, this bibliometric analysis reveals several critical research gaps that this review addresses. First, some material classes, particularly sorbent materials, remain underexplored under realistic flue-gas conditions. Second, the scarcity of terms related to *in situ*/*operando* characterization (*e.g.*, DRIFTS, ambient-pressure XPS) and kinetic modelling signals a lack of fundamental insight into $CO_2$ activation at the capture–catalytic interface. Third, the analysis highlights a disconnect between lab-scale innovation and industrial translation, as techno-economic assessments (TEA) and pilot-scale demonstrations (TRL $\geq$ 4) remain negligible in current literature, representing a major bottleneck for industrial translation of ICCC technologies.

## Composition of flue gas

The composition of flue gas is a critical factor in determining both the efficiency and cost of $CO_2$ capture and conversion systems, as $CO_2$ concentrations vary significantly across power generation and industrial processes[18] (Table 1). For example, flue gases from power plants typically contain 12.6%–14% $CO_2$, depending on the fuel type, whereas industrial sources such as urea, hydrogen, steel, and cement production can emit streams with $CO_2$ concentrations approaching 20%. In certain cases, such as ethanol or ethylene production, the exhaust may consist of nearly pure $CO_2$,[19] while carbon capture costs can differ substantially based on the $CO_2$ source (Fig. 4). In industries with dilute $CO_2$ streams, such as power generation, capture is considerably more expensive, with costs ranging from USD 52–86 per ton of $CO_2$, and levelized costs between USD 50–100 per ton.[20,21] By contrast, processes that emit concentrated $CO_2$ streams typically incur significantly lower capture costs, on the order of USD 14–32 per ton.[22]

While impurity tolerance is a key differentiator, the fundamental selection between thermocatalytic and electrocatalytic systems rests on their distinct operational requirements and capabilities. Thermocatalytic systems rely on high temperatures (100–500 °C) and elevated pressures (0.1–10 MPa) to drive reaction kinetics, requiring a supply of external molecular hydrogen ($H_2$) and often hitting thermodynamic equilibrium ceilings that limit conversion

Table 1 Summary of flue gas compositions, $CO_2$ capture costs, and the levelized cost of CCUS across major industrial sectors

| Industrial process | $CO_2$ concentration in feed (vol%)[19] | Main impurities (vol%)[19] | Capture cost of $CO_2$ (US$ per ton $CO_2$)[20] | Levelized cost of CCUS (US$ per ton $CO_2$)[21] |
|---|---|---|---|---|
| Power generation (coal-fired) | 12.6%–14% | 71.4%–74% $N_2$, 8%–10.8% $H_2O$, 3%–4.3% $O_2$, trace $SO_x$, $H_2S$, $NO_x$ | 52–86 | 50–100 |
| Hydrogen plant (steam methane reforming) | 12% | 29% $H_2O$, 50% $H_2$, 1% CO | >50 | 50–80 |
| Cement industry | 19% | 61% $N_2$, 13% $H_2O$, 8% $O_2$ | 62–94 | 60–120 |
| Steel industry (Blast furnace) | 20% | 56% $N_2$, 21% CO, 3% $H_2$ | >75 | 40–100 |
| Natural gas processing | 99%[22] | 1% $H_2O$[22] | 14–20 | 15–25 |
| Ammonia production | 99%[22] | 1% $H_2O$[22] | 19[22] | 25–35 |
| Bioethanol (fermentation) | 100% | — | 32[22] | 25–35 |
| Ethylene oxide (vented stream) | 100% | — | 26[22] | 25–35 |
| Air (for reference) | 0.04% | 78% $N_2$, 20% $O_2$, 1% Ar | — | 134–342 |

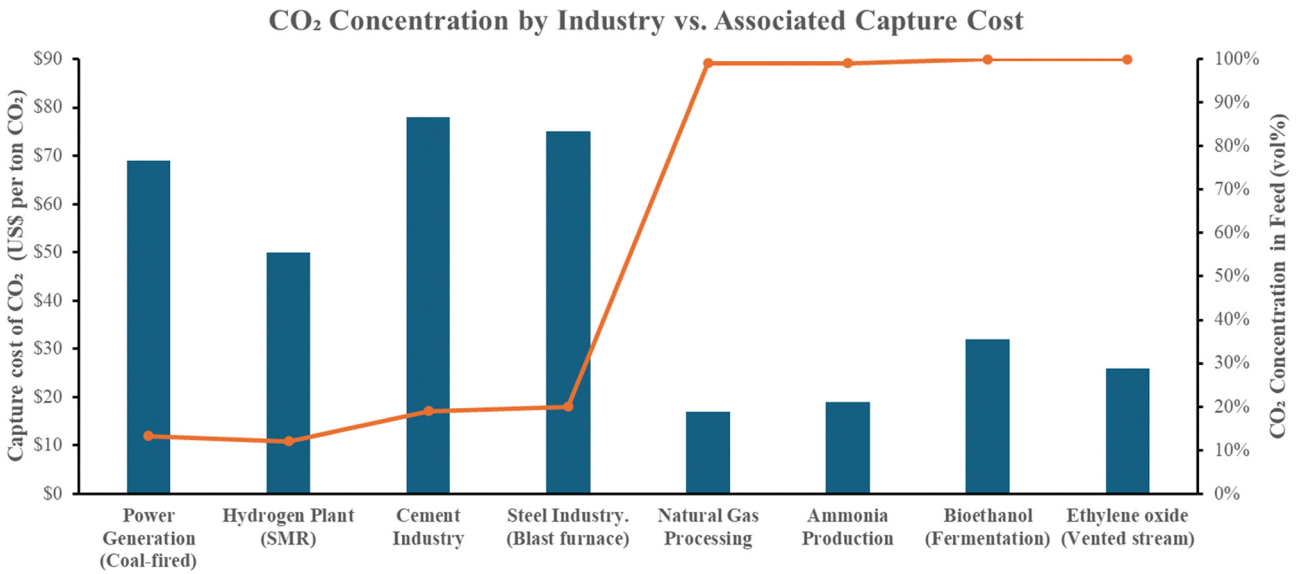


Fig. 4 Variation of $CO_2$ concentration in flue gas across different industries and impact on capture costs. The plotted data show estimated averages, reflecting the variability documented in the literature for each industrial application.

Open Access Article. Published on 12 fevral 2026. Downloaded on 01.06.2026 11:06:26.
This article is licensed under a Creative Commons Attribution-NonCommercial 3.0 Unported Licence.

efficiency; however, electrocatalytic approaches offer a compelling alternative by operating under mild, ambient conditions (<100 °C, <1 MPa).[23] By utilizing renewable electricity and water as a direct proton source, electrocatalysis eliminates the need for energy-intensive hydrogen storage and transport and leverages applied overpotentials to overcome thermodynamic limits, unlocking superior selectivity for valuable multi-carbon ($C_{2+}$) products like ethylene that are difficult to synthesize thermochemically. However, beyond $CO_2$ concentration, the stability of ICCC materials is critically compromised by flue gas impurities, which trigger distinct poisoning mechanisms that must be accounted for in reactor design. First, sulfur oxides ($SO_x$), being stronger acids than $CO_2$, react irreversibly with basic active sites to form heat-stable salts (sulfates) that survive standard regeneration, leading to permanent pore plugging and progressive capacity decay.[24] Second, nitrogen oxides ($NO_x$) compete *via* stronger adsorption on Lewis's acid sites (metal oxides, zeolites) and accelerate sorbent degradation through nitration/reduction side reactions, reducing faradaic efficiency.[25] Third, moisture exerts a dual negative effect: it competitively adsorbs on hydrophilic sites, hindering $CO_2$ uptake, and promotes hydrothermal sintering of dispersed metal nanoparticles during the high-temperature conversion step, effectively deactivating the catalyst.[26] Fourth, oxygen ($O_2$) selectively oxidizes hydrogenation catalysts (*e.g.*, Ru/Rh) and induces carbonate decomposition in solid DFMs.[27]

Regarding the impact of flue gas impurities on the direct electrochemical $CO_2$ conversion, Pimlott *et al.* assessed this using a reactive carbon electrolyzer for electrocatalytic (bi)carbonate conversion.[28] They found that flue gas containing sulfur oxides ($SO_x$), and nitrogen oxides ($NO_x$) exhibit markedly different impacts on the $CO_2$ electrolysis: $SO_x$ have minimal impact on CO selectivity, whereas $NO_x$ drastically reduce faradaic efficiency (FECO), from ~60% to <5% at 2000 ppm (Fig. 5a). Besides that, gas-fed $CO_2$ electrolyzer exhibited a +90% reduction in CO selectivity with 10% oxygen ($O_2$) in the feed while liquid-fed electrolyzer was unaffected, the same FECO of 65% at 100 mA $cm^2$ at an $O_2$-saturated feedstock and $O_2$-depleted feedstock (Fig. 5b). Thus, both $CO_2$ concentration and impurity composition must be considered when evaluating the economics and scalability of capture–conversion systems. Accordingly, the following sections will provide a detailed overview of state-of-the-art carbon capture technologies and separation techniques, followed by an in-depth analysis of the electrochemical conversion process.

## Overview of $CO_2$ capture technologies

There are three major approaches for carbon capture: post-combustion,[29] pre-combustion,[30] and oxyfuel combustion.[31] Determining the optimal carbon capture technique is a multi-faceted decision that requires evaluating a variety of technological and economic factors, such as the properties of flue gas, the required gas purity, the costs of plant construction and operation, the availability of commercial expertise, and the process's reliability and flexibility in operation. Thus, a thorough comparison of the three key $CO_2$ capture technologies for flue gas is summarized in (Table 2) and (Fig. 6).

As shown in (Fig. 7),[32,33] all three $CO_2$ capture technologies achieve high capture removal efficiency, with post-combustion and pre-combustion at 90% and oxyfuel combustion at over 90%, but they differ in their techno-economic performance. The pre-combustion process exhibits the lowest energy consumption and the most competitive capture cost at 3.35 GJ $t^{-1}$ $CO_2$ and $34–63 per t $CO_2$, respectively. In contrast, post-combustion is the least economically favorable, with the highest energy requirement of 4.14 GJ $t^{-1}$ $CO_2$ and a cost of $46–74 per t $CO_2$. At a middle ground, oxyfuel Combustion occupies as high energy consumption as Post-Combustion at 4.05 GJ $t^{-1}$ $CO_2$ but its capture cost remains moderately lower at $52 per t $CO_2$. Thus, this analysis indicates that, based on these metrics, the economic viability of the three carbon capture technologies

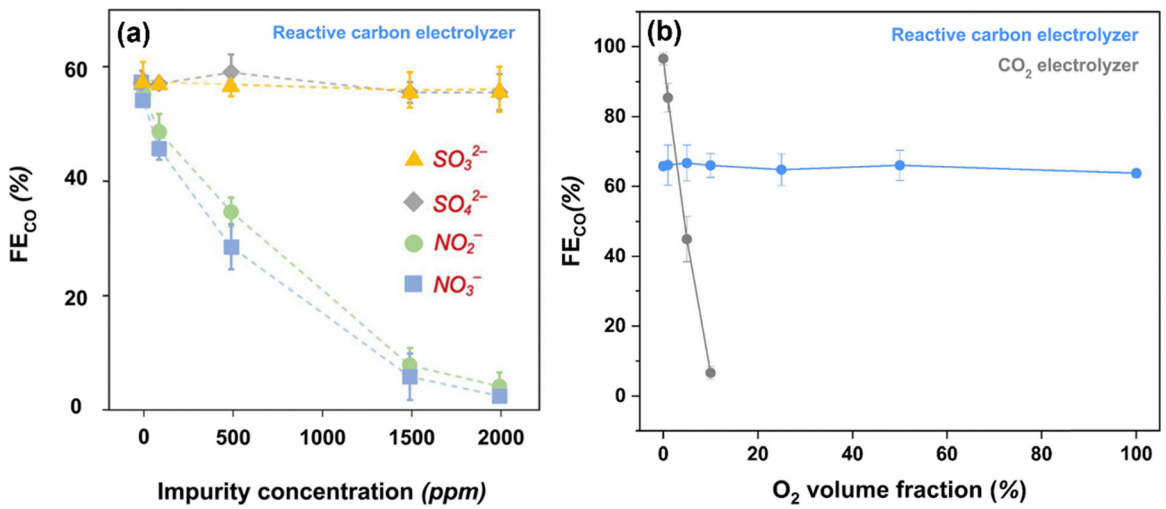


Fig. 5 Effect of flue gas impurities of (a) sulfur oxides ($SO_x$), nitrogen oxides ($NO_x$), and (b) oxygen ($O_2$) on CO selectivity in the direct electrochemical $CO_2$ electrolysis. Reprinted (adapted) from *Chem. Soc. Rev.*, 2025,**54**, 590–600. Copyright © 2025 the Royal Society of Chemistry.


© 2026 The Author(s). Published by the Royal Society of Chemistry

Open Access Article. Published on 12 fevral 2026. Downloaded on 01.06.2026 11:06:26.
This article is licensed under a Creative Commons Attribution-NonCommercial 3.0 Unported Licence.

Table 2 SWOT analysis of $CO_2$ capture technologies[32,33]

| Carbon capture technology | Mechanism | Strengths | Weaknesses/threats | Opportunities |
|---|---|---|---|---|
| Post combustion | A process involves $CO_2$ capture from gas streams produced after the combustion of fossil fuels or other carbonaceous materials | – Mature, retrofittable technology.<br>– Higher thermal efficiency *vs.* pre-combustion method.<br>– Additional removal of NOx and SOx emissions | – Low $CO_2$ concentration reduces efficiency<br>– High flue gas temperatures and volumes cause design challenges<br>– Trace impurities such as NOx and SOx significantly affect the adsorption method<br>– Requires powerful chemical solvents to capture $CO_2$ at low concentrations<br>– Energy-intensive solvent regeneration | – Research into hybrid systems (*e.g.* membrane-pressure swing adsorption)<br>– Improving pulverized coal systems to reduce emissions<br>– Plant productivity enhancement |
| Pre combustion | A process transformes fuels into a gasified state to separate the $CO_2$ before burning the hydrogen-rich fuel like the SMR process | – 38–45% cheaper than post-combustion<br>– 50% less energy for $CO_2$ separation than post-combustion due to high concentration and partial pressures<br>– Minimal regeneration energy<br>– Low-cost physical solvents | – Heat transfer and efficiency issues due to the high temperature of $H_2$-rich gas<br>– Extensive supporting systems, such as an air separation unit and flue gas cooling<br>– Complex chemical processes lead to additional plant shutdowns<br>– Higher energy loss than post-combustion for reforming and air separation processes<br>– Requires special non-gaseous feedstocks and NOx control | – Research needed for high-value chemical feedstock production<br>– Flexible hydrogen/electricity production<br>– Syngas as alternative turbine fuel |
| Oxyfuel combustion | A process involves oxygen rather than air burns fuel to produce flue gas with high $CO_2$ concentration | – 70–95% less expensive than other carbon capture methods due to lower flue gas volume and higher $CO_2$ concentration<br>– 60–70% less $NO_x$ emissions than air-fired combustion due to the absence of nitrogen<br>– High-pressure operation reduces compression energy<br>– Preserves high-efficiency steam cycles<br>– Can be retrofitted into existing power plants | – Technology needs validation at a large scale<br>– Pure oxygen combustion challenges due to the high temperatures involved<br>– High capital expenditure and energy consumption costs due to the required larger amounts of oxygen, air separation, and flue gas recirculation costs<br>– High risk of $CO_2$ leakage | – Research needed for heat-resistant materials and oxygen separation beyond cryogenic distillation<br>– Improvements to reduce economic and efficiency penalties<br>– Multiple fuel compatibility such as biomass and municipal solid waste for carbon neutrality |

falls in the sequence: pre-combustion > oxyfuel combustion > post-combustion, especially for high-pressure, high-$CO_2$-concentration applications like IGCC and hydrogen production.

## $CO_2$ separation techniques

The primary factors to consider when employing ICCC technologies are the $CO_2$ generation process, the technical readiness level (TRL), the efficiency of $CO_2$ separation, the economic costs, the environmental impact, which can be assessed through life cycle assessment (LCA) and the potential for $CO_2$ utilization either on-site or in nearby areas of a facility. And, each $CO_2$ capture technology applies different separation techniques such as chemical absorption, physical absorption, adsorption, membrane filtration, cryogenic separation, chemical looping combustion, calcium looping, and electroswing, which are summarized in (Table 3)[10,20,32–35] and (Fig. 8).

As Fig. 8 illustrates, among the $CO_2$ separation techniques, physical absorption stands out as the sole Tier 1 performer, demonstrating a high $CO_2$ removal efficiency of 93%, coupled with low energy consumption (1.03 GJ per $tCO_2$) and minimal capture cost (USD 12.38 per $tCO_2$).[36] In contrast, technologies such as chemical absorption (90%, ~3 GJ per $tCO_2$, USD 48.07 per $tCO_2$[36]), membrane filtration (up to 88%, ~2 GJ per $tCO_2$, USD 36.78 per $tCO_2$[36]), and calcium looping (89%, 2.8 GJ per $tCO_2$, USD 32 per $tCO_2$[37,38]) fall under Tier 2, primarily due to their moderate energy demands and higher capture costs. Meanwhile, chemical looping combustion (96%, 0.95 GJ per $tCO_2$, USD 59.2 per $tCO_2$[33]), cryogenic separation (95%, 3.8 GJ per $tCO_2$, USD 55 per $tCO_2$[39,40]), and adsorption (90%, 4 GJ per $tCO_2$, USD 47 per $tCO_2$[39,40]) are categorized as Tier 3, reflecting a trade-off wherein high capture efficiencies are accompanied by significant energy penalties and costs. It should be noted that all of these values represent averages, which may be influenced by various

Open Access Article. Published on 12 fevral 2026. Downloaded on 01.06.2026 11:06:26.
This article is licensed under a Creative Commons Attribution-NonCommercial 3.0 Unported Licence.

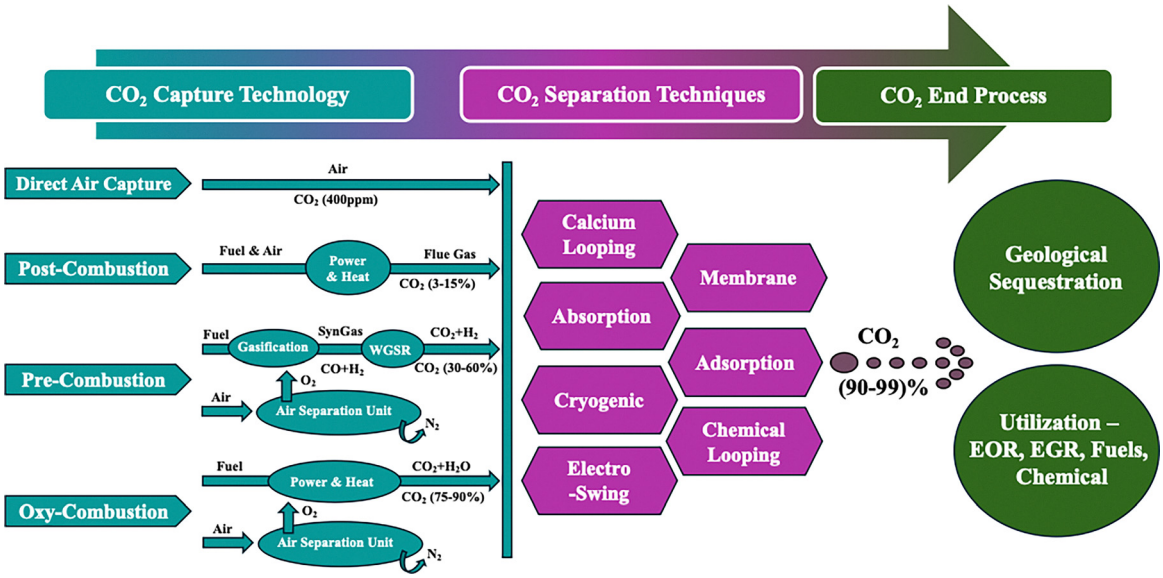


Fig. 6 Process flow of major $CO_2$ capture technologies, subsequent separation techniques, and the final pathways for either geological sequestration or industrial utilization.

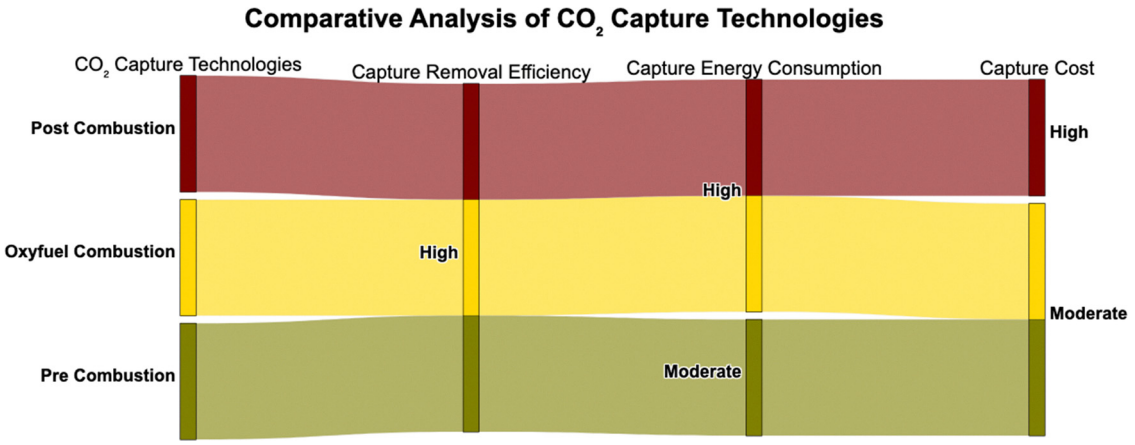


Fig. 7 Sankey diagram comparing three major $CO_2$ capture methods in terms of capture efficiency, energy consumption, and cost. These pathways illustrate general trends, as actual performance may vary significantly depending on scale, technology maturity, and operating conditions.

factors, including operating temperature and pressure, flue gas composition, properties of the capture agent, scale of deployment, and, most notably, the technology readiness level (TRL), which is addressed subsequently.

## Technology readiness level (TRL)

Regarding Technology readiness level (TRL), as defined by the US Government Accountability Office (US GAO), Technology readiness level (TRL) is a nine-level scale system used to assess the maturity of a technology, ranging from the initial observation and reporting of fundamental principles to the successful implementation in mission operations, which was adopted by the Electric Power Research Institute (EPRI) for use with $CO_2$ processes.[41] Accordingly, TRL spectrum for ICCC can be divided into three phases: the research phase covers TRLs 1–3, the development phase encompasses TRLs 4–6, and the demonstration or deployment phase covers TRLs 7–9. In detail, the stages of technology readiness levels (TRL) begin with the basic principles (TRL 1), progress through application formulation (TRL 2), laboratory-scale development (TRL 3–5), pilot-scale trials (TRL 6), demonstration scale (TRL 7), commercial refinement (TRL 8), and eventually reaching full commercial scale (TRL 9). In (Fig. 9), a comparative overview of the Technology Readiness Levels (TRL) is presented for major $CO_2$ separation techniques in specific industries.[39,40,42,43] Among these, absorption is the most mature technology and has full commercial deployment among the other separation methods, depending on the type of solvents such as Amine, Selexol, and Rectisol. In contrast, separation techniques like Chemical Looping, Membrane Filtration, and cryogenic separation exhibit lower technology


© 2026 The Author(s). Published by the Royal Society of Chemistry

Open Access Article. Published on 12 fevral 2026. Downloaded on 01.06.2026 11:06:26.
This article is licensed under a Creative Commons Attribution-NonCommercial 3.0 Unported Licence.



Table 3 SWOT analysis of $CO_2$ separation technologies

| Separation method | Mechanism | Strengths | Weaknesses/threats | Opportunities |
|---|---|---|---|---|
| Physical absorption | Absorption of $CO_2$ in the solvent is governed by its solubility, as defined by Henry's law, with solubility varying in response to temperature and pressure changes like in materials of Selexol and Fluor | – Low energy needed for sorbent regeneration<br>– Low corrosivity and toxicity<br>– More cost-effective at higher $CO_2$ partial pressures | – Limited operating temperature range; solvent capacity is optimized at lower temperatures to avoid any reduction in the solvent<br>– High capital and operational costs | – Potentially operating at lower temperatures than chemical methods, so less energy consumption and cost |
| Chemical absorption | Upon interaction with the solvent, $CO_2$ forms an intermediate through a reversible or irreversible chemical process, which subsequently breaks down, releasing $CO_2$ upon heating like in materials of amines, ionic liquids, and Phase-change solvents | – Mature technology due to its high absorption capacities, such as amine absorption<br>– High product purity > 99% vol.<br>– Well-suited for retrofit<br>– Effective at low $CO_2$ partial pressures | – Higher water consumption<br>– Exhaust gases (water, SOx, and NOx) need to be treated<br>– High regeneration energy costs<br>– Requires a large absorber volume | – Further advancements needed for amines and ionic liquids |
| Adsorption | The flue gas flows over a solid sorbent, where $CO_2$ is adsorbed, and other gases are allowed to pass, with the desorption of $CO_2$ occurring through changes in temperature and pressure like in materials of zeolite, metal–organic, framework, activated carbon, and polymeric resins | – Flexibility in operating conditions with low-maintenance operation and Easy installation<br>– Regeneration occurs at lower temperatures, so less heat than absorption methods<br>– Waste biomass or industrial by-products can be used in adsorbent synthesis<br>– The process is reversible through physical adsorption<br>– Adsorbent can be recycled, hence low waste generation | – Sensitive to contaminants like sulfur, and nitrogen oxides, affecting their efficiency<br>– Poor adsorbent durability, resulting in additional costs for frequent material replacements<br>– Challengeable to achieve the optimal operating temperature | – Advances in developing composite adsorbents to have cost-effective, reusable, and non-corrosive sorbents<br>– A wide range of potential sorbent materials exist<br>– Dry gas products can be addressed |
| Membrane filtration | $CO_2$ is separated from the main gas stream using a membrane that operates in two ways: the gas separation membrane, which exposes flue gas to the high-pressure side and separates $CO_2$ on the low-pressure side, and the gas absorption microporous membrane, which enables both gas flow and absorption like in materials of graphene, organic, inorganic, and mixed matrix | – Simple, modular system design for easy adaptation<br>– No regeneration energy required, leading to lower costs<br>– Higher energy efficiency compared to absorption and adsorption methods<br>– Zero waste by-products generated<br>– Continuous separation, offering efficiency over time | – Structural problems under high-pressure conditions lead to instability<br>– Long-term performance degradation due to sensitivity to corrosive gases makes sustained operation challenging<br>– Moderate product purity | – Advances in composite hollow-fiber membranes, mixed matrix membranes, and hybrid membrane-cryogenic processes<br>– Low separation costs and minimal energy requirements might push this technology forward<br>– Minimal footprint, making it ideal for offshore applications<br>– High commercial availability with efficient separation capabilities |
| Cryogenic separation | $CO_2$ is separated from a gas mixture through consecutive refrigeration at different condensation temperatures, inducing phase changes only in carbon dioxide based on its dew point or sublimation like in materials of ceramic, glass, and aqueous | – Commercially proven and well-established technology<br>Easily integrated into power stations and other industrial point sources<br>– Energy savings by reducing the need for compression<br>– No chemicals required for the process, making it simpler and more sustainable<br>– Capable of filtering other pollutants, offering additional environmental benefits | – Moisture removal is required from flue gas to prevent ice formation and equipment blockages<br>– Energy-intensive due to the extreme cooling requirements, increasing operational costs<br>– Accumulation of solid $CO_2$ reduces evaporator or heat exchanger efficiency over time | – High purity of the captured $CO_2$ raises its economic value for various industrial uses |

© 2026 The Author(s). Published by the Royal Society of Chemistry

Open Access Article. Published on 12 fevral 2026. Downloaded on 01.06.2026 11:06:26.
This article is licensed under a Creative Commons Attribution-NonCommercial 3.0 Unported Licence.



Table 3 (*continued*)

| Separation method | Mechanism | Strengths | Weaknesses/threats | Opportunities |
|---|---|---|---|---|
| Chemical looping combustion | The combustion process is split into oxidation and reduction phases, each carried out separately, with a solid oxygen carrier being oxidized by air in the first phase and then reduced with a hydrocarbon in the second phase, producing $CO_2$ and $H_2O$ | – Simple operation, with compatibility for low $CO_2$ partial pressures<br>– The exhaust stream from the fuel reactor contains $CO_2$ and water, where $CO_2$ can be efficiently separated by condensation<br>– The process relies on low-cost oxygen carriers | – Early-stage technology<br>– Fuel needs to be desulfurized to avoid metal sulfide formation<br>– Sensitivity to any air leakage<br>– Retrofitting the system is complex<br>– Costly oxygen production | – Exhaust gas from the air reactor is primarily nitrogen, with no harmful compounds<br>– No need for energy-heavy air separation, as the process yields high concentrations of $CO_2$ |
| Calcium looping combustion | $CO_2$ is captured through reversible reactions between CaO and $CO_2$, known as carbonation and calcination for the respective stages | – Cost-effective raw materials for sorbent synthesis<br>– Ideal technique for retrofitting pulverized coal-fired power plants and enhancing sorption-based hydrogen production | – Rapid decline in limestone (sorbent) capacity after several $CO_2$ reaction cycles<br>– Environmental concerns relate to limestone mining, waste from Ca-looping, and high operational temperatures<br>– Need for an air separation unit to supply pure oxygen ($O_2$) for calcination | – Offering a minimal decrease in power plant efficiency, with the potential for further reduction |
| Electroswing | It operates by using a reversible electric current to either directly charge an electrode for $CO_2$ adsorption or to manipulate a solution's pH, creating a chemical swing that captures and then releases the gas like in materials of quinones, ferrocenes, and carbon nanotubes | – Ambient operating conditions<br>– Low cost due to the decreasing cost of renewable electricity | – Technology readiness is still at the pilot stage<br>– Low current density due to their inability to operate at high current densities, limited to less than 5 mA $cm^{-2}$<br>– High energy consumption and cost: to run at higher current densities results in large overpotentials, which lead to a higher energy demand and increase the capital cost | – Developing novel electrode materials to overcome current limitations, *e.g.*, advanced redox-active organics and electrode designs<br>– Further scaling and optimization are needed for commercialization |



© 2026 The Author(s). Published by the Royal Society of Chemistry

Open Access Article. Published on 12 fevral 2026. Downloaded on 01.06.2026 11:06:26.
This article is licensed under a Creative Commons Attribution-NonCommercial 3.0 Unported Licence.

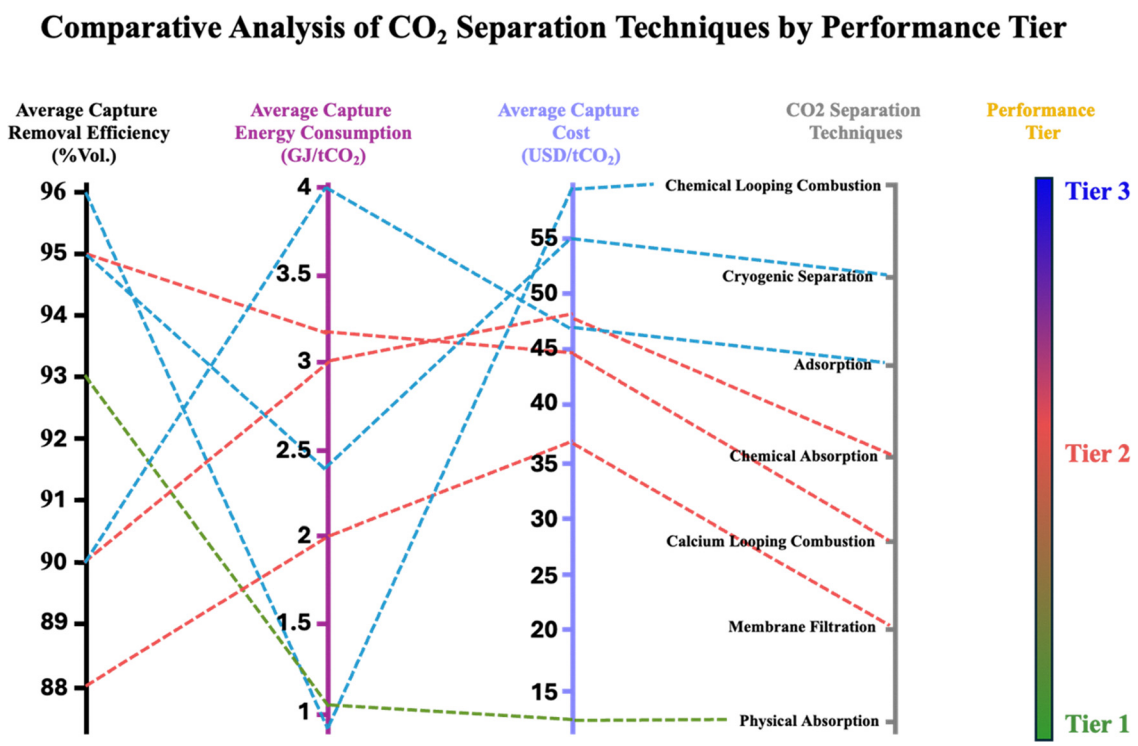


Fig. 8 Parallel coordinates plot comparing seven $CO_2$ separation methods across three techno-economic indicators: average removal efficiency, energy consumption, and capture cost, color-coded by three performance tiers (Tier 1: green; Tier 2: red; Tier 3: blue). The plotted values are representative benchmarks and an indicative guide from the literature and are subject to variation based on real-world operating conditions.

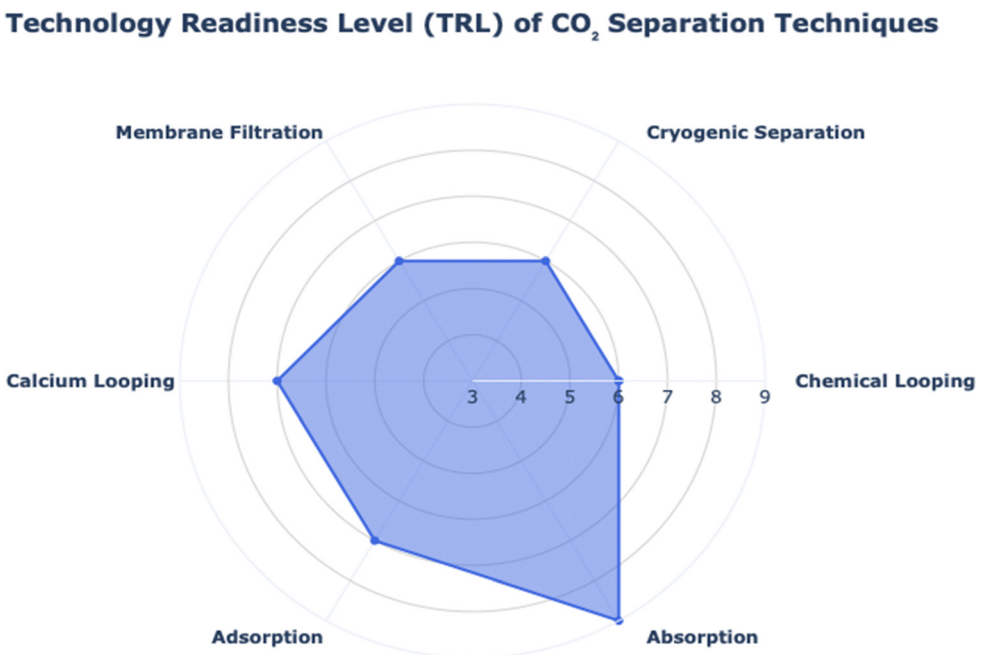


Fig. 9 Comparative TRL assessment for each of across the $CO_2$ separation techniques. TRLs are dynamic and context-dependent, varying with system design, operating conditions, and demonstration scale, and the values shown correspond to the highest levels reported in the literature for each technique.

maturity (TRL 5-6)[44,45] which reflects their limited operational experience and deployment beyond laboratory or pilot scales. Meanwhile, separation techniques such as adsorption and calcium looping are positioned at intermediate (TRL 6-7),[46] which indicates active development and initial field demonstrations, but not yet full commercial viability. Assessing these TRL levels underscores which $CO_2$ capture and separation technologies are approaching commercialization, and which still require significant scale-up and

Open Access Article. Published on 12 fevral 2026. Downloaded on 01.06.2026 11:06:26.
This article is licensed under a Creative Commons Attribution-NonCommercial 3.0 Unported Licence.

practical field validation since technology maturity significantly impacts both the feasibility and short-term adoption prospects of these carbon capture approaches.

## Electrochemical conversion: mechanism

Besides the direct use of $CO_2$ in several industrial processes such as enhanced oil recovery, urea production, food and beverage, water treatment, and fire retardants, there are several routes to convert $CO_2$ into commercial products, including thermal, electrochemical, photocatalytic, photosynthetic, biological, copolymerization, and mineralization.[47] While extensive research in academia has focused on developing materials for $CO_2$ capture from point sources and ambient air, and subsequent conversion to value-added chemicals[48] such as fuel production, like methane,[49] methanol,[50] and formic acid,[51] this review paper primarily emphasizes the electrochemical conversion process.

Among the various $CO_2$ conversion techniques, electrochemical conversion has multiple advantages, including mild reaction conditions, potential synergy with renewable energy sources, high environmental compatibility, and controllable reaction rate and product selectivity by modulating the applied electrode potential; however, several challenges still need to be addressed such as high energy requirements, durability, environmental impacts and sustainability of certain conversion products, and high thermodynamic and kinetic barriers.[17]

After efficient capture and separation of $CO_2$ gas, the $CO_2$ undergoes electrochemical conversion to valuable carbon-based products such as carbon monoxide, ethylene, ethanol, and more through a multi-proton-coupled and multi-electron transfer process.[52] Generally, the electrochemical $CO_2$RR can be presented as

$$xCO_2 + n(H^+ + e^-) \rightarrow \text{product} + yH_2O$$

Noting that the anodic reaction is the oxygen evolution reaction (OER) while the contemporaneous reduction of $H^+$ is accompanied by the hydrogen evolution reaction (HER), which should be restricted during the electrolytic reduction of $CO_2$ by considering the thermodynamics involved in the whole conversion process to get the desired product.[53] Additionally, the electrocatalytic reduction of $CO_2$ follows a three-part reaction mechanism: electron transfer, electrochemical reaction, and catalytic reaction.[54]

Initially, $CO_2$ dissolved in the electrolyte gets in contact with the electrode, where it adsorbs onto the catalyst for activation. Secondly, the reduction of adsorbed $CO_2$ occurs through proton-electron transfer on the catalyst surface, which breaks the C=O bond and requires about 750 kJ per mole as a thermodynamically uphill reaction, forming a new chemical bond (COOH*), where * denotes surface-bound species or vacant catalytically active sites. Subsequently, the reduction products are desorbed from the electrode and diffuse into the response medium, which depends not only on the stability but also on the reduction of COOH*, but also on the catalyst's capacity.

## Integrated carbon capture and conversion: ICCC mechanism

Regarding $CO_2$ capture and conversion from diluted sources, the electrochemical conversion has been operated in three distinct processes: independent, coupled, and integrated.[55] The independent process involves multiple decoupled processes, in which $CO_2$ capture occurs independently of electrochemical $CO_2$ conversion, leading to energy losses and costs associated with $CO_2$ compression, transportation, purification, and release. In the integrated process, it simultaneously exhibits complete integration between the capture and electrochemical conversion of $CO_2$, directly converting the captured $CO_2$ at the electrode

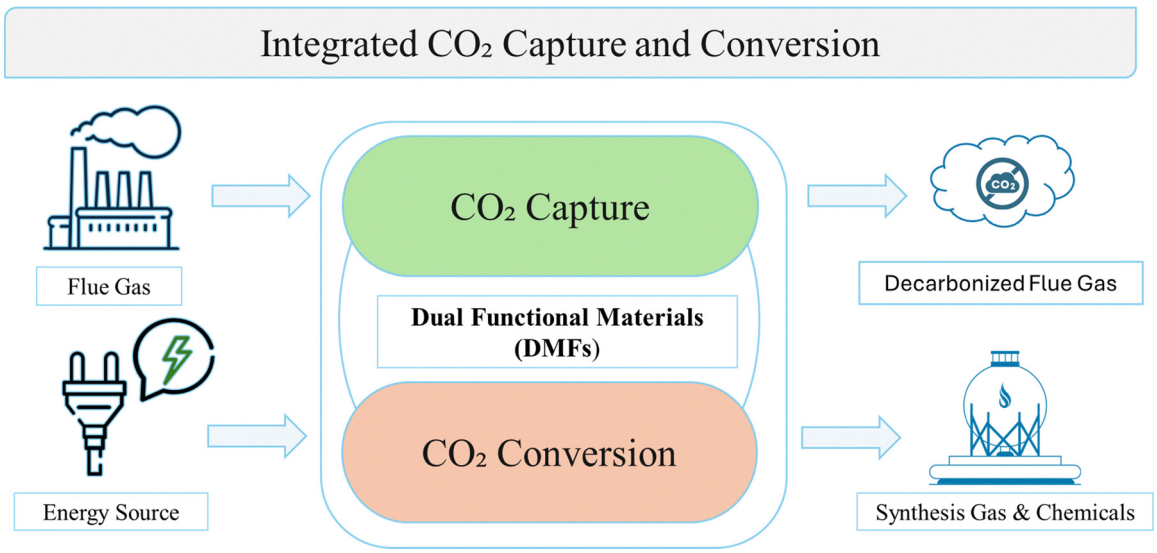


Fig. 10 Conceptual overview of the integrated $CO_2$ capture and conversion (ICCC) process by using dual functional materials (DFMs).


© 2026 The Author(s). Published by the Royal Society of Chemistry

Open Access Article. Published on 12 fevral 2026. Downloaded on 01.06.2026 11:06:26.
This article is licensed under a Creative Commons Attribution-NonCommercial 3.0 Unported Licence.

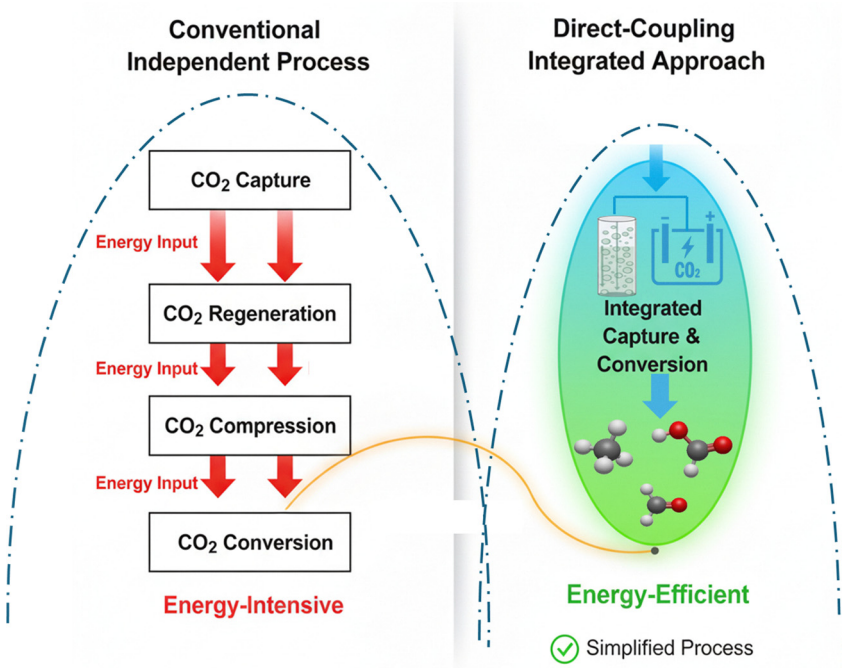


Fig. 11 A conceptual energy diagram contrasting the conventional, energy-intensive independent process *versus* the direct coupling 'integrated' approach of carbon capture and conversion.

surface to the regeneration of the capture media and the production of valuable products, which reduces the complexity and energy consumption of the overall process, as shown in (Fig. 10 and 11). For electrochemical ICCC pathways operated at industrially relevant current densities ($\sim$200–800 mA cm$^{-2}$), solid oxide and molten carbonate electrolysis systems achieve $>$70–90% energy efficiency, with electricity consumption below $\sim$2.5–3.4 kWh Nm$^{-3}$ CO at $\sim$200 mA cm$^{-2}$ (equivalent to $\sim$2200 kWh t$^{-1}$ CO produced), while maintaining near-unity faradaic efficiencies ($>$99%) at current densities exceeding 750 mA cm$^{-2}$.[56] Therefore, the integrated process bypasses the $CO_2$ stripping steps, thereby compensating for capture costs and making commercial deployment economically more feasible. Consequently, the following section will explore dual-functional materials for Integrated Carbon Capture and Conversion (ICCC), with a particular focus on key adsorbent and absorbent materials.

## Dual functional materials (DFMs): adsorbents and absorbents materials

As flue gases are characterized by high temperatures (around 373 K), low pressures, and low $CO_2$ levels (1 atm and 10–15% mol), absorption and adsorption processes are likely the most efficient methods for $CO_2$ separation under these conditions, with the highest TRL among $CO_2$ separation methods, which are the primary focus of this review,[57] and the process itself simply illustrated in (Fig. 12). Regarding absorption, it refers to $CO_2$ dissolving into a solvent with 60–95% $CO_2$ removal efficiency, where it may either chemically react with the solvent as in chemical solvents such as Amines or be held by weak van der Waals forces as in physical solvents such as Selexol, Fluor, Purisol, and Sulfinol.[58] On the other hand, adsorption method is divided into two types: chemisorption, where covalent bonds are created, and physisorption, where electrostatic and van der Waals forces dominate the interaction, using solid adsorbents such as activated carbon and silicates, with 80–95% $CO_2$ removal efficiency.[59]

In this context, this timely and thorough review paper summarizes the latest developments of the integrated process progress with an emphasis the following promising dual functional materials: adsorbents such as porous organic polymers (POPs), covalent organic frameworks (COFs), metal–organic frameworks (MOFs), zeolites and absorbents such as amines, ionic liquids, eutectics, and molten salts, the mechanism (Fig. 13).

## Sorbent-based $CO_2$ capture and conversion

This section focuses on solid-phase techniques for $CO_2$ capture, emphasizing advanced sorbents such as porous organic polymers (POPs), covalent organic frameworks (COFs), zeolites, metal–organic frameworks (MOFs), and metal oxides, and their applications in integrated electrochemical $CO_2$ capture and conversion systems. This analysis will highlight their advantages, challenges, future outlook, and potential for rapid implementation in carbon-neutral technologies.

## Porous polymer materials

Recently, porous materials such as zeolites,[60] porous carbon compounds,[61] and porous polymers[62] have been used in intriguing research advancements in $CO_2$ recuperation and electrocatalytic reduction (Fig. 14). Because of their finely engineered

Open Access Article. Published on 12 fevral 2026. Downloaded on 01.06.2026 11:06:26.
This article is licensed under a Creative Commons Attribution-NonCommercial 3.0 Unported Licence.

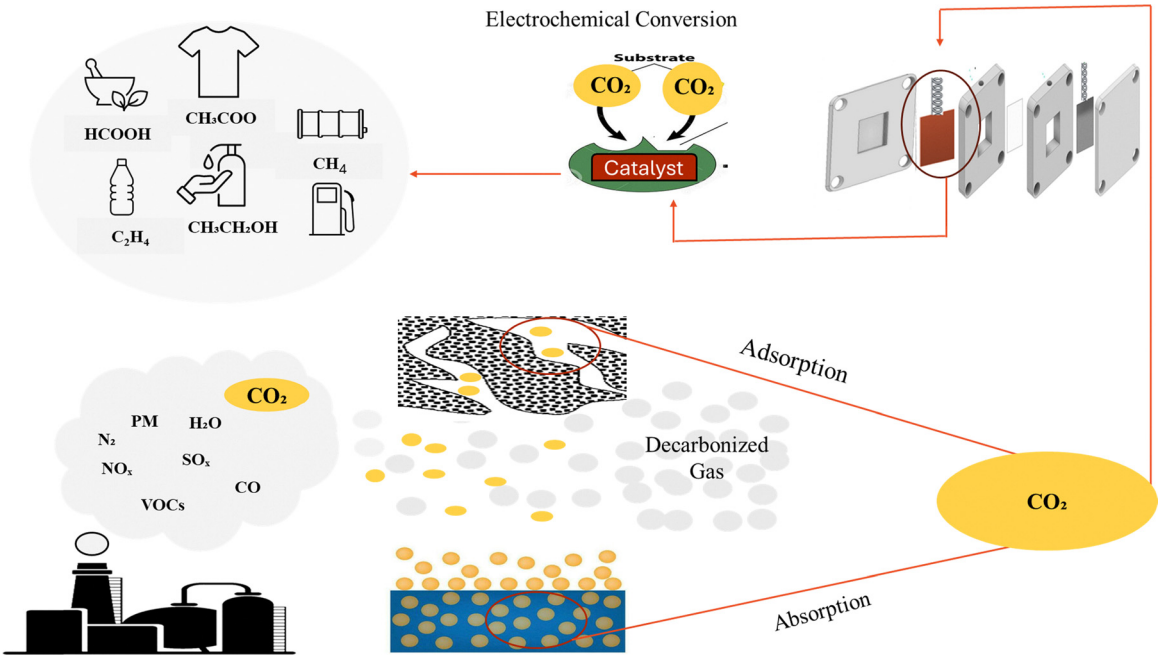


Fig. 12 A schematic of the two-step process involving carbon capture with a sorbent or solvent material, followed by carbon conversion into final products.

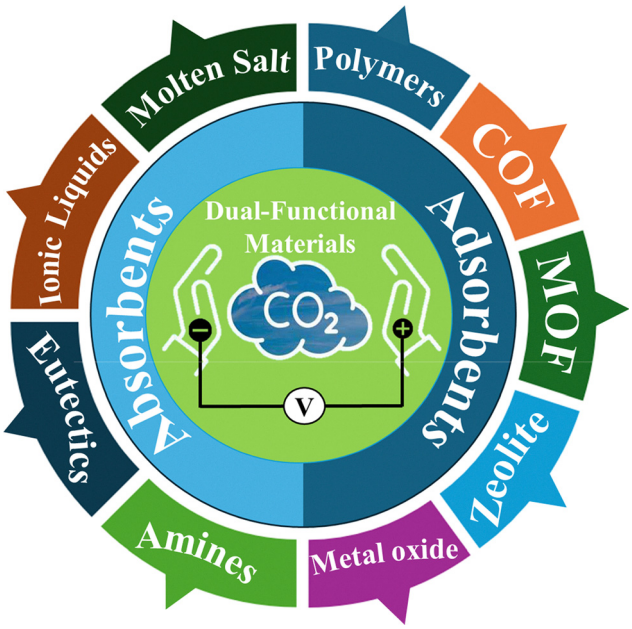


Fig. 13 Examples of the dual-functional materials used in integrated processes, with emphasis on the adsorbents and absorbents highlighted in this review.

active sites, high specific surface area, and controllable porosity, porous polymers stand out among the others.[63,64] There are four primary types of porous polymer materials utilized for $CO_2$ capture and electrocatalytic reduction, which are nitrogen-containing polymers (N-polymers), covalent organic frameworks (COFs), porous organic polymers (POPs), and porous coordination polymers (PCPs) (Table 4). Numerous synthetic techniques, such as solvothermal, iono-thermal, microwave, mechanochemical, and interfacial synthesis approaches, can be used to create such porous polymeric materials. The most popular preparation technique among them is the solvothermal approach.[65,66] The solvent thermal method's main drawback is that it is not appropriate for large-scale production because the reaction conditions are harsh and the solvent is primarily organic, which will pollute the environment when used in large quantities. However, it can increase synthesis efficiency by switching the solvent. The iono-thermal approach is not appropriate for commercial applications since it is primarily employed for the synthesis of covalent triazine frameworks (CTFs) and requires more stringent reaction conditions than the solvent thermal method.[67] One interesting synthesis technique is the microwave approach, which may efficiently shorten reaction times while preserving porosity.[68] Due to its simplicity, the mechanochemical approach is a suitable green synthesis method since it doesn't use solvents, which prevents contamination of the environment.[69] Three stages are typically involved in the $CO_2$ reduction reaction ($CO_2$RR): $CO_2$ adsorption, electrocatalytic reduction, and desorption. Specifically, a $CO_2$-saturated electrolyte is created by first dissolving gaseous $CO_2$ molecules in the solvent. On the electrode surface, the $CO_2$ dissolved in the solvent then undergoes a reaction. To finish the entire reaction process, the reaction products are finally desorbed off the electrode surface. Defined reaction mechanisms are yet unknown due to the many products and intricate intermediates in the multi-step reactions of $CO_2$RR. By transferring varying quantities of electrons, $CO_2$ can experience varying degrees of electrochemical reduction processes, as shown by the reaction equations in the table. The products of these reactions include HCOOH, $CH_3OH$, CO, $CH_4$, $CH_3COOH$, $C_2H_4$,


© 2026 The Author(s). Published by the Royal Society of Chemistry

Open Access Article. Published on 12 fevral 2026. Downloaded on 01.06.2026 11:06:26.
This article is licensed under a Creative Commons Attribution-NonCommercial 3.0 Unported Licence.

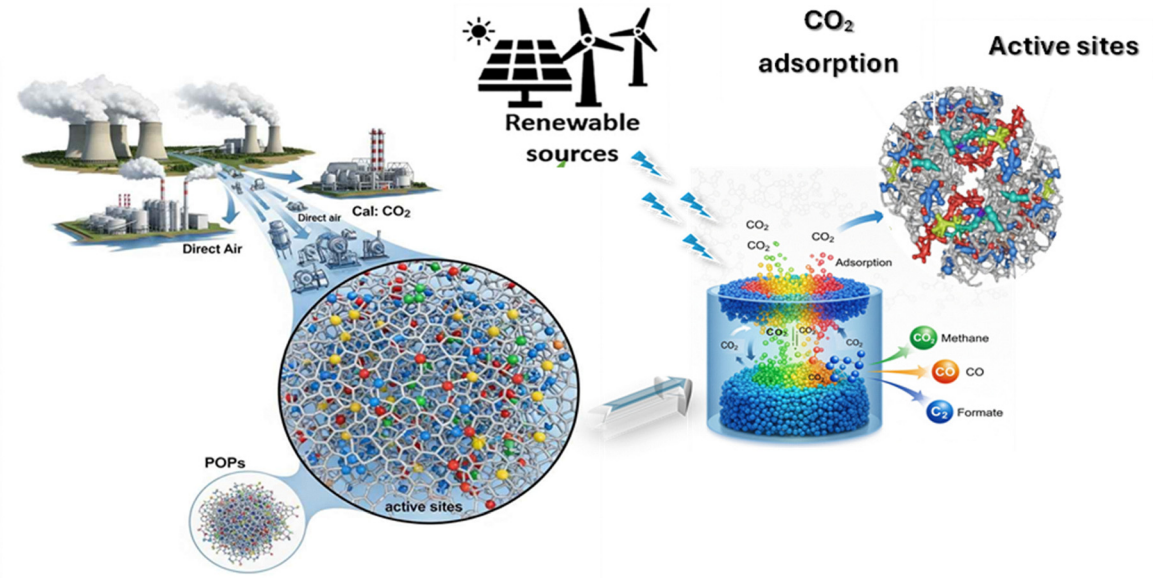


Fig. 14 Graphical abstract of POPs for $CO_2$ capture and electrocatalytic conversion.

Table 4 Advantages and disadvantages of porous polymer materials for $CO_2$ capture and electrocatalytic reduction[63]

| Materials | Structural features | Advantages | Disadvantages (technical) | Techno-economic barriers |
|---|---|---|---|---|
| POPs | 2D/3D covalent networks from organic polymerization | – Large SSA (up to 3000 $m^2 g^{-1}$) | – Poor microporosity ($V_{micro}$ <50%) | – High monomer cost ($50–200 per kg) |
| | | – Controllable functionality | – Oxidative degradation (+0.8 V) | – Solvothermal scale-up ($ZnCl_2$, 400 °C) |
| | | – Tunable porosity<br>– Good thermal stability (>400 °C) | – Swelling in humid flue gas | – Poor recyclability (30% SSA loss/cycle) |
| PCPs | Metal ions/clusters + organic linkers (crystalline) | – Ultra-high SSA (>7000 $m^2 g^{-1}$)<br>– Adjustable pore function | – Poor thermal stability (<300 °C)<br>– Hydrolysis in humid flue gas | – Metal salt cost ($100–500 per kg)<br>– Multi-step solvothermal (DMF, 120 °C) |
| | | – High $CO_2$ capacity (10 mmol $g^{-1}$) | – Metal leaching under bias | – Non-recyclable (framework collapse) |
| COFs | Crystalline covalent organic frameworks | – Large SSA (4210 $m^2 g^{-1}$)<br>– Abundant active sites (N-doping)<br>– Diverse synthesis routes | – Poor crystallinity control<br>– Hydrolysis (>50% loss @80% RH)<br>– Low conductivity | – High cost ($200–1000 per kg)<br>– Slow crystallization (days–weeks)<br>– Non-recyclable (irreversible hydrolysis) |
| N-polymers | Nitrogen-functional polymers (± metals) | – Simple preparation<br>– Cost-efficient ($10–50 per kg) | – Poor conductivity ($R_{ct}$ >100 Ω)<br>– Mechanical instability | – Large-scale mixing challenges<br>– Moderate recyclability (50% capacity loss) |
| | | – Adjustable pores | – Low SSA (<500 $m^2 g^{-1}$) | – Limited flue-gas tolerance |

$CH_3CH_2OH$, $C_2H_6$, and so on. Furthermore, HER on the cathode coincides with the $CO_2$ decrease.

## Porous organic polymers (POPs)

Porous organic polymers (POPs) constitute a category of lightweight, porous network materials characterized by extensive surface areas, adjustable pore sizes, and customizable components and structures. They consist of biological building units linked by covalent bonds. POPs utilized as electrocatalysts have exhibited notable activity and achieved substantial advancements in numerous electrocatalytic reactions, including the hydrogen evolution reaction, oxygen evolution reaction, oxygen reduction reaction, $CO_2$ reduction reaction, $N_2$ reduction reaction, nitrate/nitrite reduction reaction, nitrobenzene reduction reaction, hydrogen oxidation reaction, and benzyl alcohol oxidation reaction, owing to their well-maintained structural and compositional attributes. This section presents a comprehensive description of recent advancements in the application of POPs in electrocatalytic $CO_2$ reduction.[62,70,71] $CO_2$ reduction reactions ($CO_2$RRs) are transforming $CO_2$ molecules into hydrocarbon fuels through sustainable operations. These processes require unique catalytic systems, such as transition-metal dichalcogenides/phosphides, single-atom catalysts, perovskite materials, graphene derivatives, layered double hydroxides, metal oxides, two-dimensional metal-carbonitride and metal-boride layered materials, and POPs, which are recognised for

Open Access Article. Published on 12 fevral 2026. Downloaded on 01.06.2026 11:06:26.
This article is licensed under a Creative Commons Attribution-NonCommercial 3.0 Unported Licence.

their physicochemical properties and potential for energy-driven operations.[72]

## Physicochemical properties of porous organic polymers

Porous organic polymers (POPs) are regarded as a promising candidate for $CO_2$RR applications because of their superior stability, adaptability, perpetual porosity, and structural and compositional customization. Researchers have employed heteroatom-rich microporous structures and surface functionalization to increase $CO_2$RR activity.[62] Porosity tailoring has recently produced cutting-edge POPs materials with surface-active spots that catalyze reactions. Covalent bonds hold organic connections together to form POPs. The ability to tune $CO_2$ adsorption can be achieved *via* engineering by selectively functionalizing monomers and adding $CO_2$-philic metallic or nonmetallic sites. Transition-metal ions or nanoparticles can be immobilized on the POP surface to create metallized POPs. POP materials with various organic functional groups also use conjugated architectures to increase catalytic performance.[73–75] It has very good physicochemical features, such as high specific surface areas (up to 3001 $m^2\ g^{-1}$) and tunable pore designs (from microporous to hierarchical) made up of stiff organic building pieces that form covalent networks. They are very stable at high temperatures (up to 800 °C) and resistant to chemicals in severe settings. Fluorination makes them even more water-repellent. Because Lewis's acid–base interactions happen in ultra-micropores, POPs are good at adsorbing gases like $CO_2$ (up to 6.58 mmol $g^{-1}$ at 273 K). Transition-metal coordination enables electrocatalytic $CO_2$ reduction, while π-conjugated complexes facilitate modulation of photoluminescence for optoelectronic applications. These materials are light, easy to change once they are made, and can be made into networks that dissolve or do not dissolve. POPs have a reduced density, better chemical stability, and conductivity that may be changed by hybrid topologies.[76]

## Classification of porous organic polymers

POPs are crystalline and amorphous equivalents of multidimensional porous materials with large surface areas and adjustable functionality. As shown in (Fig. 15), CMPs, PIMs, HCPs, and PAFs are examples of amorphous POPs, whereas COFs and CTFs are examples of crystalline POPs. Like nanoporous

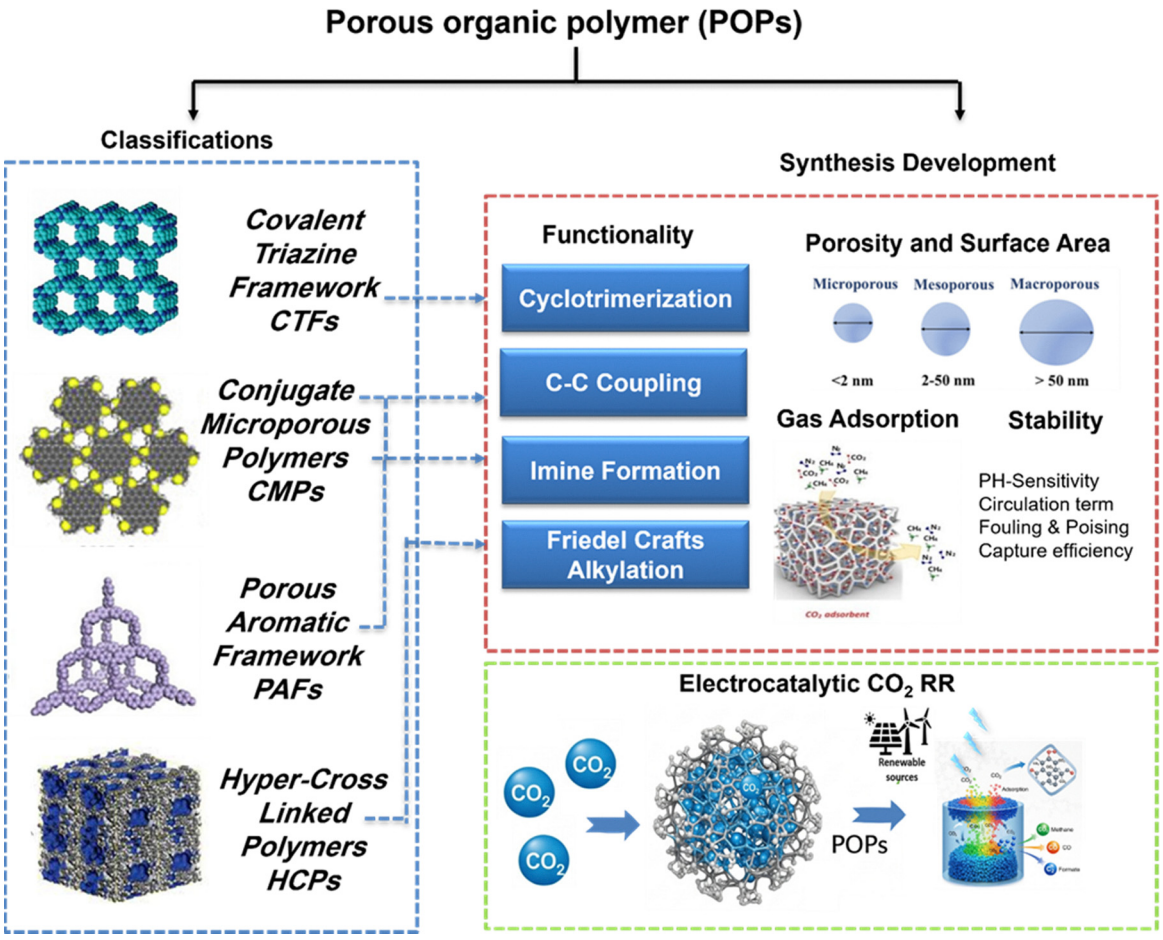


Fig. 15 The classifications, synthesis development and electrocatalytic $CO_2$ RR of POPs.


© 2026 The Author(s). Published by the Royal Society of Chemistry

Open Access Article. Published on 12 fevral 2026. Downloaded on 01.06.2026 11:06:26.
This article is licensed under a Creative Commons Attribution-NonCommercial 3.0 Unported Licence.

materials, POPs are inexpensive, lightweight, adjustable, and have good stability.[77–79] Because of their many chemical reactions and uniform pore widths, they are appropriate for a wide range of applications. With their large specific surface area and adjustable structure, POPs are the primary benefits for $CO_2$ electrochemical conversion. Examples include PAF-1, with a surface area of 5600 $m^2$ $g^{-1}$ BET, and 3D COF-103, with a surface area of 4210 $m^2$ $g^{-1}$ BET.[80,81]

## Covalent triazine framework (CTFs)

CTFs have high surface area, a well-defined pore structure, good physicochemical stability, and surface-active sites that can be designed, making them promising functional materials for a range of applications. CTFs offer a flexible framework for heterogeneous catalysis, particularly for $CO_2$ conversion and adsorption. They are mostly made up of well-defined building pieces that create triazine moieties by covalent bonding. The main synthesis methods for CTF are the Iono-thermal trimerization molten $ZnCl_2$ that yields most functionalized CTF-based products. $P_2O_5$-catalyst for direct condensation of amide monomers, polycondensation, and superacid-catalyzed trimerization of aromatic nitriles (Fig. 16).[82] There are two types of CTFs: crystalline and amorphous. Since the strong covalent bond (C═N) is highly stable and the synthesis conditions are severe, the majority of reported CTFs are amorphous. However, crystalline CTFs with many highly ordered holes and periodic architecture provide substrate specificity and a better understanding of their basic properties. Recent developments in a range of CTF-based catalysts derived from task-specific nitrile monomers are compiled for $CO_2$-involved catalytic processes, including $CO_2$ cycloaddition, $CO_2$ carboxylation, $CO_2$ hydrogenation, $CO_2$ photoreduction, and $CO_2$ electroreduction. This review emphasizes the structural design and synthesis of common CTFs from a sustainable perspective, as well as the relationship between structure and properties in $CO_2$ catalysis. Significant opportunities and strategies in this field are examined to develop precisely designed CTFs with superior $CO_2$-catalytic capability.[83]

CTFs have a nitrogen-rich, electron-deficient structure with their inherent 1,3,5-triazine rings, which results in interesting heteroatom effects such as H-bonding, metal chelation, and π–π interactions. CTFs have an alkaline nature owing to the high nitrogen content, which makes them suitable for base-catalyzed organic reactions. The incorporation of stoichiometric, precisely defined coordination sites into triazine frameworks can enhance their capacity for metal ion complexation, while the meticulous integration of heteroatoms and other functional groups can further broaden their use. CTFs are commonly used as homogenous catalysts and as a pathway for stabilizing metal nanoparticles. They can also be used as precursors of nitrogen-doped porous carbon materials, which can be easily obtained after pyrolysis. The main classifications of CTFs as catalysts and support materials are: metal-free catalysts, supports

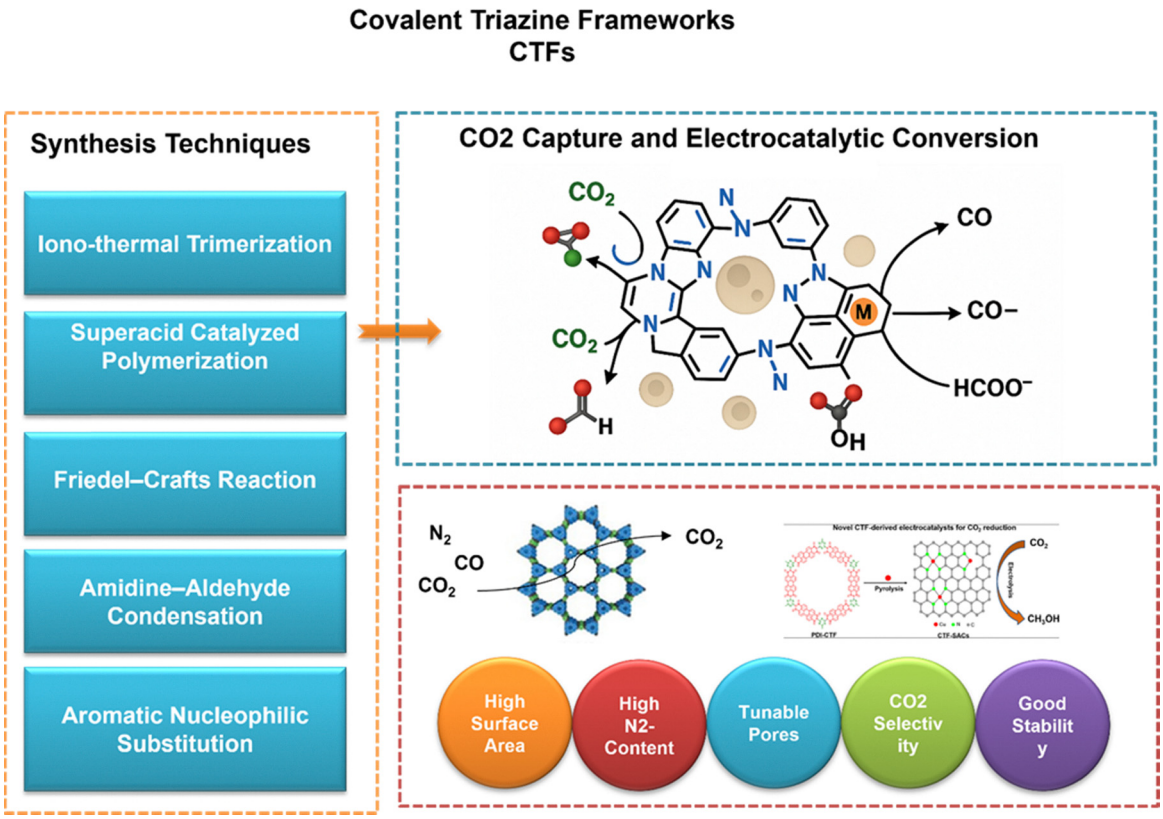


Fig. 16 Schematic illustration of CTFs for $CO_2$ capture and electrocatalytic reduction.

Open Access Article. Published on 12 fevral 2026. Downloaded on 01.06.2026 11:06:26.
This article is licensed under a Creative Commons Attribution-NonCommercial 3.0 Unported Licence.

for solid molecular catalysts, supports for nanoparticulate catalysts, and precursors of N-doped porous carbon materials. The initial method employs CTFs as a primary catalyst to activate $CO_2$ *via* acid–base interactions; the second method utilizes CTFs as carriers for solid molecular catalysts; the third method involves CTFs as functionalized supports for the stabilization of metal nanoparticles with catalytically active species; and the fourth method utilizes CTFs as precursors for N-doped porous carbon materials through high-temperature pyrolysis.[84,85]

## CTFs for $CO_2$ capture

CTFs are considered exceptionally promising materials for $CO_2$ capture owing to their physicochemical characteristics, including nitrogen-rich backbones, permanent porosity, great thermal and chemical durability, and adjustable pore architectures as shown in (Table 5). It mainly comprises triazine-based bonds generated through the trimerization of nitrile monomers, resulting in resilient covalent networks that display microporosity and elevated surface areas, generally between 500 and 2500 $m^2\ g^{-1}$.[86] Rational design of carbonaceous frameworks involves the incorporation of heteroatoms, specific functional groups such as amines and pyridine units, as well as metals like Ni, Co, and Cu, with customized pore size distributions to augment $CO_2$ adsorption capacity and selectivity for electroreduction into value-added products. CTFs possess advantages over MOFs as they do not depend on metal sites for $CO_2$ adsorption. The elevated density of nitrogen sites facilitates robust dipole-quadrupole interactions with $CO_2$ molecules, rendering them particularly effective for low-pressure $CO_2$ collection.[86,87] A pyridine-rich CTF demonstrates a $CO_2$ absorption of 4.2 mmol $g^{-1}$ at 1 bar and 273 K, whereas the functionalization of CTFs with ionic liquids, urea, or amine groups improves $CO_2$ adsorption capabilities in flue gas conditions and humid settings. The integration of CTFs with metal single atom sites, such as Ni and Co, creates coordinated binding sites for $CO_2$, facilitating adsorption and selective reduction while ensuring good chemical stability and renderability. CTFs exhibit competitive $CO_2/N_2$ selectivity and substantial working capacity, alongside strong cycling performance throughout numerous adsorption/desorption cycles.[86,88] The $CO_2$ adsorption capacity at low pressures is a crucial factor in assessing porous materials for post-combustion carbon capture, where selective $CO_2$ separation is vital. In this regime, $CO_2$ absorption is governed more by the intensity of $CO_2$ interactions with the pores and active sites than by the surface area of the material. CTFs with micropores smaller than 1 nm are highly efficient for $CO_2$ adsorption, since their pore size roughly aligns with the molecular diameter of $CO_2$ (0.36 nm), hence improving adsorption efficacy. For instance, PHCTF-1a, PHCTF-4, and PHCTF-6 exhibit variations in porosity: PHCTF-4 and PHCTF-6 exhibit a greater surface area as determined by BET, although they possess smaller micropore volume fractions ($V_{micro}/V_{total}$ = 58% and 39%, respectively) in contrast to PHCTF-1a (79%). Notwithstanding the substantial surface area of PHCTF-4 (52.4 $cm^3\ g^{-1}$) and PHCTF-6 (51.9 $cm^3\ g^{-1}$), their $CO_2$ uptake was comparable to that of PHCTF-1a (51.9 $cm^3\ g^{-1}$), underscoring the pivotal influence of micropore structure beyond surface area alone. The rational design of homogeneous or ultra-microporous CTFs is a viable approach for enhancing $CO_2$ collection at low pressures.[89,90] In addition to the microporosity design and extensive surface area, the incorporation of polar functional groups into the framework markedly improves $CO_2$ affinity by reinforcing dipole-quadrupole interactions. For instance, FCTF-1 and FCTF-1-600, characterized by polar C–F linkages, demonstrated elevated heat of adsorption ($Q_{st}$) and improved $CO_2$ binding relative to CTF-1 and its thermally treated derivative, CTF-1-600. The nitrile groups in CTF-1-600 were more effective for $CO_2$ binding than the triazine nitrogen sites in CTF-1. Nitrogen doping generally enhances $CO_2$ adsorption compared to oxygen doping, underscoring the significance of surface chemistry in low-pressure $CO_2$ collection. In high-pressure $CO_2$ capture applications, including natural gas purification and vehicular storage, pore volume and surface area significantly influence the adsorption efficacy of CTFs. Under elevated pressure, multilayer adsorption transpires, and an increased surface area correlates with a greater adsorption capacity for $CO_2$. MCTP-1, possessing a greater surface area, demonstrated superior $CO_2$ absorption compared to MCTP-2 at 300 K and 35 bar. The CTF TRIPTA demonstrated an escalating $CO_2$ adsorption with pressure, attaining 290.8 $cm^3\ g^{-1}$ at 273 K and 5 bar, with no saturation evident at this pressure, indicating potential for greater capacity at elevated pressures. The polymer TRITER-1 exhibited a similar pattern, reaching a peak $CO_2$ absorption of 300 $cm^3\ g^{-1}$ at 273 K under 5 bar. The results demonstrate the significant reliance of high-pressure $CO_2$ adsorption on textural characteristics, including surface area and pore volume, rather than solely on chemical functionality.[90–92]

Table 5 Comparison of CTFs for $CO_2$ capture

| CTF | Surface area ($m^2\ g^{-1}$) | Pore volume ($cm^3\ g^{-1}$) | Pore size (nm) | $CO_2$ capacity ($cm^3\ g^{-1}$@273 K) low pressure | $Q_{st}$ (kJ $mol^{-1}$) | Ref. |
|---|---|---|---|---|---|---|
| CTF-CSU37@post | 488 | 0.39 | — | 29.0 | — | 93 |
| TAT-DHBD (1) | 750 | 0.36 | 2.61, 3.79 | 30.4 | 27.2 | 94 |
| TFM-1 ($CH_3SO_3H$) | 738 | — | — | 30.8 | 27.8 | 95 |
| PCBZL | 341 | 0.36 | — | 32.6 | 39.6 | 96 |
| PAF-1-6-2 | 979 | — | — | 42.2 | 30.3 | 97 |
| Zn@CTF | 598.2 | 0.35 | 0.53, 1.26 | 23.0 | 32.5 | 98 |
| CTF-CSU41 | 333 | 0.78 | — | 52.3 | 44.6 | 93 |
| PHCTF-4 | 1270 | 0.79 | — | 52.4 | 24.3 | 99 |
| PCTF-8 | 625 | 0.32 | — | 56.0 | 37.0 | 100 |


© 2026 The Author(s). Published by the Royal Society of Chemistry

Open Access Article. Published on 12 fevral 2026. Downloaded on 01.06.2026 11:06:26.
This article is licensed under a Creative Commons Attribution-NonCommercial 3.0 Unported Licence.

## 1. CTFs for electrocatalytic $CO_2$ conversion

For the $CO_2$ conversion process to lower $CO_2$ levels,[101,102] CTF catalysts with an abundance of pyridinic-N doped active sites were first explained in 2018. The synthesized catalyst demonstrates an effective reduction of $CO_2$ to CO, achieving a faradaic efficiency (FE) of approximately 82% at an overpotential of 560 mV. This study facilitates the systematic design of porous CTFs for electrocatalytic $CO_2$ reduction reactions.[103] The fluorination of CTFs was identified as an effective electrocatalyst, demonstrating remarkable selectivity for the conversion of $CO_2$ to $CH_4$, with a FE of 99.3% under aqueous conditions.[104] A boron-doped CTF was investigated in a separate study for the electroreduction of $CO_2$ to CO. The researchers found that boron doping significantly improved the selectivity of CO up to 91.2%. CTF/CNTs hybrids demonstrate efficacy as electrocatalysts for the $CO_2$ reduction reaction, producing carbon monoxide with a FE of around 81%.[105] Altering the surface of CNTs with $OH^-$ groups enhances the interaction between the CTF and CNT, thereby promoting electron transfer during the $CO_2$RR process. The integration of metals such as Cu, Ni, Co, *etc.* into CTF effectively modulates the electrocatalytic $CO_2$ reduction reaction ($CO_2$RR).[106,107]

Kai Ao *et al.* (2024) investigate an interesting instance of exceptional Ni–N/CNT@CTF electrocatalyst, exhibiting a high %FE for the reduction of $CO_2$ to CO. The catalyst was synthesized through the pyrolysis of residual nickel species within carbon nanotubes (CNTs), utilizing a soluble, π-conjugated CTF nanosheet as a nitrogen precursor and interfacial stabilizer. CTF's slender two-dimensional structure enables it to conform closely to carbon nanotubes, preserving their inherent curvature while preventing excessive graphitic overgrowth. High-resolution HRTEM, HAADF-STEM, and EDS mapping revealed the formation of atomically dispersed Ni–$N_x$ sites (Fig. 17a). Electrochemical experiments demonstrated the catalyst's high performance: in H-type cells, it achieved a FE of 96% at −0.77 V *vs.* RHE, while in a flow-cell system, it exhibited a CO partial current density of 201 mA $cm^{-2}$ at −0.9 V with 98% FE. The stability observed exceeded 10 hours in H-cells and 5 hours in flow systems. The Tafel slope analysis, measured at 56 mV $dec^{-1}$, indicated that the rate-limiting step was the formation of COOH* (Fig. 17b–d). The identification of the $Ni_3$ configuration as the primary active site through DFT calculations was significant. The curvature of the CNT induced compressive strain, resulting in shorter Ni–N bonds (1.83 Å compared to 1.84 Å in planar graphene), thereby enhancing the binding strength of $*CO_2$ and *COOH. The alteration in structure rendered the reaction energetics more thermoneutral, thereby enhancing turnover efficiency.[108]

Feng *et al.*[99] reported a family of MPTFs (M = Mn, Fe, Co, Ni, Cu), synthesized by iono-thermal trimerization of porphyrin units with incorporated metal centers (Fig. 18a). Among these, NiPTFs-600 exhibited outstanding catalytic performance as shown in (Fig. 18b and c), achieving a remarkable FE for CO production of 97.6% at −0.8 V *vs.* RHE, with a broad potential window (−0.55 to −0.95 V) where FE > 90% was maintained. The high performance was attributed to the abundant, homogeneously distributed Ni–$N_x$ active sites (8.43 at% N content, 696 $m^2$ $g^{-1}$ surface area) that promote $CO_2$ activation and protonation steps ($*CO_2$ → *COOH → *CO) (Fig. 18d). NiPTFs-600 also demonstrated a high CO partial current density (10.8 mA $cm^{-2}$ at −0.8 V) and stability over 10 hours with negligible structural degradation (Fig. 18e). Compared to other MPTFs, Ni-based frameworks showed superior kinetics (Tafel slope of 129.8 mV $dec^{-1}$) and minimal charge

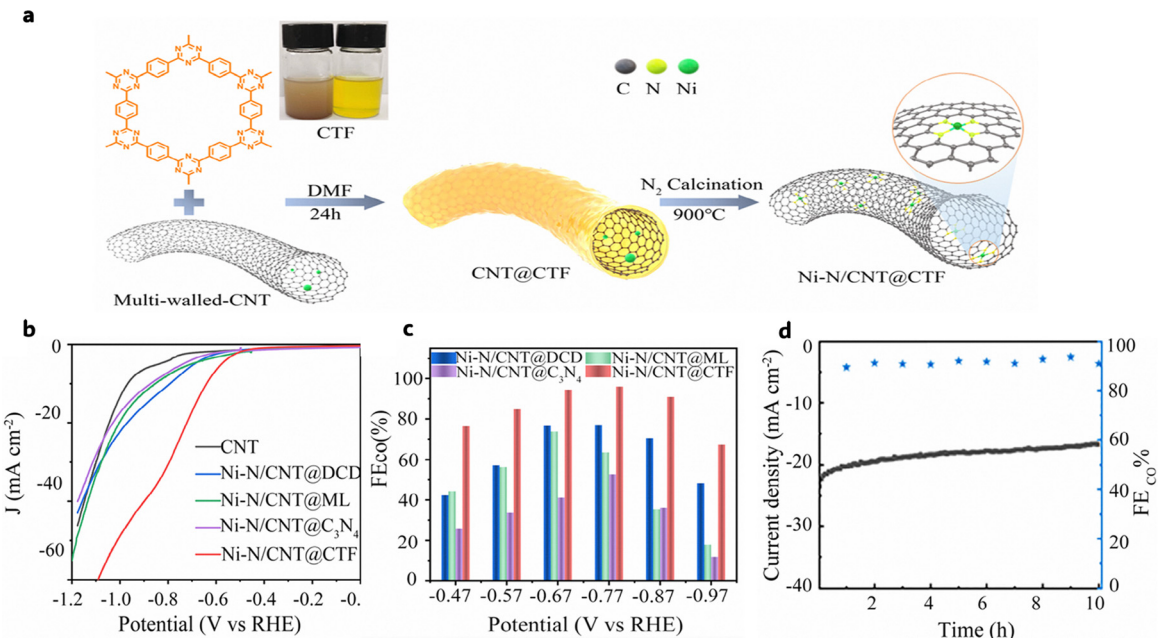


Fig. 17 (a) Schematic illustration for the synthesis, TEM image of Ni–N/CNT@CTF. (b) and (c) Electrocatalytic activity tests (d), stability of CNT, Ni–N/CNT@DCD, Ni–N/CNT@ML, Ni–N/CNT@$C_3N_4$, and Ni–N/CNT@CTF in a H-type cell. Reprinted (adapted) from *Small Struct.*, **5**, 2300500. Copyright © 2024 The Authors. Small Structures published by Wiley-VCH GmbH under the terms of CC-BY license.

Open Access Article. Published on 12 fevral 2026. Downloaded on 01.06.2026 11:06:26.
This article is licensed under a Creative Commons Attribution-NonCommercial 3.0 Unported Licence.

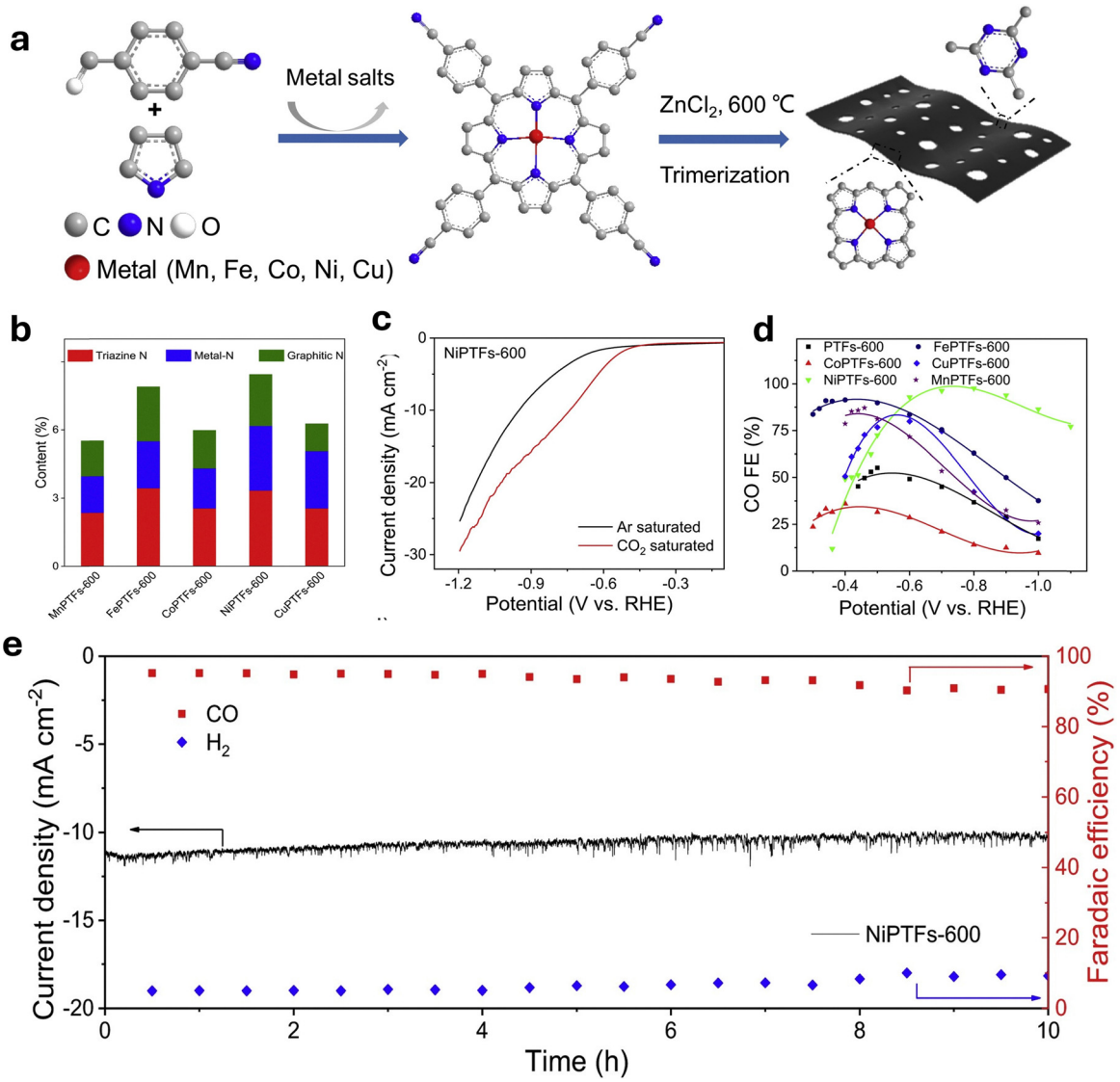


Fig. 18 (a) Schematic illustration of the fabrication process for MPTFs-600. (b) The percentages of fitted N species on MPTFs-600. (c) Polarization curves of NiPTFs-600 in 0.5 M $KHCO_3$ solution under Ar and $CO_2$ flowing. (d) Corresponding CO Fes for MPTFs-600. (e) Stability tests of NiPTFs-600 at −0.8 V and corresponding FEs of CO and $H_2$ productions at each half an hour. Reprinted (adapted) from *Appl Catal B*, 2020, **270**, 118908. Copyright © 2020 Elsevier B.V. All rights reserved.

transfer resistance (9.7 Ω), underscoring the key role of Ni–$N_x$ sites in facilitating efficient $CO_2$RR.[109]

Su *et al.*[88] investigated the incorporation of coordinatively unsaturated 3d transition metals, such as Co and Ni, within CTFs, and how it will enhance the electrocatalytic $CO_2$RR. M-CTFs were prepared by polymerization reaction of 2,6-dicyanopyridine and incorporating carbon black for conductivity, followed by metalation using $MCl_2$ (M = Co, Ni, or Cu). The as-prepared M-CTFs are dispersed atomically within the microporous structure of the support. High-resolution XPS, and EXAFS analysis confirmed that these metal atoms were in a highly unsaturated coordination significantly different from the saturated planar geometry found in conventional tetraphenyl porphyrin (TPP) complexes. Notably, Ni-CTF exhibited a first-shell coordination number of approximately 3.4, lower than the tetra-coordinate Ni-TPP standard, indicating that Ni was stabilized within the CTF matrix in a catalytically advantageous unsaturated state (Fig. 19a–c). This structural tuning translated into a dramatic improvement in catalytic performance specifically for Ni-CTF achieve 90% FE for CO at −0.8 V *vs.* RHE which is shown in LSV measurement under $CO_2$-saturated 0.5 M $KHCO_3$ solution showed a marked increase in cathodic current, indicating active $CO_2$ conversion (Fig. 19c and d). CO and $H_2$ as the main products, with the Ni-CTF showing a CO : $H_2$ ratio far superior to Co-CTF and Cu-CTF, which was confirmed by GC measurements. While for Ni-CTFs, a Tafel slope analysis revealed a value of ∼86 mV $dec^{-1}$ for Ni-CTF, indicating a favorable kinetic profile consistent with COOH* formation as the rate-determining step. In addition to the electrocatalytic activity, the material also possessed high stability and durability across prolonged electrolysis sessions.


© 2026 The Author(s). Published by the Royal Society of Chemistry

Open Access Article. Published on 12 fevral 2026. Downloaded on 01.06.2026 11:06:26.
This article is licensed under a Creative Commons Attribution-NonCommercial 3.0 Unported Licence.

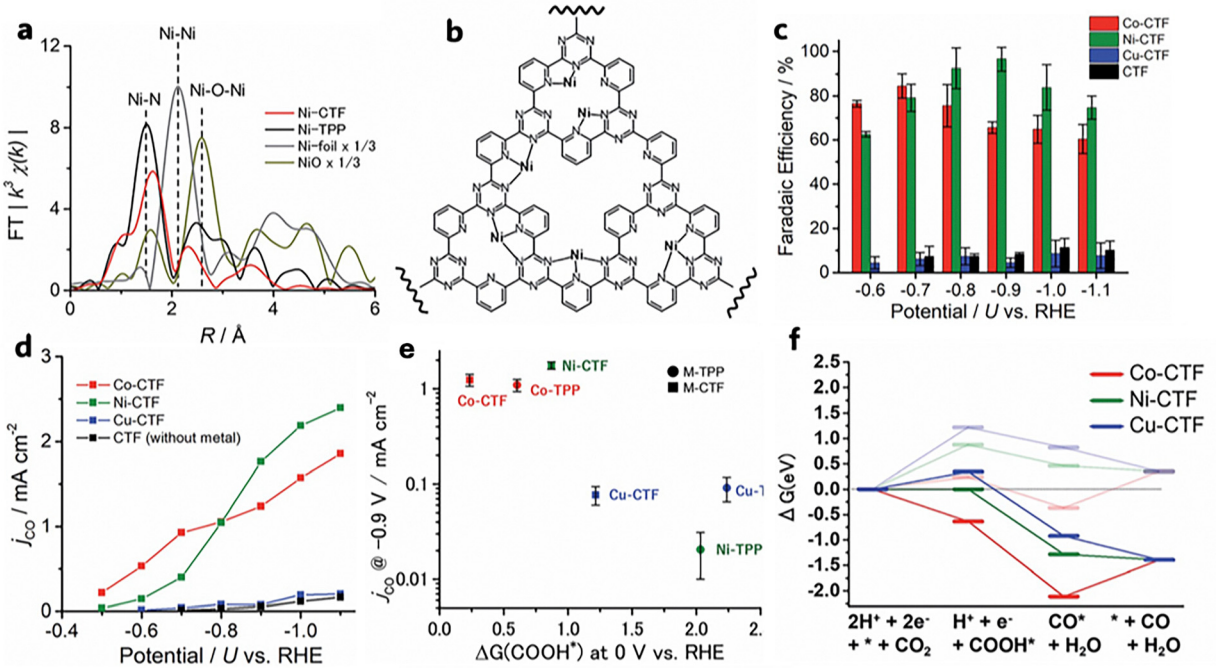


Fig. 19 (a) The $k^3$-weighted Fourier transform EXAFS spectra at the Ni K-edge. (b) An illustration showing the Ni sites in Ni-CTF. (c) Faradaic efficiency values during the $CO_2$RR to generate CO. (d) Partial current density values during the CO generation reaction. (e) and (f) Free energy diagrams for $CO_2$ reduction to CO. Reprinted (adapted) from *Chem. Sci.*, 2018, **9**, 3941. Copyright © 2018 the Royal Society of Chemistry under the terms of CC-BY license.

The experimental outcomes are concise with the DFT calculations. These revealed that the free energy barrier for COOH* formation on Ni-CTF was significantly lower than on Ni-TPP (0.59 eV *vs.* 0.85 eV), due to both the reduced steric hindrance and the stronger electronic coupling between the unsaturated Ni centers and the π-conjugated triazine framework. Moreover, the adsorption energies of *CO and *COOH intermediates followed an optimal volcano-type relationship that aligned Ni-CTF near the top of the activity curve. This synergy between structural engineering and electronic optimization demonstrates how coordination in well-defined porous supports like CTFs can unlock new electrocatalytic pathways, particularly for metals like Ni that are traditionally inactive under standard configurations, as shown in (Fig. 19e and f).[88]

### 2. CTFs for integrated $CO_2$ capture and electrocatalytic conversion

CTFs exhibit bifunctionality for $CO_2$ capture and electrochemical conversion into value-added products. The significant affinity of CTFs for $CO_2$ uptake is due to the high surface area and microporous structure through physisorption within the pores and $CO_2$ interaction *via* dipole–quadrupole with triazine and other nitrogen-rich groups.[86] The reduction process is initiated by the formation of active intermediates on the surface from the electron-transfer step, such as $CO_2^{\bullet -}$, which subsequently form the products.[106] Enhancement of $CO_2$ adsorption on CTFs can occur by rational design of CTFs through the incorporation of functional groups such as –$NH_2$, –OH, or –F, which alter local polarity, thereby enhancing the adsorption of $CO_2$ on the surface and facilitating electron transfer during the reduction process. In addition, enhancement of the selectivity of CTFs for $CO_2$ reduction by incorporation of metal centers such as Ni, Co, and Cu into the nitrogen coordination of CTFs creates isolated catalytic sites that are selective for the reduction of $CO_2$ into $C_{2+}$ products.[106] By introducing such functional groups or metal centers that make the modifications which reduce the energy barrier for $CO_2$ reduction and control the product distribution by stabilizing intermediates. Additionally, the modifications on pore dimensions and their interconnections affect gas diffusion and the stability of transition states during $CO_2$ reduction reactions. Their approach integrates selective $CO_2$ adsorption with efficient catalytic conversion within a single, chemically stable material.[106,110]

(Fig. 20) quantifies how ICCC integration reprograms $CO_2$RR thermodynamics through co-adsorption: capture platforms (CTFs/MOFs) pre-concentrate flue-gas $CO_2$ ($\Delta G_{ads}$ = −0.35 eV *via* N-quadrupole), eliminating mass-transport limits at 0.01–0.15 bar $P_{CO_2}$ and slashing the prohibitive $*CO_2 \rightarrow *COOH$ barrier from 1.05 eV (conventional gas-phase, dashed red) to 0.45 eV (ICCC, solid blue), positioning the rate-determining step within the Sabatier volcano optimum (±0.2 eV) while suppressing competing HER (0.45 → 0.75 eV *via* pore-confined pH). This pathway bifurcation explains Ni-CTF's 90% FECO (0.59 eV *COOH barrier, 86 mV $dec^{-1}$ Tafel), NiPor-CTF's 92.3% FECO at 12.8 mA $cm^{-2}$ over 20 h (0.58 eV), and Cu/ICTF-50's $C_2H_4$ selectivity (35% FE, 4.14 mA $cm^{-2}$ *via* 1.3 mmol $g^{-1}$ adsorption boost), enabling >90% FE across −0.6 to −1.0 V directly from dilute feeds and transforming kinetic bottlenecks into thermoneutral pathways for industrial currents ≥200 mA $cm^{-2}$.[86,88,91,106,110]

Open Access Article. Published on 12 fevral 2026. Downloaded on 01.06.2026 11:06:26.
This article is licensed under a Creative Commons Attribution-NonCommercial 3.0 Unported Licence.

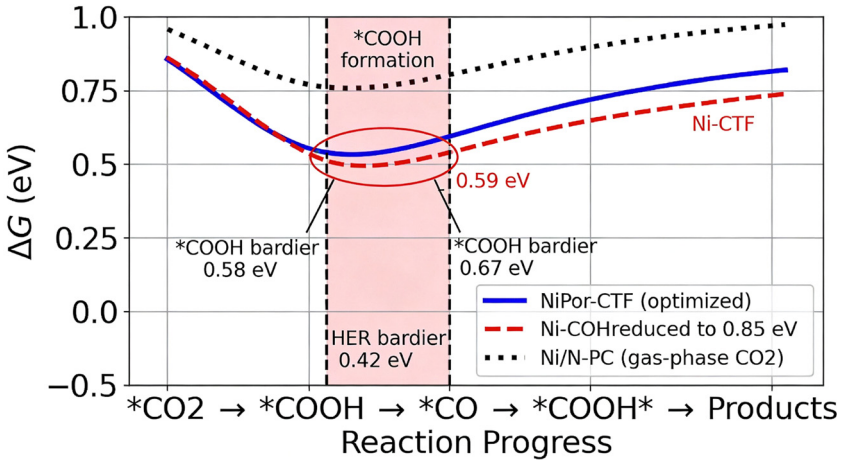


Fig. 20 Gibbs free energy profiles demonstrating capture-enhanced $CO_2$RR in integrated carbon capture and conversion (ICCC).

In a compelling demonstration of dual-function material design, Lu *et al.*[91] reported a Ni-porphyrin-based covalent triazine framework (NiPor-CTF) that integrates atomically dispersed $NiN_4$ centers into a nitrogen-rich, microporous polymeric matrix, offering both efficient $CO_2$ capture and electrocatalytic $CO_2$ conversion. Synthesized *via* an ionothermal method using $ZnCl_2$ as both solvent and Lewis acid catalyst, NiPor-CTF was formed by trimerizing 5,10,15,20-tetrakis(4-cyanophenyl) porphyrin–nickel at 400 °C for 40 h (Fig. 21a). Structural characterization using XPS and EXAFS confirmed that Ni atoms were uniformly anchored in a square-planar $NiN_4$ configuration, with no evidence of Ni nanoparticles or clusters (Fig. 21f). The Por-CTF exhibits higher adsorption capacity of $CO_2$ uptake in comparison with NiPor-CTF as listed in (Table 6). However, the electrocatalytic activity is coming from Ni metal center. The higher adsorption capacity is attributed to BET surface area of 815 $m^2\ g^{-1}$ and thus a $CO_2$ uptake capacity of 2.4 mmol $g^{-1}$ at 298 K, outperforming Ni/N-PC analogues. The NiPor-CTF showed superior electrochemical activity and selectivity of $CO_2$ reduction into CO where the measurements in $CO_2$-saturated 0.5 M $KHCO_3$ electrolyte revealed a low onset potential of approximately 443 mV *vs.* RHE, with faradaic efficiencies exceeding 90% across a wide potential window (−0.6 to −0.9 V), peaking at 92.3% at −0.8 V, and delivering a corresponding current density of 12.8 mA $cm^{-2}$. Compared with catalysts (Ni-free Por-CTF and Ni/N-PC), NiPor-CTF exhibited superior electrocatalytic performance, attributed to the dense population of $NiN_4$ active sites and to efficient mass transport enabled by the porous network (Fig. 21b and c). In addition to the activity and selectivity, the catalysts exhibit Long-term durability, which was confirmed through chronoamperometric tests over 20 hours, showing negligible loss in current density or CO selectivity (Fig. 21d and e). The superior performance is also explained by DFT calculations (Fig. 21g and h). (Fig. 20) illustrates how CTF-localized $CO_2$ adsorption ($\Delta G_{ads}$ = −0.4 eV *via* N-quadrupole) lowers the $*CO_2$ → COOH barrier from 0.85 eV (Ni/N-PC, gas-phase $CO_2$) to 0.58 eV (NiPor-CTF), while raising the competing HER barrier (H → $H_2$) from 0.42 eV to 0.67 eV—achieving thermoneutral *COOH formation and suppressed $H_2$ evolution. This pathway bifurcation positions NiPor-CTF at the volcano peak: *COOH $\Delta G$ = 0.12 eV (optimal range ±0.2 eV), *versus* Ni-TPP's over-stabilized *CO ($\Delta G$ = −0.45 eV, desorption limit). Similarly, Su *et al.* report Ni-CTF's unsaturated $Ni_3$ coordination reduces *COOH barrier to 0.59 eV (*vs.* 0.85 eV Ni-TPP), with Tafel slope 86 mV $dec^{-1}$ confirming fast *COOH formation. (Fig. 19) contrasts neutral CTF *vs.* Cu/ICTF-50: imidazolium cations enhance $CO_2$ adsorption (1.3 mmol $g^{-1}$ ↑ at 273 K), stabilizing *CO dimerization ($\Delta G$ = −0.22 eV) for $C_2H_4$ (35% FE, 4.14 mA $cm^{-2}$) *versus* neutral CTF's *CO desorption pathway. These diagrams quantify how capture-modulated adsorption energies shift RDS from $*CO_2$ activation (gas-phase) to *CO dimerization (integrated), enabling >90% FE across wide potential windows (−0.6 to −1.0 V).

Mao *et al.*[111] recently reported a complex bifunctional electrocatalyst that incorporated copper nanoparticles (Cu/ICTF) and was prepared from imidazolium-functionalized cationic covalent triazine frameworks (ICTFs). The adsorption capacity is enhanced by the cationic nature of the imidazolium moieties, resulting in strong electrostatic interactions. During the reduction reaction the Cu–C bonds are formed as the imidazolium groups undergo additional *in situ* transformation into N-heterocyclic carbene (NHC) species (Fig. 22a). In addition to locally enriching $CO_2$, this dual mechanism stabilizes the Cu NPs, avoiding agglomeration and guaranteeing sustained catalytic activity in comparison with neutral Cu/CTF, the Cu/ICTF-50 composite (containing 50 weight percent Cu) performed noticeably better. For 10 hours, Cu/ICTF-50 maintained a partial ethylene current density of 4.14 mA $cm^{-2}$ and a $C_2H_4$ faradaic efficiency of 35% at −1.0 V *vs.* RHE in $CO_2$-saturated 0.1 M $KHCO_3$ electrolyte, which is noted to be better than Cu/CTF (Fig. 22c–e). From physicochemical characterization such as PXRD and Raman verified the ICTF's structural integrity, while TEM showed uniform Cu NP dispersion that enhances the $CO_2$ adsorption and electroreduction. The adsorption capacity of $CO_2$ by ICTF is confirmed from BET measurements, The imidazolium-induced adsorption enhancement was highlighted by $CO_2$ adsorption isotherms (Micromeritics ASAP 2020), which showed a higher adsorption capacity than neutral CTF by 1.3 mmol $g^{-1}$ at 273 K. Furthermore, Cu/ICTF


© 2026 The Author(s). Published by the Royal Society of Chemistry

Open Access Article. Published on 12 fevral 2026. Downloaded on 01.06.2026 11:06:26.
This article is licensed under a Creative Commons Attribution-NonCommercial 3.0 Unported Licence.

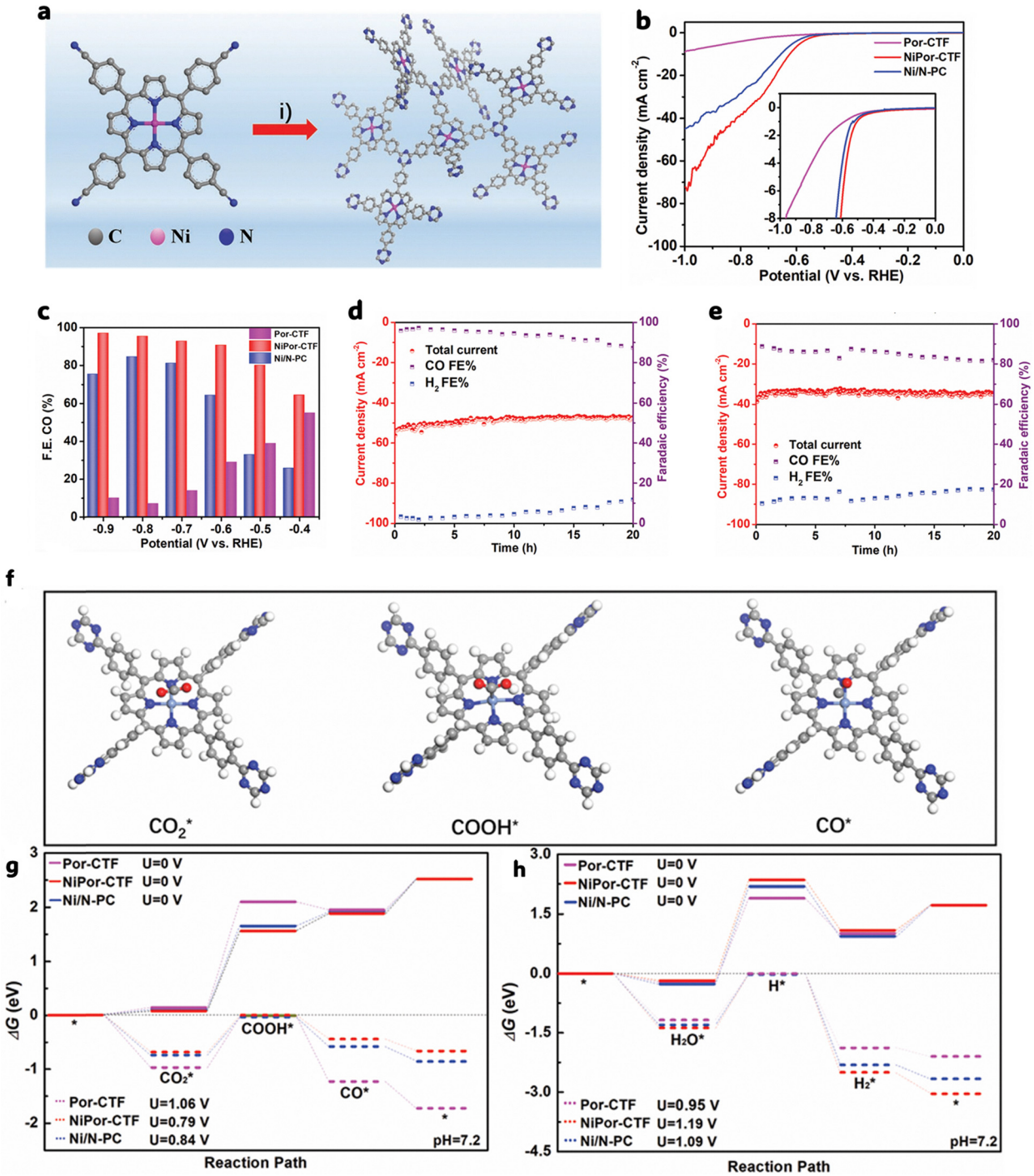


Fig. 21 (a) Schematic representation of NiPor-CTF synthesis by ionothermal strategy. (b) LSV curves and (c), CO faradaic efficiency at various specific potentials of of Por-CTF, NiPor-CTF, and Ni/N-PC in $CO_2$ saturated 0.5 m $KHCO_3$ solution. (e) and (d) Current–time curve for NiPor-CTF, and Ni/N-PC. (f) The DFT-calculated representative models: NiPor-CTF with $CO_2$, COOH, and CO adsorbed. (g) Schematic Gibbs free energy profile for the $CO_2$RR pathway on the three models with a pH of 7.2, and (h), schematic Gibbs free energy profile for the HER pathway on the three models with a pH of 7.2. Reprinted (adapted) from *Adv. Funct. Mater.* 2019, **29**, 1806884. Copyright © 2019 Wiley-VCH Verlag GmbH & Co. KGaA, Weinheim.

exhibited decreased charge-transfer resistance in EIS measurements, indicating better electron transfer kinetics (Fig. 22b). Key reaction intermediates (*CO, *COH, and *CHO) were identified by *operando* FTIR spectroscopy, confirming a multistep mechanistic pathway that leads to the formation of $C_2H_4$.

## Conjugated microporous polymers (CMPs)

A vital class of POP materials with uses in energy and environmental concerns are CMPs, which are amorphous polymers

Open Access Article. Published on 12 fevral 2026. Downloaded on 01.06.2026 11:06:26.
This article is licensed under a Creative Commons Attribution-NonCommercial 3.0 Unported Licence.

Table 6 $N_2$ and $CO_2$ physisorption results of as-prepared materials

| Sample | $S_{BET}$[a] ($m^2\ g^{-1}$) | $S_{micro}$[b] ($m^2\ g^{-1}$) | $V_{Tot}$[c] ($cm^3\ g^{-1}$) | $V_{micro}$[d] ($cm^3\ g^{-1}$) | $D_{av}$[e] (nm) | $CO_2$[f] [mmol $g^{-1}$] 273 K | 298 K |
|---|---|---|---|---|---|---|---|
| Por-CTF | 1099 | 113 | 1.77 | 0.13 | 6.5 | 6.7 | 2.5 |
| NiPor-CTF | 815 | 89 | 0.75 | 0.08 | 3.7 | 5.0 | 2.4 |
| Ni/N-PC | 959 | 94 | 0.95 | 0.11 | 4.0 | 3.9 | 1.6 |

[a] Specific surface area measured by BET model. [b] The microporous surface area analyzed by *t*-plot method. [c] The total pore volume measured at $P/P_0 = 0.99$. [d] The microporous volume analyzed by *t*-plot method. [e] Average pore size. [f] $CO_2$ physisorption data.

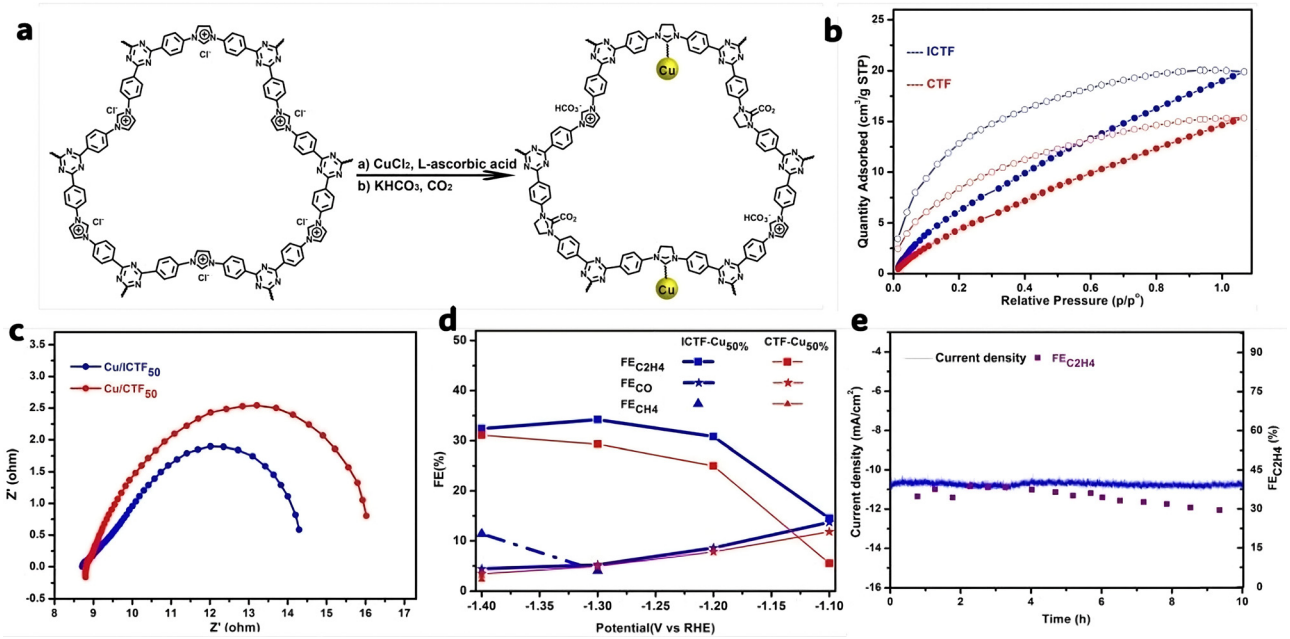


Fig. 22 (a) Schematic representation of the preparation of Cu/IC. (b) $CO_2$ adsorption–desorption isotherms at 298 K for ICTF and CTF. (c) Nyquist plots of different samples over the frequency range from 100 kHz to 10 mHz. (d) Faradaic efficiency of $CO_2$ reduction products from Cu/ICTF50 modified electrode (blue) and Cu/CTF50 modified electrode (red) at various potentials. (e) Stability curve. Reprinted (adapted) from *ChemCatChem* 2020, **12**, 3530. Copyright © 2020 Wiley-VCH Verlag GmbH & Co. KGaA, Weinheim.

with a three-dimensional network backbone. Since 2007 synthesis by Jiang *et al.*,[112] CMPs have been developed and found applications in energy storage, light harvesting, supercapacitors, $CO_2$ reduction and capture, and fuel cells (Fig. 23). Large surface areas, variety, modularity, structural tunability, and exceptional physiochemical stability are all provided by them.

Because of their appealing characteristics, such as enhanced π-conjugation and tunability, CMPs are attracting more attention as adaptable solutions for a variety of energy and environmental problems, including light harvesting, energy storage, adsorbents, heterogeneous catalysts, and luminous materials. One of the main benefits of CMPs is the variety of synthesis methods that are accessible.[113] Several metal-catalyzed couplings to metal-free condensation processes can be used to create CMPs on a much bigger scale. Most processes used in the synthesis of COFs are reversible at high temperatures, which limits the choice of functional building blocks to those that can resist these harsh conditions. The primary difference between CMPs and COFs is their structural makeup; CMPs are more flexible in their design since they are amorphous, whereas COFs are crystalline. It is challenging to create multi-component CMP catalysts using COF materials, but this characteristic allows for the development of multi-step tandem reactions, expanding the design options.[113,114] This modular framework architecture makes it possible to create hierarchical pore systems to improve transport kinetics and, in certain cases, well-accessible pores. Catalytic moieties may be directly integrated into the CMP framework to create heterogeneous CMP catalysts, which is a significant advancement in the utilization of CMPs for heterogeneous catalysis. Based on these fundamental ideas, it is quite possible to develop and synthesize CMPs with one or more active site types that will help collect and catalyze the conversion of $CO_2$.[115,116]

### 1. CMPs for $CO_2$ capture

By incorporating metal centers, CMPs can enhance $CO_2$ affinity through chemisorption, further improving their capture efficiency. Moreover, CMPs uniquely combine gas storage and catalytic properties, enabling simultaneous $CO_2$ capture and conversion into valuable products. These features position CMPs as a


© 2026 The Author(s). Published by the Royal Society of Chemistry

Open Access Article. Published on 12 fevral 2026. Downloaded on 01.06.2026 11:06:26.
This article is licensed under a Creative Commons Attribution-NonCommercial 3.0 Unported Licence.

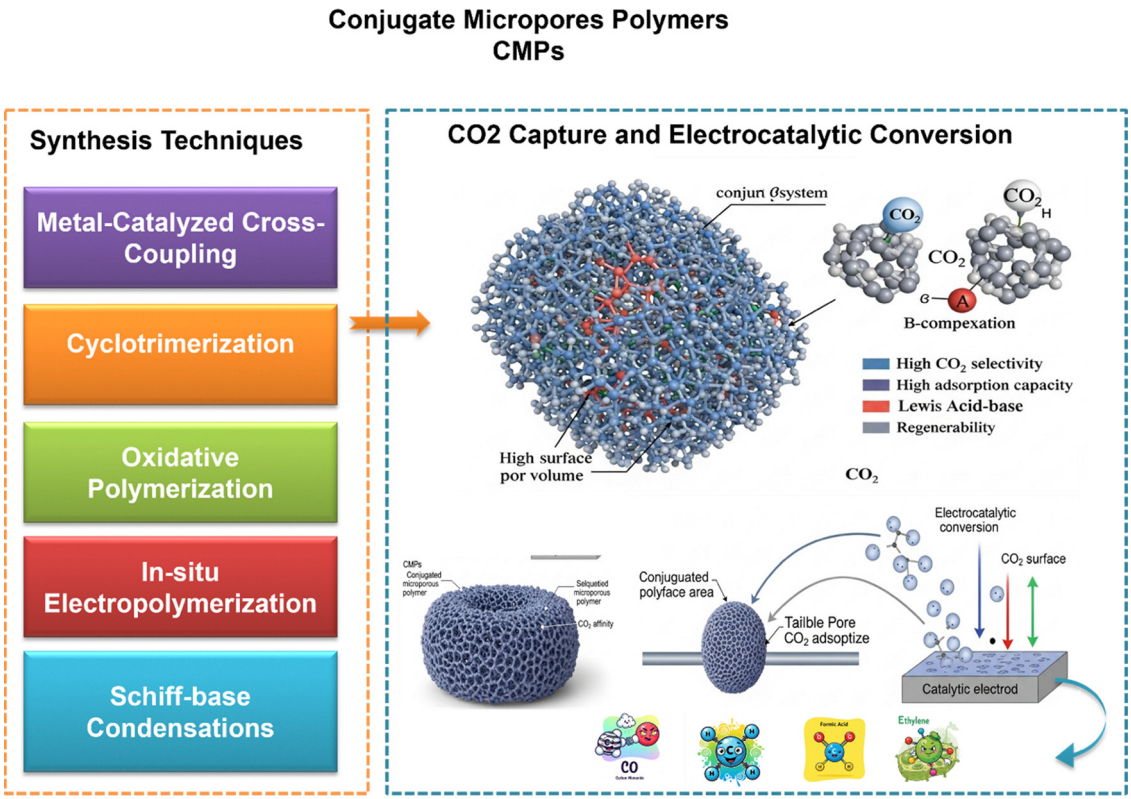


Fig. 23 Schematic illustration of CTFs for $CO_2$ capture and electrocatalytic reduction.

promising platform for sustainable carbon management technologies. Xie *et al.*[117] developed a Co/Al coordinated CMP that exhibits exceptional capabilities in capturing and converting $CO_2$ at room temperature and atmospheric pressure. These polymers, characterized by extended p-conjugation in an amorphous organic framework, demonstrate $CO_2$ storage capacities comparable to metal–organic frameworks while also serving as effective catalysts for $CO_2$ and propylene oxide reactions. Metal-functionalized CMPs, like the Salen-Co/Al-coordinated CMPs discussed, offer combined gas sorption and catalytic capabilities, making them ideal candidates for $CO_2$ capture and conversion. The synthetic procedure for preparing Co-CMP involved synthesizing dibromo-functionalized precursor monomers (Salen-Co) and treating them with 1,3,5-triethynylbenzene in the presence of a Pd(0) catalyst to produce Co-CMP. Al-CMP was prepared differently. The Co-CMP structure exhibited a porous three-dimensional network structure with high thermal stability and insolubility in organic solvents (Fig. 24a). Morphological analysis revealed that both polymers consisted of uniform solid sub-micron spheres with nanometer-sized pores on the surface (Fig. 24b and c). Nitrogen and $CO_2$ analyses indicated both micropores and mesopores in Co-CMP and Al-CMP. Co-CMP had a much higher BET surface area (965 $m^2\ g^{-1}$) than either Al-CMP (798 $m^2\ g^{-1}$) or CMP (772 $m^2\ g^{-1}$) (Fig. 24d). According to Table 7, the total pore volume of Co-CMP was 2.81 $cm^3\ g^{-1}$, which is substantially larger than the volume of several high-pore-volume MOFs, including UMCM-2 (2.31 $cm^3\ g^{-1}$), MOF-177 (1.89 $cm^3\ g^{-1}$) and NOTT-112 (1.62 $cm^3\ g^{-1}$). Co-CMP and Al-CMP exhibited high $CO_2$ adsorption capacities at atmospheric pressure and room temperature. The $CO_2$ uptake reached 79.3 mg $g^{-1}$ and 76.5 mg $g^{-1}$ in Co-CMP and Al-CMP, respectively. Under the same conditions, CMP absorbed 71.0 mg $g^{-1}$ $CO_2$, possibly as a result of the relatively low BET surface area (Fig. 24e), in comparison with the $CO_2$ adsorption capacities of Co-CMP and Al-CMP with those of the MOFs in the literature. Under identical conditions to those in our study, $CO_2$ uptakes of 106.7 mg $g^{-1}$, 71.5 mg $g^{-1}$ and 10.4 mg $g^{-1}$ were reported for MC-BIF-2H, MC-BIF-3H and MC-BIF-5H, respectively. Despite having a relatively low surface area, Co-CMP and Al-CMP exhibited comparatively high $CO_2$ absorption, indicating that Co-CMP and Al-CMP are good $CO_2$ capture materials (Fig. 24f).

### 2. CMPs for $CO_2$ electrocatalytic reduction

Electrochemical transformation of $CO_2$ into valuable chemicals and fuels is a crucial endeavor, particularly when powered by renewable energy sources. Given $CO_2$'s inherent inertness and the multi-electron and multi-proton pathways involved in its reduction, electrocatalysts are indispensable for lowering the energy barrier and enhancing selectivity. CMPs offer advantages such as permanent micropores and robust structures, making them promising photo-/electrocatalysts. However, CMPs often face challenges with conductivity for electrocatalysis and precise control over their amorphous structures to effectively expose catalytic sites and facilitate charge transfer. Molecular catalysts like metal phthalocyanines (MePcs) are highly selective for producing single C-containing products, primarily CO. Wang *et al.*[118] presented a compelling case for

Open Access Article. Published on 12 fevral 2026. Downloaded on 01.06.2026 11:06:26.
This article is licensed under a Creative Commons Attribution-NonCommercial 3.0 Unported Licence.

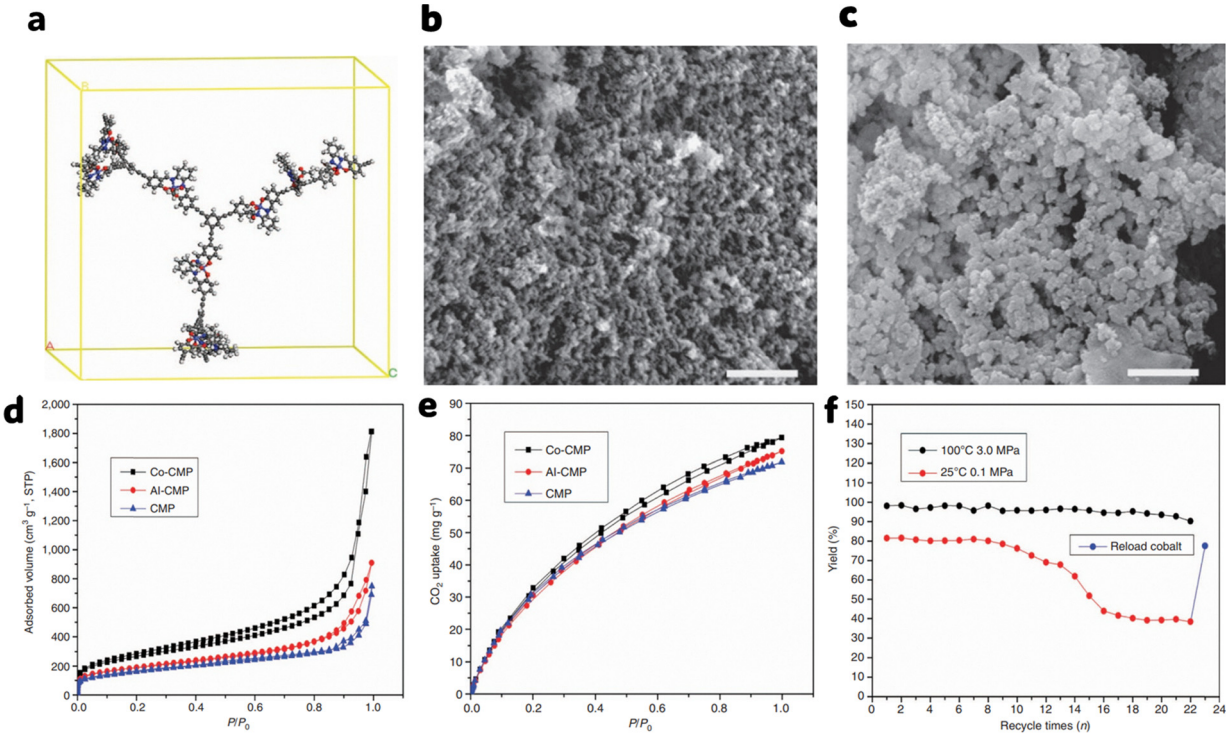


Fig. 24 (a) The amorphous structure of CMP in 3d. SEM images of (b), Co-CMP, (c) Al-CMP, (d) $N_2$ adsorption isotherms, and (e) $CO_2$ Uptake isotherm. (f) The recycling stability of Co-CMP under various experimental conditions. Reprinted (adapted) from *Nat. Commun.*, 1960, **4**, 2013. Copyright © 2013, The Authors. Published by Springer Nature under the terms of CC-BY license.

Table 7 Surface area and $CO_2$ uptake of the CMP, Co-CMP, Al-CMP

| CMPs | $S_{BET}$ ($m^2 g^{-1}$) | $S_{micro}$ ($m^2 g^{-1}$) | $V_{tot}$ ($cm^3 g^{-1}$) | $V_{micro}$ ($cm^3 g^{-1}$) | $M_{calc}$ (wt%) | $M_{ICP}$ (wt%) | $CO_2$ uptake ($mg g^{-1}$) |
|---|---|---|---|---|---|---|---|
| CMP | 772 | 283 | 1.21 | 0.117 | 0 | 0 | 71.0 |
| Co-CMP | 965 | 293 | 2.81 | 0.419 | 8.20 | 7.19 | 79.3 |
| Al-CMP | 798 | 315 | 1.41 | 0.298 | 4.01 | 3.46 | 76.5 |

the design of highly efficient electrocatalysts for $CO_2$ reduction to CO, addressing the limitations of traditional metal phthalocyanine (MePc)-based catalysts, which often suffer from limited molecular modulation and unsatisfactory conductivity. The researchers successfully synthesized an ultrathin CMP sheath around carbon nanotubes (CNTs) through an iono-thermal copolymerization of cobalt phthalocyanine (CoPc) and metal-free phthalocyanine ($H_2Pc$) *via* a Scholl reaction. This innovative approach ensures the atomic dispersion of CoII metal as single atoms on the polymer sheath, maximizing catalytic sites, while the $H_2Pc$ moieties act synergistically as proton/electron donors, enhancing the nucleophilicity of Co sites for $CO_2$ binding and stabilizing reactive intermediates through H-bonding interactions (Fig. 25a). The resulting CNT@CMP(CoPc-$H_2Pc$) composite demonstrated remarkable performance, achieving a high faradaic efficiency (FE) of up to 97% for CO production at −0.9 V (*vs.* RHE) within broad potential windows, and an exceptional turnover frequency (TOF) of 97 592 $h^{-1}$ at −0.65 V, along with a large current density exceeding 200 mA $cm^{-2}$. Furthermore, the catalyst exhibited superior selectivity and stability compared to other related catalysts, maintaining high CO FE for at least 10 hours of continuous electrolysis, with only a marginal decrease in current density (Fig. 25b and c).

## 3. CMPs for integrated $CO_2$ capture and electrochemical conversion

CMPs have shown significant results as a bifunctional electrocatalyst for integrated $CO_2$ capture and electrocatalytic conversion due to their cross-linked polymeric skeleton, high carrier space, and wide contact surface areas. These properties ensure fast kinetics and high electrochemical performance in energy-driven catalytic applications. The π-conjugated structure enhances physiochemical stability and surface area, while suppressing active material dissolution in organic electrolytes. The utilization of CMPs in $ECO_2R$ introduces a novel field of inquiry; thus, there is a scarcity of published studies that explore the application of CMPs as electrocatalysts. At present, the predominant types of reported CMPs for $ECO_2R$ are metal-based and hybrid systems that incorporate conductive carbon materials, as elaborated upon in the following sections.[119]

In the study of integrated $CO_2$ capture and electrocatalytic conversion, Qui *et al.*[120] introduces a new class of CPMs, with


© 2026 The Author(s). Published by the Royal Society of Chemistry

Open Access Article. Published on 12 fevral 2026. Downloaded on 01.06.2026 11:06:26.
This article is licensed under a Creative Commons Attribution-NonCommercial 3.0 Unported Licence.

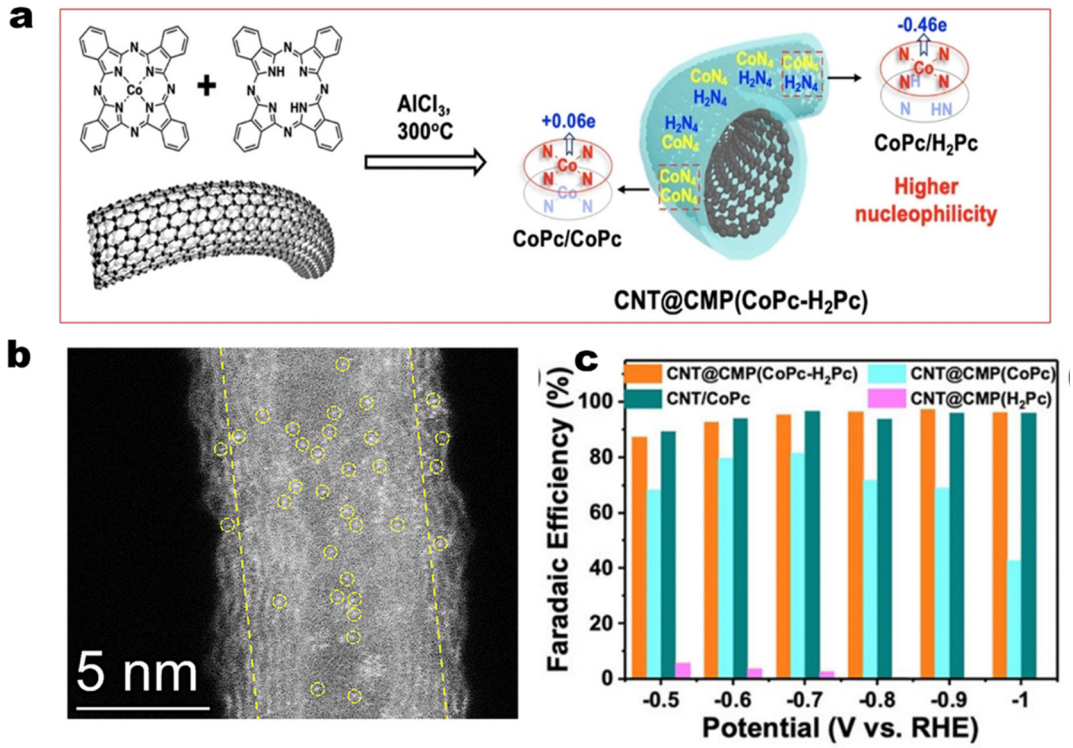


Fig. 25 Represents the (a), the schematic synthesis of CNT@CMP (CoPc-$H_2$Pc), (b) HAADF-STEM image and (c), CO FEs for the CNT@CMP(CoPc-$H_2$Pc) in a flow cell. Reprinted (adapted) from *Chem. Int. Ed.* 2022, **61**, e202115503. Copyright © 2021 Wiley-VCH GmbH.

CMPANI-3 that acts as a promising catalytic material due to its exceptional design incorporating pyrazine-functionalized with cobalt porphyrin functions (Fig. 26a). The synergetic effect generated from cobalt embedded in the CPM structure with porphyrin function enhances both $CO_2$ adsorption and catalytic performance. As detailed in (Table 8), CMPANI-3 exhibits the highest $CO_2$ uptake capacity with 0.88 mmol $g^{-1}$ at 273 K. This result is explained by the strong Lewis acid–base interactions

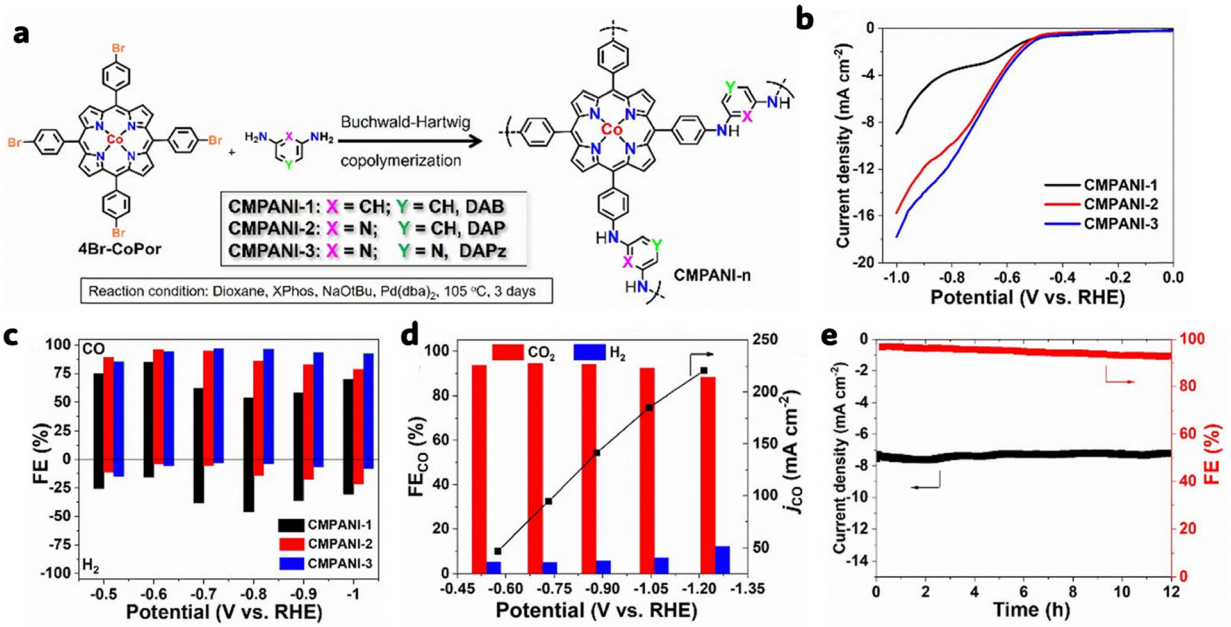


Fig. 26 (a) Synthesis route to CMPANi-*n* with different diamino aromatics. (b) Linear sweep voltammetry curves. (c) CO faradaic efficiency (d), potential-dependent FECO and partial current density; and (e), long-term stability of CMPANI-1 and CMPANI-3 in $CO_2$-saturated 0.5 M $KHCO_3$ electrolyte. Reprinted (adapted) from *J. Mater. Chem. A*, 2024, **12**, 33572–33580. Copyright © 2024 Royal Society of Chemistry.

Open Access Article. Published on 12 fevral 2026. Downloaded on 01.06.2026 11:06:26.
This article is licensed under a Creative Commons Attribution-NonCommercial 3.0 Unported Licence.

Table 8 $N_2$ and $CO_2$ physisorption properties of CMPANi-*n*

| Sample | $S_{BET}$[a] ($m^2\ g^{-1}$) | $V_{tot}$[b] ($cm^3\ g^{-1}$) | $D_{av}$[c] (nm) | $CO_2$[d] (mmol $g^{-1}$)@ 273 K | $CO_2$[d] (mmol $g^{-1}$)@ 298 K |
|---|---|---|---|---|---|
| CMPANI-1 | 12 | 0.09 | 2.2 | 0.46 | 0.38 |
| CMPANI-2 | 30 | 0.12 | 3.1 | 0.52 | 0.35 |
| CMPANI-3 | 34 | 0.26 | 2.7 | 0.88 | 0.66 |

[a] Specific surface area calculated using the BET equation. [b] Total pore volume at $P/P_0$ = 0.99. [c] Average pore size. [d] Calculated from $CO_2$ physisorption isotherms.

between the electron-deficient pyridinyl nitrogen atoms and $CO_2$ molecules. Additionally, the high porous structure of CPM is acquired with a surface area of 34 $m^2\ g^{-1}$ to enhance the gas diffusion and adsorption capacity on the active sites. The electrocatalytic activity and selectivity of CMPANI-3, evaluated in a $CO_2$-saturated 0.5 M $KHCO_3$ electrolyte, reveals an outstanding FE (CO) of 97% at −0.7 V *vs.* RHE, with a corresponding partial current density more than 200 mA $cm^{-2}$; moreover, a turnover frequency (TOF) of 2264 $h^{-1}$ for CO, significantly surpassing its counterparts CMPANI-1 and CMPANI-2 (Fig. 26b–d). These improvements stem from the engineered coordination microenvironment around the $CoN_4$ active site, where the pyrazine-N groups act as internal proton relays, effectively accelerating the proton-coupled electron transfer step critical for *COOH intermediate formation. This mechanism is clearly evidenced by *in situ* ATR-FTIR spectroscopy, which shows stronger and earlier formation of *COOH species in CMPANI-3, and KIE analysis that confirms enhanced proton transfer dynamics. Electrochemical analysis further supports this claim Tafel plots demonstrate the lowest slope (174 mV $dec^{-1}$) for CMPANI-3, indicating faster kinetics, while Nyquist plots show it has the lowest charge transfer resistance (31.89 Ω), suggesting superior conductivity and reaction interface dynamics. Moreover, when integrated into a gas diffusion electrode and tested in a flow cell, CMPANI-3 maintains FECO above 90% even at 200 mA $cm^{-2}$, reaching a TOF of 52 390 $h^{-1}$, and thus rivals or surpasses leading $CO_2$-to-CO catalysts including CoPc, Au–C, and Ag systems (Fig. 26e).

Smith *et al.*[121] investigated a novel metal–organic conjugated microporous polymer (CMP-(bpy)20-Mn) that has dual functionality for $CO_2$ capture and electrocatalytic conversion (Fig. 27a and b). The material maintains substantial porosity after Mn incorporation with a surface area of 549 $m^2\ g^{-1}$ and achieves moderate $CO_2$ uptake of 1.06 mmol $g^{-1}$ at 298 K and 1 bar, though this capture performance remains below benchmark materials like BPL carbon (Fig. 27c). Most notably, the rigid CMP structure prevents the problematic reductive dimerization of the $[Mn(bpy)(CO)_3Br]$ catalyst that typically occurs in solution-based systems, enabling direct formation of the catalytically active $[Mn(bpyCMP)(CO)_3]^-$ species as evidenced by a single reduction peak at −1.35 V (Fig. 27d). The material is affected by two catalytic pathways: a slow pathway (−1.2 to −1.4 V) showing modest current enhancement with $CO_2$ binding, and a fast substrate-limited pathway (−1.6 to −1.8 V) with scan-rate dependent behavior indicating higher TOF. Bulk electrolysis at

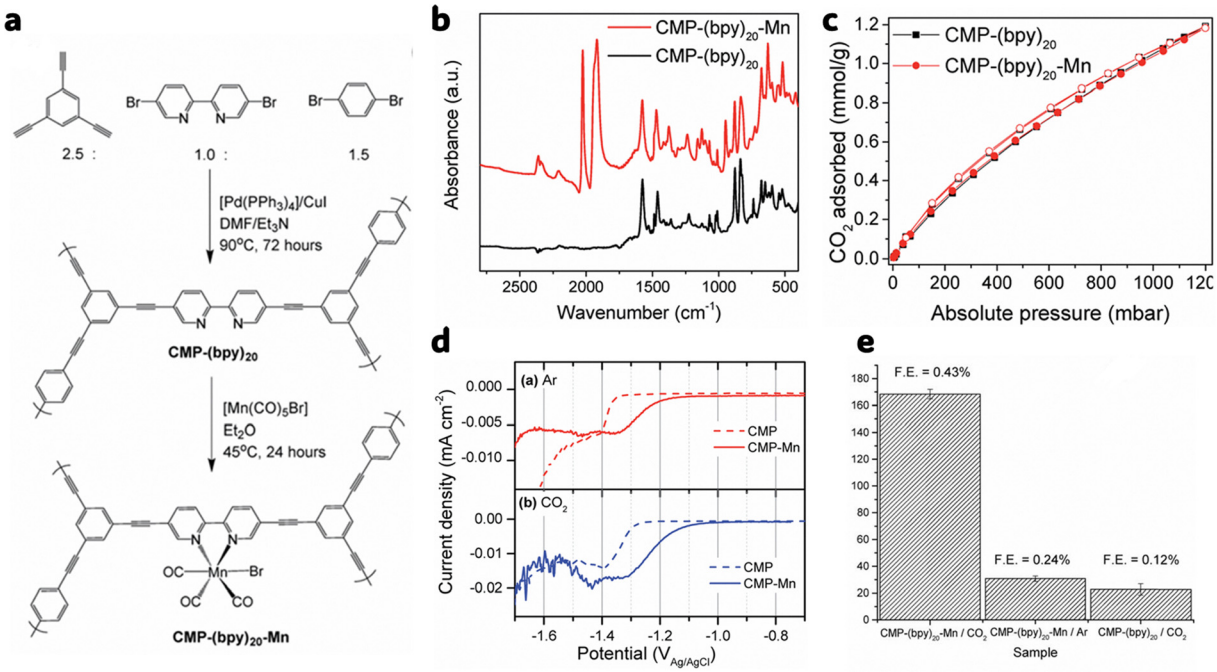


Fig. 27 (a) Synthetic route to CMP-(bpy)20-Mn, (b) FTIR spectra and (c), $CO_2$ adsorption–desorption isotherms measured at 298 K for CMP-(bpy)20 (black) and CMP-(bpy)20-Mn (red), (d) square wave voltammograms (a) and (b) of CMP-(bpy)20 (dashed) and CMP-(bpy)20-Mn (solid), CMP-(bpy)20-Mn shows an additional reduction (−1.35 V) assignable to $[Mn(bpy)(CO)_3Br]$ moieties (e), CO evolution rate during bulk electrolysis experiments at −1.6 V Ag/AgCl for 3 hours. The faradaic efficiencies are for CO. $H_2$ was the only other product detected. Reprinted (adapted) from *Sustainable Energy Fuels*, 2019, **3**, 2990–2994. Copyright © 2019 Royal Society of Chemistry.


© 2026 The Author(s). Published by the Royal Society of Chemistry

Open Access Article. Published on 12 fevral 2026. Downloaded on 01.06.2026 11:06:26. This article is licensed under a Creative Commons Attribution-NonCommercial 3.0 Unported Licence.

Table 9 Summary of CMP-based electrocatalysts for $ECO_2RR$

| Polymeric material | BET [$m^2$ $g^{-1}$] | Electrolyte | Applied potential [V] | Main product [FE%] | Ref. |
|---|---|---|---|---|---|
| PF-5 film | 1000 | 0.1 M $Et_4NBF_4$/acetonitrile solution | n.r. | CO | 122 |
| PyPOP@G | 582.7 | 0.1 M $KHCO_3$ | −1.0 (*vs.* RHE) | n.r. | 123 |
| CMP-$(bpy)_{20}$-Mn | 549 | 0.06 M Phosphate buffer | −1.6 (*vs.* $Ag/Ag^+$) | CO (0.43%) | 124 |
| CNS-NiSA | 458 | 0.5 M $KHCO_3$ | −0.8 (*vs.* RHE) | CO (95%) | 118 |
| CNT@CMP (CoPc-$H_2$Pc) | 70 | 0.5 M $KHCO_3$ | −0.9 (*vs.* RHE) | CO (97%) | 125 |
| COP-SA | 106.33 | 0.5 M $KHCO_3$ | −0.65 (*vs.* RHE) | CO (96.5%) | 125 |
| Pt/TPE-CMP | 360 | 0.5 M $KHCO_3$ | −1.5 (*vs.* $Ag/Ag^+$) | (C1–C8) (>95%) | 126 |
| CoPPc-TFPPy-CP | 464.9 | 0.1 M KCl | −1 (*vs.* RHE)<br>−1.2 (*vs.* RHE) | $C_2H_5OH$ 43.25%<br>HCOOH 13.91% | 127 |
| BNPI-1 (NaF 0.99) | 54 | 0.1 M $KHCO_3$ | 0.03 (*vs.* RHE) −0.26 | HCOOH 91% | 128 |
| BNPI-1 (NaI 0.66) | 728 | | −0.26 (*vs.* RHE) | $CH_3OH$ 85% | |
| BNPI-2 | 26 | | −0.26 (*vs.* RHE) | HCOOH 45%<br>$CH_3OH$ 67% | |
| pPI-1 | 20 | 0.1 M $KHCO_3$ | −0.76 (*vs.* RHE)<br>−0.26 (*vs.* RHE) | HCOOH 14%<br>$CH_3OH$ 52% | 129 |
| pPI-2 | 342 | | −0.56 (*vs.* RHE)<br>−0.26 (*vs.* RHE) | HCOOH 20%<br>$CH_3OH$ 95% | |

Table 10 A comparative analysis of various POPs for $CO_2$ capture and electrocatalytic conversion, emphasizing faradaic efficiency (FE%) and key reduction products

| Catalyst | Synthesis method | Surface area ($m^2$ $g^{-1}$) | Faradaic efficiency (FE%) | Reduction products | $CO_2$ uptake (mmol $g^{-1}$) | Ref. |
|---|---|---|---|---|---|---|
| TTF-1 | Triazine linkage polymerization | 1234 | 82% at −0.6 V *vs.* RHE | CO, HCOOH | 2.86 | 63 |
| POP-Py(0)/CoTCPP | Benzyl bromide & pyridine reaction | Not specified | 83% at −0.6 V *vs.* RHE | CO | Not specified | 63 |
| PyPOP@G | Pyrimidine-based polymer on graphene | Not specified | 85% at −0.7 V *vs.* RHE | CO, $CH_4$ | Not specified | 63 |
| POP@MWCNT | Polymerization on multi-walled CNTs | Not specified | 80% at −0.75 V *vs.* RHE | CO, HCOOH | Not specified | 63 |
| Bi-MOF | Solvo-thermal | Not specified | 92% at −0.9 V *vs.* RHE | COOH | 1.50 | 63 |
| FePC-POP | Friedel–Crafts alkylation | 427 | 88% at −0.65 V *vs.* RHE | CO | 1.50 | 130 |
| DTTBQ-CMP | Polycondensation | Not specified | 92% at −0.8 V *vs.* RHE | CO, $C_2H_4O$ | Not specified | 130 |
| BSPOP-Co | Triptycene-based polycondensation | 280 | 87% at −0.7 V *vs.* RHE | CO | 1.70 | 130 |
| $CuPcF_8$-CoNPc-COF | Condensation of phthalocyanine derivatives | 452 | 97% at −0.62 V *vs.* RHE | CO, $CH_4$ | 0.80 | 131 |
| 2D-Co-COF500 | COF formation on Mg/Al-LDH | 123 | 96.5% at −0.8 V *vs.* RHE | CO | Not specified | 131 |
| f 2D cobalt(II)-phthalocyanine based COFs | Triazine-based framework | Not specified | 87% at −0.6 V *vs.* RHE | CO | Not specified | 131 |
| isox-CTF-500 | Triazine-based framework | 1683 | 90% at −0.75 V *vs.* RHE | CO, $CH_3OH$ | 4.92 | 131 |
| acac-CTF-500 | Triazine-based framework | 1556 | 85% at −0.6 V *vs.* RHE | CO, HCOOH | 3.30 | 131 |
| cCTFs-400 | Triazine-based framework | 744 | 89% at −0.65 V *vs.* RHE | CO, $CH_4$ | 2.86 | 131 |
| cCTFs-450 | Triazine-based framework | 861 | 91% at −0.7 V *vs.* RHE | CO, $C_2H_4$ | 2.25 | 131 |
| cCTFs-500 | Triazine-based framework | 1247 | 95% at −0.75 V *vs.* RHE | CO, $CH_3OH$ | 3.02 | 131 |
| LKK-CMP-1 | 1,3-Dialkyne linkage polymerization | 467 | 86% at −0.7 V *vs.* RHE | CO, $CH_4$ | 2.24 | 132 |
| 6FA-PEPH-CL | Crosslinked polyimide | 653 | 82% at −0.6 V *vs.* RHE | CO, HCOOH | 1.65 | 63 |
| 6FA-PE-CL | Crosslinked polyimide | 698 | 88% at −0.65 V *vs.* RHE | CO, $CH_3OH$ | 2.02 | 63 |
| Tt-POP-2 | Triptycene-based polymerization | 368 | 85% at −0.7 V *vs.* RHE | CO, $CH_4$ | 0.40 | 133 |
| Tt-POP-3 | Triptycene-based polymerization | 974 | 90% at −0.75 V *vs.* RHE | CO, $C_2H_4O$ | 0.62 | 133 |

−1.6 V demonstrates selective CO production as the sole carbon-based product with a 7-fold enhancement over the catalyst-free control and an estimated turnover number of ∼1296 over 4 hours, though the faradaic efficiency remains low at 0.43% due to competing hydrogen evolution (Fig. 27e). More examples of CMP-based electrocatalysts for $ECO_2RR$ are summarized in (Table 9) while comparative analysis of various POPs for $CO_2$ capture and electrocatalytic conversion are detailed in (Table 10).

## 4. Future outlook of CTFs and CMPs

CTFs and CMPs exhibit superior affinity for capturing $CO_2$ and electrocatalytic conversion, owing to large surface areas, adjustable pore architectures, and amazing stability in heat and chemicals. The triazine function of CTFs, which can be made in several ways, like high-temperature iono-thermal trimerization with $ZnCl_2$ and superacid-catalyzed approaches, which let you control the porosity and nitrogen content very well, both of which are important for selective and effective $CO_2$ adsorption.[63,134] Ultramicroporous CTFs (pore width <7 Å) have a lot of nitrogen, which makes dipole-quadrupole interactions with $CO_2$ stronger. This gives them great selectivity for $CO_2$ over $N_2$ and $CH_4$, and they can hold up to 57.2 cc $g^{-1}$ at 298 K, with some frameworks getting $CO_2/N_2$ selectivity ratios above 100. The chemical diversity of CTFs is enhanced by the incorporation of charged or functional groups, or by their combination with active metal sites. This increases their capacity for $CO_2$ adsorption and improves their efficacy as electrocatalysts.[135,136]

Open Access Article. Published on 12 fevral 2026. Downloaded on 01.06.2026 11:06:26.
This article is licensed under a Creative Commons Attribution-NonCommercial 3.0 Unported Licence.

The π-conjugation and microporosity of CMPs give them enormous interior surface areas up to 556 $m^2$ $g^{-1}$ BET and excellent $CO_2$ adsorption capabilities, usually more than 1 mmol $g^{-1}$ at room temperature. Adding different electron-rich parts, such as triazine, pyrrole, and thiophene, through modular synthesis processes can change the structure of the pores and how well they absorb $CO_2$.[77,96,136] CMPs, like CTFs, are very thermally stable, with decomposition temperatures often over 300 °C. They can also be chemically modified to add catalytic centers that help $CO_2$ reduction into products like CO, formate, or methane. While the CTFs and CMPs are good for capturing and $CO_2$ reduction owing to their excellent properties such as tunable pore size distribution and can be designed at the molecular level to maximize adsorption and catalytic activity. However, it is still hard to control crystalline and active site dispersion precisely. For example, CTFs often have low crystallinity under iono-thermal conditions, and the uneven pore distribution in CMPs can make it harder to predict how easily sorption or catalytic sites can be accessed.[77,96,136] Moreover, research is also needed on scalability and long-term operating stability under electrochemical circumstances. Future goals include making greener, more scalable syntheses, enhancing structural order (to come closer to single-crystalline domains in CTFs), and using hybridization with conductive support or targeted functionalization like site-specific metalation or heteroatom doping. The combination of computational design and systematic structure–property studies is expected to accelerate the development of next-generation POPs with finely tuned performance for capturing $CO_2$ and converting it efficiently *via* electrocatalysis, which directly help technologies that fight climate change.[77,98,135]

## Covalent organic frameworks (COFs)

Covalent organic frameworks (COFs) significantly enhance integrated $CO_2$ capture and conversion systems, providing a transformational platform due to their outstanding porosity, design flexibility, and strong chemical stability. The crystalline, lightweight materials, composed of multiple parts and interconnected by strong covalent bonds, demonstrate huge surface areas and adjustable pore sizes, making them effective for $CO_2$ capture and catalytic conversion into valuable chemicals.[137,138] Additionally, the bottom-up reticular synthesis approach enables precise control through molecular building design, allowing the addition of specific functional groups that enhance charge transport and catalytic efficiency, particularly for $CO_2$ reduction. COFs are crystalline and porous polymers made up of covalently bonded, organic building blocks with different structural configurations, such as benzene rings, triazine units, Imine linkages, and porphyrin.[139] The structural flexibility and durability of COFs make them a promising material for developing integrated systems that effectively combine $CO_2$ capture and conversion[140–142] as shown in (Fig. 28).

The primary synthetic methods for COFs include solvothermal synthesis, iono-thermal synthesis, mechanochemical synthesis, and microwave-assisted synthesis (Fig. 29).[143–145] COFs can be modified with metal centers or functional groups to enhance $CO_2$ adsorption, leading to the conversion of $CO_2$ into valuable products, such as CO, methane, or ethylene.[137,138,146] Also, as the majority of COFs are produced through cross-coupling or condensation reactions involving organic aromatic building blocks and linkers, the entire framework.[144,147–149]

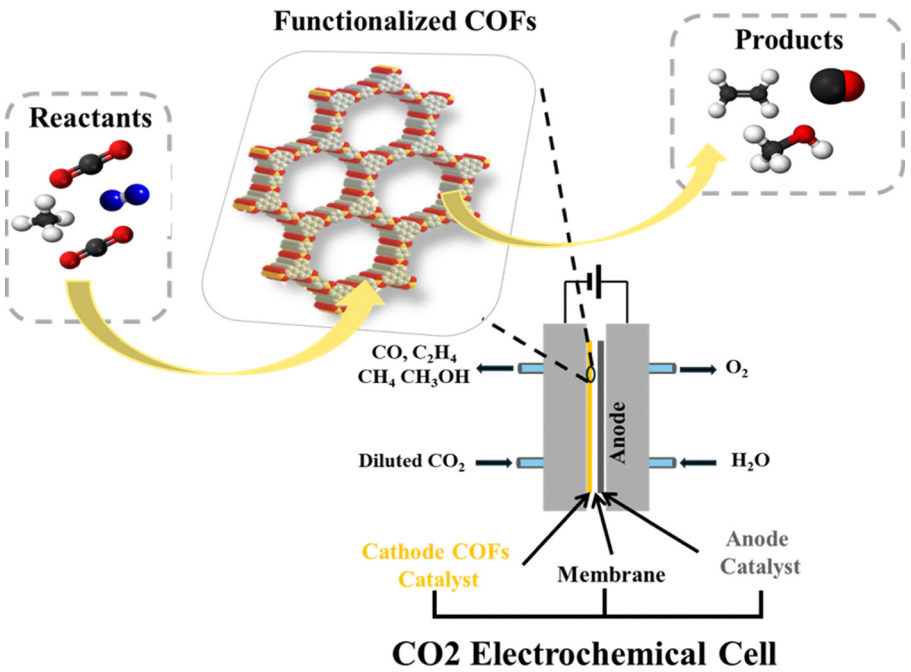


Fig. 28 Graphical abstract of COF for $CO_2$ capture and electrocatalytic conversion.


© 2026 The Author(s). Published by the Royal Society of Chemistry

Open Access Article. Published on 12 fevral 2026. Downloaded on 01.06.2026 11:06:26.
This article is licensed under a Creative Commons Attribution-NonCommercial 3.0 Unported Licence.

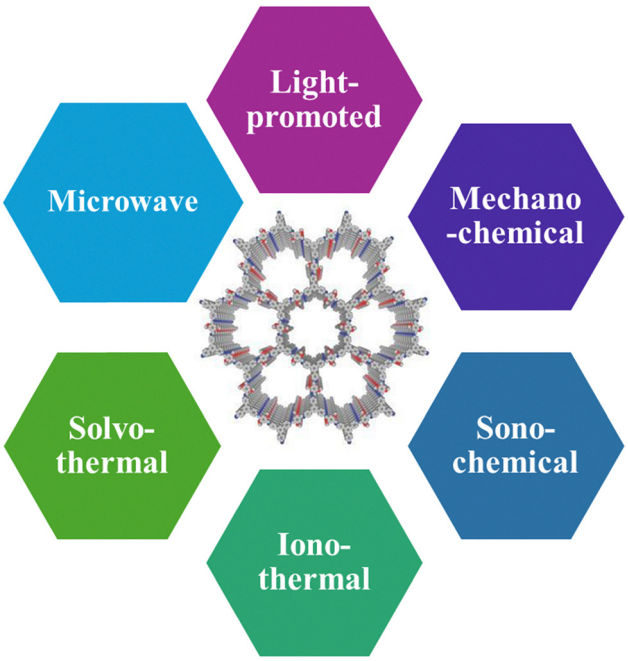


Fig. 29 Schematic illustration of COFs different synthesis techniques.

## 1. Structure and properties of COFs

COFs exhibit a unique structural flexibility and tunable properties, making them promising candidates for $CO_2$ capture and conversion. The crystalline, microporous structures constructed from organic building blocks through reticular synthesis offer large, adjustable pore sizes and high surface areas, enabling efficient $CO_2$ diffusion, adsorption, and enrichment near catalytic sites.[148,150] They are also suitable for long-term electrocatalytic applications due to their unique, porous, and stable properties at high temperatures. The modular nature of COFs facilitates the integration of conductive elements, such as graphene or electron-attracting groups, which enhance electron transport and boost overall catalytic performance.

## 2. Mechanisms of $CO_2$ adsorption in COFs

COFs' capture process initiates as $CO_2$ molecules infiltrate the porous structure and are adsorbed onto active sites, including metal centers (Co, Ni, Cu) or nitrogen-rich linkers. This comprehensive method allows for the rapid activation of $CO_2$, facilitating the electron transfer of the adsorbed molecules to generate reactive intermediates such as $CO_2^-$ or *COOH.[151] After that, the intermediates go through several steps of proton-electron transfer, which create products such as CO, formic acid, methane, or even multi-carbon hydrocarbons, depending on the catalyst design and reaction conditions.[149] The mechanisms of $CO_2$ adsorption can be clarified by examining several critical factors, such as the type of adsorption (physisorption or chemisorption), the significance of functional groups, and the impact of pore size and topology.[144]

In the first step, $CO_2$ is adsorbed through physisorption, characterized by weak van der Waals forces, without a change in the electronic structure of COFs.[144,152] Chemisorption, on the other hand, involves the formation of chemical bonds between $CO_2$ and the functional groups present in the COFs. This process may result in more stable adsorption; however, it could necessitate increased energy for desorption.[150] Regarding Functional groups, such as amines and imides, they play a crucial role in enhancing $CO_2$ adsorption. These groups can interact with $CO_2$ through hydrogen bonding or coordinate covalent bonding, significantly increasing the adsorption capacity. The existence of nitrogen-rich sites is especially advantageous, as they can provide additional binding sites for $CO_2$, thereby enhancing the overall effectiveness of the COF in $CO_2$ capture. Han *et al.* demonstrate that the two-dimensional polyimide-linked phthalocyanine COFs (CoPc-PI-COF-1 and CoPc-PI-COF-2) exhibit similar nitrogen-rich sites that facilitate effective $CO_2$ capture, demonstrating the importance of these functional groups in the adsorption process.[148] The other crucial factor, the pore size and topology of COFs, determines their $CO_2$ adsorption performance. Larger pore sizes enhance the accessibility of $CO_2$ molecules, allowing for greater adsorption. Additionally, the specific arrangement of the pores can influence the diffusion of $CO_2$, affecting the overall efficiency of the adsorption process.[147]

## 3. COFs for $CO_2$ capture

Materials scientists have recently developed an interest in COFs due to their highly porous, crystalline structures, which offer the flexibility of adjusting pore sizes and functional groups. COFs were first discovered by Yaghi and colleagues in 2005,[153] marking a significant step forward in reticular chemistry, as they enabled scientists to use pre-made molecular building blocks, such as porphyrin cores, triazine, and benzene, to control the shape of the framework precisely.[154,155]

The outstanding $CO_2$ adsorption properties of COFs naturally correspond to their structure–property relationships. The π-stacking between layers makes the structure more rigid, allowing guests and hosts to interact more easily due to induced dipole and quadrupolar interactions, particularly in reactions, given $CO_2$'s linear geometry and quadrupole moment. The formation of COFs relies on dynamic covalent chemistry, which enables reversible reactions (such as imine condensation and boronate ester formation) that allow self-correction during synthesis. To successfully design COFs for $CO_2$ capture, three key elements are required:[137] (1) the selection of building blocks (such as triazine, benzene, or porphyrin cores) that dictate functionality and binding affinity toward $CO_2$, (2) the geometrical integrity of the framework to ensure periodicity and stable pore architectures, and (3) reversible covalent bond formation, which is important for crystallinity, recyclability, and defect healing. Three primary factors determine how COFs capture $CO_2$:[143] the kind of linkage between the building units, the porosity type, and the types of COF building blocks. In this section, the main properties of COFs' effectiveness in $CO_2$ capture and conversion will be discussed: the dimensionality effect, the types of covalent bonds, the textural properties effect, and the functional groups and active sites effect.

Open Access Article. Published on 12 fevral 2026. Downloaded on 01.06.2026 11:06:26.
This article is licensed under a Creative Commons Attribution-NonCommercial 3.0 Unported Licence.

The dimensionality of COFs significantly influences their porosity, gas diffusion properties, and adsorption capacity. 1D COFs are primarily non-centrosymmetric linear crystalline polymers formed by the haphazard packing of organic chains caused by entropy.[139] These chains consist of 1D COFs, confined covalent bonds, and non-covalent interactions such as hydrogen bonding and π–π interactions. Singh and Nagaraja[156] developed $SO_3H$-functionalized 1D-COFs with polar channels to improve adsorption. Two-dimensional COFs are composed of planar building blocks that stack *via* π–π interactions, resulting in layered crystalline structures.[157] These frameworks are effective platforms for $CO_2$ capture because they typically have large surface areas, accessible channels, and well-organized micropores. For example, Gao *et al.*[158] developed TPE-COF-II, a 2D COF with a frustrated bonding network resulting from an unusual [2+4] condensation pathway. The $CO_2$ uptake capacity of 23.2 weight percent (118.8 $cm^3\ g^{-1}$ at 273 K and 1 atm) is among the highest reported for 2D COFs due to its open pores and unreacted functional groups that enhance host–guest interactions.

In contrast, three-dimensional COFs (3D COFs) have longer, more interconnected networks with more internal voids and structural rigidity, resulting in better $CO_2$ adsorption capacities than their two-dimensional counterparts.[159,160] For instance, Zhu *et al.*[161] developed a family of crystalline 3D COFs (RICE-3 to RICE-7) made from logically constructed trigonal and rectangular-planar linkers to demonstrate the structural advantages of 3D COFs over 2D counterparts. To illustrate, (Fig. 30a–f), shows how these linkers form interconnected polyhedral cages with hierarchical porosity and long-range order. The remarkable $CO_2$ uptake performance of ∼50 $cm^3\ g^{-1}$ at 273 K and 1 bar made RICE-5 stand out due to its large mesopore aperture (∼4.6 nm), high porosity (∼94.2%), and exceptionally low framework density (∼0.094 g $cm^{-3}$). RICE-3 and RICE-7 visualizations (Fig. 30g and h), show how pore size distribution affects gas adsorption. RICE-7 is more microporous (1.0 nm), resulting in lower uptake, whereas RICE-3 has larger mesopores and wider inter-channel windows, which promote better diffusion. The 3D COFs featuring hierarchical and interconnected pores, such as RICE-5, exhibit enhanced adsorption capacities due to improved accessibility, effective packing, and diminished diffusion resistance, as evidenced by the $CO_2$ isotherms (Fig. 30i and j). The findings underscore the significant influence of topology and dimensionality in 3D frameworks on the advancement of COF-based greenhouse gas capture technologies.

Covalent bonds can be classified as follows: ether bonds (–C–O–C–), thioether (–C–S–C–), hydrazone bonds (–C═N–$NH_2$), azine bonds (–C═N–), boronate ester bonds (–B(OR)–O–), imine bonds (–C═N–), and triazine bonds (–$C_3N_3$–).[162,163] Noting that, Amine bonds (N-based) and boronate ester bonds (B-based) are widely used in $CO_2$ capture and conversion processes because of their ability to interact with $CO_2$ *via* Lewis' acid–base interaction. Also, COFs with reversible imine linkages (–C═N–) can adsorb and release $CO_2$ molecules under

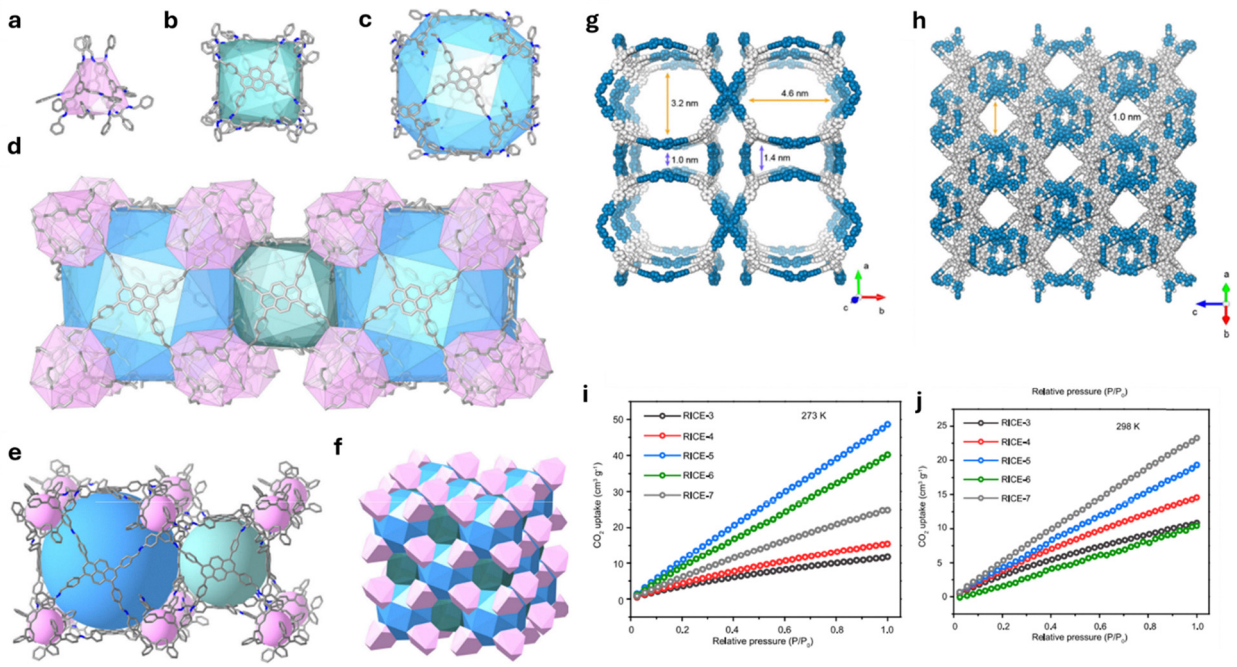


Fig. 30 Structural design, pore geometry, and $CO_2$ adsorption performance of RICE-COFs. (a)–(c) Polyhedral cages in RICE-7, including a truncated tetrahedron ($T^6$, pink), a small cube ($B^{66}$, green), and a large cube ($C^{66}$, blue). (d)–(f) Crystal structure of RICE-7 showing cage connectivity and the *mhq-z* net topology formed *via* face-sharing packing. (g) and (h) Pore visualizations of RICE-3 and RICE-7, highlighting their mesoporous (∼4.6 nm) and microporous (∼1.0 nm) structures, respectively. (i) and (j) $CO_2$ adsorption isotherms of RICE-3 to RICE-7 at 273 K and 298 K, confirming the superior uptake of RICE-5 (∼50 $cm^3\ g^{-1}$ at 273 K) due to its low framework density and hierarchical porosity. Reprinted (adapted) from *Nat Commun*, 2023, **14**, 2865. Copyrights © 2023 The Authors. Published by Springer Nature under the terms of CC-BY license.


© 2026 The Author(s). Published by the Royal Society of Chemistry

Open Access Article. Published on 12 fevral 2026. Downloaded on 01.06.2026 11:06:26.
This article is licensed under a Creative Commons Attribution-NonCommercial 3.0 Unported Licence.

various conditions, including temperature, pressure, and gas composition changes.[164] $CO_2$ adsorption can cause Imine-linked COFs to expand structurally, leading to increased capacity for storage. Additionally, Imine bonds improve the catalytic potential of COFs for $CO_2$ conversion by facilitating coordination and promoting reaction pathways. A notable example is the 3D-Ru-COF, which is composed of tetrakis (4-aminophenyl) methane (TAPM) and N-functionalized [2,2′-bipyridine]-5,5′-dicarbaldehyde (BPDCA). Kumar *et al.*[165] demonstrated that THF-assisted solvent treatment increased $CO_2$ uptake by 21% by causing flexible "pedal motion" in imine linkages (from 3.94 to 4.76 mmol $g^{-1}$ at 273 K). Imine-linked 3D COFs exhibit dynamic and reusable properties in gas capture and catalytic applications, as evidenced by their structural modulation stability over seven consecutive adsorption–desorption cycles.

Increased $CO_2$ uptake is correlated with higher surface areas (*e.g.*, >3000 $m^2$ $g^{-1}$), which are determined by textural properties such as surface area, pore volume, and pore size distribution.[166] Yaghi *et al.*[153] developed 3D covalent organic frameworks (COFs) like COF-102 and COF-103 using a rational topological approach that combines tetrahedral (*e.g.*, TBPM, TBPS) and trigonal (*e.g.*, HHTP) building blocks *via* boroxine or boronate ester linkages (Fig. 31).

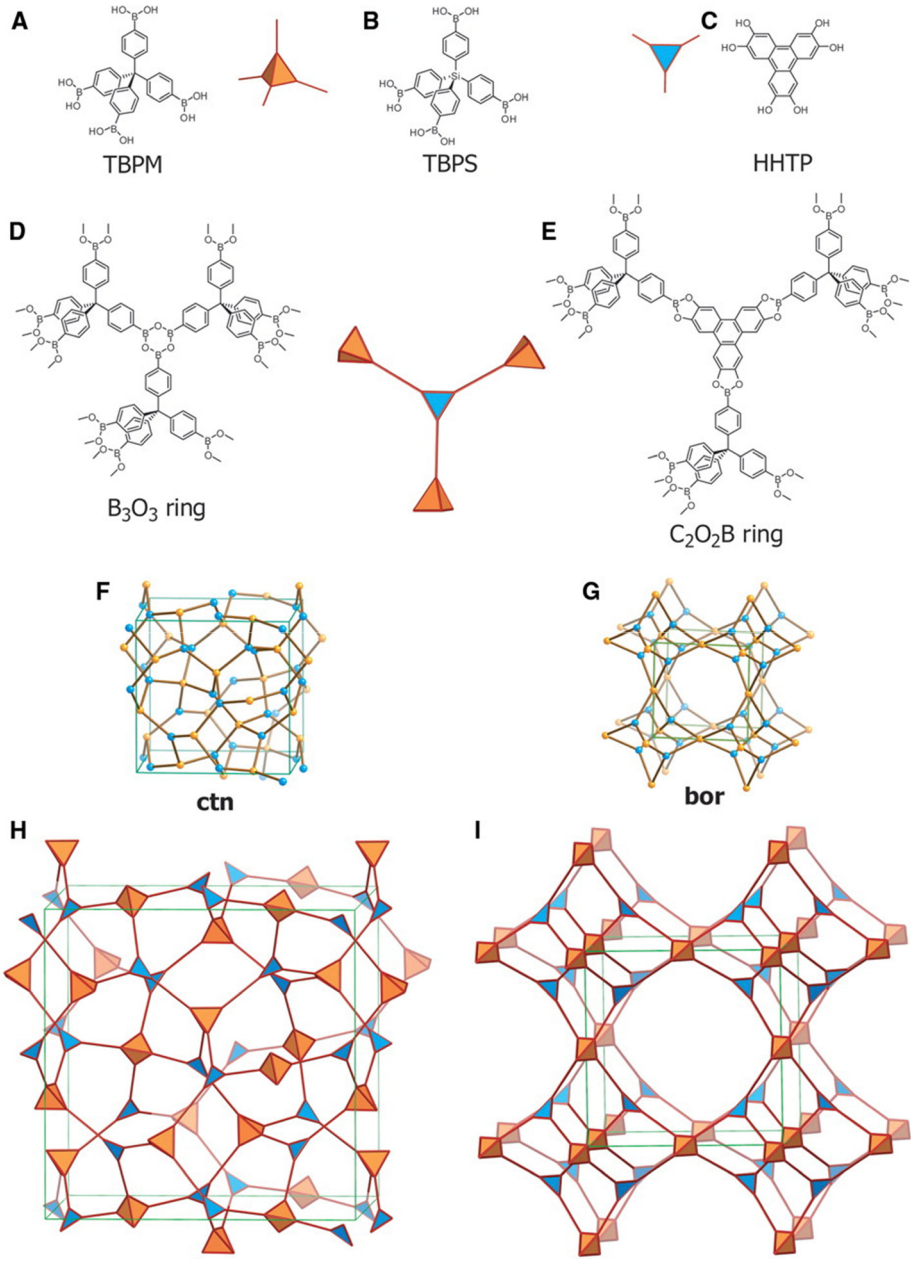


Fig. 31 Representative building units and topologies for 3D COFs. (A) and (B) Tetrahedral. (C) Trigonal. (D) Linkers form boroxine. (E) Boronate ester. (F) and (H) Rings, assembling into *ctn*. (G) and (I) *Bor* networks, as observed in COF-102 and COF-103. Reprinted (adapted) from *Science* (5822), 268–272. Copyright © 2007, The American Association for the Advancement of Science.

Open Access Article. Published on 12 fevral 2026. Downloaded on 01.06.2026 11:06:26.
This article is licensed under a Creative Commons Attribution-NonCommercial 3.0 Unported Licence.

These configurations yield highly crystalline and porous frameworks with ctn and bor net topologies. The precise reticular design creates ultrahigh surface areas of 3472 $m^2 g^{-1}$ for COF-102 and 4210 $m^2 g^{-1}$ for COF-103, resulting in exceptional $CO_2$ uptake capacities of up to 27 mmol $g^{-1}$ at 298 K and 1 bar, respectively. Also, Alahakoon *et al.*[167] developed an azine-linked COF (HEX-COF-1) with a BET surface area of 1214 $m^2 g^{-1}$ and a narrow pore size distribution of ~1 nm. With an enthalpy of adsorption of 42 kJ $mol^{-1}$ and a relatively moderate surface area, HEX-COF-1 showed a high uptake of $CO_2$ of over 20 weight percent at 273 K, indicating strong quadrupolar interactions between $CO_2$ and the polar framework.

The inclusion of functional groups and active sites, such as $-SO_3H$, $-NH_2$, triazine, or metal centers, improves $CO_2$-framework interactions through polar binding or catalytic activation.[168] Functionalization strategies, whether post-synthetic or through direct monomer design, allow for modification of the chemical environment, adsorption strength, and selectivity.[169] Wei *et al.*[168] conducted a thorough study on several 3D COF-300 derivatives featuring $-SO_3H$, $-NO_2$, –OH, and $-NH_2$ groups to investigate their ability to capture $CO_2$. While selectively changing the chemical environment inside the pores, these COFs were derived from a common parent framework (COF-300-THF) and retained the same underlying topology (Fig. 32a), the addition of polar functional groups considerably altered the behavior of $CO_2$ uptake. As illustrated in (Fig. 32b), COF-300-$SO_3H$ nearly five times outperformed the unmodified COF-300-THF in terms of adsorption capacity, reaching a maximum of 6.23 mmol $g^{-1}$ at 298 K and 100 kPa. The strong hydrogen-bonding and electrostatic interactions facilitated by the sulfonic acid groups, which serve as high-affinity binding sites, are responsible for this improvement. The nitro-functionalized framework (COF-300-$NO_2$) also showed high uptake (~4.8 mmol $g^{-1}$), whereas substitutions with –OH and $-NH_2$ produced moderate improvements over the parent material. Significant gains in $CO_2/N_2$ selectivity resulted from the $N_2$ adsorption isotherms (Fig. 32c), which showed little uptake across all COFs, especially in the more polar variants. This effect is shown in (Fig. 32d), selectivity of (~393) for COF-300-$SO_3H$ was significantly higher than that of COF-300-$NO_2$ (~31), COF-300-OH (~11), and COF-300-$NH_2$ (~10), demonstrating the crucial role that electronegativity and functional group polarity play in gas separation performance. Radial distribution function (RDF) analyses and $CO_2$ density distribution maps provided additional mechanistic insights. $CO_2$ molecules were found to preferentially localize close to the functional groups at both low (10 kPa) and high (100 kPa) pressures, particularly in COF-300-$SO_3H$ and COF-300-$NO_2$. This pattern is supported by the RDF plots, which show that the $NO_2$ group also exhibited favorable interaction behavior. In contrast, the $SO_3H$–$CO_2$ interaction displays the shortest and most intense peak (~2.5 Å), indicating strong binding affinity. The distributions of $NH_2$ and OH groups, on the other hand, were wider and less intense. This is consistent with their lower selectivity and weaker binding.

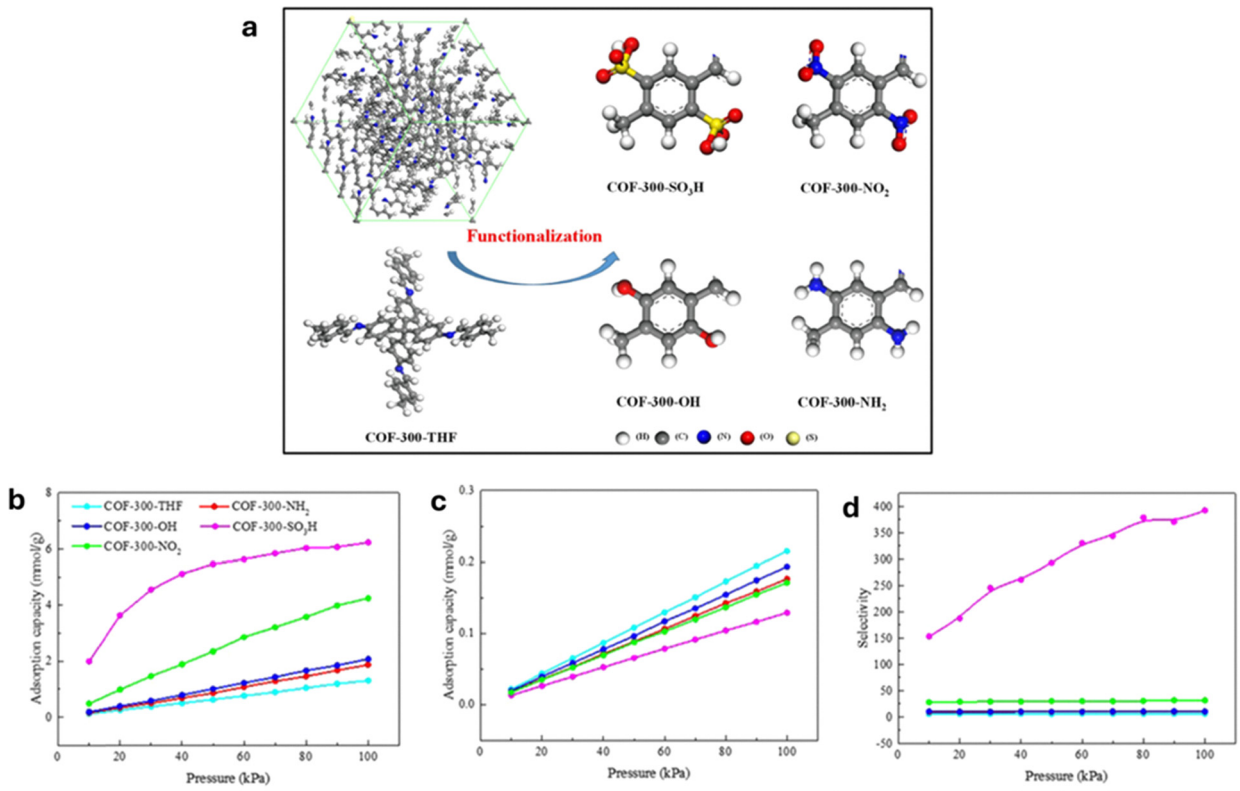


Fig. 32 (a) COF-300s with different functional groups. (b) $CO_2$ adsorption isotherms, (c) $N_2$ adsorption isotherms, and (d) selectivity of $CO_2$ over $N_2$ in COF-300s at 298 K. Reprinted (adapted) from *Adv. Theory Simul.* 2022, **5**, 2200588. © 2022 Wiley-VCH GmbH.


© 2026 The Author(s). Published by the Royal Society of Chemistry

Open Access Article. Published on 12 fevral 2026. Downloaded on 01.06.2026 11:06:26.
This article is licensed under a Creative Commons Attribution-NonCommercial 3.0 Unported Licence.

## 4. COFs for $CO_2$ electrochemical conversion

Electrocatalytic technology, which facilitates faster electron transfer between electrodes, reduces $CO_2$. It has several advantages, including mild operating conditions, reactors that can be successfully integrated, controlled reaction rates and selectivity, and the ability to utilize renewable energy sources. The electrocatalytic process consists of three fundamental steps: (1) adsorption of reactant species on the surface of active sites; (2) formation of intermediate states; and (3) desorption of the products.[143,170] COFs can provide a useful platform for enhancing $CO_2$ conversion efficiency through the $CO_2$RR process due to their unique structural components and chemical properties. COFs converted a large surface area into numerous active sites by incorporating organic components into their structure, which produced spaces that reacted well. Additionally, transition metal species (*e.g.*, Fe, Ni, Co) present in COFs are used as active centers for the conversion of $CO_2$ in electrochemical reactions due to their active d-electrons and vacant orbitals.[171] Atomic size and electronegativity are two fundamental properties of metal active sites in COFs that significantly impact their inherent selectivity and activity. This approach has been demonstrated in the investigation of Lin *et al.*;[172] wherein isolated cobalt porphyrin units were incorporated into ultrathin 2D COF nanosheets. The atomic dispersion of cobalt provided a consistent coordination environment, minimizing electronic fluctuations across sites and resulting in improved CO selectivity and enhanced catalytic stability.

The successful outcome of $CO_2$ reduction can be significantly enhanced by incorporating transition metals, alkaline-earth metals, and single-atom sites into organic or carbon-based frameworks, as numerous studies have demonstrated. For instance, Wu *et al.*[173] reported that single-atom Mg and Ca attached to nitrogen-doped carbon exhibited outstanding selectivity for formate production at near-zero overpotentials by favoring *OCHO intermediate formation. Dagnaw *et al.*[174] demonstrated a unique molecularly cationic covalent organic frameworks that incorporate transition metals (Cu and Pd) as active sites for the extremely selective electrochemical reduction of $CO_2$ into CO. They synthesized two COFs, CuCOF and CuCOF$^+$, by coordinating Cu(I)-bisphenanthroline complexes with terpyridine-based organic linkers. CuCOF$^+$ was further modified with ethyl groups to improve its positive surface charge and hydrophilicity, which ultimately promoted $CO_2$ accessibility and inhibited the HER side reaction. The COFs displayed a distinctive, three-dimensional woven framework (Fig. 33). The resulting CuCOF-Pd and CuCOF$^+$-Pd catalysts showed significant increases in faradaic efficiency after loading Pd nanoparticles (NPs) into the pores of CuCOF and CuCOF$^+$. For CuCOF$^+$-Pd, the selectivity of CO reached up to 95.45% at −0.8 V *vs.* RHE.

Additionally, catalytic activity and electron transport efficiency in $CO_2$ reduction systems can be improved simultaneously by combining metal active centers and conductive structural units in a single framework. For instance, Zhu *et al.*[175] designed a series of metalloporphyrin–tetrathiafulvalene-based covalent organic frameworks (M-TTCOFs) that provide a convincing example of how combining metal active centers and conductive structural units within a single framework can simultaneously enhance catalytic activity and electron transport efficiency in $CO_2$ reduction systems. The M-TTCOFs were produced by Schiff-base condensation between 4-formyl-TTF and M-TAPP (where M = Co or Ni), as shown in (Fig. 34a). This resulted in 2D layered structures with a unique porous structure and π-conjugated frameworks. The embedded metalloporphyrin moieties (such as Co or Ni) act as catalytically active sites in this system. While tetrathiafulvalene (TTF) acts as a highly conjugated electron donor, creating direct charge-transport pathways. This building improves the accessibility of redox-active centers and facilitates effective charge migration throughout the framework. As shown in the LSV curves (Fig. 34b) and FECO profile (Fig. 34c), the Co-TTCOF exhibited the highest catalytic activity, maintaining over 90% selectivity within a wide potential range (−0.6 to −0.9 V) and achieving a faradaic efficiency for CO ($FE_{CO}$) of 91.3% at −0.7 V *vs.* RHE. After exfoliation into nanosheets (~5 nm thick), the $FE_{CO}$ further increased to a maximum of 99.7% at −0.8 V, among the highest reported for COF-based electrocatalysts.

## 5. COFs for integrated $CO_2$ capture and electrochemical conversion

Recent progress in COFs has demonstrated that they can integrate $CO_2$ capture and electrochemical conversion into a single material. This addresses the significant issue of separating $CO_2$ from flue gas, which requires an energy-intensive process. For instance, Liu *et al.*,[176] demonstrated a dual-functional covalent organic framework (PA-Co-COF) that combines $CO_2$ capture and

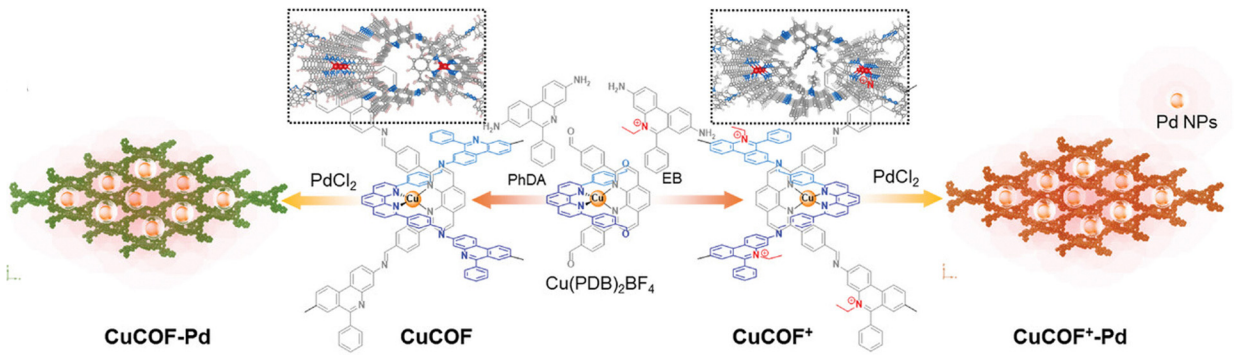


Fig. 33 Synthesis of CuCOF, CuCOF$^+$, CuCOF-Pd, CuCOF$^+$-Pd. Reprinted (adapted) from *Adv. Sci.* 2024, **11**, 2408152. Copyrights © 2024 The Author(s). Published by Wiley-VCH GmbH under the terms of CC-BY license.

Open Access Article. Published on 12 fevral 2026. Downloaded on 01.06.2026 11:06:26.
This article is licensed under a Creative Commons Attribution-NonCommercial 3.0 Unported Licence.

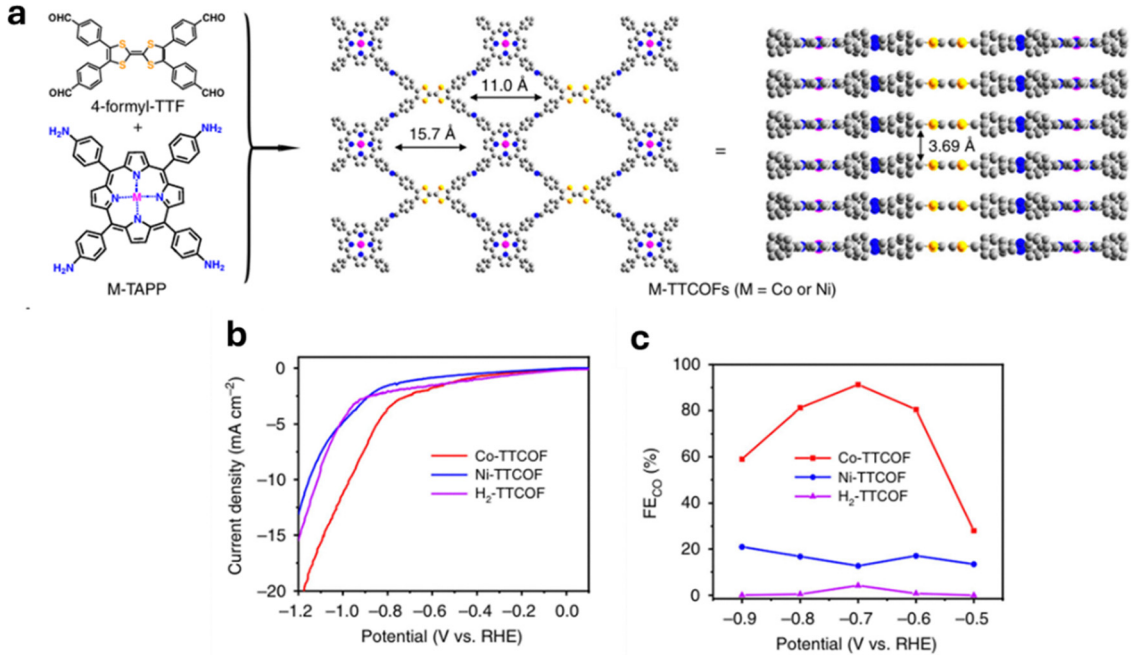


Fig. 34 Structural design and electrocatalytic performance of M-TTCOFs (M = Co or Ni) for $CO_2$ reductio. (a) Synthesis of 2D M-TTCOFs *via* condensation of 4-formyl-TTF and M-TAPP, forming ordered frameworks with defined pores. (b) LSV curves showing enhanced activity of Co-TTCOF over Ni- and $H_2$-TTCOFs. (c) Faradaic efficiency for CO production across −0.5 to −0.9 V, with Co-TTCOF showing superior selectivity. Reprinted (adapted) from *Nat Commun*, 2020, **11**, 497. Copyright © 2020, The Author(s). Published by Springer Nature under the terms of CC-BY license.

electrochemical conversion within a single material. This material is effective in environments with low $CO_2$ concentrations, such as flue gas (approximately 15% $CO_2$). (Fig. 35) illustrates that the framework consists of phytic acid (PA), which binds to $CO_2$, and cobalt-porphyrin (CoPor), serving as the catalytic center. (Fig. 35a) shows the conventional Co-COF with unmodified channels, while (Fig. 35b) demonstrates how the inclusion of PA creates $CO_2$-trapping channels that guide $CO_2$ molecules toward the catalytic sites. The synthetic pathway in (Fig. 35c) highlights the *in situ* formation of the PA-Co-COF from PYTA, DHTA, CoPor, and PA. Structural analysis in (Fig. 35d) confirms that incorporation of PA and CoPor preserves the crystalline order of the COF framework. The proposed mechanism in (Fig. 35e) shows the elementary steps of $CO_2$ reduction to CO, proceeding *via* the *COOH intermediate. Electrochemical data presented in (Fig. 35f and g) demonstrate that PA-Co-COF achieves a CO faradaic efficiency of 86.97% at −0.7 V and a maximum turnover frequency (TOF) of 1208.8 $h^{-1}$ at −1.0 V, far above the performance of the unmodified Co-COF. Density functional theory (DFT) calculations in (Fig. 35h and i) expose that PA lowers the energy barrier for *COOH formation (from 0.495 eV to 0.323 eV) and increases the barrier for the competing hydrogen evolution reaction (HER) (from 0.666 eV to 0.887 eV), thereby enhancing both selectivity and activity. Also, some selected COF-based catalysts are summarized in (Table 11) for $CO_2$ capture and electrochemical reduction.

### 6. Future outlook of COFs

COFs are emerging as a versatile platform for integrated $CO_2$ capture and electrochemical conversion. By combining strong $CO_2$-binding functionalities, such as amine groups, with conductive, π-conjugated networks, COFs can simultaneously adsorb $CO_2$ and catalyze its reduction, potentially within a single device. Recent reviews highlight the feasibility of bifunctional porous electrodes composed of COFs that act as both capture media and electrocatalysts. Importantly, techno-economic analyses indicate that coupling capture with electrochemical conversion can significantly reduce overall energy consumption, particularly by eliminating energy-intensive $CO_2$ desorption steps. Future development will focus on enhancing chemical and electrochemical robustness, for instance *via* stable linkers and hydrophobic coatings, and improving charge transport through conductive dopants or metal sites. Scaling up from laboratory microwave synthesis to continuous-flow reactors will also be critical for real-world deployment. Altogether, these integrated COF systems offer a compelling pathway toward compact, energy-efficient $CO_2$ conversion devices, merging capture and catalysis into streamlined, resilient technologies.

## Zeolites

Zeolite is a crystalline, microporous material made up of alumina-silicate structures. It is used in many industrial processes, such as gas separation, ion exchange, and catalysis.[183,184] Its unique properties allow it to effectively adsorb and trap molecules, making it essential in various chemical processes and environmental remediation efforts, as shown in (Fig. 36). Different ways are used, such as an adsorbent, an ion exchanger, and a catalyst.[183,185] Zeolite performs well as a catalyst for conventional uses in refineries and petrochemical businesses.[186]


© 2026 The Author(s). Published by the Royal Society of Chemistry

Open Access Article. Published on 12 fevral 2026. Downloaded on 01.06.2026 11:06:26.
This article is licensed under a Creative Commons Attribution-NonCommercial 3.0 Unported Licence.

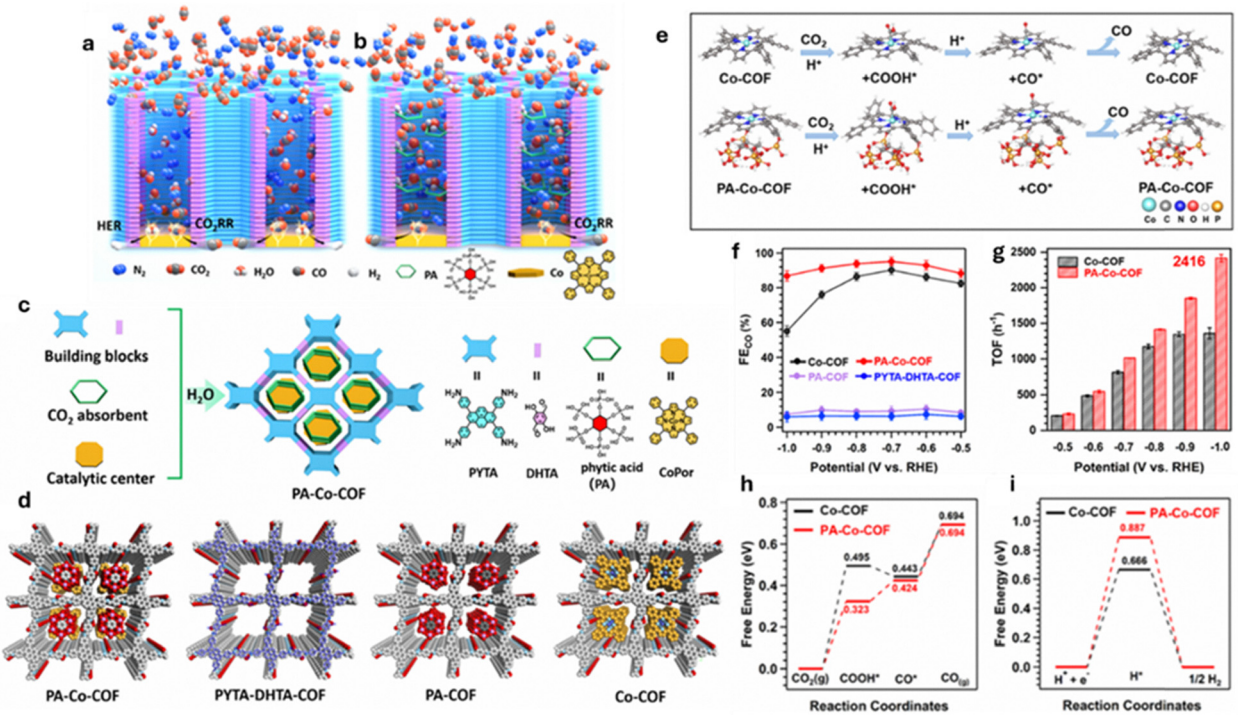


Fig. 35 Integrated schematic and performance data of PA-Co-COF for $CO_2$ electroreduction under simulated flue gas. (a) Schematic illustration of Co-COF. (b) PA-Co-COF showing transport and catalytic channels for $CO_2$ reduction reaction ($CO_2RR$). (c) *In situ* synthesis of PA-Co-COF from PYTA, DHTA, and Co-porphyrin, with phytic acid (PA) acting as both template and pore-filling $CO_2$ absorbent. (d) Crystal structures of PA-Co-COF, PYTA-DHTA-COF, PA-COF, and Co-COF highlighting retention of crystalline order. (e) Proposed reaction pathway for $CO_2$-to-CO conversion on CoPor active sites. (f) CO faradaic efficiency ($FE_{CO}$) of different COF structures from −0.5 to −1.0 V *vs.* RHE. (g) Calculated turnover frequency (TOF) for CO, showing enhanced reaction kinetics for PA-Co-COF. (h) DFT-calculated Gibbs free energy profile for the $CO_2$ reduction reaction, indicating a lower energy barrier for PA-Co-COF. (i) DFT-calculated Gibbs free energy profile for the competing hydrogen evolution reaction (HER), showing that $H_2$ formation is suppressed on PA-Co-COF. Reprinted (adapted) from *ACS Catal.* 2024, **14**, 14, 11076–11086. Copyright © 2024 American Chemical Society.

Zeolite is characterized by microporous structure (less than 2 nm) that is organized by $TO_4$ tetrahedra, where (T stands for tetrahedrally coordinated Si or Al).[187–189] Molecular shape selectivity, a large surface area, and great thermal stability are some of the wonderful properties of zeolite that make it a great host matrix for metal clusters or nanoparticles.[190,191] This makes multipurpose composite materials with great properties owing to these characteristics, it offers a catalytic site for the conversion of the intermediate produced by $CO_2$ activation in the active metal site to generate hydrocarbons from $CO_2$.[192,193] Therefore, it would be possible to manipulate the zeolite catalyst's structural or textural characteristics to arrange the hydrocarbon goal yield.[190,194]

During the process of $CO_2$-integrated collection and conversion, zeolites can perform the functions of both adsorbents and catalysts.[195] The microporous structure of these materials allows them to selectively adsorb carbon monoxide (CO). Because they are catalytic, CO can be changed into compounds with added value, like methanol, hydrocarbons, or syngas.[193] Metal-loaded zeolites, such as those containing nickel, copper, or iron, enhance catalytic performance by enabling the electrochemical reduction or hydrogenation of carbon dioxide. When it comes to structural qualities, product selectivity was found to have a significant relationship between the arrangement of the perfect acid density and the strength of the zeolite catalyst.[196]

Zeolites can be sub-grouped into natural and synthetic. On the one hand, natural zeolites such as ZAPS can be used as dryers and deodorants for air separation and ion exchange for water treatment and soil improvement (Fig. 37). On the other hand, synthetics such as FAU have advantages over natural ones, such as achieving high control over the material's porosity and crystallinity, but they are more expensive compared to affordable natural zeolites. Despite the lower cost of natural zeolites, they have reduced purity, varying composition, and inferior sorption properties.[197,198]

### 1. Zeolites for $CO_2$ capture

Boer *et al.* divided the zeolite into two groups. The first is medium and large-pore zeolites, with pore sizes in the range of 4.5–6.0 Å and 6.0–8.0 Å, respectively. The second group is small-pore zeolites, which have pores in the range of 3.0–4.5 Å (Fig. 38).[199] $CO_2$ is preferentially adsorbed on zeolite surfaces due to its considerably higher quadrupole moment and polarizability relative to other gases in flue gas (Table 12). This understanding is crucial because the 8-membered rings are the only structures in small-pore zeolites that encourage $CO_2$ diffusion, while the pore sizes of smaller rings (*e.g.*, 6-membered rings) are excessively closed. The capture mechanism for the selective adsorption and separation of $CO_2$ from gas mixtures utilizing zeolites as adsorbents primarily encompasses equilibrium separation, kinetic separation, and molecular sieving separation.[199–201]

Open Access Article. Published on 12 fevral 2026. Downloaded on 01.06.2026 11:06:26.
This article is licensed under a Creative Commons Attribution-NonCommercial 3.0 Unported Licence.



Table 11 Summary of selected COF-based catalysts reported for $CO_2$ capture and electrochemical reduction

| Catalysts | Pore size (Å) | Dimensional | Linkage type | BET surface area ($m^2\ g^{-1}$) | Capacity $CO_2$ ($mg\ g^{-1}$) | Electrochemical application | Electrochemical TOF or selectivity | Ref. |
|---|---|---|---|---|---|---|---|---|
| TFPc-PBBA-COF | 22 | 3D | Boronate Ester | 111.8 | 16.7 | $CO_2$RR | Selectivity for CO 95%<br>TOF = 1695 $h^{-1}$ | 177 |
| CoPc-PI-COF-1 | 16 | 2D | Imine (polyimide) | 181 | 38.52 | $CO_2$RR | Selectivity for CO 97%<br>TOF = 2.2 $s^{-1}$<br>TON = 277 000 | 148 |
| CoPc-PI-COF-2 | 18 | 2D | Imine (polyimide) | 291 | 37.78 | $CO_2$RR | Selectivity for CO 96%<br>TOF = 1.9 $s^{-1}$<br>TON = 71 000 | 148 |
| CoPor-DPP-COF | 20.08 | 2D | Imine | 1021 | 3.72 | $CO_2$RR | Selectivity for CO 82% | 178 |
| Cu-Tph-COF-Dct | 12–18 | 2D | Imine (Porphyrin-based) | 335 | 120.4 | $CO_2$RR | Selectivity for $CH_4$ 80% | 179 |
| COF-102 | 12 | 3D | Boronated Ester | 3620 | 1200 | $CO_2$ storage | N/A | 166 |
| COF-103 | 12 | 3D | Boronate Ester | 3530 | 1190 | $CO_2$ storage | N/A | 166 |
| (3D-HNU5) | 10 | 3D | Azine | 864 | 123.1 | Cyclic carbonate synthesis | TON = 990, Yield > 99% | 180 |
| Tz-COF | 21 | 2D | Imine | 1439 | 154 | Gas separation | Higher $CO_2$ selectivity than $N_2$ (20/12) | 181 |
| Cz-COF | 20 | 2D | Imine | 871 | 110 | Gas storage & separation | Good recyclability and selectivity | 181 |
| Zn-Salen-COF-SDU113 | 35 | 2D | Imine | 1143 | 19.8 | Cycloaddition with epoxides to carbonates | Yield = 98.2%,<br>TON = 3068.9 | 182 |
| Cu-COF+ | 28 | 2D | Imine (Cationic, ethyl-modified) | 27.6 | 13.7 | $CO_2$RR | Selectivity for CO 57.81% | 174 |
| Cu-COF+-Pd | 28 | 2D | Imine (Cationic + Pd) | 4.1 | 8.4 | $CO_2$RR | Selectivity for CO 95.45% | 174 |
| PA-Co-COF | 16.9 | 2D | Imine | 689 | 102.9 | $CO_2$RR from the flow gas | Selectivity for CO 86.97%<br>TOF = 1208.8 $h^{-1}$ | 176 |
| Co-TTCOF | 25.4 | 2D | Imine (porphyrin + TTF) | 486 | 39.3 | $CO_2$RR | Selectivity for CO 99.7%<br>TOF = 1.28 $s^{-1}$ | 175 |
| COF-367-Co (1%) | 12–23 | 2D | Imine | 1470 | N/A | $CO_2$RR | Selectivity for CO 40%<br>TOF = 764 $h^{-1}$<br>TON > 24 000 (TONEA ≈ 296 000) | 172 |
| COF-367-Co | 12–23 | 2D | Imine | 1470 | N/A | $CO_2$RR | Selectivity for CO 91%<br>TOF = 165 $h^{-1}$<br>TON = 3901<br>(TONEA ≈ 48 000) | 172 |



© 2026 The Author(s). Published by the Royal Society of Chemistry

Open Access Article. Published on 12 fevral 2026. Downloaded on 01.06.2026 11:06:26.
This article is licensed under a Creative Commons Attribution-NonCommercial 3.0 Unported Licence.

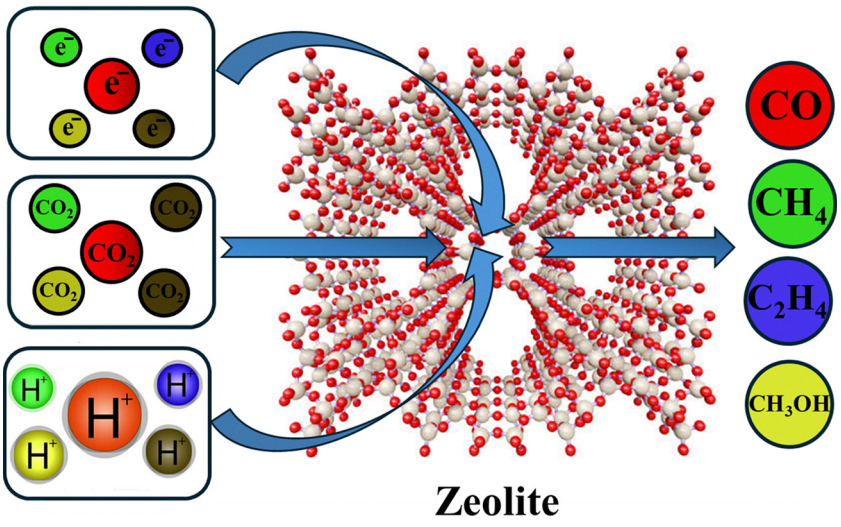


Fig. 36 Schematic illustration of zeolite for $CO_2$ capture and electrocatalytic conversion.

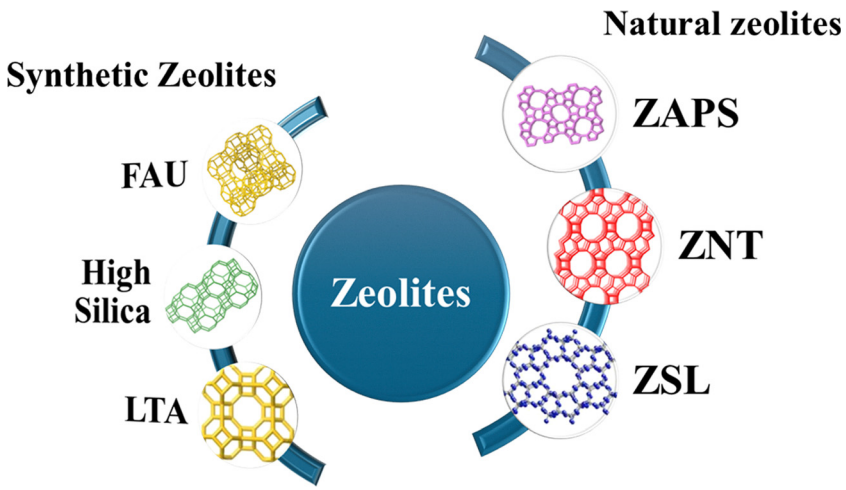


Fig. 37 Classification of zeolites.

Equilibrium separation depends on how the guest molecules and the zeolite micropores interact with each other.[204] These interactions could be physisorption (which involves van der Waals forces and electrostatic interactions) and chemisorption (which involves π-complexation).[205,206] What affects the electric charge exchange between gas molecules and zeolite surfaces are the polarity, polarizability, Si/Al ratios, and the types of metal cations. Kinetic separation relies on the different speeds at which guest molecules move through the tiny holes in zeolite.[207] Kinetic separation is limited by molecular sieving, which needs zeolite micropores that are big enough to let $CO_2$ through, but not any other exhaust gases.[199,208]

A compelling example of a zeolite-based material for $CO_2$ capture is the hierarchical ZIF-L nanostructure reported by Ding *et al.* In this study, the authors synthesized a cross-shaped hierarchical ZIF-L using a simple hydrothermal method involving zinc nitrate and 2-methylimidazole at 125 °C. This hierarchical structure, composed of symmetrically connected ZIF-L leaf-like plates, exhibited a significantly enhanced Brunauer–Emmett–Teller (BET) surface area of 304 $m^2\ g^{-1}$ compared to 161 $m^2\ g^{-1}$ for conventional two-dimensional ZIF-L. As a result, the $CO_2$ adsorption capacity reached 1.56 mmol $g^{-1}$ at 298 K and 1 bar, outperforming both the 2D ZIF-L (0.94 mmol $g^{-1}$) and even ZIF-8 (0.68 mmol $g^{-1}$), despite ZIF-8 having a much higher surface area. This superior performance is attributed to the unique cushion-shaped cavities of ZIF-L and the hierarchical architecture, which provides enhanced accessibility to active sites and reduces particle aggregation.

### 2. Factors affecting $CO_2$ adsorption over zeolite

Zeolites are commonly used as absorbents for the absorption of $CO_2$ from flue gas, namely in $CO_2/N_2$ separation processes.[205] In their study, Zhang *et al.* look at the zeolite extra-framework cation, secondary-pore system, particle size, and Si/Al ratio as important factors that have a big effect on the adsorption mechanism, capacity, and selectivity (Fig. 39).[200]

Open Access Article. Published on 12 fevral 2026. Downloaded on 01.06.2026 11:06:26.
This article is licensed under a Creative Commons Attribution-NonCommercial 3.0 Unported Licence.

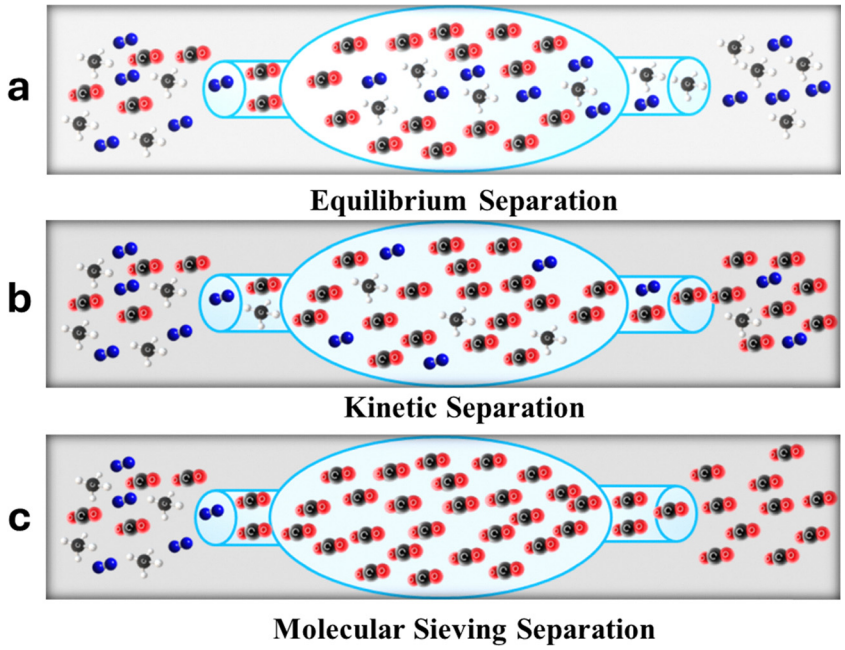


Fig. 38 Different types of $CO_2$ separation over zeolites. (a) Equilibrium separation, in which $CO_2$ preferentially adsorbs on the surface of the adsorbent. (b) Kinetic separation, in which $CO_2$ diffuses faster through the pores. (c) Molecular sieving separation, in which only $CO_2$ can enter the pores.

Table 12 Properties of gases relevant to $CO_2$ separation from flue-gas[202,203]

| Gases | Kinetic diameter (Å) | Quadrupole ($C\ m^{-2}$) | Polarizability ($cm^3$) |
|---|---|---|---|
| $CO_2$ | 3.30 | $13.4 \times 10^{-40}$ | $2.65 \times 10^{-24}$ |
| $N_2$ | 3.64 | $4.6 \times 10^{-40}$ | $1.76 \times 10^{-24}$ |
| $O_2$ | 3.50 | — | $1.58 \times 10^{-24}$ |
| $CH_4$ | 3.80 | 0 | $2.60 \times 10^{-24}$ |

**(A) Type of framework.** Different types of zeolites are distinguished by the size and shape of the channels and cages present within their framework, with about 258 fully ordered zeolite frameworks and a few partially disordered frameworks. All zeolite frameworks talked about in the previous chapter can be found in (Table 13).[209] Several essential characteristics can be defined by the zeolite framework type, such as the number of Si/Al atoms in the rings and the related pore size (Å). As the $CO_2$ molecule only diffuses through at least 3.3 Å of the pore aperture, the ring should be an 8MR or larger. Additionally, zeolites with the same structure and similar crystal size should, in principle, have a similar surface area in their H-form. Additionally, the topography of zeolitic pores is classified into three main types. Cage structures (C), such as LTA, CHA, and FAU, where spherical cavities are interconnected *via* small windows, allowing size-selective diffusion. MFI and BEA serve as exemplars of Intersecting channel systems (IC), which provide a three-dimensional interconnected network enabling multidirectional transport and high accessibility. FER and MOR frameworks represent one-dimensional channels connected to cages (1D+C) which include linear diffusion pathways to isotropic central regions called cages that are usually, but not always severely restricted in mobility due to steric or electrostatic forces.[199,210,211]

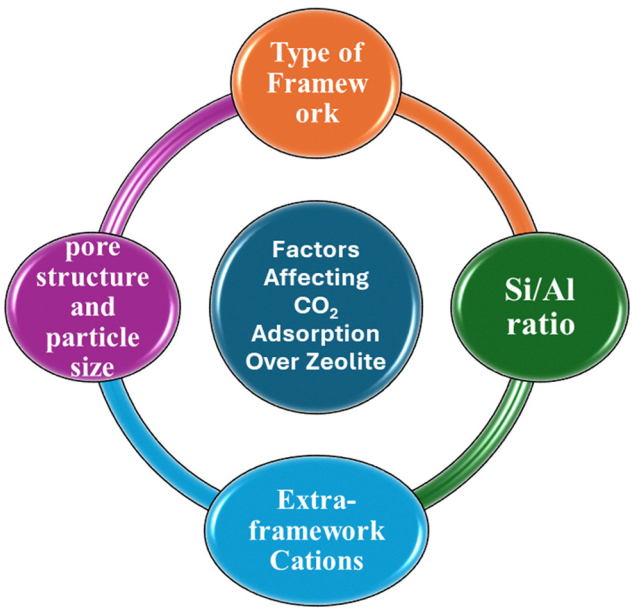


Fig. 39 Factors affecting $CO_2$ adsorption over zeolites.

Also, the diffusion of adsorbates is affected by the pore topology, the pore size, and the shape of a zeolite, which define its performance as adsorbent as well. Although zeolite frameworks have a certain degree of flexibility, they are often assumed to be rigid and can be induced by temperature, the extra-framework cations, or the presence of adsorbates.[212,213] Also, the studied zeolites of MER and RHO showed an unusual adsorption isotherm with an inflection point attributed to the increase in the pore size, called breathing, and/or the window size.[205,214]


© 2026 The Author(s). Published by the Royal Society of Chemistry

Open Access Article. Published on 12 fevral 2026. Downloaded on 01.06.2026 11:06:26.
This article is licensed under a Creative Commons Attribution-NonCommercial 3.0 Unported Licence.

Table 13 Some representative zeolite materials widely used in $CO_2$ capture and conversion[209]

| Framework type | Secondary building units | Max free sphere (Å) (*a*, *b*, *c*) | Ore topology | Composite building units | Framework image |
|---|---|---|---|---|---|
| Small-pore zeolites the rings that are large enough to allow $CO_2$ to diffuse through them | | | | | |
| LTA | 8 or 4-4 or 6-2 or 6 or 1-4-1 or 4 | 4.21 × 4.21 × 4.21 Å | C | 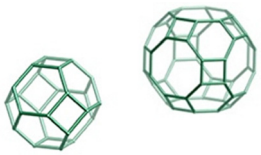 | 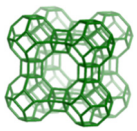 |
| CHA | 6-6 or 6 or 4-2 or 4 | 3.72 × 3.72 × 3.72 Å | C | 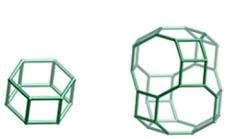 | |
| MER | 8-8 or 8 or 4 | 3.12 × 3.12 × 4.2 Å | 1D+C | 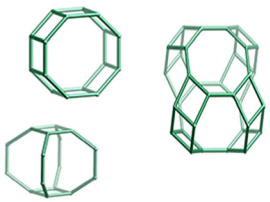 | 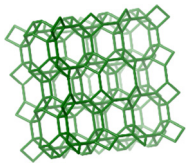 |
| Medium- and large-pore zeolites the rings that are large enough to allow $CO_2$ to diffuse through them | | | | | |
| MFI | 5-1 | 4.7 × 4.46 × 4.46 Å | IC | 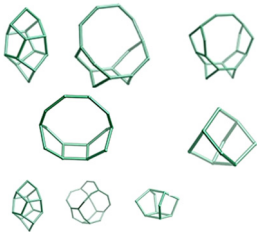 | 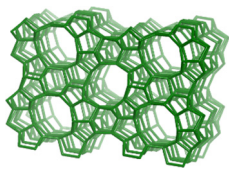 |
| FAU | 6-6 or 6-2 or 6 or 4-2 or 1-4-1 or 4 | 7.35 × 7.35 × 7.35 Å | C | 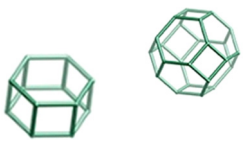 | 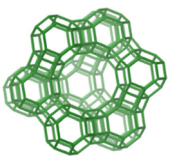 |
| MOR | 5-1 | 1.57 × 2.95 × 6.45 Å | 1D+C | 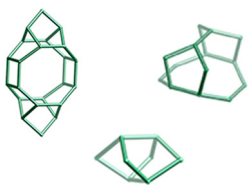 | 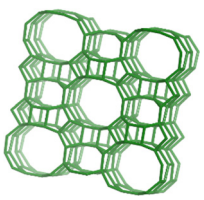 |
| FER | 5-1 | 1.56 × 3.4 × 4.69 Å | 1D+C | 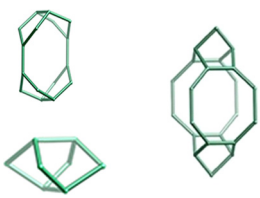 | 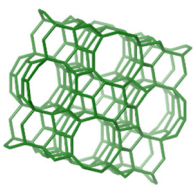 |

**(B) Si/Al ratio.** The Si/Al ratio profoundly influences zeolite $CO_2$ adsorption by controlling framework charge density, cation site density, and pore accessibility. Low Si/Al ratios increase Al content, creating more charge-balancing cations (*e.g.*, $Ca^{2+}$, $Na^{+}$) and Lewis basic O atoms adjacent to Al, which strengthen electrostatic interactions with acidic $CO_2$.[215,216] The zeolite may absorb more CO as the Si/Al ratio decreases, due to an increased number of adsorption sites per unit mass of material.[217] Moreover, silicoaluminate zeolites possess Lewis base sites derived from the oxygen atoms next to aluminum, as a result, the number of these essential sites per unit mass of zeolite escalates with an increase in aluminum content.[218,219] A lower Si/Al ratio suggests more aluminum atom presence inside the framework, thereby producing more negatively charged

Open Access Article. Published on 12 fevral 2026. Downloaded on 01.06.2026 11:06:26.
This article is licensed under a Creative Commons Attribution-NonCommercial 3.0 Unported Licence.

sites needing charge-balancing cations like $Ca^+$. Stronger electrostatic interactions with an acidic $CO_2$ molecule help these cations to bind additional $CO_2$ more easily.[196,199,200] For instance, palomino *et al.* illustrated that zeolite LTA with a Si/Al ratio of 1 has a decreased adsorption capacity compared to zeolite LTA with Si/Al ratios of 2 or more, which has been linked to the decreased visible pore volume in the zeolite with Si/Al = 1.[220] Following these assumptions, many studies show that the ability of zeolites to absorb $CO_2$ usually goes up when the Si/Al ratio goes down.[221] The cation count decreases commensurate with a change in the Si/Al ratio. Strong cations can produce steric hindrance inside the pores, therefore limiting $CO_2$ transport, for instance, the studies by Hong *et al.* unequivocally show this kind of nature. Na-GIS zeolites with low Si/Al ratios (1.5 and 2.2) showed limited $CO_2$ absorption ($\leq$0.7 mmol $g^{-1}$) because of steric hindrance generated by the predominance of $Na^+$ cations blocking pore access. Reduced cation density allowing more effective $CO_2$ transfer clearly boosted adsorption (up to 3.7 mmol $g^{-1}$) seen by increasing Si/Al ratios (2.5–4.7). This work shows how much the Si/Al ratio affects adsorption performance.[222]

**(C) Extra-framework cations.** Modulating extra-framework cations tunes zeolite pore size, volume, framework basicity, and electrostatic interactions, profoundly affecting $CO_2$ adsorption capacity and selectivity as shown in (Table 14). Ion exchange of $Na^+$ with mono- or multivalent cations creates acidic cation sites and basic Al–O sites, where lower cation electronegativity boosts oxygen negative charge and basicity (Cs > Rb > K > Na > Li). Stronger basicity enhances acidic $CO_2$ interactions, but larger ionic radii weaken polarizing power (Li > Na > K > Rb > Cs), creating an optimal charge-to-radius balance.[223,224] Cation radius also tunes zeolite pore size and volume, altering diffusion kinetics and molecular sieving. Shang *et al.* showed with LTA-type zeolites that the cation charge-to-size ratio is a key descriptor for $CO_2$ uptake in direct air capture. Higher-charge, smaller cations ($Ca^{2+}$, $Ni^{2+}$, $Cu^{2+}$) strengthen electrostatic interactions and sometimes π-back-bonding with $CO_2$, giving higher capacities, whereas low-charge or large cations ($K^+$, $Y^{3+}$, $La^{3+}$) perform worse.[225]

Table 14 Shows how cation properties affect metal-exchange LTA zeolite $CO_2$ absorption capability

| $CO_2$ uptake (mmol $g^{-1}$) | Charge/size ratio ($z/r$) | Ionic radius (Å) | Charge ($z$) | Cation |
|---|---|---|---|---|
| Low | 0.98 | 1.02 | +1 | $Na^+$ |
| Low | 0.72 | 1.38 | +1 | $K^+$ |
| Moderate | 2.78 | 0.72 | +2 | $Mg^2$ |
| High | 2.00 | 1.00 | +2 | $Ca^2$ |
| Moderate | 2.41 | 0.83 | +2 | $Mn^2$ |
| Moderate | 2.53 | 0.79 | +2 | $Co^2$ |
| High | 2.90 | 0.69 | +2 | $Ni^2$ |
| High | 2.74 | 0.73 | +2 | $Cu^2$ |
| Moderate | 2.70 | 0.74 | +2 | $Zn^2$ |
| Low | 3.33 | 0.90 | +3 | $Y^3$ |
| Low | 2.91 | 1.03 | +3 | $La^3$ |
| Low | 2.97 | 1.01 | +3 | $Ce^3$ |
| Low | 3.16 | 0.95 | +3 | $Eu^3$ |
| Low | 3.26 | 0.92 | +3 | $Tb^{3+}$ |
| Low | 3.49 | 0.86 | +3 | $Yb^{3+}$ |

**(D) Impact of secondary pore structure and particle size.** Secondary pore systems and particle size strongly impact zeolite $CO_2$ adsorption performance by improving mass transport and accessibility. Smaller particles reduce diffusion path lengths, enabling faster equilibrium, as seen in CHA-type zeolites where nano-sized crystallites exhibit sharper, more dynamic $CO_2$ breakthrough curves compared to larger ones. Hierarchical meso-micro networks further enhance capacity and kinetics: Dabbawala *et al.* reported Y (FAU) zeolites rising from 4.5 to 5.4 mmol $g^{-1}$, while Singh *et al.* found mesoporous LTA zeolites with 29 s faster adsorption, 92 s faster desorption, 20% lower water uptake, and 13 °C lower regeneration temperature *versus* microporous LTA.[226] Concurrently, Dabbawala *et al.* reported an increase in adsorption capacity for hierarchical Y zeolites, from 4.5 mmol $g^{-1}$ for conventional Y (FAU-type) zeolites of $CO_2$. Increasing the hierarchical Y zeolites to 5.4 mmol $g^{-1}$ under the same conditions is ascribed to the presence of the interconnected micro-meso channel network.[227] Moreover, these mesoporous features also showed a 20% drop in water adsorption capacity, a 14% reduction in the heat of $CO_2$ adsorption, and a 13 °C lower temperature required for desorption compared to traditional LTA zeolites, signifying energy efficiency.[60] Similarly, two-dimensional 1.38 nm thick LTA zeolites with a lamellar structure demonstrated superior $CO_2$ capture and separation efficacy than the conventional 3D LTA zeolites.[200,228]

These theoretical insights into the effects of framework topology are well illustrated in the recent work by Al Atrach *et al.* (Fig. 40).[229] The study offers a compelling demonstration of how key structural and compositional factors influence $CO_2$ adsorption over zeolites, using LEV-type zeolite as a case study. By comparing two LEV samples with different morphologies and compositions: a nanosized sample (Si/Al ≈ 6.6) and a micron-sized sample (Si/Al ≈ 3.5). The LEV framework, characterized by

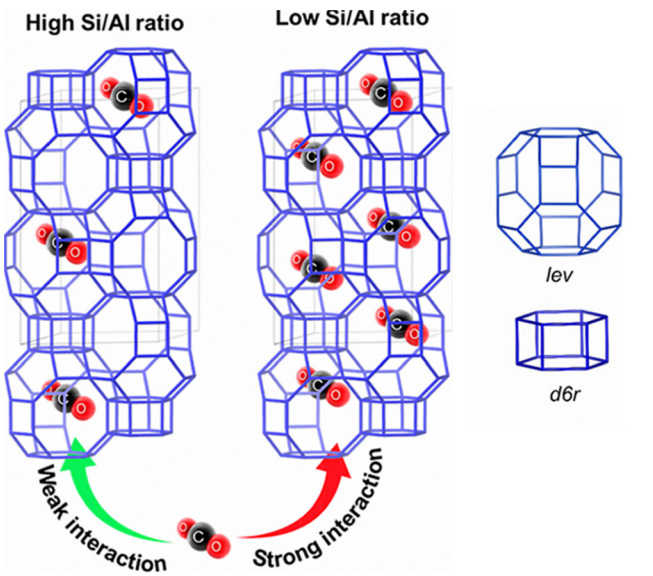


Fig. 40 LEV-type zeolite framework and its composite building units. Reprinted (adapted) from *ACS Appl. Mater. Interfaces* 2025, **17**, 4, 7119–7130. Copyright © 2025 American Chemical Society.


© 2026 The Author(s). Published by the Royal Society of Chemistry

Open Access Article. Published on 12 fevral 2026. Downloaded on 01.06.2026 11:06:26.
This article is licensed under a Creative Commons Attribution-NonCommercial 3.0 Unported Licence.

its small-pore topology and pore dimensions of 3.6 × 4.8 Å, offers a favorable steric and electrostatic environment for $CO_2$ capture due to its compatibility with the kinetic diameter and quadrupole moment of $CO_2$. As a result, the micron-sized sample exhibits a 22% higher $CO_2$ uptake (5.81 mmol $g^{-1}$ at 0 °C) and superior selectivity ($CO_2/N_2$ = 84 at 25 °C) compared to the nanosized sample. Although the nanosized LEV has a higher surface area and mesoporosity, contributing to faster adsorption–desorption kinetics and better reversibility, its lower $Na^+$ content results in weaker $CO_2$ binding and reduced capacity.

## 3. Zeolite in $CO_2$ conversion

Integrating capture and conversion in zeolites boosts efficiency by eliminating compression and transport steps, as in reactive $CO_2$ capture (RCC). Electrocatalytic $CO_2$ reduction ($CO_2$RR) stands out for its ambient conditions, controllable kinetics, and recyclability *versus* energy-intensive thermal routes.[230,231]

The conversion of carbon dioxide ($CO_2$) into valuable chemicals is a primary step in carbon capture and utilization (CCU) technology, but $CO_2$ is a very stable molecule, which makes it difficult for its conversion into alternative compounds difficult, with a high dissociation energy of 750 kJ $mol^{-1}$ as $CO_2$ possesses strong C═O bonds, which indicates that breaking these bonds requires a significant quantity of energy. Consequently, to split $CO_2$ molecules, high pressure, high temperatures, or catalysts are needed.[196] In this context, the thermal catalytic conversion of $CO_2$ into hydrocarbons has primarily followed two main pathways. Also, the selective hydrogenation of $CO_2$ to CO *via* the reverse water–gas shift (RWGS) reaction is highlighted, which serves as a precursor step to further hydrocarbon in thermochemical systems.[232] Notably, this intermediate step-CO-formation can also be achieved *via* electrochemical $CO_2$ reduction ($CO_2$RR), offering an energy-efficient and scalable route under ambient conditions, as will be discussed in subsequent sections. The RWGS can be completed by either of two approaches:

**(A) Fischer–Tropsch synthesis.** Hydrogenation of $CO_2$ to CO, after which comes hydrogenation to hydrocarbons employing the Fischer–Tropsch process.

$$CO_2 + H_2 \rightarrow CO + H_2O.\ \{\Delta H = 41.3\ \text{kJ mol}^{-1}\}\ \text{endothermic}$$

**(B) Methanol synthesis pathway.** $CO_2$ was initially transformed into methanol and then converted into hydrocarbons.

$$CO_2 + 4H_2 \rightarrow CH_4 + 2H_2O.\ \{\Delta H = -164.7\ \text{kJ mol}^{-1}\}\ \text{exothermic}$$

However, at atmospheric pressure, methanol yield is typically negligible, making this route less favorable. Moreover, methanation is thermodynamically dominant at low temperatures, often suppressing RWGS selectivity. Thus, designing catalysts that favor CO production over $CH_4$ remains a key challenge.[196,200]

Zhang *et al.*,[233] illustrate the intricate design and mechanistic pathways alongside the electrochemical performance of the CdO@Zn@Zeolite-Y system in a single diagram (Fig. 41a). The schematic captures the entire process of catalyst fabrication. The first step entails the ion exchange of $Zn^{2+}$ into Zeolite-Y to yield ZnY. Subsequent incorporation of $Cd^{2+}$ ions give rise to $Cd(NO_3)_2$@ZnY, and under thermal treatment, it converts to the final perovskite structure of CdO nanoclusters encapsulated within the microporous framework of Zn-doped Zeolite-Y. This form of nanoconfinement not only stabilizes the active sites but also preserves the structural integrity of the zeolite support. Electrochemical activity as defined in (Fig. 41b) is assessed

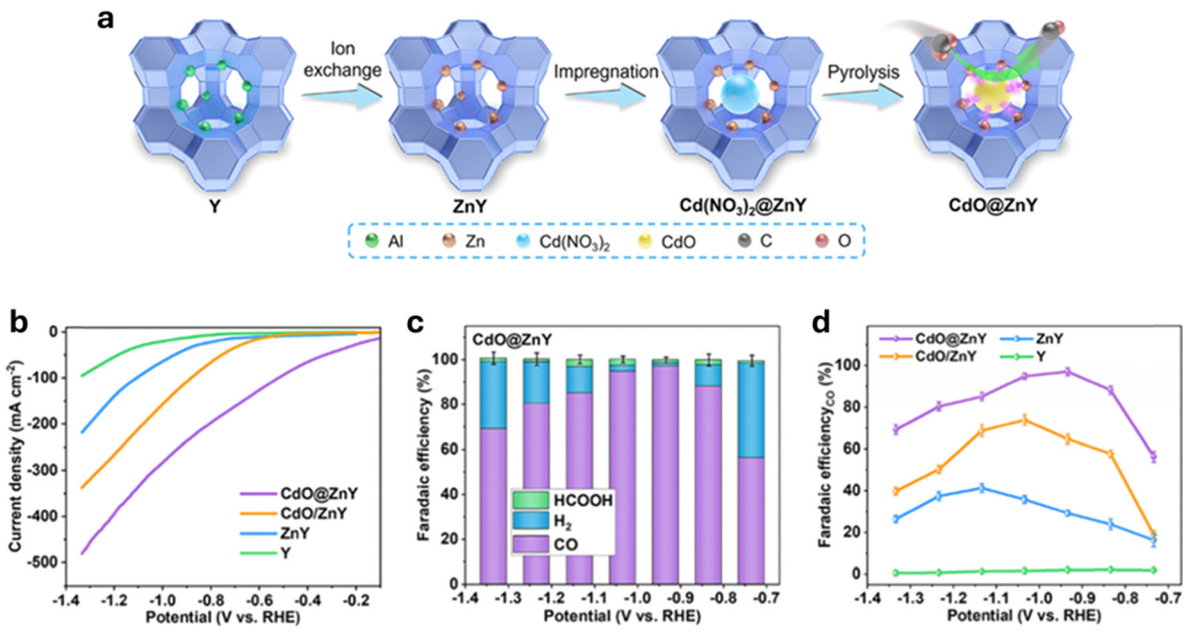


Fig. 41 Overview of structural design, mechanistic insight, and electrochemical performance of CdO@Zn@Zeolite-Y; (a) illustrates the schematic synthesis process; (b) displays total current density in Linear Sweep Voltammetry; (c) assessing faradaic efficiency for CO, $H_2$, and HCOOH at varying potentials; (d) comparison of CO selectivity between samples. Reprinted (adapted) from *J. Am. Chem. Soc.* 2024, **146**(9), 6397–6407. Copyright © 2024 American Chemical Society.

Open Access Article. Published on 12 fevral 2026. Downloaded on 01.06.2026 11:06:26.
This article is licensed under a Creative Commons Attribution-NonCommercial 3.0 Unported Licence.

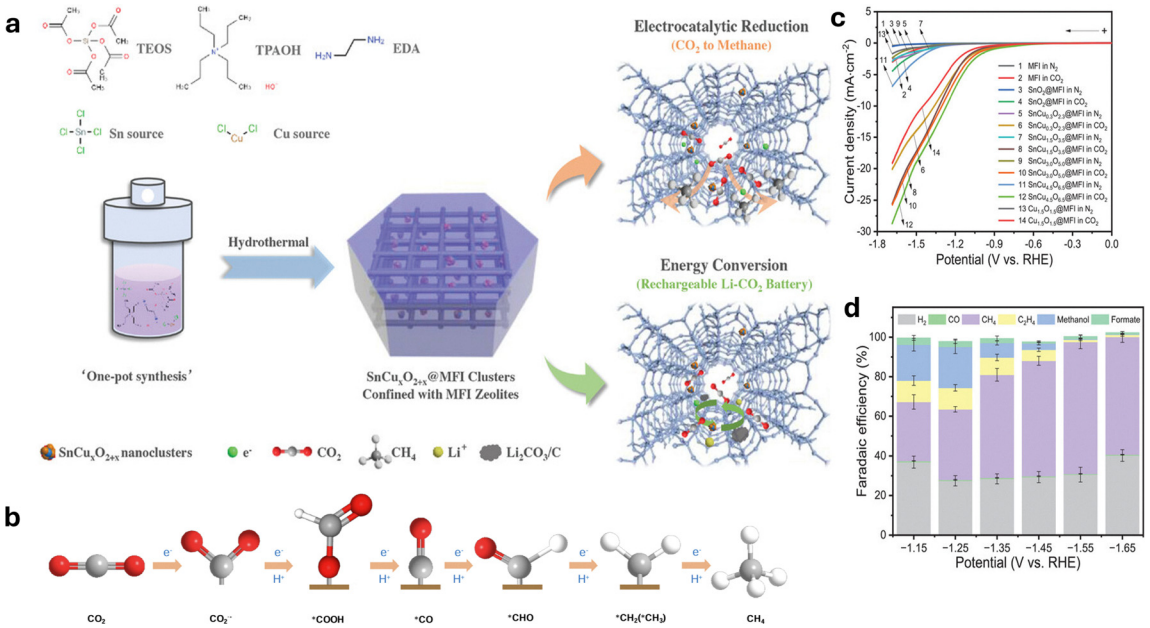


Fig. 42 (a) Schematic of one-pot synthesis of $SnCu_xO_{2+x}$ ($x$ = 0, 0.3, 1.5, 3.0, 4.5) nanoclusters confined within purely siliceous MFI zeolites. (b) Mechanistic View of $CH_4$ Formation *via* *COOH and *CHO Intermediates. (c) LSV curves in $CO_2$-saturated 0.5 M KOH. (d) Faradaic efficiencies for $CH_4/C_2H$. Reprinted (adapted) from *Adv. Energy Mater.*, **13**, 2204143. Copyright © 2023 Wiley-VCH GmbH.

through Linear Sweep Voltammetry (LSV) profiles, and as expected, CdO@ZnY doesn't disappoint. This hybrid catalyst achieves the highest total current density among all tested catalysts, suggesting unparalleled activity in $CO_2$RR. In (Fig. 41c), product distribution analysis confirmed that CO was the dominant product, with a faradaic efficiency exceeding 90% at −0.8 V *vs.* RHE, while $H_2$ and HCOOH contributions were almost negligible. In (Fig. 41d), it further compared the CO selectivity of all samples, which, alongside galvanostatic experiments, resulted in reinforcing the performance of CdO@ZnY in all tested voltages. Overall, (Fig. 41) serves as a strong multidisciplinary argument on how catalyst design, specifically based on zeolite nanoconfinement and bimetallic synergies integrated, can enhance $CO_2$ conversion technologies.

Following the work of Zhang *et al.*, Zhu *et al.*[234] proposed a confined $SnCu_xO_{2+x}$@MFI catalyst that goes beyond $CO_2$ capture to activation and electrochemical conversion into $C_1$ and $C_2$ products, including methane and ethylene. This shift highlights the increasing multifunctionality of zeolite support, from enabling *CO evolution to incorporating multi-step, multi-carbon sculpting processes. They designed a zeolite-constrained bimetallic oxide system, $SnCu_xO_{2+x}$@MFI, to promote high-efficiency $CO_2$ electroreduction to methane production. As depicted in (Fig. 42a), the synthesis strategy involved the nanoconfinement of Sn–Cu oxide nanoclusters within the micropores and mesoporous framework of MFI zeolite. This spatial confinement stabilized the active metal–oxide interface, prevented nanoparticle aggregation, and significantly enhanced ion/electron transport due to the resulting mesoporosity (~3.2 nm). (Fig. 42b) illustrates the comprehensive mechanistic and electrochemical activity of the $SnCu_xO_{2+x}$@MFI catalyst in the electrochemical reduction of $CO_2$. A detailed top diagram describes the multi-step conversion of $CO_2$ into $CH_4$. Initiation commences with the $CO_2$ adsorption and activation step, which is *COOH-intermediate forming, an essential species confirmed *via* the *in situ* SEIRAS analysis. Subsequent decoupling steps yield *CO, *CHO, and finally, *$CH_x$ intermediates, which lead to methane. Electrolysis of $CO_2$ is demonstrated in (Fig. 41c), illustrating the electrochemical performance and LSV curves, where $SnCu_{1.5}O_{3.5}$@MFI was found to have the greatest $CO_2$ current density within the $CO_2$ saturated conditions, indicative of improved performance compared with reference catalysts. As shown in (Fig. 42d), faradaic efficiency attributed to $C_2H_4$ as a secondary function of *$CH_4$ and C1 products reveals that a high-grade level is attained below −1.2 V, further supporting the previously mentioned hypotheses, while the production of $H_2$ and HCOOH remains at the decuple level.

## 4. Future outlook of zeolite

Zeolites remain strong contenders for $CO_2$ capture due to their high selectivity, thermal stability, and well-defined micropores. To improve real-world performance, ongoing research aims to engineer hydrophobic or hierarchical pore structures, introducing mesopores or cation-exchanged frameworks, to enhance moisture resistance and mass transfer. Future efforts will likely focus on creating zeolite–metal hybrid systems or membrane-reactor designs that can conduct $CO_2$ capture and conversion in a single unit, leveraging the high $CO_2/N_2$ selectivity and thermal resilience of zeolite membranes.

To realize this vision, key innovations include:

- Water-resistant coatings and pore tuning to maintain capture efficiency in humid streams.
- Mesostructuring to accelerate the diffusion of reactants and products.
- Hybrid material design, embedding zeolites in electrodes with catalytically active metals or conductive supports.


© 2026 The Author(s). Published by the Royal Society of Chemistry

Open Access Article. Published on 12 fevral 2026. Downloaded on 01.06.2026 11:06:26.
This article is licensed under a Creative Commons Attribution-NonCommercial 3.0 Unported Licence.

• Membrane reactor integration, enabling one-step $CO_2$ separation and conversion in a compact, energy-efficient system.

## Metal–organic frameworks (MOFs)

Metal–organic frameworks (MOFs) constitute a relatively recent category of crystalline porous materials made up of multimetallic clusters, referred to as secondary building units (SBUs), which are linked by organic connectors known as linkers (Fig. 43).

Through the careful design and modification of these SBUs, linkers, and pore environments, MOFs provide an extraordinary level of structural and chemical adaptability to tackle global energy and environmental challenges.[235] Because of their varied, customizable structural properties, which include but not limited to highly porous surface area, powerful organic and inorganic catalytic sites and tunable postsynthetic structure, MOFs are intriguing materials.[236–238] These relatively new materials indicate themselves for general use in catalysis (photo-, electrocatalysis), energy storage, gas storage, hazardous adsorption, and so forth.[236,239–242] MOFs have proven to be particularly effective as adsorbents and catalysts because of several significant benefits: (i) predictable and functionalizable structures. The design flexibility of MOFs allows for precise control of their architecture, facilitating the integration of accessible adsorption and catalytically active sites. (ii) Hybrid compatibility – MOFs can be combined with other materials to create composites or act as precursors/templates for MOF-derived structures that exhibit improved physical and chemical attributes. (iii) Superior catalytic performance. MOFs serve as a link between homogeneous and heterogeneous catalysis, delivering high catalytic efficiency while ensuring stability, easy separation, and reusability. (iv) Tailorable structure–property relationships. The well-defined, customizable nature of MOFs yields important insights into how alterations in structure impact catalytic performance, aiding in the rational design of catalysts. These distinctive features make MOFs extremely promising candidates for $CO_2$ capture and utilization, fueling ongoing research aimed at optimizing them for sustainable energy and environmental uses as illustrated in (Fig. 44).

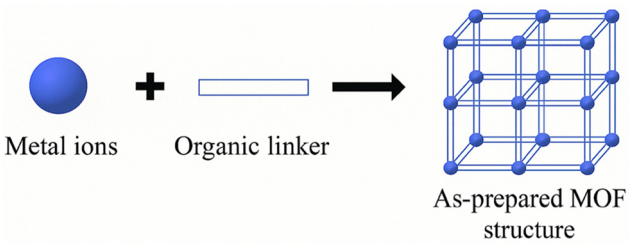


Fig. 43 Metal ions act as nodes bonding with organic linker to form MOF structure.

### 1. MOFs for $CO_2$ capture

MOFs are considered highly promising materials for $CO_2$ capture due to their exceptional porosity, tunable structures, and high surface areas. MOFs are crystalline materials that consist of metal ions or clusters linked by organic ligands with high design fixability that enables high degree of optimization of their pore size, functionality, and chemical environment to boost $CO_2$ adsorption.[235,243,244] MOFs are one of the most studied class of materials for gas storage and separation applications, with special focus on $CO_2$ capture from flue gases and direct air capture.[235,245]

MOFs with their physiochemical adsorption strategy have shown high $CO_2$ absorption capacities under both low- and high-pressure conditions, which is one of their primary advantages over conventional adsorbents like zeolites and activated carbon that depend solely on physical adsorption. For example, the well-defined pore structures and the presence of open metal sites in MOF-808 and its derivatives have demonstrated a better

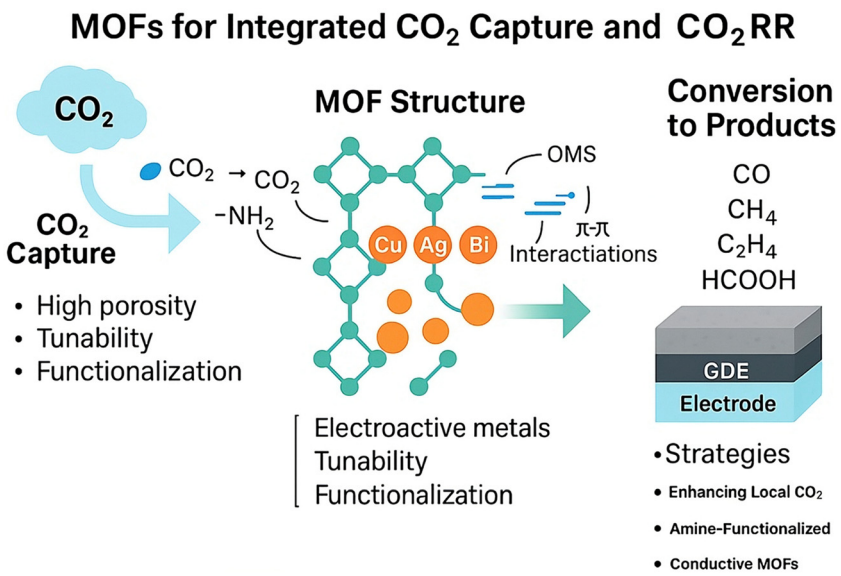


Fig. 44 Graphical abstract of MOFs for integrated $CO_2$ capture and electrocatalytic conversion.

Open Access Article. Published on 12 fevral 2026. Downloaded on 01.06.2026 11:06:26.
This article is licensed under a Creative Commons Attribution-NonCommercial 3.0 Unported Licence.

ability to absorb $CO_2$.[246] Another group investigated the $CO_2$ absorption of HKUST-1 (MOF with OMSs) at 42 par and room temperature,[247] recording roughly 10 mmol $g^{-1}$. The $CO_2$ adsorption isotherm of HKUST-1 at ambient temperature resulted in a typical Type I isotherm, reflecting that most of the gas is adsorbed at low pressures, indicating the MOF's high affinity for $CO_2$ at low partial pressures. Given that the material will have a substantial $CO_2$ capture working capacity, these conditions are intriguing for practical $CO_2$ adsorption from gas streams. Because of its exceptional $CO_2$ uptake capacities at low pressures, the M-MOF-74 (M = $Mg^{2+}$, $Ni^{2+}$, $Co^{2+}$, $Zn^{2+}$) isoreticular series, which consists of a sequence of one-dimensional hexagonal channels with OMSs at the SBUs, has emerged as one of the most extensively researched sets of MOFs for $CO_2$ capture. The accessibility of coordinatively unsaturated metal sites in the pores, the integration of heteroatoms within the pores and their covalently linked functionality to the backbone, the specific interactions of MOF building units, the hydrophobicity of the pores, and a combination of these structural features are the main strata involved in the $CO_2$ capture by MOF, as shown in (Fig. 45) represent the main strategies involved in the $CO_2$ capture by MOF including presence of accessible coordinatively unsaturated metal sites in the pores; integration of heteroatoms within, as well as covalently linked functionality to, the backbone; specific interactions of MOF building units; hydrophobicity of the pores; and a hybrid of these structural features. While MOFs are well-recognized for their $CO_2$ uptake capacities, their modular structure also makes them highly tunable for catalytic activity.

## 2. MOFs for $CO_2$RR

One interesting path to energy conversion and/or high-value chemical manufacture is the electroreduction of $CO_2$.[248,249] Electrochemical $CO_2$ reduction ($CO_2$RR) offers a sustainable approach to converting $CO_2$ into valuable chemicals and fuels, leveraging renewable electricity to operate the system under mild conditions. An appealing platform to lower the negative impacts of carbon dioxide, as well as a supply of fine chemicals, is this electrochemical approach for converting $CO_2$ into fuels using plenty of renewable energy resources.[249–251] However, the slow reaction kinetics, which consist of numerous steps of electron and proton transfers, along with competing hydrogen evolution reaction (HER), produce low productivity and efficiency. These are the main challenges to the practical application of an electrocatalyst to lower $CO_2$ emissions.[252,253]

MOFs were originally applied as electrocatalysts for $CO_2$RR in 2012;[254,255] the copper rubeanate MOF (CR-MOF) had shown enhanced $CO_2$RR performance. Since the $CO_2$RR occurs at a complicated three-phase interface between liquid electrolyte gaseous $CO_2$ solid catalyst. The primary crucial steps of the electrocatalytic processes are $CO_2$ activation, surface reaction, and product desorption processes comprising (1) electron transfer, (2) mass diffusion, and (3) electrochemical reaction on the surface *via* three-phase interface. These three elements define the whole basis of the resulting catalytic activity; they are summed under the name ''proficiency of active sites''. MOFs offer a wide range of possibilities in creating varied catalytic materials with many benefits, especially after electrochemical/thermal breakdown/pyrolysis, including (i) high mass transfer and availability of active sites, (ii) controls the electronic

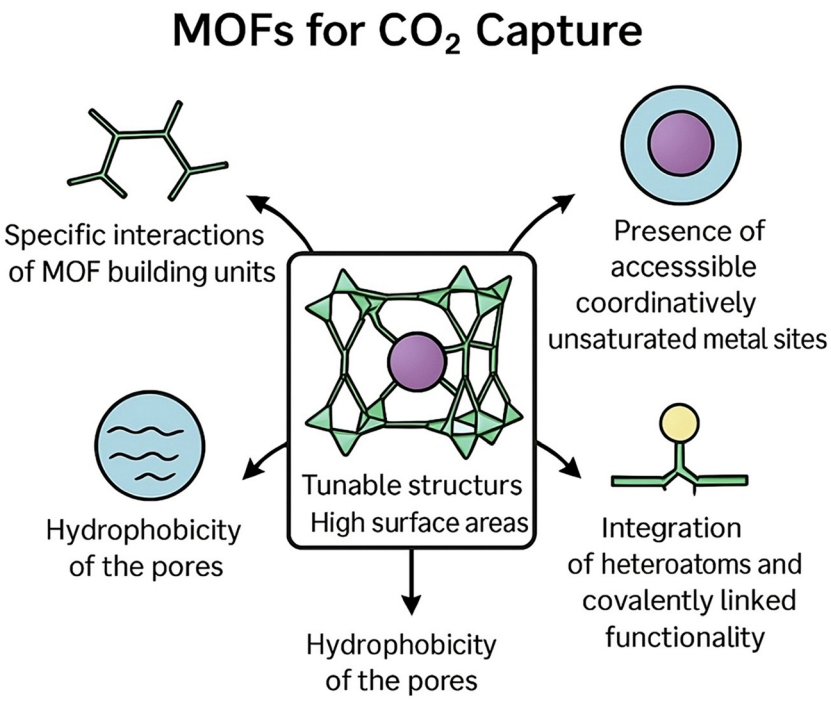


Fig. 45 Main strategies involved in the $CO_2$ capture by MOF.


© 2026 The Author(s). Published by the Royal Society of Chemistry

Open Access Article. Published on 12 fevral 2026. Downloaded on 01.06.2026 11:06:26.
This article is licensed under a Creative Commons Attribution-NonCommercial 3.0 Unported Licence.

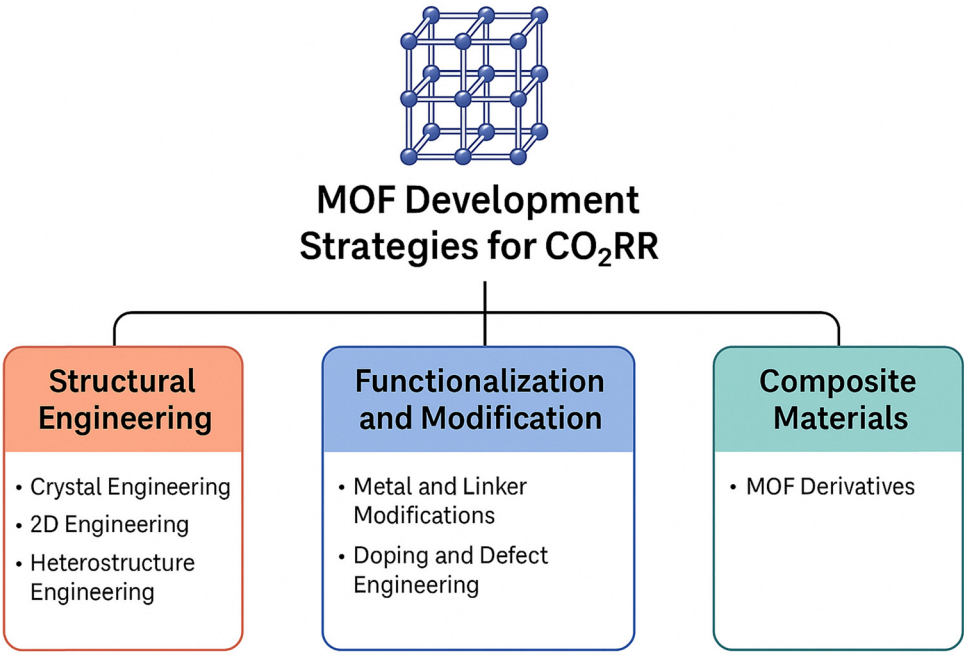


Fig. 46 A summary of MOF's development strategies for $CO_2$RR.

structure by simple heteroatom doping, and (iii) inherits the features of the pristine-MOFs. Consequently, MOF-based porous materials with the above-described properties are quite interesting candidates for $CO_2$ electrocatalysis. Due to their highly adjustable architectures, vast surface areas, and variety of chemical functions, MOFs have become very adaptable platforms for the electrochemical reduction of carbon dioxide ($CO_2$RR). Nevertheless, inherent difficulties including low electrical conductivity and restricted active site accessibility have prompted the creation of a number of engineering techniques to improve their catalytic effectiveness. The efficiency of $CO_2$ conversion has been increased by structural engineering techniques, summarized in (Fig. 46), including crystal engineering to maximize electron transport, two-dimensional (2D) engineering to enhance surface exposure, and heterostructure formation to integrate MOFs with conductive or catalytically active materials.[256] The modification of MOF's metal centers and organic linkers substitution significantly enhances the $CO_2$RR selectivity and stability.[257,258] Defect engineering and heteroatom doping can also improve overall reaction kinetics by introducing additional catalytically active sites and adjusting the electronic characteristics.[259] Their use in $CO_2$RR applications is further supported by the improved durability and charge transfer provided by MOF-based composites and derivatives, such as MOF-derived porous carbons or hybrids with conductive supports.[260] There are comprehensive reviews discussing the utilization of MOFs and their derivatives in $CO_2$RR, which is not the focus of this review.[261–263]

## 3. MOF for integrated $CO_2$ capture and conversion

Most of the $CO_2$ electroreduction systems operate using concentrated $CO_2$, which requires numerous energy to separate from $N_2$ ($CO_2$ purification cost per ton is \$70–100).[264] Utilizing MOFs in integrating $CO_2$ capture and electrochemical conversion can eliminate the need for having capture and conversion in separated unites, which offers a highly efficient and scalable approach to carbon utilization.[265] The precise engineering of MOF's porous structure and the organic linker with specific functional groups facilitates $CO_2$ adsorption. MOFs can possess Lewis acidic metal sites, basic nitrogen-rich functionalities, and π-electron-rich surfaces, which enhance $CO_2$ affinity, allowing $CO_2$ capture from mixed gases even under low partial pressures.[266–270] The fixability of MOFs construction allows for the incorporation of electroactive metal centers (Cu, Fe, Co, or Ni) for $CO_2$RR.[271] Once $CO_2$ is captured, multi-electron reduction take place and valuable carbon product can be produced over the MOF's electrocatalytically active sites. It is worth noting that dispersing these electroactive metal centers within MOF matrix offers higher utilization efficiency and can insure agglomeration prevention.[243] Although MOFs are electrochemically inactive and considered insulating materials, several strategies can be employed to make them conductive. For instance, using conductive linkers, redox-active centers incorporation, or synthesizing them with conductive materials (*e.g.*, carbon nanotubes, graphene, or metal nanoparticles) considerably boost electron transport.[271] Pyrolyzing MOFs is another approach that can result in conductive metal–nitrogen–carbon structure and maintaining the original framework properties such as the high surface area and the hierarchical porosity. Furthermore, MOF's high porosity can overcome $CO_2$ and electrolyte diffusion limitations and enhance the kinetics of the reaction. The morphology control of MOFs in the form of nanosheets or core–shell structures enables charge transfer and electrolyte accessibility optimisation. Another important key

Open Access Article. Published on 12 fevral 2026. Downloaded on 01.06.2026 11:06:26.
This article is licensed under a Creative Commons Attribution-NonCommercial 3.0 Unported Licence.

determining factor for product selectivity is the ability of MOFs to stabilize reaction intermediates by modifying the electronic environments. By modifying the ligand environment or introducing co-catalysts, researchers can further steer reaction pathways to favor specific reduction products.[243] Here we will discuss how MOFs were utilized in $CO_2$ capture and conversion process.

Liu *et al.* 2023[272] engineered gas diffusion electrodes (GDEs) consisting of a series of silver cluster-based MOFs intended for the concurrent capture and reduction of $CO_2$ to carbon monoxide (CO) from simulated flue gas containing 15% $CO_2$ in nitrogen. The MOFs employed in this research possess amine groups, acknowledged for their capacity to absorb and concentrate $CO_2$ from simulated flue gases in humid environments (Fig. 47a). These frameworks demonstrate significant porosity, allowing for efficient $CO_2$ capture, while the silver clusters inside the MOFs promote the electrochemical reduction of the captured $CO_2$ to CO. The $CO_2/N_2$ adsorption selectivity of Ag-MOF, Ag-MOF-$CH_3$, and Ag-MOF-$NH_2$ were 67, 42, and 280 at 298 K, respectively (Fig. 47b). When using NH2-MOF with pure $CO_2$, the catalyst achieved a CO partial current density of 380 mA $cm^{-2}$ and dropped slightly to 355 mA $cm^{-2}$ despite an 85% decrease in $CO_2$ concentration (Fig. 47c). In contrast, limited retention of 44% and 37% was observed on Ag-MOF and Ag-MOF-$CH_3$, respectively. The findings indicated that the faradaic efficiency (FE) for CO production and the CO partial current density were markedly affected by the presence of amine groups when utilizing flue gas as the feedstock. When the $CO_2$ concentration reduced from 15% to 5%, the e$CO_2$RR performance decreased significantly, and the minimum $CO_2$ concentration that didn't influence the performance of the 1-$NH_2$ significantly was 10%. The performance metrics obtained with flue gas were analogous to those recorded under pure $CO_2$ circumstances, highlighting the essential function of amine groups in improving $CO_2$ capture efficiency. It is worth noting that the continuous operating time of 1-$NH_2$ is much longer than that of the materials reported to date (<100 hours).

Embedding MOFs into mixed matrix membranes (MMMs) is a promising approach for enhancing their stability and been intensively utilized in $CO_2$ capturing. Al-Attas *et al.*, 2023 reported a permselective MOF-GDL (PGDE):[273] an innovative method for $CO_2$ conversion from quasi-flue gas utilizing a permselective gas diffusion electrode (PGDE). This novel design combines a metal–organic framework (MOF)-based mixed matrix membrane (MMM) with a silver electrocatalyst, facilitating selective $CO_2$ penetration and its conversion into carbon monoxide (CO) with high efficiency (Fig. 47d). The MMM integrates CALF-20, a metal–organic framework recognized for its capacity for $CO_2$ physisorption in humid gas streams. This concept seeks to improve $CO_2$ selectivity while preserving mechanical stability in industrial environments. The PGDE is designed with the MMM on the gas diffusion side of a porous PTFE electrode, which selectively permits $CO_2$ to permeate while restricting the passage of other gases such as $N_2$ and $O_2$. $CO_2$ diffuses through the membrane by concentration gradient. CALF-20 exhibited more than 4.5 times higher uptake for $CO_2$ (3.97 mmol $g^{-1}$) as compared to $N_2$ and $O_2$ at 298 K and 1 bar based on the $CO_2$ physisorption isotherm and low adsorption affinity toward the $CO_2$R (CO) target product of this study. When a mixed gas of 10% $CO_2$ balanced with $N_2$ permeated through the PGDE, it showed 1.1 × $10^6$ gas permeation units (GPUs) with selectivity of 2.1 for $CO_2/N_2$. That is confirmed by the remarkable drop of $N_2$ partial pressure across

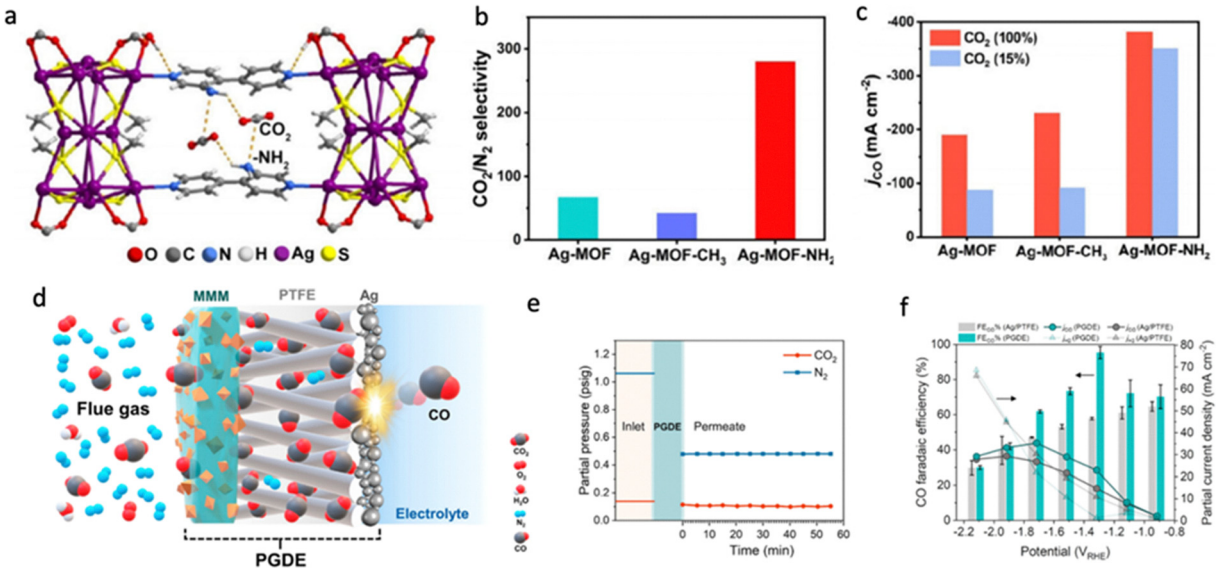


Fig. 47 (a) Schematic illustration of the interaction between the Ag-MOF-$NH_2$ catalyst and the $CO_2$ molecule. (b) $CO_2/N_2$ selectivity from $CO_2/N_2$ adsorption for different catalysts. (c) Comparison of the CO partial current density for different catalysts in pure $CO_2$ and 15% $CO_2$. Reprinted (adapted) from *Angew. Chem., Int. Ed.* 2023, **62**, e202311265. Copyrights © 2023 Wiley-VCH GmbH. (d) Schematic diagram of $CO_2$ capture and conversion through MOF permselective gas diffusion electrode (PGDE). (e) $CO_2$ permeation through PGDE (7 mg $cm^{-2}$ CALF-20 in the MMM layer), and (f) faradaic efficiency of CO and partial current density for CO and $H_2$ obtained at different applied potentials on the Ag/PTFE and PGDE (7 mg $cm^{-2}$ CALF-20 in the MMM layer). Reprinted (adapted) from *ACS Energy Lett.* 2023, **8**(1) 107–115. Copyright © 2022 American Chemical Society.


© 2026 The Author(s). Published by the Royal Society of Chemistry

Open Access Article. Published on 12 fevral 2026. Downloaded on 01.06.2026 11:06:26.
This article is licensed under a Creative Commons Attribution-NonCommercial 3.0 Unported Licence.

the PGDE from 1.06 to ~0.48 psig while $CO_2$ partial pressure only decreased ~0.03 psig (Fig. 47e). The PGDE attained an impressive CO FE of 95% in the conversion of $N_2$-diluted $CO_2$ streams compared to 58% for the Ag/PTFE at −1.32 (Fig. 47f). The ideal loading of CALF-20 in the MMM was determined to be 7 mg $cm^{-2}$, which optimized efficiency and inhibited pore obstruction. The PGDE exhibited resilience to the introduction of $O_2$, sustaining 84% of its performance and displaying minimal impact from the wetness of the gas stream. However, the MMM's propensity for water absorption may result in the degradation of $CO_2$-selective binding sites, a crucial factor for sustained operation, which was revealed while testing the stability. Also, the high overpotential applied means more energy is needed per mole of CO produced, hindering their scalability.

Zhang *et al.*, 2018[274] introduced $Cu_3(BTC)_2$ (Cu-MOF) into a carbon paper-based gas diffusion electrode (GDE) as a $CO_2$ capturer, mixed with copper nanoparticles serving as the active catalyst. The $CO_2$ adsorption capacity of Cu-MOF was quantified at 1.8 mmol $g^{-1}$, signifying moderate efficacy in augmenting local $CO_2$ concentration at the catalyst interface. The GDE was altered by 10 weight percent. Cu-MOF exhibited enhanced catalytic activity for $CO_2$ reduction, achieving faradaic efficiencies for methane production that were 2–3 times greater than those of GDEs lacking Cu-MOF. The incorporation of Cu-MOF markedly inhibited the competitive hydrogen evolution process (HER), diminishing its faradaic efficiency to 30%. The study elucidates two opposing effects of Cu-MOF in the $CO_2$ reduction reaction: an insulating effect that may impede electron transfer to Cu active sites and an augmentation of $CO_2$ concentration at the electrode–electrolyte interface, which promotes the reaction. The interaction between these factors ultimately determines the reaction rate and product selectivity. Although $CH_4$ FE was enhanced by introducing Cu-MOF compared to the blank, the maximum FE was moderate (17%), with the optimum Cu-MOF content relative to the theoretical maximum, and a significant portion of the current was directed to HER (30%), especially at higher overpotentials. Moreover, the Cu-MOF structure showed stability issues when used for 24 h due to hydrolysis or phase transformation in aqueous solution.

Selectivity is one of the main challenges in $CO_2$RR, especially towards $C_{2+}$ products, given their high benefit-to-cost ratio.[275] The electrochemical reduction of $CO_2$ ($CO_2$RR) to ethylene ($C_2H_4$) is a viable approach for sustainable chemical synthesis. Nonetheless, attaining industrially significant productivity (>200 mA $cm^{-2}$) and energy efficiency (>50%) poses challenges due to the solubility constraints of $CO_2$ in aqueous electrolytes and the occurrence of competing side reactions. Nam *et al.*, 2022[276] developed MOF-augmented gas diffusion electrodes (MOF-GDEs) to increase local $CO_2$ availability in proximity to catalytically active copper sites, therefore improving $CO_2$RR selectivity and rate. The hierarchical electrode structure comprises a hydrophobic polytetrafluoroethylene (PTFE) substrate, a metal–organic framework (MOF) interlayer, and a sputtered copper catalyst (Fig. 48a). Two metal–organic frameworks, HKUST-1 and SIFSIX-3-Cu, with differing

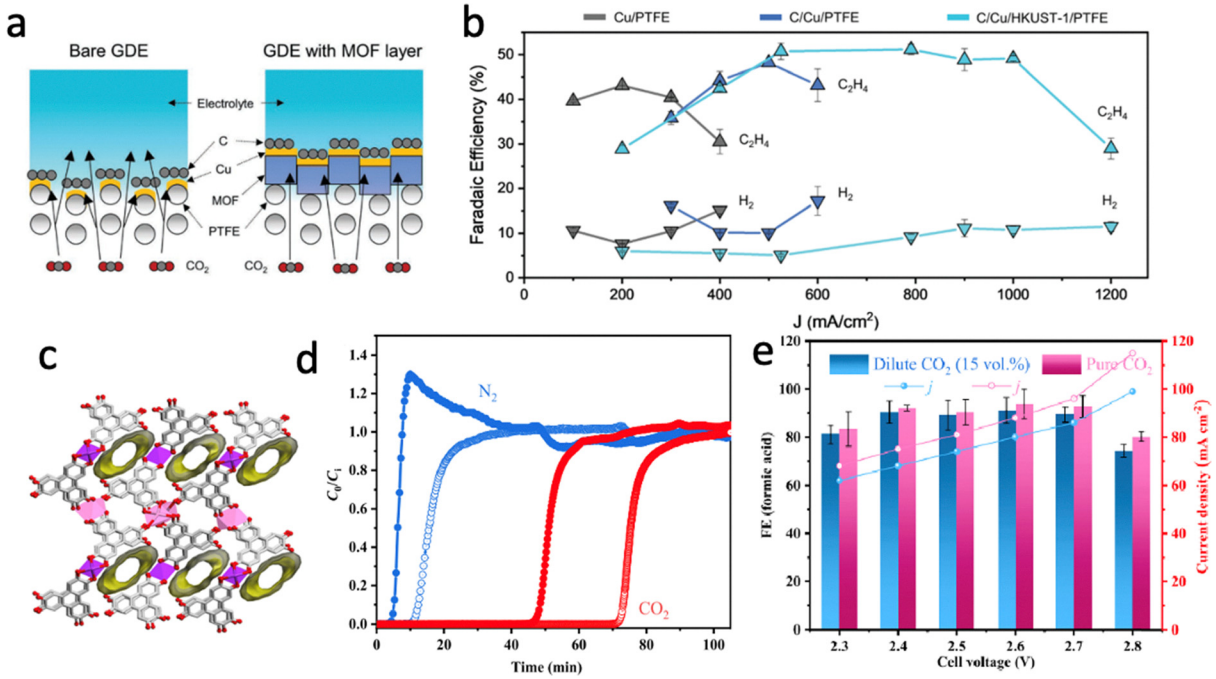


Fig. 48 (a) Cross-sectional schematic diagram of bare GDE (Cu/PTFE) and MOF-augmented GDE (Cu/MOF/PTFE) during $CO_2$RR in the flow cell. (b) Electrochemical $CO_2$RR of MOF-augmented GDE in the flow cell. Reprinted (adapted) from *Adv. Mater.* 2022, **34**, 2207088. Copyrights © 2022 Wiley-VCH GmbH. (c) 3D π−π stacking structure of Bi-HHTP with 1D pores along the *b*-axis direction. (d) Breakthrough curves for a 15 : 85 $CO_2/N_2$ (v/v) mixture with 0% (open) and 40% relative humidity (solid) at 298 K and 1 bar. Ci and C0 are the concentrations of each gas at the inlet and outlet, respectively. (e) (FEs) formic acid and current densities under different cell voltages in high-purity $CO_2$ and dilute $CO_2$ (15 vol%, $CO_2/N_2$ = 15 : 85, v/v) atmospheres, respectively. Reprinted (adapted) from *J. Am. Chem. Soc.* 2024, **146**(20), 14349–14356. Copyright © 2024 American Chemical Society.

Open Access Article. Published on 12 fevral 2026. Downloaded on 01.06.2026 11:06:26.
This article is licensed under a Creative Commons Attribution-NonCommercial 3.0 Unported Licence.

$CO_2$ adsorption capabilities, were evaluated for their efficacy in enhancing $CO_2$ concentration at the catalyst interface. The MOF-enhanced GDEs exhibited significant enhancements in ethylene production. In flow cell systems, MOF-modified electrodes attained a faradaic efficiency (FE) of 49% for ethylene at a current density of 1 A $cm^{-2}$, surpassing traditional Cu/PTFE electrodes (Fig. 48b). The elevated local $CO_2$ concentration enhanced $CO_2$ adsorption and inhibited the hydrogen evolution reaction (HER), hence augmenting $C_{2+}$ selectivity. The notion was further corroborated in zero-gap MEA electrolyzers, where MOF films situated on Cu electrodes markedly improved ethylene output. A peak ethylene partial current density (J $C_2H_4$) of 220 mA $cm^{-2}$ was attained, representing a 2.7-fold enhancement compared to unmodified GDEs. Furthermore, for the carbon monoxide reduction reaction (CORR), the MOF-enhanced GDEs exhibited a 15-fold increase in ethylene production rate compared with bare Cu/PTFE electrodes, underscoring the significant impact of $CO_2$ enrichment in high-current-density operations. The X-ray absorption spectroscopy (XAS) indicated that the MOF layers experienced structural alterations under electrochemical circumstances, resulting in the creation of organic-metal interfaces that enhanced $CO_2$ adsorption and reaction kinetics. The electrodes' stability was evidenced after 65 hours of uninterrupted operation, sustaining ethylene selectivity above 50%. The results underscore the necessity of enhancing MOF characteristics, such as porosity, $CO_2$ adsorption capacity, and hydrophobicity, to optimize electrocatalytic efficacy. The MOF-augmented GDEs maintain $>50\%$ FE for ethylene over 65 hours at industrially relevant current densities, with total $C_{2+}$ product FE above 70% for 59 hours. Although the system achieves high current densities and good selectivity, the cell voltages required (up to $-4.2$ V in MEA mode) are relatively high, implying significant energy input per mole of product.[277]

Zhao *et al.*, 2024[278] reported a groundbreaking approach for the integrated capture and $eCO_2RR$ of dilute $CO_2$ (15 vol%, mimicking flue gas) into 100% pure aqueous formic acid with 90% FE, addressing two challenges in $CO_2$ utilization; (i) the need for high-purity $CO_2$ as a feedstock and (ii) the separation of liquid products after the reaction. A conductive bismuth-based-MOF, Bi-HHTP (where HHTP = 2,3,6,7,10,11-hexahydroxytriphenylene), was utilized and served as a $CO_2$ adsorbent and as an electrocatalyst. The Bi-HHTP possesses a microstructure π-conjugated framework with one-dimensional (1D) zigzag chains of distorted tetrahedral and pentahedral $BiO_4$ nodes, interconnected through π–π stacking to form a 3D architecture (Fig. 48c), which enable a high $CO_2$ selectivity and uptake (23.6 $cm^3$ $g^{-1}$ = 1.05 mmol $g^{-1}$ at 298 K, $CO_2/N_2$ selectivity ~91), under humid conditions (40% RH) (Fig. 48d), which is critical for industrial applications. The adsorption mechanism involves electrostatic interaction, hydrogen bonding and metal coordination, resulting in strong binding between $CO_2$ and Bi-HHTP. It was found that $H_2O$ binds well to Bi-HHTP, forming hydrogen bonds, competing slightly with $CO_2$, yet adsorbed $H_2O$ provides protons supporting the $eCO_2RR$. Formic acid FE was slightly lower in dilute $CO_2$ ($CO_2/N_2$ = 15 : 85, v/v) than in a high-purity $CO_2$ atmosphere, with maximum values of 91% and 93% at 2.6 V, respectively (Fig. 48e). The formation of *OCHO intermediate* was confirmed by *Operando* ATR-FTIR spectroscopy, which is a key intermediate for formic acid formation. The DFT showed Bi-HHTP requires less energy ($\Delta G$ = 0.31 eV) to carry out the rate-determining step in the process compared to other bismuth-based catalysts like metallic Bi or $Bi_2CO_5$. The OCHO binds to Bi-HHTP just strongly enough ($\Delta E$ = −0.22 eV) to react efficiently, without poisoning the surface or releasing too early. The Technoeconomic analysis estimates a production cost ($0.74 per kg), highlighting commercial feasibility. Further examples of MOF-based materials for integrated $CO_2$ capture and conversion are summarized in (Table 15).

Generally, when designing an adsorbent layer on a GDE, it is crucial to create robust adsorbents with elevated $CO_2$ adsorption capacity and selectivity, while also considering factors such as kinetic rate, active porosity, surface area for adsorption, and resistance to moisture and contaminants.

The electrochemical stability of metal–organic frameworks (MOFs) is a critical factor determining their applicability in electrocatalytic systems. During electrochemical operation, the applied potential drives the migration of ionic species from the electrolyte toward the MOF surface, leading to the formation of an electrical double layer.[279] The accumulation of charge at this interface generates pronounced local ion concentration gradients, particularly involving protons or hydroxide ions, which can cause substantial deviations of the interfacial pH from that of the bulk electrolyte. Such localized pH fluctuations impose chemical stress on both the metal nodes and organic linkers, often resulting in partial or complete structural degradation of the framework.[280,281] This instability is especially problematic under neutral and strongly alkaline conditions, where many MOFs are inherently susceptible to hydrolysis or ligand displacement. As a result, achieving durable performance in these media remains a key challenge for MOF-based catalysts in the $CO_2$ electroreduction reaction ($CO_2RR$). Moreover, repeated potential cycling further accelerates degradation by continuously reshaping cationic and anionic distributions at the electrochemical interface. These dynamic chemical gradients can promote metal leaching and coordination bond cleavage, ultimately driving the *in situ* conversion of MOFs into metal oxides, hydroxides, or oxyhydroxides during prolonged electrocatalytic operation.[279,282]

Achieving concurrent chemical, structural, and electrochemical robustness in metal–organic frameworks (MOFs) under operating electrocatalytic conditions remains intrinsically challenging, as strategies that enhance stability (*e.g.*, stronger metal–ligand bonds, increased hydrophobicity) often compromise properties such as electronic conductivity, porosity, or active-site accessibility. Over roughly the past decade, sustained progress in linker design, node selection, and composite engineering has nevertheless enabled significant improvements in MOF durability under electrochemical $CO_2$ reduction ($CO_2RR$) conditions, particularly in aqueous and humid environments. Despite these advances, a central question persists regarding the true nature of the catalytically active phase: in many reported systems, it remains ambiguous whether the pristine


© 2026 The Author(s). Published by the Royal Society of Chemistry

Open Access Article. Published on 12 fevral 2026. Downloaded on 01.06.2026 11:06:26.
This article is licensed under a Creative Commons Attribution-NonCommercial 3.0 Unported Licence.

Table 15 MOF-based materials for integrated $CO_2$ capture and conversion

| Material | Composition and structure | $CO_2$ adsorption capacity | Faradaic efficiency (FE) | Key findings | Ref. |
|---|---|---|---|---|---|
| Cu-MOF-GDE | $Cu_3$(BTC) 2 (Cu-MOF) incorporated into carbon paper-based gas diffusion electrode with copper nanoparticles | 1.8 mmol $g^{-1}$ | $CH_4$ FE increased 2–3× with Cu-MOF (~20%); HER FE reduced to 30% | Cu-MOF enhances local $CO_2$ concentration at the catalyst interface | 274 |
| Permselective MOF-GDL (PGDE) | CALF-20 MOF-based mixed matrix membrane (MMM) combined with silver electrocatalyst | CALF-20 exhibited 4.5 times higher uptake for $CO_2$ (3.97 mmol $g^{-1}$) as compared to $N_2$ and $O_2$ at 298 K and 1 bar. The PGDE showed 1.1 × $10^6$ gas permeation units (GPUs) with a $CO_2/N_2$ selectivity of 2.1 for a mixed gas stream of ~ 10% $CO_2$ and $N_2$ balance | CO FE up to 95% | The MMM selectively allows $CO_2$ permeation while restricting other gases. The weak binding of $CO_2$ coupled with the specific pore structure minimizes $CO_2$ chemisorption | 273 |
| MOF-functionalized GDE | HKUST-1 and SIFSIX-3-Cu MOFs as interlayers on hydrophobic PTFE substrate with sputtered copper catalyst | SIFSIX-3-Cu showed higher $CO_2$ affinity (2.4 mmol $g^{-1}$ *vs.* 0.3 mmol $g^{-1}$ for HKUST-1) and better stability at lower mass loading | $C_2H_4$ FE up to 49% at 1 A $cm^{-2}$ in flow cell (2.7-fold compared to bare Cu/PTFE electrodes), 52% for $C_2H_4$ in MEA, in CORR, the modified GDE demonstrated a 15-fold increase in ethylene production | MOF layers increase local $CO_2$ concentration, enhancing ethylene production and suppressing hydrogen evolution | 276 |
| $Ag_{12}$ cluster-MOF-GDE | Silver cluster-based MOFs with amine function groups | 1-$NH_2$ MOF exhibited a $CO_2$ uptake of 0.90 mmol $cm^{-3}$ (≈ 9 mmol $g^{-1}$) | CO FE ~96.4% under simulated flue gas ($CO_2/N_2$ = 15 : 85) at 120 mAcm2 ~96.3–97.3% under pure $CO_2$ | Amine-functionalized MOFs enhance $CO_2$ capture from flue gas, with silver clusters promoting electrochemical reduction to CO. Performance under flue gas conditions is comparable to pure $CO_2$ | 272 |
| Bi-HHTP-MOF | Bismuth-based-MOF, Bi-HHTP (HHTP = 2,3,6,7,10,11-hexahydroxytriphenylene) | 1.05 mmol $g^{-1}$ at 298 K | 100% pure aqueous formic acid with 90% FE | Conductive Bi-HHTP acts both as a $CO_2$ adsorbent and an electrocatalyst | 278 |

MOF operates as the genuine electrocatalyst, or whether the framework instead serves as a sacrificial or pre-catalyst that reconstructs into metal oxides, hydroxides, oxyhydroxides, or other derived phases under applied bias. Resolving this ambiguity requires rigorous *operando* or *in situ* characterization, such as X-ray absorption spectroscopy, X-ray diffraction, vibrational spectroscopy, and electron microscopy, combined with systematic post-reaction structural and compositional analyses to verify chemical integrity, crystallinity, and metal speciation after prolonged electrolysis. Such mechanistic insight is essential for the rational design of MOF-based architectures that can sustain $CO_2$RR over technologically relevant timescales.[282,283]

During electrochemical operation, MOFs are subjected to a complex and dynamic reaction environment that includes liquid water, electrolyte cations and anions, dissolved reactants and products, interfacial electric fields, and continuous electron and ion fluxes. Among these factors, water frequently plays a primary role in triggering degradation, as it can coordinate to metal nodes and promote competitive ligand exchange or hydrolysis of coordination bonds, ultimately yielding hydrated or hydroxylated metal species in alkaline media and protonated or partially detached organic linkers in acidic media.[282,283] These processes often lead to partial or complete leaching of metal centers and ligands into the electrolyte, progressively eroding the long-range order of the framework. In parallel, specific electrolyte anions can substantially accelerate degradation pathways: strongly coordinating species such as phosphate, carbonate, or sulfate may outcompete the MOF linker for binding to high-valence metal centers, thereby destabilizing the metal–ligand coordination network. Zirconium-based carboxylate frameworks, which are otherwise chemically robust, have been reported to undergo rapid degradationin phosphate-containing electrolytes, where strong Zr–phosphate interactions drive fast deterioration of the $Zr_6$-oxo clusters and loss of crystallinity on experimentally relevant timescales.[284,285]

Framework instability under electrochemical conditions is not confined to carboxylate-based MOFs. Zeolitic imidazolate frameworks (ZIFs), despite their topological analogy to zeolites and relatively strong metal–imidazolate bonds, can also undergo structural transformation or collapse under $CO_2$RR- or ORR-relevant potentials, particularly in electrolytes containing additional metal cations. Ion-exchange processes at the node, followed by nucleation and growth of metal (oxy)hydroxide phases, have been widely observed, frequently leading to the formation of mixed-metal hydroxide or oxide nanostructures at the expense of the original framework.[286] Beyond purely chemical degradation, reaction-derived products impose additional mechanical and chemical stress on MOFs: gas-evolving reactions often generate nanoscale bubbles at or within the porous structure, imposing localized pressure and shear that can induce cracking, delamination, or fragmentation of MOF crystallites. Furthermore, soluble products or intermediates from $CO_2$RR (*e.g.*, formate, carbonate, or multicarbon species) may coordinate to metal nodes or interact strongly with linkers, promoting further reorganization or dissolution of the framework over extended operation.[287,288]

Open Access Article. Published on 12 fevral 2026. Downloaded on 01.06.2026 11:06:26.
This article is licensed under a Creative Commons Attribution-NonCommercial 3.0 Unported Licence.

The intrinsic susceptibility of many MOFs to humidity and aqueous environments commonly manifests as rapid performance degradation, especially in neutral and alkaline media, where moisture-mediated attack on metal centers and linkers leads to decomposition or phase transformation. In this context, metal–ligand bond strength has emerged as a key design parameter governing MOF stability under electrochemical conditions. Stronger coordination interactions generally correlate with enhanced resistance to hydrolysis, ligand displacement, and nucleophilic attack. Guided by this principle, stability is often improved by employing high-valent, hard metal centers and appropriately matched ligands. Frameworks constructed from hard, high-charge-density metal ions—such as $Zr^{4+}$, $Cr^{3+}$, $Al^{3+}$, and $Fe^{3+}$ paired with oxygen-donor carboxylate ligands typically display superior chemical robustness, in line with Hard–Soft Acid–Base (HSAB) considerations. These strong metal–oxygen bonds not only increase resistance to hydrolysis and ligand loss in aqueous and humid environments but can also impart persistence under moderately acidic conditions, particularly when the carboxylate linkers possess low p$K_a$ values and form highly stable coordination clusters (*e.g.*, $Zr_6O_4(OH)_4$ nodes in UiO-type frameworks).[289–292] Collectively, these design concepts underpin ongoing efforts to develop MOF-based electrocatalysts that combine structural integrity, chemical resilience, and sustained activity for $CO_2$ electroreduction.

### 4. Future outlook of MOF

Despite these advances in utilizing MOFs in integrated $CO_2$ capture and conversion, several encounters still need to overcome to address their practical application. Some of these challenges are long-term stability under electrochemical conditions, the large-scale production of MOF, and developing conductive MOFs at a reduced cost. Recent advances in synthesis techniques, including microwave-assisted and mechanochemical methods, are addressing these issues by enabling faster, more cost-effective production of robust MOFs.[293] Another determining factor is the faradaic efficiency and current densities that requires further improvement to meet industrial-scale necessities. Nonetheless, continued advancements in MOF design, hybridization strategies, and *in situ* characterization techniques hold great promise for optimizing MOFs as next generation electrocatalysts for sustainable $CO_2$ capture and conversion.

## Metal oxides

A series of amine-functionalized $SnO_x$ nanoparticles were developed by[294] demonstrating an interesting strategy for $CO_2$ capturing from simulated flue gas (15% $CO_2$, 8% $O_2$, 77% $N_2$) and selective conversion to formate spontaneously; a general concept has been illustrated in (Fig. 49).

DEA–$SnO_x$/C was synthesized by a one-pot hydrothermal reaction of carbon black, $SnCl_2$, and DEA in ethanol, as shown in (Fig. 50a). The dual-function catalyst developed *via* grafting alkanolamines such as diethanolamine (DEA) onto $SnO_x$ surfaces (DEA–$SnO_x$/C) that augments local $CO_2$ concentration *via* Lewis base interactions while also tailoring reaction selectivity toward formate. DEA–$SnO_x$/C exhibited significantly higher $CO_2$ adsorption capacity than the non-functionalized $SnO_x$ ($SnO_x$/C) (Fig. 50b), indicating the strong interaction between DEA and $CO_2$. This combined with the enhanced hydrophobicity and suppression of side reactions resulted in a standout performance of 84.2%

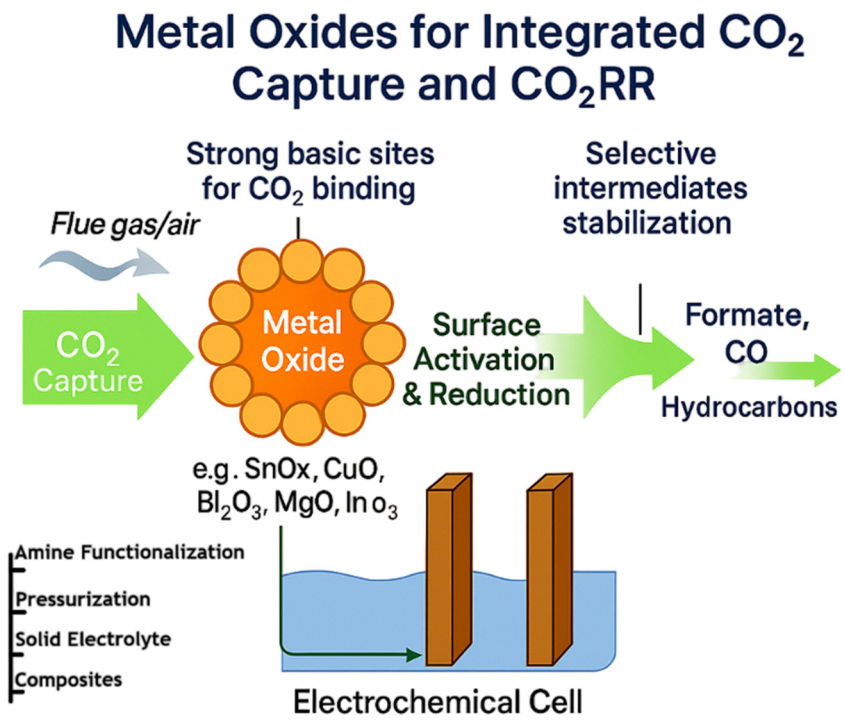


Fig. 49 Graphical abstract of metal oxides for integrated $CO_2$ capture and electrocatalytic conversion.


© 2026 The Author(s). Published by the Royal Society of Chemistry

Open Access Article. Published on 12 fevral 2026. Downloaded on 01.06.2026 11:06:26.
This article is licensed under a Creative Commons Attribution-NonCommercial 3.0 Unported Licence.

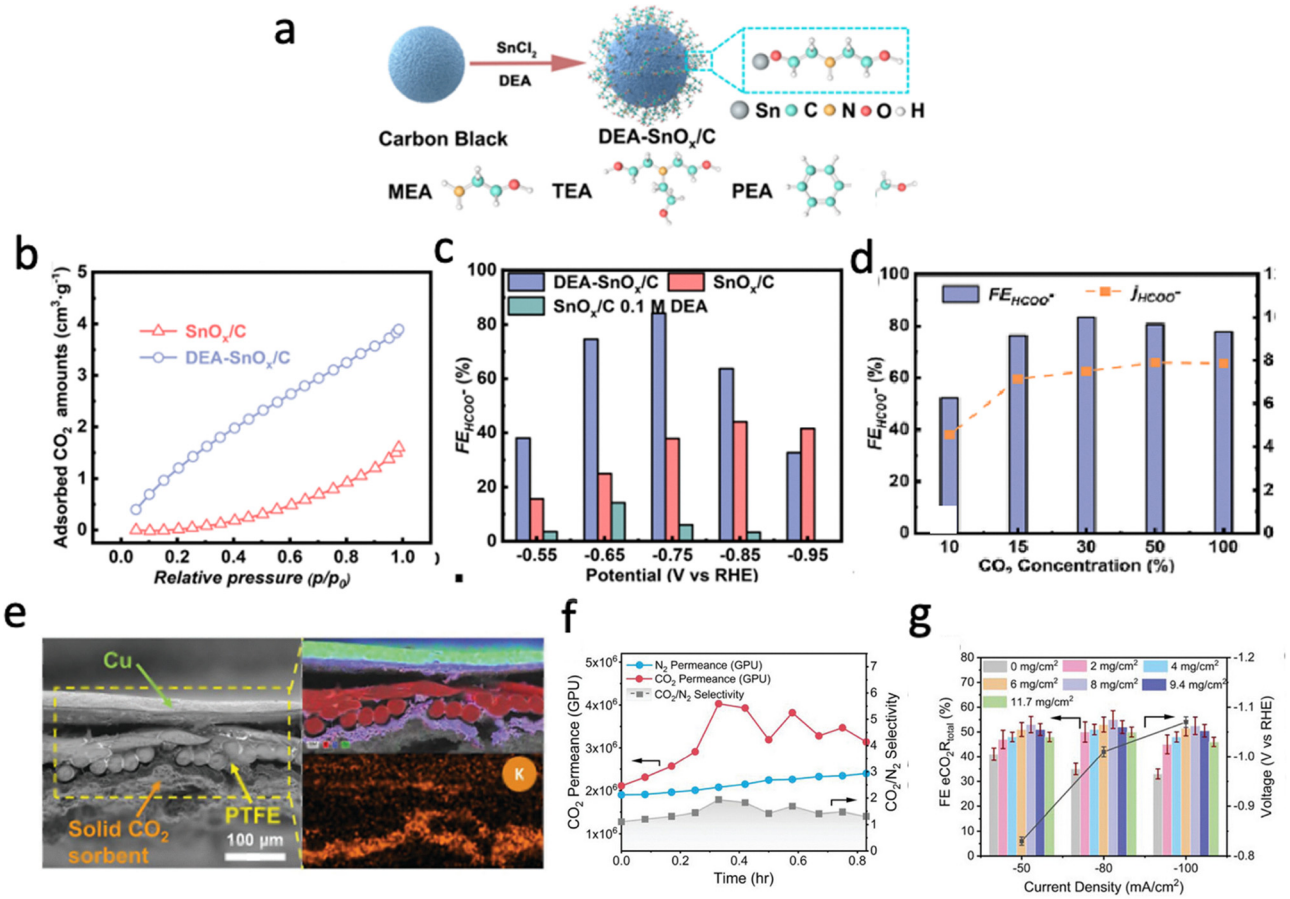


Fig. 50 (a) Fabrication of DEA–$SnO_x$/C and structures of alkanolamines. (b) $CO_2$ adsorption isotherms of $SnO_x$/C and DEA–$SnO_x$/C (b). $FEHCOO^-$. (c) $jHCOO^-$ of the above samples in 0.5 M $KHCO_3$ electrolyte under SFG (glassy carbon, 0.071 $cm^2$). (d) $FEHCOO^-$ and jHCOO at −0.75 V *vs.* RHE of DEA–$SnO_x$/C using different concentrations of $CO_2$ (0.5 M $KHCO_3$, glassy carbon, −0.071 $cm^2$). Reprinted (adapted) from *ACS Energy Lett.* 2021, **6**(9), 3352–3358. Copyright © 2021, American Chemical Society. (e) SEM image showing the cross section of the integrated BGDE with both HPC and polycrystalline copper while energy dispersive X-ray spectroscopy (EDX) mapping reveals the presence of C, F, Cu, and K (from synthesis). The copper layer may appear to be thicker than 300 nm owing to handmade sectioning by the razor blade. (f) Mixed gas $CO_2$ permeance and $CO_2/N_2$ selectivity for *in situ* configuration (BGDE with Cu/HPC). (g) Operating conditions: $CO_2$ flow = 10 $cm^3$ (STP) $min^{-1}$, $N_2$ flow = 90 $cm^3$ (STP) $min^{-1}$, feed pressure = 1.0 psig (1.07 atm), HPC loading = 8 mg $cm^{-2}$. Optimization of sorbent loading for maximum $eCO_2R$ product formation at $P_{CO_2}$ = 0.1 atm. (c) $eCO_2R$ product distribution at $P_{CO_2}$ = 0.1 atm and sorbent loading of 8 mg $cm^{-2}$. Reprinted (adapted) from *Adv. Mater.* 2023, **35**(24), 2300389. Copyrights © 2023 The Authors. Published by Wiley-VCH GmbH under the terms of CC-BY license.

faradaic efficiency for formate at −0.75 V *vs.* RHE (Fig. 50c). The DEA–$SnO_x$/C can operate at low $CO_2$ concentration (10%) and $FE_{hcoo^-}$ reaching over 80% ($CO_2$ = 30%) whereas the jHCOO peaked when the concentration was 50% reaching 7.9 mA $cm^{-2}$ (Fig. 50d). Despite this notable selectivity performance, the formate jHCOO of 6.7 mA $cm^{-2}$ is below industrially relevant benchmarks (≥100 mA $cm^{-2}$). Furthermore, the degradation of amine groups limited the catalyst's stability over a prolonged period, and the catalyst was evaluated in a static setup (single-compartment design) with a small electrode area (0.071 $cm^2$), not in continuous flow or gas diffusion configurations, limiting scalability.

A recent study by Nabil *et al.*[295] reported an integrated approach for the simultaneous capture and electrochemical conversion of $CO_2$ from dilute gas streams using a bifunctional gas diffusion electrode (BGDE). A high-density polyethylene-derived porous carbon (HPC) was employed as a physisorbent combined with polycrystalline copper as the electrocatalyst (Fig. 50e). The BGDE structure utilized a concentration gradient-driven desorption mechanism, which allows efficient $CO_2$ capture and release at low $CO_2$ concentration (~10 vol%), eliminating the need for energy-intensive regeneration steps commonly applied with traditional capture technologies. HPC permeance of $CO_2$ was as high as $4.0 \times 10^6$ GPU and a $CO_2/N_2$ selectivity of ≈1.3. When testing the $CO_2$RR without sorbent (HPC) the total selectivity for $eCO_2R$ products with partial pressure $P_{CO_2}$ = 0.1 atm (10% $CO_2$90% $N_2$) ranged from 33% to 41% depending on the voltage and current density, while with the sorbent (HPC = 8 mg $cm^{-2}$) it increased by about 20% (Fig. 50f). However, lower selectivity resulted with higher HPC loading due to the blocking PTFE pores during airbrushing and thus deterring $CO_2$ diffusion (Fig. 50g). Notably, the BGDE maintained its performance under humid environments, due to the hydrophobic and $CO_2$-selective characteristic of carbonaceous HPC. Based on molecular dynamics

Open Access Article. Published on 12 fevral 2026. Downloaded on 01.06.2026 11:06:26.
This article is licensed under a Creative Commons Attribution-NonCommercial 3.0 Unported Licence.

simulations and gas permeance studies, the high $CO_2/N_2$ selectivity ($\approx$1.3) is emphasized, caused by the molecular sieving properties incorporated within the micropores of HPC, significantly boosting the $CO_2$ transport to the catalyst interface. The techno-economic study showed that this *in situ* system could dramatically diminish the minimum selling price of ethylene up to ~79% when compared to the decoupled capture and conversion method.

Yan *et al.* (2024)[296] developed a redox-mediated electrochemical platform for integrated $CO_2$ capture and utilization (eCCU) utilizing anthraquinone (AQ)-grafted polymer electrodes. The polymeric film, constructed from a polyacrylamide backbone, chemically binds $CO_2$ *via* reversible carbamate production when the AQ groups are in their oxidized (quinone) state. During electrochemical reduction, the AQ units emit $CO_2$ *in situ*, which subsequently diffuses to an adjacent Ag catalyst layer for electrochemical conversion. This electrochemical regeneration circumvents thermal desorption, functions at ambient settings, and facilitates fine redox-tunable control over capture and release. *In situ* ATR-FTIR and DFT analyses (Fig. 51a–d) validate the generation of $CO_2$-AQ adducts and their reversible conversion during potential cycling. The system exhibits stable multi-cycle functionality, preserving capture–release efficiency and $CO_2$ consumption without necessitating gas-phase $CO_2$ input or supplementary purification. The system achieves a faradaic efficiency of up to 82% for CO generation on the Ag catalyst under optimal electrochemical conditions. The platform provides a solvent-free, modular design that integrates capture and conversion inside a singular reactor architecture. The capture capacity is constrained by the loading and accessibility of AQ functional groups, and increasing the film thickness or redox density presents trade-offs with ion transport and conductivity. The reaction is presently limited to $CO_2$-to-CO conversion, constraining subsequent chemical flexibility. Future work may concentrate on broadening the platform to encompass multi-carbon product catalysts, augmenting the stability of AQ functions, and designing more conductive or porous film morphologies to enhance throughput and scalability. This redox-active electrode method represents a notable step towards low-energy, continuous electrochemical carbon capture and utilization systems, providing a framework for integrating $CO_2$ binding and conversion into a single electrochemical unit.

Xu *et al.* (2020)[297] attempted to use pressurization (10–15 bar) to enhance $CO_2$ mass transfer as a strategy to produce $C_{2+}$ from simulated flue gas. This strategy enabled efficient $C_{2+}$ production (91% FE, at 15 bar without $O_2$). The study showed that while pressurization enhances $CO_2$ availability and suppresses the hydrogen evolution reaction (HER), it also increases the oxygen reduction reaction (ORR), distracting most of the current towards ORR because of the lower thermodynamic and kinetic requirements for ORR compared to $CO_2$RR (Fig. 52a). To counteract this, the authors first tried mixed Nafion-bound carbon nanoparticles layer to stabilize $CO_2$RR which failed in $O_2$-containing $CO_2$ streams. They introduced a hydrophilic ionomer-$TiO_2$ catalyst layer on a Cu-based gas diffusion electrode that significantly slowed $O_2$ transport and maintained $CO_2$ accessibility (Fig. 52b). This design leverages the lower volatility of $CO_2$ compared to $O_2$, allowing selective gas transport through hydrated nanopores. The ionomer-$TiO_2$ structure stabilizes the Cu catalyst and reduces $O_2$

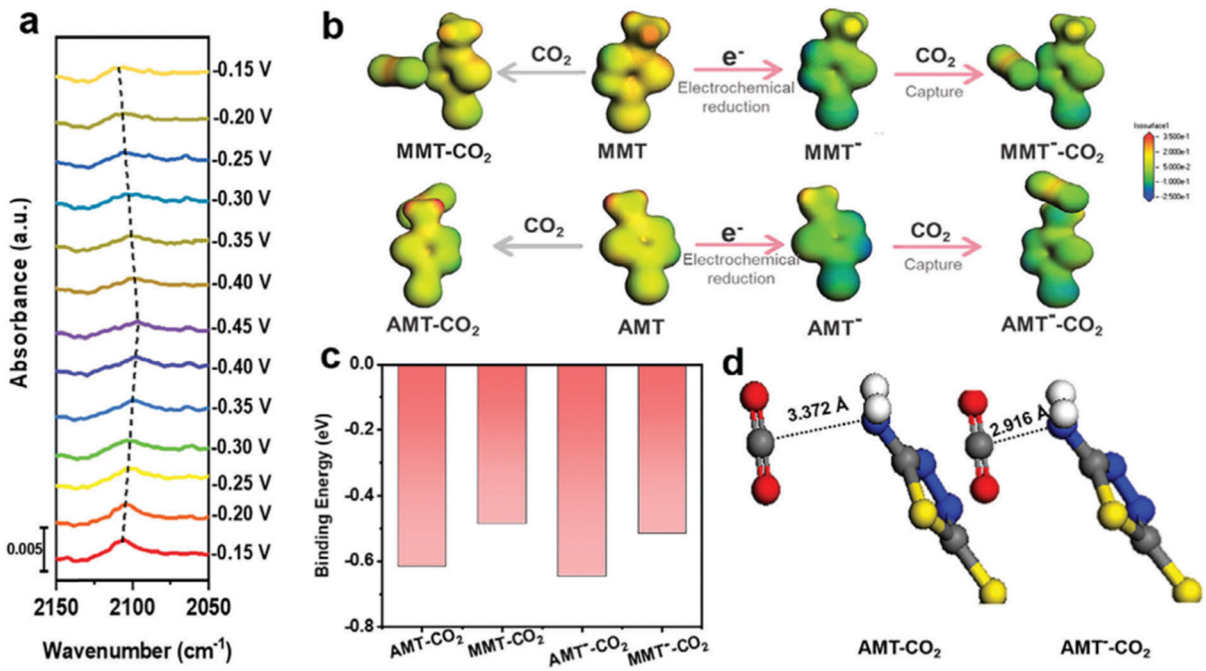


Fig. 51 (a) *In situ* IR spectra of AMT–Au at the different potential in 0.5 M $KHCO_3/H_2O$ electrolyte under SFG. (b) Electrostatic distribution mapping on the electron density surfaces. Blue indicates high electronegativity areas, and red indicates high positive charge areas. (c) The binding energy of capture $CO_2$. (d) The interaction distance of $CO_2$ with AMT and $AMT^-$. Reprinted (adapted) from *Adv. Funct. Mater.* 2024, **34**, 2311733. Copyrights © 2024 Wiley-VCH GmbH.


© 2026 The Author(s). Published by the Royal Society of Chemistry

Open Access Article. Published on 12 fevral 2026. Downloaded on 01.06.2026 11:06:26.
This article is licensed under a Creative Commons Attribution-NonCommercial 3.0 Unported Licence.

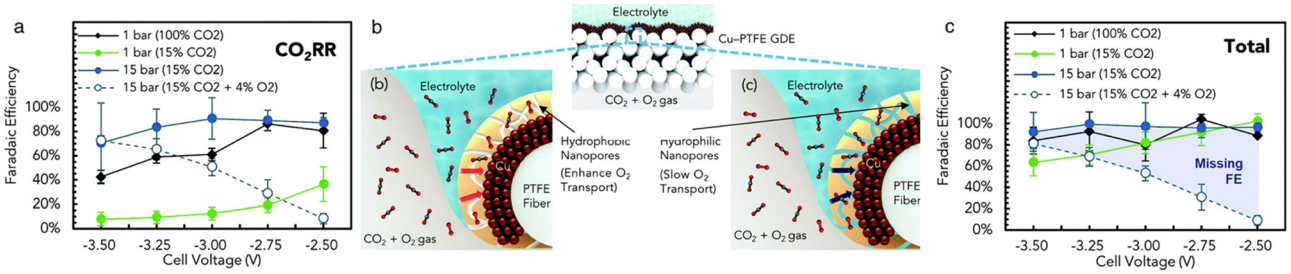


Fig. 52 (a) Effect of pressure and the presence of $O_2$ on product selectivity for $CO_2RR$ with flue gas $CO_2$ concentrations on a Cu catalyst. (b) Schematic illustration of the Cu-PTFE GDE. (c) The FE toward C2 products for different ionomers. Reprinted (adapted) from *Energy Environ. Sci.*, 2020, **13**, 554. Copyrights © 2020 Royal Society of Chemistry.

mass flux by an order of magnitude compared to hydrophobic ionomers (*e.g.*, Nafion). Fig. 52b shows 68% FE for $C_2$ products (ethylene and ethanol) was achieved at 10 bar, and 26% full-cell energetic efficiency over 10 hours, even with $O_2$, which is comparable to pure $CO_2$-fed systems (Fig. 52c). However, additional studies using real flue gas with other impurities (*e.g.*, $SO_x$, $NO_x$) and investigating long-term catalyst stability and scalability are still needed.

Zhu *et al.*, 2023[298] illustrated a pioneering, continuous, integrated system for $CO_2$ capture and release utilizing a modular electrochemical solid–electrolyte reactor (Fig. 53a–d). This concept integrates absorption and release within a single unit, operates at ambient conditions, and uses only water as input, in contrast to amine scrubbing or disconnected electrochemical/chemical systems. At the cathode, oxygen reduction (ORR) produces $OH^-$, establishing a localized alkaline environment that interacts with $CO_2$ to yield carbonate ions. The ions traverse an anion-exchange membrane into the solid–electrolyte layer, whereas protons generated by water oxidation (OER) at the anode pass through a cation-exchange membrane. The ions recombine, releasing high-purity (>99%) $CO_2$ gas continuously. The system achieves high capture rates (about 440 mA $cm^{-2}$, 86.7 kg $CO_2$ $day^{-1}$ $m^{-2}$), exceeds 90% faradaic efficiency, and approaches 98% carbon-removal efficiency in simulated flue gas (Fig. 52e–h). Notwithstanding these benefits, the methodology is constrained by limitations such as mass-transport bottlenecks at low $CO_2$ concentrations (resulting in decreases in faradaic efficiency, CO poisoning of Pt/C catalysts, and energy losses due to ohmic drops in the solid–electrolyte layer. The authors investigated the utilization of cobalt single-atom catalysts (Co-SAC) that are resistant to CO poisoning while preserving high efficiency, even at diminished $CO_2$ concentrations. They additionally suggest enhancements such as minimizing solid–electrolyte thickness, employing different redox couples (*e.g.*, $2e^-$ ORR for $H_2O_2$ production to increase electron efficiency to approximately 0.7 $CO_2$ per electron), and sophisticated catalyst and membrane engineering. These tactics could decrease capture costs from approximately $83 to around $33 per ton, establishing this electrochemical platform as a viable method for sustainable, decentralized $CO_2$ capture in conjunction with renewable energy and subsequent conversion operations.

Li *et al.* (2024)[299] enhanced this design by amalgamating direct air capture and electrochemical conversion into a unified solid-state platform, functioning effectively at ambient settings, utilizing ambient air and water as feedstocks. Utilizing CO-tolerant, non-precious Cu catalysts alongside a polymer-based electrolyte, they tackle challenges related to catalyst expense, CO poisoning, and energy inefficiency, while directly generating ethylene without the need for intermediate $CO_2$ purification, providing a more efficient and sustainable approach for decentralized carbon utilization. This study introduces a solid-state electrochemical reactor that efficiently captures $CO_2$ and $H_2O$ from ambient air and converts them into ethylene and oxygen at approximately 25 °C, achieving FE of around 34%, remarkable energy efficiency of around 80%, and operating at a low voltage of about 0.6 V with a current of 1 A. Simple and scalable cathode fabrication method is shown in (Fig. 54a). The anode structure is presented in (Fig. 54b). The solid polyelectrolyte facilitates the migration of $OH^-$ ions from the conductive cathode to the nickel anode under an electric field, while also enabling the transfer of produced water from the nickel anode to the conductive cathode (Fig. 54c). The system employs a stratified architecture: a cathode composed of conductive carbon foam integrated with copper nanoparticle-coated SWCNTs for $CO_2$ reduction catalysis, a PEO/KOH-infused polypropylene membrane serving as a solid electrolyte for $OH^-$ transport, and a nickel foam anode facilitating oxygen evolution. $CO_2$ is sequestered by PEI/zeolite 13X composites, while $H_2O$ is absorbed by $CaCl_2$-based hygroscopic salts, facilitating the *in situ* synthesis of formate and CO, which are then reduced on the Cu catalyst surface to provide ethylene by CO–CO coupling (Fig. 54d). This method facilitates compact, scalable, and continuous direct air capture (DAC) and conversion of low-concentration $CO_2$ without the need for compression or gas purification. The system effectively generates around 70 mg of ethylene per hour, demonstrating the reactor's capability to generate hydrocarbons from air-sourced carbon under ambient settings without the need for gas purification or compression.

The incorporation of metal oxides for concurrent carbon dioxide ($CO_2$) collection and electrochemical reduction ($CO_2RR$) signifies a viable approach for enhancing carbon-neutral energy and chemical output. Due to their distinctive physiochemical characteristics, such as high $CO_2$ affinity, surface tunability, and catalytic activity, metal oxides, including $SnO_x$, CuO, $Bi_2O_3$, and $In_2O_3$, have become attractive options for dual-function systems. These materials not only promote $CO_2$ adsorption *via* acid–base

Open Access Article. Published on 12 fevral 2026. Downloaded on 01.06.2026 11:06:26.
This article is licensed under a Creative Commons Attribution-NonCommercial 3.0 Unported Licence.

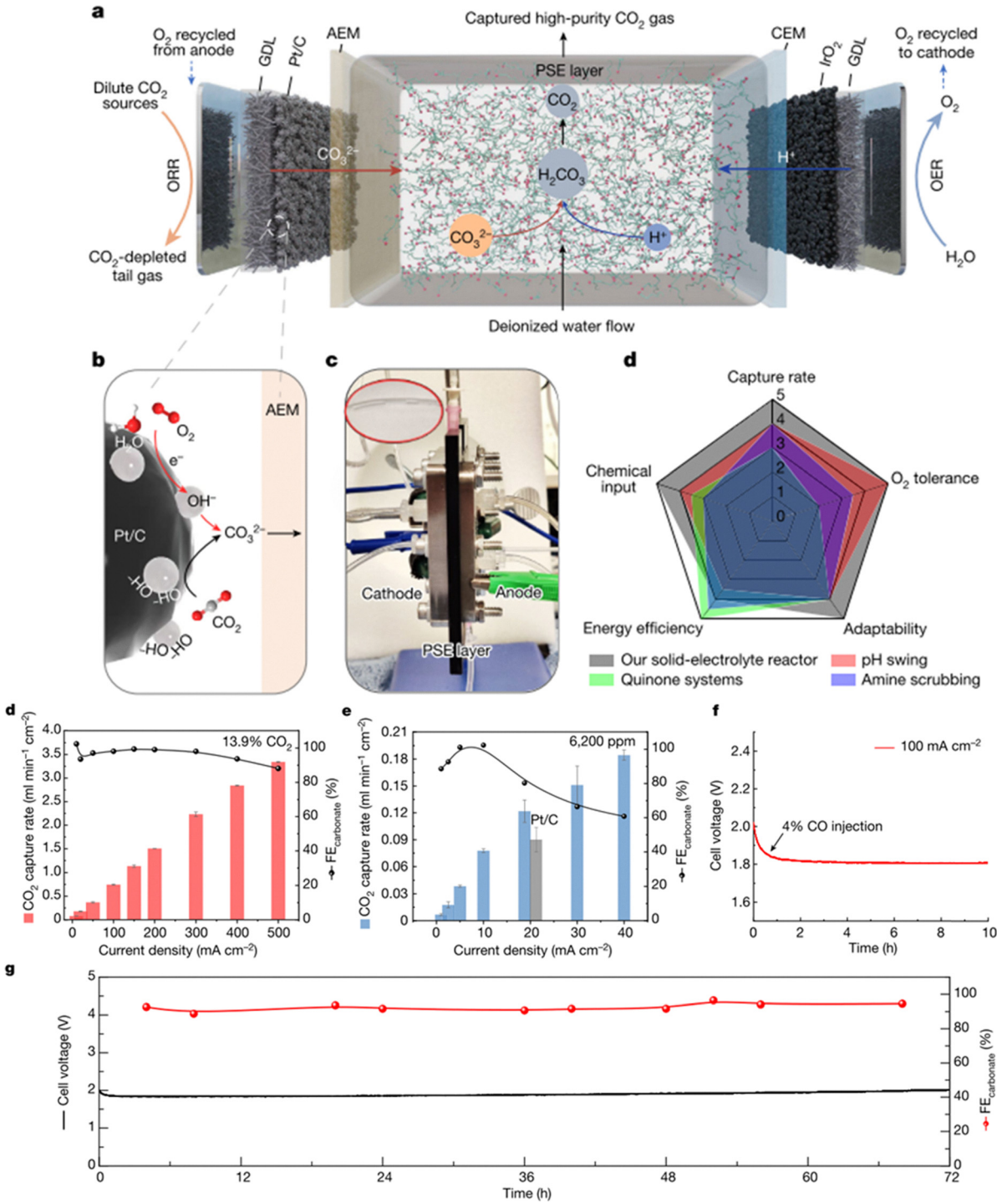


Fig. 53 Solid–electrolyte reactor design for carbon capture from different $CO_2$ sources. (a) Schematic of the solid–electrolyte reactor for carbon capture. (b) Schematic of the reaction mechanism at the catalyst–membrane interface. (c) Photograph of the solid–electrolyte reactor and captured $CO_2$ gas (inset) flowing out of the solid–electrolyte layer. (d) A radar plot comparison of different carbon-capture technologies. (e) and (f) The carbon-capture performance of Co-SAC under 13.9% and 6200 ppm $CO_2$ concentration, which showed a large improvement compared with Pt/C under low-$CO_2$-concentration regions. (g) The high resistance of Co-SAC catalysts to CO poisoning, while the cell voltage remained stable after the injection of CO gas. (h) Stability test of Co-SAC catalyst under a fixed current of 100 mA $cm^{-2}$, over 72 hours. Reprinted (adapted) from *Nature* 2023, **618**, 959–966. Copyrights © 2023, The Author(s), under exclusive license to Springer Nature Limited.

interactions and surface changes (*e.g.*, amine functionalization) but also work as active electrocatalysts that convert $CO_2$ into valuable products such as formate, carbon monoxide, ethylene, and ethanol. Notwithstanding substantial advancements, some essential knowledge deficiencies persist that must be resolved to enhance the practical implementation of metal oxide-based


© 2026 The Author(s). Published by the Royal Society of Chemistry

Open Access Article. Published on 12 fevral 2026. Downloaded on 01.06.2026 11:06:26.
This article is licensed under a Creative Commons Attribution-NonCommercial 3.0 Unported Licence.

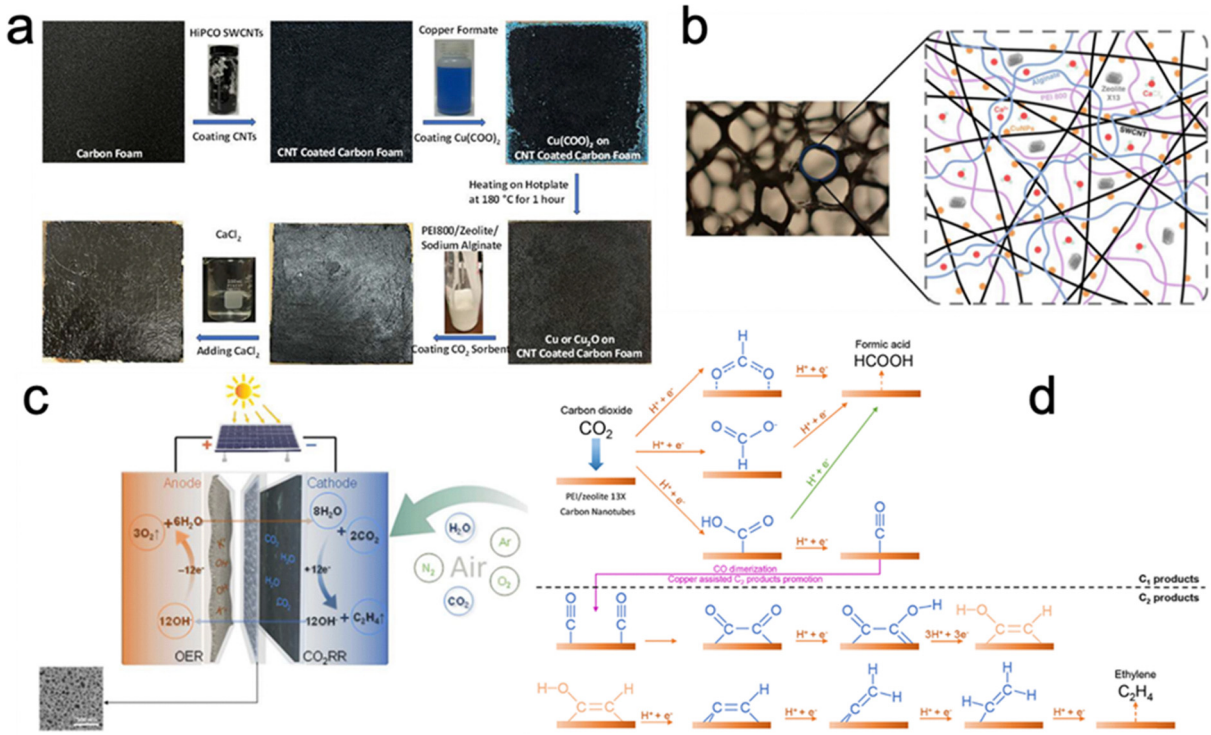


Fig. 54 (a) Procedures of cathode fabricating. (b) Photographic picture of carbon foam (left) and cartoon illustration of zeolite 13X/PEI800 and SWCNTs with copper nanoparticles embedded in the ionotropic gelation of sodium alginate and calcium chloride (right). (c) Cartoon illustration of direct air capture of $CO_2$ and $H_2O$, electroreduction of $CO_2$ into ethylene in the cathode and the oxygen evolving reaction in the anode, and the transportation of $OH^-$ and $H_2O$ in the solid electrolyte reactor. (d) Catalytic electrochemical reduction mechanism of direct air captured $CO_2$ and $H_2O$ into ethylene and $O_2$. Reprinted (adapted) from *Energy Fuels* 2024, **38**(11), 10390–10393. Copyrights © 2024 American Chemical Society.

integrated $CO_2$ capture and conversion systems. Present constraints encompass sub-industrial current densities for product generation, inadequate comprehension of the long-term stability of oxide-based catalysts (particularly under variable gas compositions and humid environments), and a lack of mechanistic understanding regarding surface transformations and intermediate stabilization during operational conditions. Further details are listed below:

• Rational interface and catalyst design: engineering hybrid systems that integrate metal oxides with conductive substrates (*e.g.*, carbon nanomaterials, metal–organic frameworks, or polymers) may enhance charge transport, catalytic stability, and overall efficiency.

• *Operando* and *in situ* characterization: utilizing sophisticated spectroscopic and microscopic methods (*e.g.*, XAS, FTIR, Raman, and TEM) under operational conditions is crucial for clarifying active sites, reaction intermediates, and degradation routes.

• Surface functionalization and defect engineering: modifying the surface characteristics of metal oxides through doping, the introduction of oxygen vacancies, or the grafting of alkanolamines can markedly improve $CO_2$ affinity and adjust product selectivity.

• System-level integration and optimization: the integration of metal oxides into modular platforms, including gas diffusion electrodes, pressurized flow reactors, and solid-state electrochemical cells, is essential for enhancing technology readiness. Employ strategies such as pressure manipulation and permselective membranes to improve gas transport and reaction kinetics.

## Solvent-based $CO_2$ capture and conversion

The following section concentrates on the description of some of the liquid-phase techniques for $CO_2$ capturing, focusing on new solvents such as amines, ionic liquids, and Eutectic Solvents, and their uses in the integrated systems of electrochemical $CO_2$ capture and conversion. These advanced liquid media will be explained in detail and then compared with traditional electrolytes in terms of prior research articles to highlight their advantages, disadvantages, and possibilities for rapid implementation in carbon-neutral technologies.

## Amines

Among the available capture technologies, Amine-based absorbents are widely used for $CO_2$ capture in industrial settings due to their rapid reactivity, ease of use, and adaptability in different applications, as Fig. 55 shows, which are applied in both pre- and post-combustion systems.[300–302]

Open Access Article. Published on 12 fevral 2026. Downloaded on 01.06.2026 11:06:26.
This article is licensed under a Creative Commons Attribution-NonCommercial 3.0 Unported Licence.

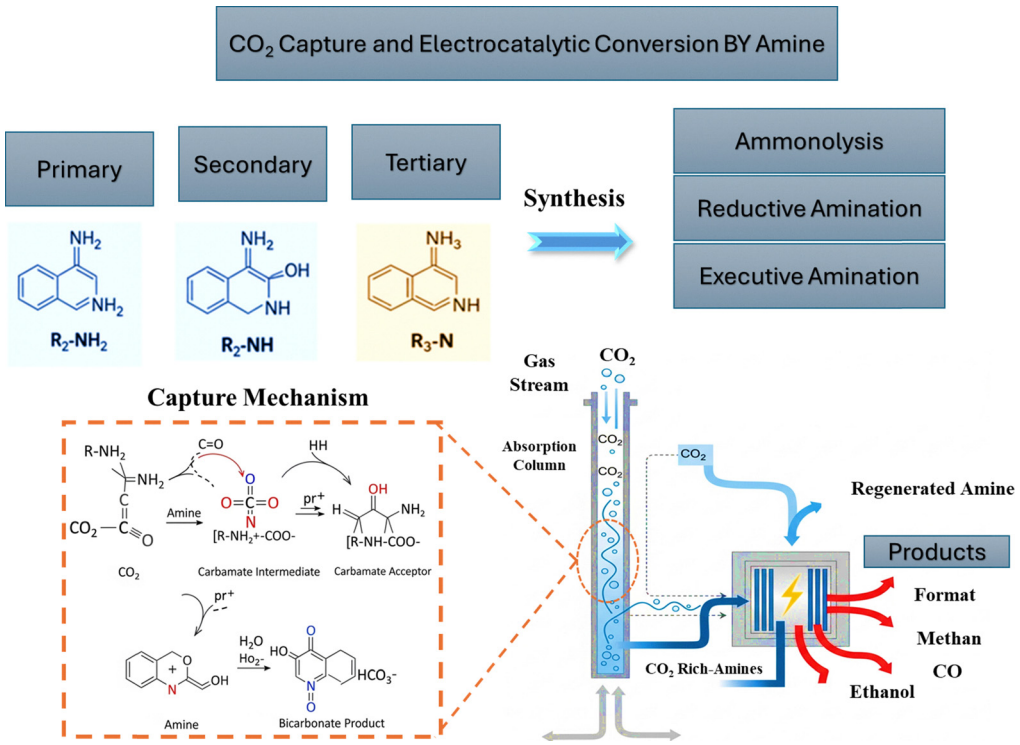


Fig. 55 Comprehensive schematic of integrated $CO_2$ capture and electrocatalytic conversion through reductive aminolysis using multifunctional amine solvents.

## 1. Amine chemistry and mechanisms of $CO_2$ capture

The fundamental chemistry behind amines capturing the $CO_2$ involves different mechanisms depending on the amine type, whether it is primary (like MEA), secondary (like DEA), or tertiary (like methyl diethanolamine (MDEA).

**(A) Primary and secondary amines.** Primary and secondary amines efficiently capture $CO_2$ by forming carbamates in a two-step process, often termed the *zwitterion mechanism*: "A zwitterion is a molecule that carries both positive and negative charges on different parts of its structure, but it remains electrically neutral overall. This charge separation arises from factors such as solvation effects, resonance, and the molecule's geometry, which localize charges to distinct functional groups. The term comes from German, meaning "hybrid" or "hermaphrodite."

*(a) Step 1: formation of the zwitterionic intermediate.* In the instance of $CO_2$ absorption, the zwitterion intermediate forms when the lone pair of the amine nitrogen bonds to the electrophilic carbon of $CO_2$, creating a positively charged nitrogen and a negatively charged oxygen.[303–305]

$$RNH_2 + CO_2 \rightleftharpoons RNH_2^+–COO^- \quad (1)$$

Due to bond angles and spatial arrangements, limited overlap means those charges are localized and cannot undergo internal proton transfer (a proton moved from one site to another) or delocalization that would neutralize them, so the intermediate zwitterion is very reactive and short-lived.

*(b) Proton transfer and carbamate stabilization.* A second amine molecule acts as a base, abstracting a proton from the zwitterion. This forms a stable carbamate ion and a protonated amine:

$$[RNH_2^+–COO^-] + RNH_2 \rightarrow RNHCOO^- + RNH_3^+ \quad (2)$$

The zwitterion is stabilized by solvent effects and structural features of the molecule, but without a second amine to abstract the proton, it cannot convert efficiently to a carbamate. This explains both the rapid reaction rates and the need for at least two amine molecules per absorbed $CO_2$ molecule. From eqn (1) and (2), the overall reaction of primary and secondary amines capturing $CO_2$ will be as follows:

$$CO_2 + 2RNH_2 \leftrightarrow RNHCOO^- + RNH_3^+ \quad (3)$$

Since these reactions don't require special conditions, they are carried out at moderate temperatures ($\sim$40 °C), making them highly effective in industrial capture systems.[305]

**(B) Tertiary amines or sterically hindered.** Tertiary amines do not form carbamates because they lack a hydrogen atom on the nitrogen. Rather, they absorb $CO_2$ in the presence of water and form bicarbonate ions:

$$CO_2 + R_3N + H_2O \leftrightarrow R_3NH^+ + HCO_3^- \quad (4)$$

Although tertiary amines react more slowly, they generally require less energy for regeneration and exhibit better thermal stability. For this reason, blends like MEA-MDEA or DIPA-MDEA are often used to balance absorption kinetics, solvent stability, and energy consumption in industrial applications.[306,307]

**(C) Aqueous ammonia and other systems.** Other chemical solvents, such as carbonate systems (*e.g.*, $K_2CO_3$) and aqueous ammonia, have been studied. However, due to slow reaction


© 2026 The Author(s). Published by the Royal Society of Chemistry

Open Access Article. Published on 12 fevral 2026. Downloaded on 01.06.2026 11:06:26.
This article is licensed under a Creative Commons Attribution-NonCommercial 3.0 Unported Licence.

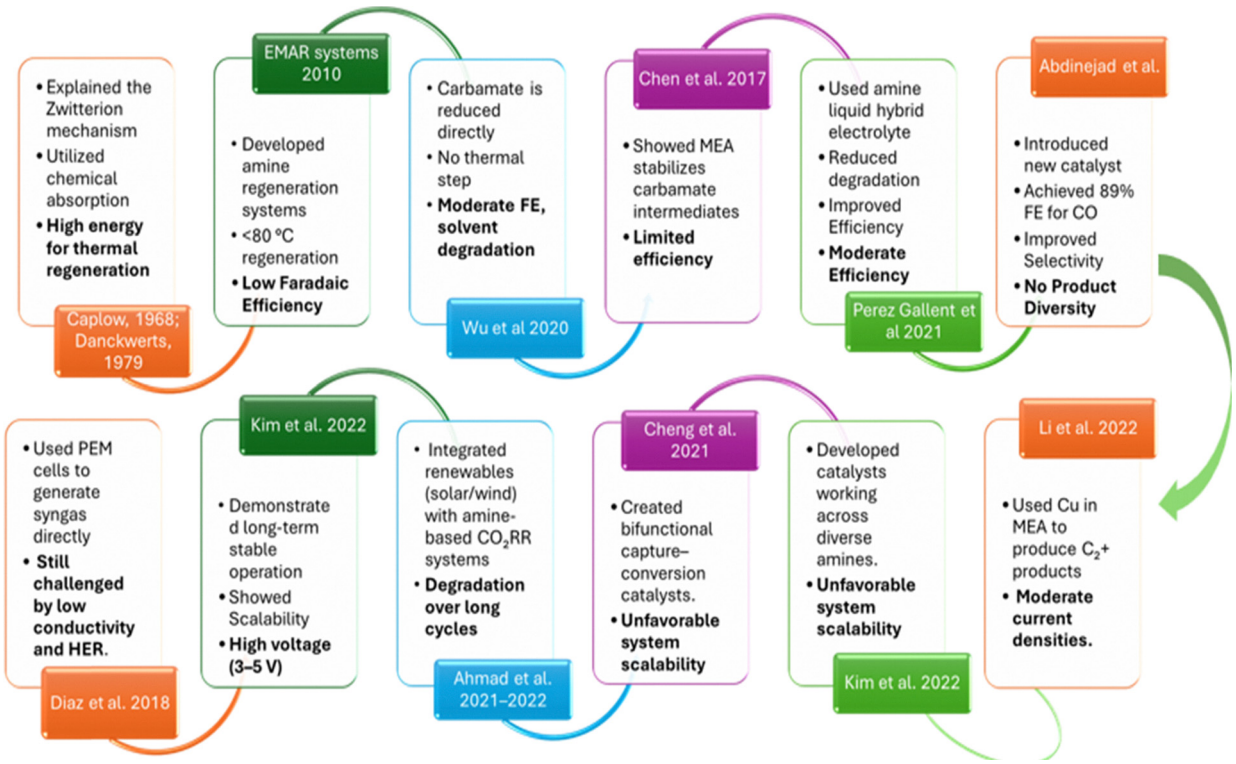


Fig. 56 A graphical timeline of the major developments in amine-based $CO_2$ capture and electrochemical conversion systems.

kinetics, carbonates are not very efficient, and ammonia slip, along with volatile losses, are problematic. Because of these issues, amine-based systems remain favored in industry for their efficiency and flexibility across a range of capture conditions.[308] Comparison between different amine types is shown in (Fig. 56).[309]

## 2. Recent studies for the use of amine in electrochemical capturing and conversion

Amines are pivotal in integrated electrochemical $CO_2$ capture and conversion by efficiently chemisorbing $CO_2$ to form carbamate and bicarbonate species, which increase local $CO_2$ concentration near catalysts and enable simultaneous capture and electrochemical reduction, thus bypassing traditional energy-intensive thermal regeneration.[310] Industrially, MEA has been a benchmark for rapid carbamate formation since the mid-20th century. Early electrochemically mediated amine regeneration (EMAR) used bipolar membranes and redox-active quinones to lower regeneration temperatures ($<80$ °C) but suffered from low faradaic efficiencies ($<50\%$), solvent degradation, and scalability issues. The direct electrochemical reduction of carbamate species, leverages alkali cation effects to compress the electrochemical double layer and enhance $CO_2$-to-CO conversion efficiency to 72%, while it was demonstrated that amine protonation aids formation of $CO_2$ radical anions for selective CO and formate production ($\sim 60\%$ FE). Hybrid amine–ionic liquid electrolytes further mitigate degradation and sustain formate production, while Amines also suppress hydrogen evolution and stabilize CO dimer intermediates, promoting multi-carbon product formation. Furthermore, catalyst innovations with iron-porphyrin and Cu-based systems have improved selectivity and product diversity. Also, advanced bifunctional catalysts, such as single-atom Ni and alkanolamine-functionalized $SnO_2$, enhance efficiency and stability. Integration with renewable energy enables efficient, scalable $CO_2$ conversion with cost savings, supported by continuous-flow reactors that sustain high current densities and employ radical scavengers or sterically hindered amines (*e.g.*, AMP) to curb degradation. Early polymer electrolyte membrane (PEM) systems demonstrated electrochemical syngas production from amine-captured $CO_2$, emphasizing the role of electrolyte conductivity and pH control, aided by inorganic salts to reduce ohmic losses.

A recent study by Pérez-Gallent *et al.* demonstrated the dual functionality of amines for an integrated $CO_2$ capture and electrochemical conversion owing to their, chemical and physical absorption functions.[311] From physical properties prospectives of amines which transforms the inherent ohmic heating into raising the reactor temperature from 15 °C to 75 °C that enhance the $CO_2$ desorption step nearly 8-fold and increase the format reaction rate by a factor of 10, reaching 0.56–0.7 mmol $m^{-2}$ $s^{-1}$ (Fig. 57a). In addition to the high capture capacity of $CO_2$, the product selectivity was also notable, with faradaic efficiencies up to 50% for formate and 45% for CO, alongside the detection of glycolate and oxalate as additional reduction products. Electrolyte composition and concentration proved critical: replacing propylene carbonate (PC) with water caused a 70% decline in formate yield due to competing hydrogen evolution, while optimizing AMP concentration at 2 M maximized efficiency and reaction rates, whereas higher concentrations introduced viscosity-related mass transfer

Open Access Article. Published on 12 fevral 2026. Downloaded on 01.06.2026 11:06:26.
This article is licensed under a Creative Commons Attribution-NonCommercial 3.0 Unported Licence.

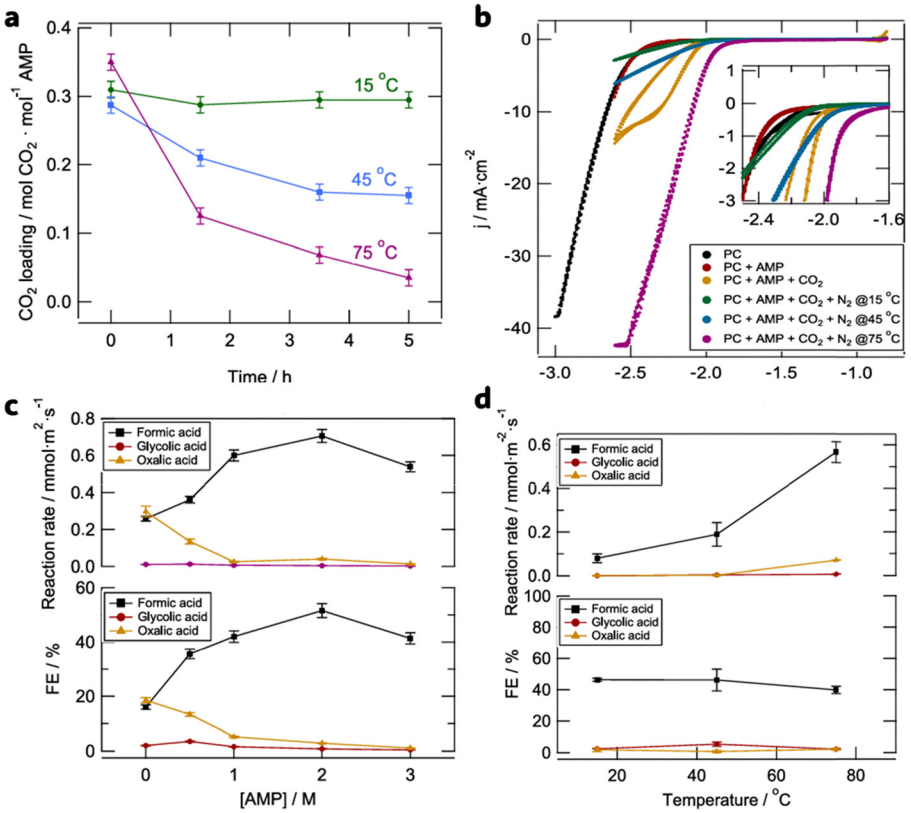


Fig. 57 (a) $CO_2$ loading as a function of electrolysis time at −2.5 V *vs.* Ag/AgCl on a Pb electrode in 0.7 M TEACl in PC containing 1 M AMP preloaded with $CO_2$ at different temperatures. (b) Cyclic voltammograms of a Pb electrode in 0.7 M TEACl in PC: without AMP (black), with 1 M AMP (red), with $CO_2$-saturated 1 M AMP at 1 bar and 15 °C (yellow), with $CO_2CO_2$-loaded 1 M AMP after $N_2$ stripping at 15 °C (green), 45 °C (blue), and 75 °C (purple). (c) Reaction rate and faradaic efficiency (FE) of formate, glycolate, and oxalate as a function of temperature. (d) Reaction rate and FE of formate, glycolate, and oxalate during electrolysis at −2.5 V *vs.* Ag/AgCl. Reprinted (adapted) from *Ind. Eng. Chem. Res.* 2021, **60**(11), 4269–4278. Copyrights © 2021 American Chemical Society.

limitations. However, in the absence of AMP, oxalate dominated with initial faradaic efficiencies of 80%, though this decreased over time (Fig. 57b and c). The reaction rate of $CO_2$ electroreduction increased strongly with electrolyte temperature, with formate production rising from 15 to 75 °C (0.56 mmol $m^{-2}$ $s^{-1}$) while maintaining a relatively constant faradaic efficiency, reaching 40% at 75 °C. Compared to Alvarez-Guerra *et al.*, who reported lower rates (0.075 mmol $m^{-2}$ $s^{-1}$) despite higher efficiencies (80%) on Pb in aqueous bicarbonate, the PC-based system offers a better balance of rate and selectivity. The organic solvent plays a critical role, as a high current density (40 mA $cm^{-2}$) was observed at 75 °C, compared to aqueous AMP, where the FE towards formate dropped to 3% after five h due to increased HER. $CO_2$ loading studies further revealed that higher temperatures accelerate $CO_2$ desorption, with only 10% retained after five h at 75 °C, compared with 93.5% at 15 °C (Fig. 57d).

A side-by-side comparison of main catalyst-electrolyte systems and their performance metrics is presented in Table 16, emphasising the variation in faradaic efficiencies, operating potentials, and current densities achieved in different configurations.

The (Table 16) indicates amine-based media are promising for electrochemical conversion of $CO_2$ with moderate to high selectivity towards CO and formate, especially when co-catalysts, salts, or surfactants are added. Besides electrode design, mass transport, and electrolyte conductivity improvements, additional progress is needed toward industrially meaningful current densities.

## 3. Remaining challenges and outlook

Despite these developments, some of the most significant challenges remain:

- Low ionic conductivity and high Ohmic losses: technologies based on amines are less ionic in their conductivity than alkaline electrolytes, resulting in greater cell voltages and energy consumption. Alkali cation electrolyte engineering increases electron transport but does not fully eliminate this challenge.[318]
- Competing hydrogen evolution reaction (HER): HER decreases $CO_2$ reduction selectivity, especially at high overpotentials and current densities. Catalyst and electrolyte modification decreases HER to some extent, but cannot eliminate it.
- Amine degradation: oxidative and thermal degradation of amines during electrolysis creates byproducts that decrease solvent lifetime and increase operating expenses. Use of sterically hindered amines, radical scavengers, and optimal operating conditions reduces but cannot prevent degradation.
- Scalability and moderate current densities: while continuous-flow systems can sustain current densities of as


© 2026 The Author(s). Published by the Royal Society of Chemistry

Open Access Article. Published on 12 fevral 2026. Downloaded on 01.06.2026 11:06:26.
This article is licensed under a Creative Commons Attribution-NonCommercial 3.0 Unported Licence.

Table 16 Studies on the use of amine solutions in electrochemical capturing and conversion

| Catalyst/electrode | Potential (V *vs.* RHE) | Product | FE (%) | Current density (mA $cm^{-2}$) | Solvent/conditions | Ref. |
|---|---|---|---|---|---|---|
| Ag/carbon-black on 300 nm Ag film | −0.8 | CO | 72 | 50 | 30 wt% MEA + 2 M KCl, 60 °C | 312 |
| Ag/carbon-black on 300 nm Ag film | −0.8 | CO | 100 | 30 | 30 wt% MEA + 2 M KCl, 60 °C | |
| Ag/carbon-black on 300 nm Ag film | −0.66 | CO | 30 | — | 2 M MEA + 2 M CsCl, 25 °C | |
| Ag/carbon-black on 300 nm Ag film | −0.66 | CO | <5 | — | 2 M MEA, no salt | |
| Cu + MEA | −0.78 | CO | 22 | 14.8 | 0.1 M $NaClO_4$ aq. + $CO_2$-loaded MEA | 313 |
| Cu + EDA | −0.78 | CO | 58 | 18.4 | 0.1 M $NaClO_4$ aq. + $CO_2$-loaded EDA | |
| Cu + DCA | −0.78 | CO | 19 | 9.7 | 0.1 M $NaClO_4$ aq. + $CO_2$-loaded DCA | |
| Ag (porous + CTAB) | −0.8 | CO | 38.2 | 39.1 | 30% MEA w/w aq., $CO_2$-saturated + 0.1% CTAB | 314 |
| In (porous + CTAB) | −0.8 | $HCOO^-$ | 54.5 | ~13.4 | $CO_2$-saturated 30% MEA, 0.1% CTAB | |
| In (porous + CTAB) | −0.8 | CO | 22.8 | ~2.0 | $CO_2$-saturated 30% MEA, 0.1% CTAB | |
| Pb (porous + CTAB) | −0.8 | $HCOO^-$ | 60.8 | ~2.2 | $CO_2$-saturated 30% MEA, 0.1% CTAB | |
| Bi (porous + CTAB) | −0.8 | $HCOO^-$ | 36 | ~18.3 | $CO_2$-saturated 30% MEA, 0.1% CTAB | |
| Sn (porous + CTAB) | −0.8 | CO | 16.6 | ~8.9 | $CO_2$-saturated 30% MEA, 0.1% CTAB | |
| Sn (porous + CTAB) | −0.8 | $HCOO^-$ | 11.6 | ~4.1 | $CO_2$-saturated 30% MEA, 0.1% CTAB | |
| HCl-modified Ag | −0.91 | CO | 91 ± 7 | ~3.0 | 1 M AMP + 0.3 mM CTAB, $CO_2$-sat. aq., RT, H-cell | 315 |
| HCl-modified Ag | −1.01 | CO | 91 | (higher than at −0.91 V) | 1 M AMP + 0.3 mM CTAB, $CO_2$-sat. aq., RT, H-cell | |
| HCl-modified Ag | −0.91 | CO | 54 | — | 1 M MEA aq., no CTAB (*vs.* AMP system) | |
| HCl-treated Cu | −0.61 | $HCOO^-$ | ~68 | — | 1 M AMP + 0.3 mM CTAB, $CO_2$-sat. aq., H-cell | |
| HCl-treated Zn | −0.91 | CO | ~40–50 | — | 1 M AMP + 0.3 mM CTAB, $CO_2$-sat. aq., H-cell | |
| Ni–N/C (single atom) | −0.9 to −1.1 | CO | 78.3 | −2.6 | 5 M MEA, H-cell | 316 |
| Ni–N/C (MEA cell) | — | CO | 64.9 | −50.0 | 5 M MEA, zero-gap membrane electrode assembly | |
| Ag nanoparticles | −0.9 to −1.1 | CO | 38.3 | −0.79 | 5 M MEA, H-cell | |
| Ag nanoparticles (MEA cell) | — | CO | 25.5 | −50.0 | 5 M MEA, membrane electrode assembly | |
| Cu Nanodendrites | −0.77 | $HCOO^-$ | 54.78 | ~21.0 | $CO_2$-sat. aq. ethanolamine (0.05 mol frac.) | 317 |
| Ag Nanodendrites | −0.77 | $HCOO^-$ | 35.84 | ~7.9 | $CO_2$-sat. aq. ethanolamine (0.05 mol frac.) | |
| Au Nanodendrites | −0.77 | $HCOO^-$ | 60.3 | ~46.6 | $CO_2$-sat. aq. ethanolamine (0.05 mol frac.) | |

much as 200 mA $cm^{-2}$, batch systems realize lower current densities, which limit throughput and industrial scalability.

• Inefficient capture medium regeneration: electrochemical conversion does not always fully regenerate amine solvents, which requires extra processing steps.

Integrated capture and conversion electrochemistry can reduce the energy requirement for carbon capture hardware by up to 44% compared with conventional thermal regeneration, primarily by excluding the high-temperature stripping step 1. However, inefficiencies in currently available systems, such as high cell voltages (3–5 V at 100 mA $cm^{-2}$), solvent degradation, and modest current densities, limit economic competitiveness. Integration of renewable power will help offset electricity costs and improve sustainability, but intermittency and system longevity remain concerns. Since amine-based electrolytes are hindered by low ionic conductivity, competition with hydrogen evolution (HER), solvent degradation, and moderate current densities, new capture media such as ionic liquids (ILs) and deep eutectic solvents (DESs) are gaining increasing research interest. These solvents have greater $CO_2$ solubility, enhanced electrochemical stability, and adjustable physicochemical properties, which can surpass the intrinsic shortcomings of amines and allow for more efficient, stable, and scalable integrated $CO_2$ capture and conversion systems.[319]

## Ionic liquid

Amines capture $CO_2$ primarily by forming a chemical bond through the direct reaction of the nitrogen lone pair with $CO_2$. However, many of these amine-derived salts are solid at room temperature, which limits molecular mobility and thus restricts mass transport. This results in reduced efficiency during $CO_2$ absorption and subsequent desorption.[320] To overcome these limitations, amine-based materials have been engineered into ionic liquids (ILs): salts that are liquid at or near room temperature. The concept of ILs originated from early studies on ammonium salts, such as ethylammonium nitrate ($[EtNH_3][NO_3]$), first reported by Paul Walden in 1914. This salt, formed from ethylamine (an amine) and nitric acid, remains liquid at room temperature (melting point 12 °C) and is considered the archetype of ionic liquids. These early ILs were essentially ammonia- or amine-derived salts (ammonium cations paired with various anions) that could absorb gases like $CO_2$ or $NH_3$, similar to how aqueous amine solutions are used in industrial gas scrubbing, as shown in (Fig. 58).[321]

The success of ammonium-based ionic liquids demonstrated the feasibility of creating room-temperature molten salts by pairing organic (alkylammonium) cations with appropriate anions. Building on these principles, researchers have designed a wider array of ILs, moving beyond simple ammonium salts by pairing various organic cations (such as imidazolium, pyridinium, or phosphonium) with inorganic or organic anions (*e.g.*, $BF_4^-$, $PF_6^-$, $NTf_2^-$). Importantly, these new ILs do not require specific functional groups for gas binding; their effectiveness largely stems from the use of bulky, asymmetric cations (often inspired by amines or ammonium ions) and weakly coordinating anions, which ensure the resulting salt remains liquid at room temperature and provides high ionic mobility.

Open Access Article. Published on 12 fevral 2026. Downloaded on 01.06.2026 11:06:26.
This article is licensed under a Creative Commons Attribution-NonCommercial 3.0 Unported Licence.

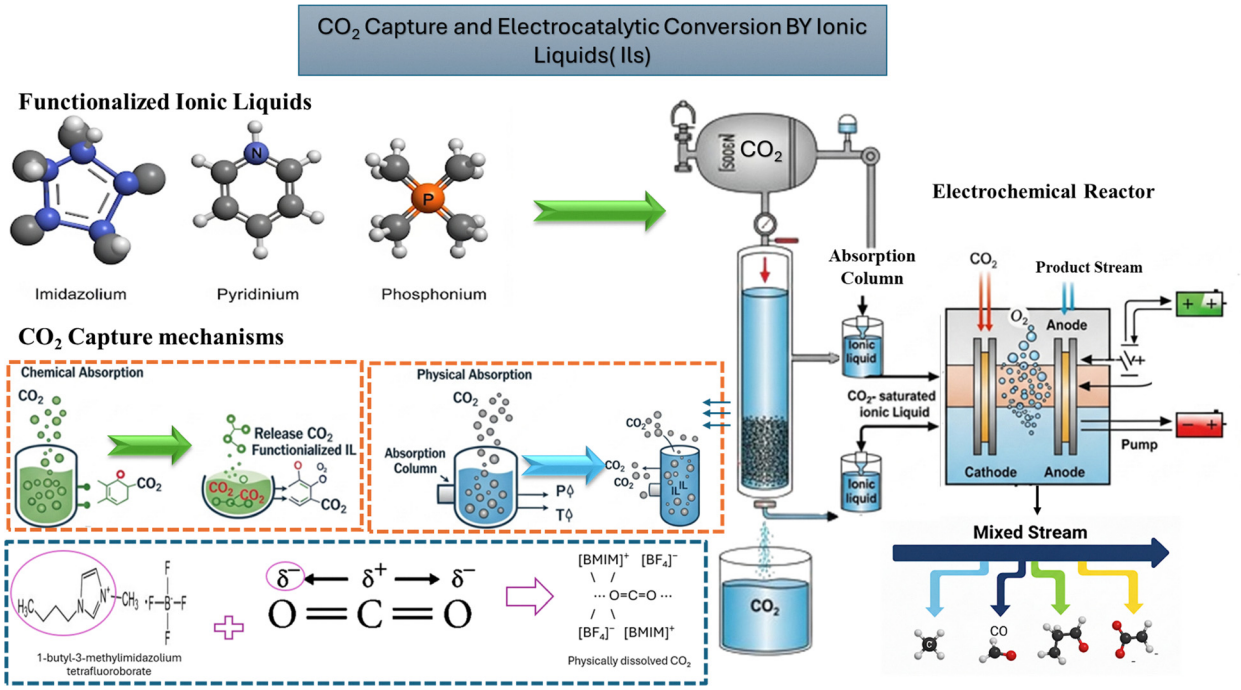


Fig. 58 Detailed process schematic of integrated $CO_2$ capture and electrocatalytic conversion using functionalized ionic liquids (ILs) in a continuous ICCC system.

ILs retain the reactive functionalities of amines while offering versatile and tunable physical properties. They serve as liquid electrolytes, demonstrate strong thermal and electrochemical stability, and can be precisely tailored for specific applications. These features make ILs ideally suited for integration with electrochemical systems, allowing the seamless co-integration of $CO_2$ capture and conversion processes, such as electrochemical reduction, thereby advancing sustainable carbon management solutions.

## 1. Ils mechanism

Ionic liquids (ILs) and aqueous amines capture $CO_2$ with two different approaches, as demonstrated in (Fig. 59). In amine-based systems (top group), reagents such as ethanolamine chemically react with $CO_2$ and form stable carbamate species through a zwitterionic intermediate. This process occurs *via* covalent bonding and proceeds at a 1 : 2 $CO_2$ : amine ratio, making it highly effective for capture but energetically costly for regeneration, as the bond must be broken to liberate $CO_2$. In contrast, ILs are salts that are entirely composed of cations and anions and are liquid at or near 100 °C, that interact with $CO_2$ primarily *via* physical absorption (bottom panel).[322] ILs such as 1-butyl-3-methylimidazolium tetrafluoroborate ([Bmim][$BF_4$]) physically dissolve $CO_2$ *via* weak, non-covalent interactions, including van der Waals forces, Coulombic attractions, and Lewis acid–base interactions (in this case with the anion).[323]

The structure of IL plays a crucial role in the $CO_2$ solubility. Fluorinated anions ([$PF_6$]$^-$, [$Tf_2N$]$^-$) and long alkyl chains on the cation can enhance free volume and hydrophobicity, favouring $CO_2$ uptake. For example, phosphonium-based ILs like [$P_{66614}$].[324] For instance, [$P_{66614}$][2-CNpyr] has a capacity of 76.5 mg $CO_2$ per g solvent at 22.1 °C and 57.4 mg $CO_2$ per g solvent at 40.1 °C and 1 bar of $CO_2$.[324,325]

Numerous studies have examined the influence of IL structural properties on $CO_2$ solubility and absorption. These reports reiterate that in conventional ILs, the physical forces dominate and solubility is principally governed by anion features, free volume, and the strength of weak intermolecular forces.[326] The following (Table 17) presents a summary of notable contributions in this sense, including some insight into the creation of ILs for $CO_2$ capture.

Conventional ionic liquids (ILs) have a great deal of potential for $CO_2$ capture due to their tunable structures, low volatility, and ability to absorb $CO_2$ through weak non-covalent interactions (*i.e.*, van der Waals forces, coulombic interactions, or Lewis acid–base interactions); however, they are limited to $CO_2$ uptake as ILs contain no chemically reactive sites. With the potential drawbacks of traditional ILs, researchers have synthesized, modified, or functionalized ILs with reactive functional groups (most commonly amino, hydroxyl, carboxyl, or heterocyclic donors) that can form covalent, or at least reversible bonds with $CO_2$, thereby enhancing uptake capacity and selectivity.[333] Incorporating chemical functionality into ILs changes the role of ILs from purely being physical solvents with non-covalent interactions and has a diverse range of possible applications because they can now be classified in two broad categories; the first category is Amino-functionalized ILs (AFILs), which are usually designed to mimic traditional alkanolamines carbamate-forming behavior relative to $CO_2$, these typically incorporate (–$NH_2$) amine groups into the alkyl side chains of cations (*e.g.* imidazolium, pyrrolidinium), or add it to the anion (which would simultaneously bond chemically to the $CO_2$ to form a carbamate or bicarbonate


© 2026 The Author(s). Published by the Royal Society of Chemistry

Open Access Article. Published on 12 fevral 2026. Downloaded on 01.06.2026 11:06:26.
This article is licensed under a Creative Commons Attribution-NonCommercial 3.0 Unported Licence.

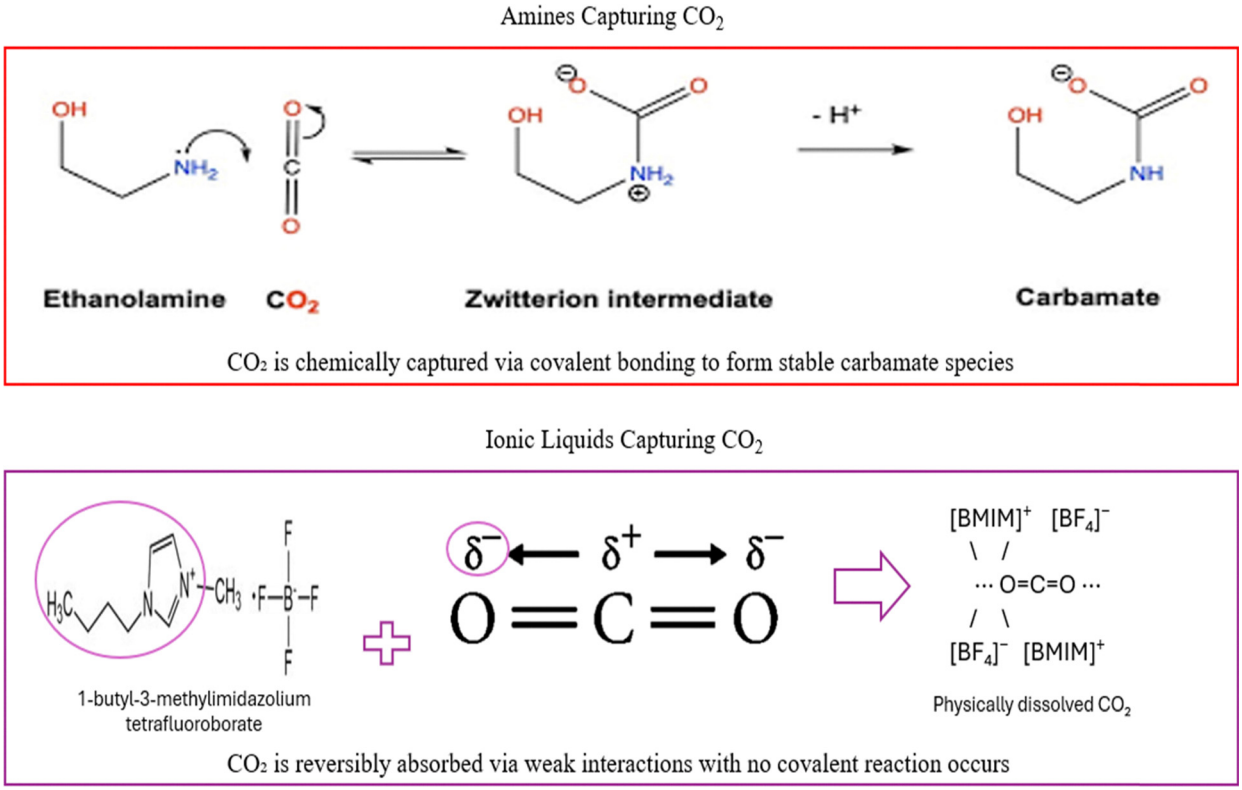


Fig. 59 ILs capturing mechanism in comparison with amines.

Table 17 Summary on the use of ILs in $CO_2$ capture

| ILs studied | Key findings | Ref. |
|---|---|---|
| [Bmim][$PF_6$] | High $CO_2$ solubility observed in [Bmim][$PF_6$]; at 40 °C and 93 bar, the IL phase contained a $CO_2$ mole fraction of 0.72 | 327 |
| General imidazolium-based ILs | $CO_2$ solubility increases with longer alkyl chains on the cation; solubilization is mainly physical | 328 |
| [Bmim][$PF_6$], [Bmim][$BF_4$] | weak Lewis acid–base interactions between $CO_2$ and IL anions, which enhance dissolution | 329 |
| Various imidazolium-based ILs | Combined experiments and simulations; concluded $CO_2$–anion interactions dominate solubility behavior | 330 |
| Various imidazolium-based ILs | Physical solubility in ILs depends on anion–$CO_2$ interactions | 331 |
| Conventional imidazolium-based ILs | Emphasized van der Waals forces and hydrogen bonding; solubility is governed by weak physical interactions, not covalent bonds | 332 |

species). In fact, according to the position of the reactive functional group, AFILs can also be classified based on:

• Cation-functionalized ILs, containing $NH_2$ or –OH groups that can react with $CO_2$ through nucleophilic attack (producing zwitterionic carbamates in a 1 : 2 $CO_2$ : IL ratio).[333,334]

• Anion-functionalized ILs, holding reactive functional groups (carboxylates, amino acids) that capture $CO_2$ through a stoichiometric path (1 : 1 equivalence) to create carbamic acids.[335,336]

• Dual-functionalized Ils combine both cationic and anionic functionalities to create multiple binding sites, thereby enhancing $CO_2$ absorption capacity (exceeding 2 mol $CO_2$ per mol IL), improving absorption kinetics, and offering greater operational flexibility.[337,338]

The nature of the functional groups, whether they are amino, carboxyl, phenolate, or nitrile, plays a role in defining the mechanism and overall efficiency of $CO_2$ capture. The functionalized group type can be tailored (Fig. 60).

Table 18 provides a comparison of several representative amino-functionalized ILs, as well as a summary of functional groups used, $CO_2$ capacities relative to non-functionalized analogues, and associated operation advantages and disadvantages.

As shown in (Table 18) and (Fig. 61), the introduction of pyrrolide, phenolate, and hydroxypyridine heterocyclics into the anion structure showcases selective tailoring of non-amino functionalized ILs (non-AFILs). These groups not only enhance $CO_2$ reactivity toward AFILs, but they also mitigate the viscosity issues that often arise from amino functionalization. Hydrophilic –$NH_2$ groups in AFILs tend to form hydrogen-bonded networks with anions, which dramatically increases viscosity and immobilizes mass transfer. Non-AFILs bypass this hydrodynamic issue with three basic design characteristics.

Open Access Article. Published on 12 fevral 2026. Downloaded on 01.06.2026 11:06:26.
This article is licensed under a Creative Commons Attribution-NonCommercial 3.0 Unported Licence.

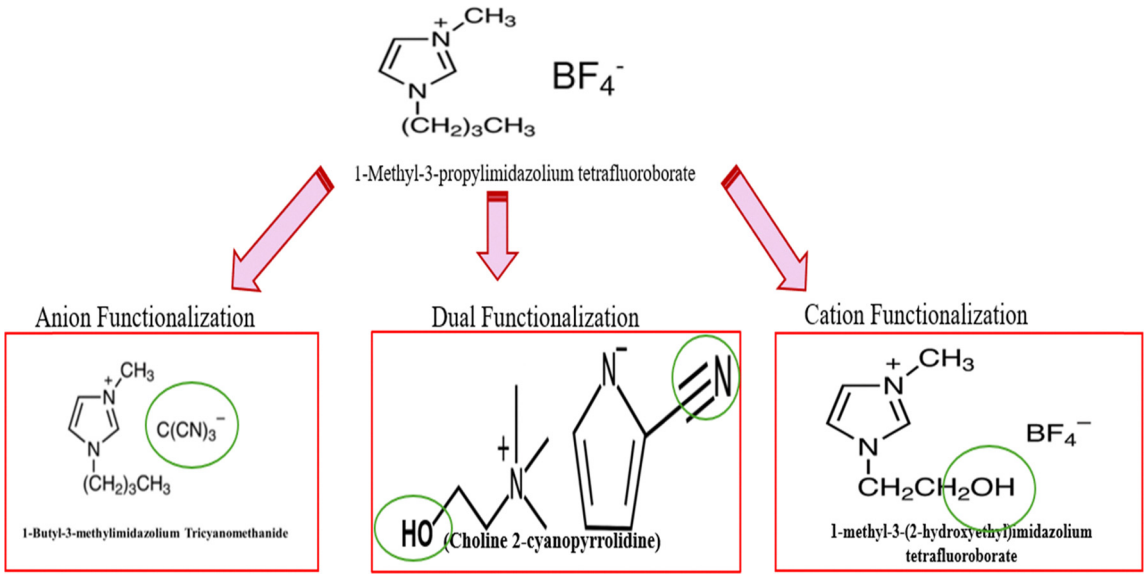


Fig. 60 ILs types (a) anion functionalized (b) dual functionalization C. Cation functionalization.

Firstly, the lack of amino groups means that no protonation or hydrogen bonding leads to viscosity surges. Secondly, cation/anion pairs like imidazolium/$[BF_4]^-$ and phosphonium/$[PF_6]^-$ have low electrostatic interaction.[343,344] Lastly, the presence of heterocyclic anions, which are poor hydrogen bond donors, enhances fluidity, completing.[345] These principles have empirically been shown to decrease viscosity relative to AFILs, enabling faster $CO_2$ mass transfer and improving performance in electrochemical applications.[346]

For instance, $[P_{66614}][2\text{-CNPyrr}]$ falls into the category of ILs that have somewhat moderate $CO_2$ capacities with limited change in viscosity. $[P_{66614}][PhO]$, on the other hand, is a phenolate based IL that has been shown to offer balance as a IL with moderate capacity (0.85 mol $CO_2$ per mol IL) and low viscosity (246.7 cP), while hydroxypyridine-based ILs such as $[P_{66614}][2\text{-Op}]$ achieve high capacities ($\sim$1.7 mol $CO_2$ per mol IL) but suffer from significant viscosity increases post-capture.[333]

Mechanistic and experimental evidence reveal that certain heterocyclic anions, for example, $[BF_4]^-$, act as hydrogen bond acceptors which are thought to stabilize both the ionic liquid network and the $CO_2$ adducts.[347] The use of some non-amino functionalized ionic liquids like phenolate-based $[P_{6614}][PhO]$ has been classified as having moderate layered $CO_2$ absorption ability (0.85 mol $CO_2$ per mol IL) and a reasonable viscosity (246.7 cP), which makes $CO_2$ capture more manageable when considering the fluid dynamics associated with high viscosity solvents. Regarding $[P_{6614}][PhO]$ a note of caution, it is unstable in some cases after it reacts with $CO_2$ which typically increases viscosity and the irreversibility of the adducts limits its practical usage, especially in humid conditions.[348,349] Lastly, it should be noted that the non-amino functionalized ILs with tunable chemistry are attractive features for the carbon capture opening frontier. As an example, $[P_{6614}]$-$[2\text{-CNPyrr}]$ has a $CO_2$ affinity that is concerned with the improvement of flow, $CO_2$ capture avoids a 1 : 1 irreversible rate of reaction with $CO_2$, and the viscosity did not change significantly after capture.[350–352]

## 2. Recent studies utilizing Ils in $CO_2$ electrochemical capturing and conversion

In integrated electrochemical carbon dioxide, Ionic Liquids can be used as electrolytes, electrolyte additives, or electrode modifiers, as shown in (Fig. 62).

**(A) Ionic liquids as electrolytes.** Ionic liquids (ILs) and particularly imidazolium-based ionic liquids have shown great potential as electrolytes for electrochemical carbon dioxide reduction ($CO_2ER$), ultimately by lowering activation barriers, increasing reaction kinetics, and improving product selectivity. These ILs lower overpotentials due to selective interactions between their cations ($[Emim]^+$, $[Bmim]^+$) and $CO_2$ while allowing for tunable outcomes that can include the generation of formate, CO, and carbonates simply through the modification of the IL's ionic components.

(Table 19) listed various ILs that have been reported in the literature, in addition to many examples in which faradaic efficiencies greater than 80% and energy consumption have been significantly lowered. For example, $[Emim][BF_4]$ has been used several times in conjunction with silver or copper electrodes, where it performed admirably due to its ability to stabilize *COOH intermediates and lower the overpotential needed for formate production.[353,354]

**(B) Ionic liquids as additives to electrolytes.** Based on work done with pure ionic liquid (IL) electrolytes, recent research approached ILs as a new additive to commonplace electrolytes to overcome the challenges of viscosity and diffusivity and cost (while retaining the added benefits of their inherent characteristics, particularly on improving $CO_2$ activation, stabilizing intermediates, and selectivity towards products). IL additives, used at low concentrations (normally 0.01 to 0.5 M) in aqueous


© 2026 The Author(s). Published by the Royal Society of Chemistry

Open Access Article. Published on 12 fevral 2026. Downloaded on 01.06.2026 11:06:26.
This article is licensed under a Creative Commons Attribution-NonCommercial 3.0 Unported Licence.

Table 18 A summary of the key characteristics of representative amino-functionalized ionic liquids

| IL example | Functionalization | Key functional group(s) | $CO_2$ absorption (*vs.* non-funct. IL) | Comparison IL | Advantages | Disadvantages | Other notes | Ref. |
|---|---|---|---|---|---|---|---|---|
| $[P_{66614}][AA]$ | Anion | $-NH_2$/–COOH (amino acid) | 1.6–2.0 mol $mol^{-1}$ (2.5–3.3× higher) | $[P_{66614}][DCA]$ (0.6 mol $mol^{-1}$) | Low viscosity | Water-sensitive; humidity effects | Carbamic acid stability is humidity-dependent | 339 |
| 1-(3-Aminopropyl)-3-butylimidazolium $BF_4$ | Cation | Primary amine ($-NH_2$) | ~0.5 mol $CO_2$/mol (much higher) | [hmim][$PF_6$] | High, reversible absorption; recyclable | High viscosity | Stable carbamate over cycles (IR/NMR confirmed) | 340 |
| [apbin][$BF_4$], *etc.*; dual-functionalized | Cation, Anion, Dual | Amino, Alkoxide, Carboxylate | Up to 2.6 mol $CO_2$ per mol (1–2× higher) | [Bmim][$BF_4$], [Bmim][$PF_6$] | High capacity; tunable properties | High viscosity; synthesis complexity | Forms carbamates, carbonates, or zwitterions | 333 |
| $[P_{66614}][2\text{-CNPyrr}]$ | Anion | Nitrile (–C≡N, AHA anion) | ~1.0 mol $mol^{-1}$ (2× *vs.* [Pro]) | $[P_{66614}][Pro]$ | Low viscosity, stable, fast kinetics | Slightly lower capacity than azolates | Zwitterionic product; minimal viscosity increase | 324 |
| $[N_2111][2\text{-CNpyr}]$, *etc.* | Cation + Anion | 2-Cyanopyrrolidine (AHA) | Much higher *via* ylide chemisorption | General RTIL/alkanolamine refs | High stability, strong chemisorption | High viscosity, cost, and complexity | Zwitterion framework, IR/thermodynamics supported | 326 |
| $[Bmim][B(CN)_4]$, *etc.* | Anion | Multiple nitrile (–CN) | Increases with more –CN | [Bmim][SCN] | Tunable high solubility, diffusivity | May increase viscosity | $CO_2$ solubility dictated by cation–anion binding | 326 |
| Amine-ILs (*e.g.*, [Apbim][$BF_4$]) | Cation | Amine ($-NH_2$/–NH–) | Up to 4× non-funct. | [Bmim][$BF_4$], [Bmim][$Tf_2N$] | High-low-P $CO_2$ capacity | Higher viscosity, regen. energy | Carbamate mechanism; good for low $P_{CO_2}$ | 333 |
| Ether-ILs ([$CH_3OCH_2$-mim]X) | Cation | Ether (–O–) | Improved (up to 0.9 mol $mol^{-1}$) | [emim][$BF_4$]/[$PF_6$] | Tunable, low volatility | Mainly physical, not chemical | Solubility boosted by the acetate anion | 341 |
| Nitrile-imidazolium ([NC-C3mim][$Tf_2N$]) | Cation | Nitrile (–CN) | Enhanced *vs.* alkyl ILs | Alkyl-imidazolium ILs | Good selectivity (separation) | Viscosity/stability may vary | Useful for post-combustion $CO_2$ | 341 and 342 |

or organic solvents, generate cooperative reactions that may enhance reaction kinetics and efficiency, with no obligation to scale. Some principal means for the improved aspect are:

- greater the solubility and mobility of $CO_2$ (*e.g.*, [Emim][$BF_4$] is a 3× increase *versus* water)
- reaction of ''electroactive'' monolayers of cations at the interface $[Emim]^+$ ($334 \times 10^{-3}$ M), reducing activation energy
- transfer of protons will be influenced by anions like $[TFO]^-$ chosen to suppress $H_2$ evolution
- selectivity will be influenced by the functionalization of ions necessary to get products such as CO or formate.

There are some critical merits to using this strategy rather than pure IL systems (as seen in Table 20): very low viscosity ($\leq$5 cP as compared to 50–500 cP), good economic performance ($\leq$20% IL weight %), optimized $H^+$ conductivity, and suitability for industrial applications. Both Neubauer *et al.* and Yuan *et al.* demonstrated a peak in efficiency depending upon concentration (0.01–0.5 M), with both systems favoring formate and MeCN improved CO selectivity. Functionalized cations such as $[Emim]^+$ completely dominate because OH–$CO_2$ (binding energy of −0.36 eV), and flow reactors were used for 10+ hours at (83%+ efficiency). This method has been proven to resolve viscosity/cost problems, but the key challenges still exist (*i.e.* all of the other effects with regard to deliquescent interactions of co-additives/solvents; long-term stability; and the optimal triads of screening). Therefore, future work should focus on obtaining *operando* interface measurements using machine learning with suitable IL. Consequently, hybrid systems still hold the greatest industrial promise for electrocatalytic carbon capture.[366–368]

**(C) Ionic liquid as electrode modifier.** Transitioning from bulk electrolytes and additives, ionic liquids (ILs) deployed as electrode surface modifiers offer a transformative strategy that overcomes viscosity, conductivity, and cost constraints while enabling precise interfacial engineering. By immobilizing ILs directly onto electrode surfaces (*e.g.*, *via* covalent tethering or self-assembled monolayers), this approach creates a tailored microenvironment that enhances $CO_2$ adsorption, stabilizes critical intermediates (*CO, *COOH, *OCCO), and suppresses competing hydrogen evolution, all without requiring high-volume IL usage. Key mechanisms include:

- Microenvironment tuning: ILs generate structured interfacial layers, aligning and optimizing local charge distribution and reaction pathways, increasing selectivity[369]
- Intermediate stabilization: noncovalent interactions (*e.g.* binding of $CO_2$ to imidazolium) decrease the energy barriers for *COOH formation by 0.3–0.5 eV.[330]
- Chain length optimization: moderate length (*e.g.*, $[Bmim^+]C_4$) *N*-alkyl chains maximize the surface interaction by balancing increasing thickness with accessibility; longer chains ($>C_8$) significantly decreased efficiency and accessibility to the site[330]
- Pathway steering: functionalized ILs direct products toward specific outputs (*e.g.* $C_2H_4$ or methanol) by influencing electron/proton transfer[370]

As summarized in (Table 21), this strategy offers several notable performance improvements:

Open Access Article. Published on 12 fevral 2026. Downloaded on 01.06.2026 11:06:26.
This article is licensed under a Creative Commons Attribution-NonCommercial 3.0 Unported Licence.

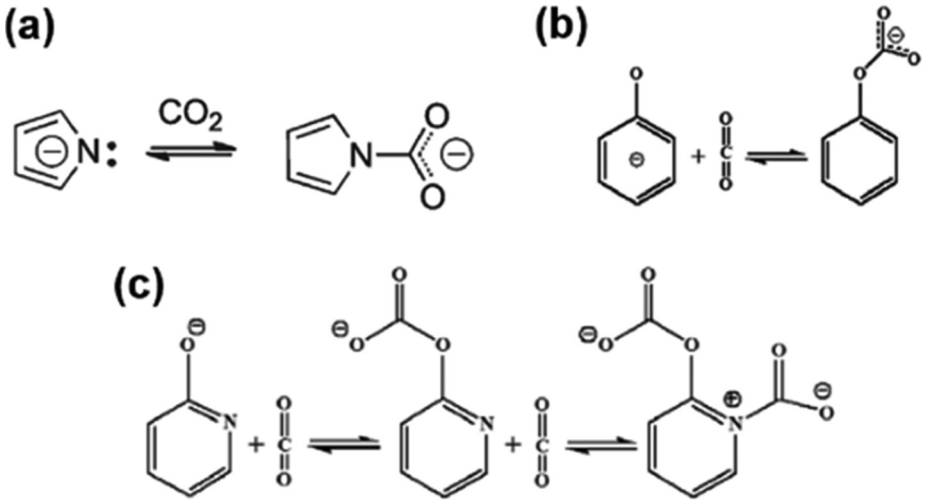


Fig. 61 Illustration of chemical absorption mechanisms of carbon dioxide by different organic anions: pyrrolide, phenolate, and hydroxypyridine.

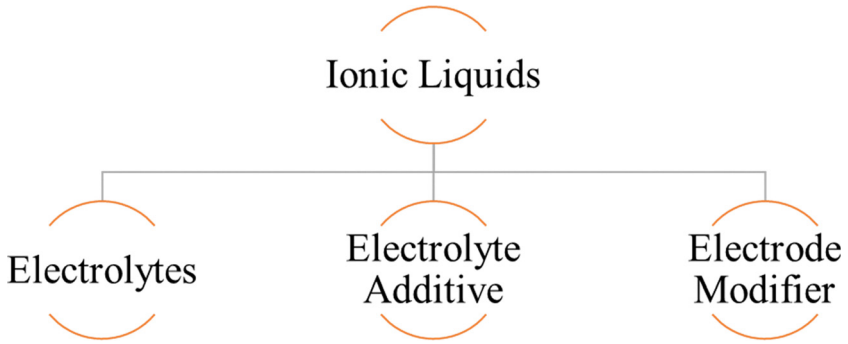


Fig. 62 The three primary roles of Ionic Liquids in integrated carbon capture and electrochemical conversion: electrolytes, electrolyte additives, or electrode modifiers.

• CO selectivity: hydrophobic imidazolium ILs toward Ag foam surface increased the production rate of CO from $CO_2$RR

• $C_2$ efficiency: [Bmim][$NO_3$] on Cu lowers the energy barrier for *CO dimerization, giving greater $C_2H_4$ yield

• Low energy conversion: phosphonium-ILs toward Au support formate/methanol at record low overpotentials

• Hydrogen evolution reaction (HER) suppression: polymerized ILs on graphene gave $>$ 40% suppression of $H_2$ evolution while increasing efficiency for formate production

From the above table, although IL-modifiers address the volumetric barriers associated with ILs, they still have:

• Stability: capacity to retain IL longevity under high-current operation.

• Synthesis: covalent grafting is still a multi-step functionalization process.

• Structure–activity trade-offs: alkyl chain length must be balanced based on accessibility *vs.* strength of interaction factors.

Ionic liquid (IL) surface modifiers have multiple distinct advantages relative to the bulk and additive options. In terms of relative IL consumption, bulk IL electrolytes require significant IL amounts (100% consumption) while IL additives require moderate amounts (typically in the range of 5–20%), whereas surface modifiers only need to use modest quantities due to the monolayer-level deployment. In terms of viscosity, bulk ILs increase the viscosity significantly (by 50, 500 cP), with the viscosity increase of IL additives being moderate (viscosity increase of 2–10 cP), and negligible from surface modifiers.[377]

Dongare *et al.* have recently investigated the bifunctional ionic liquid (IL) 1-ethyl-3-methylimidazolium 2-cyanopyrrolide ([Emim][2-CNpyr]) dissolved in acetonitrile as a multifunctional electrolyte for integrated $CO_2$ capture and conversion (Fig. 63a).[378] This IL has a dual role by its capability for $CO_2$ adsorption and electrochemical activity, which lets it selectively reduce CO on silver electrodes. The system exhibited elevated CO selectivity ($>$94%) with consistent performance over 12 hours. The addition of 0.1 M [Emim][2-CNpyr] resulted in a positive shift of the $CO_2$ reduction onset potential by 240 mV, indicating a substantial reduction in energy input relative to benchmark electrolytes (Fig. 63b and c). The $CO_2$ capture mechanism is shown through the synergetic effect of imidazolium cation ($[Emim]^+$) and the 2-cyanopyrrolide anion ($[2\text{-CNpyr}]^-$). The anion binds $CO_2$ by attacking it with a nucleophile, which makes carbamate-like adducts. The protonated anion can produce a carbene


© 2026 The Author(s). Published by the Royal Society of Chemistry

Open Access Article. Published on 12 fevral 2026. Downloaded on 01.06.2026 11:06:26.
This article is licensed under a Creative Commons Attribution-NonCommercial 3.0 Unported Licence.



Table 19 A summary of ILs as electrolytes in the integrated carbon capture and electrochemical conversion

| Electrode/ catalyst | Ionic liquid electrolyte | Functionalized? | Product | Faradaic efficiency | Enhancement | Comparison/other electrolytes | Disadvantages | Ref. |
|---|---|---|---|---|---|---|---|---|
| Ag electrode | [Emim][$BF_4$] | No | Formate | >96% | Overpotential <0.2 V; activation energy reduction | Aqueous electrolytes | Not specified | 355 |
| Carbon nanofibers | [Bmim][$BF_4$] | No | Formate | Not specified | Overpotential reduced to 0.17 V; $CO_2$ complexation | Not specified | Not specified | 356 |
| Not specified | [Bmim][$NTf_2$] | No | Formate/ carbonate | Not specified | Optimal cation-dependent onset potential | Other ILs | Excess IL disrupts proton flux | 357 |
| Not specified | [Emim][$BF_4$] | No | Formate | Not specified | $CO_2$ pre-activation (binding: −0.36 eV) | Water (binding: −0.11 eV) | Not specified | 358 |
| Not specified | [Bmim][$BF_4$] | No | Formate | Not specified | [Bmim-COOH] intermediate stabilization | Not specified | Not specified | 359 |
| Not specified | [Emim][$BF_4$] | No | Formate | Not specified | [Emim-COOH] pathway *via* DFT; monolayer formation | Not specified | Not specified | 360 |
| Large electrode (495 $cm^2$) | IL-based ($[BF_4]^-$) | No | Formate | 83.90% | Stable selectivity for 10+ hours | Not specified | Not specified | 361 |
| Not specified | [Emim][TFO] | Cation-functionalized | CO | ~80% | Monolayer formation; minimal IL usage | Acid electrolytes | High viscosity at scale | 362 |
| Porous dendritic Cu | [Emim][$BF_4$] | Cation-functionalized | Formate | ~75% | $CO_2$ activation; H-atom redirection | Aqueous electrolytes | Concentration sensitivity | 363 |
| Not specified | [Bmim][$PF_6$], [DBU-H][$PF_6$] | Dual-functionalized | CO/formate | CO ~70%, formate ~60% | Anion-dependent selectivity: $[PF_6]^-$ promotes CO/formate | MeCN solvent | Cost-intensive synthesis | 364 |
| Not specified | [Emim][$BF_4$] | Cation-functionalized | Not specified | Not specified | *COOH stabilization *via* non-covalent interactions | Molecular dynamics simulations | High IL concentrations reduce activity | 365 |
| Large-scale flow cell | Various ILs | Various | CO | 83.90% | Optimized flow rate; stable long-term operation | Water-based | Scalability challenges | 361 |

Table 20 A summary of ILs as additives to electrolytes in the integrated carbon capture and electrochemical conversion

| IL used | Cation | Anion | Electrolyte system | Main product | FE | Solvent | IL type | Key findings | Ref. |
|---|---|---|---|---|---|---|---|---|---|
| [Emim][TFO] | Ethyl-methylimidazolium | Trifluoromethane-sulfonate | Water-based | CO | ~80% | Water | Cation-functionalized | Optimal IL concentration (0.334 M) forms monolayers, boosting efficiency with minimal IL usage | 362 |
| [Emim][$BF_4$] | Ethyl-methylimidazolium | Tetrafluoroborate | Water-based | Formate | ~75% | Water | Cation-functionalized | Activates $CO_2$ and redirects H atoms, enhancing formate on porous Cu electrodes | 363 |
| [Bmim][$PF_6$] | Butyl-methylimidazolium | Hexafluorophosphate | MeCN-based | CO | ~70% | Acetonitrile | Non-amine | Promotes CO; [DBU-H][$PF_6$] favors formate, demonstrating IL-driven selectivity | 364 |
| [Emim][$BF_4$] | Ethyl-methylimidazolium | Tetrafluoroborate | Simulations | — | — | — | Cation-functionalized | Stabilizes *COOH intermediates *via* non-covalent interactions, reducing energy barriers | 365 |
| [Emim][$BF_4$] | Ethyl-methylimidazolium | Tetrafluoroborate | Molecular dynamics | — | — | — | Cation-functionalized | High IL concentrations disrupt proton transfer, degrading catalytic activity | 365 |
| Various ILs | Various | Various | Water-based flow cell | CO | 83.90% | Water | Various | Optimized flow rate + IL additives achieve 83.9% CO efficiency with long-term stability | 361 |

© 2026 The Author(s). Published by the Royal Society of Chemistry

Open Access Article. Published on 12 fevral 2026. Downloaded on 01.06.2026 11:06:26.
This article is licensed under a Creative Commons Attribution-NonCommercial 3.0 Unported Licence.

Table 21 A summary of ILs as additives to electrolytes in the integrated carbon capture and electrochemical conversion

| IL Used | Electrode material | Main product | Key findings | Ref. |
|---|---|---|---|---|
| Hydrophobic imidazolium ILs | Ag foam | CO | Enhanced CO selectivity/production; alkyl chain length dictates surface accessibility | 371 |
| [Bmim][$NO_3$] | Cu | $C_2H_4$ | Reduced *CO → *OCCO barrier; boosted $C_2H_4$ efficiency | 372 |
| Phosphonium-IL + imidazole | Au | Formate/methanol | Formate/methanol synthesis at low potentials; intermediate stabilization | 373 |
| Imidazolium SAMs | Au | Ethylene glycol | High activity at low overpotentials; enabled ethylene glycol production | 374 |
| Polymerized IL (PIL) | Graphene | HCOOH | Suppressed HER by >40%; enhanced formate formation | 375 |
| Imidazole-based ILs | Au(111) | Not specified | Vertical $CO_2$ adsorption mode; improved activation energy | 376 |

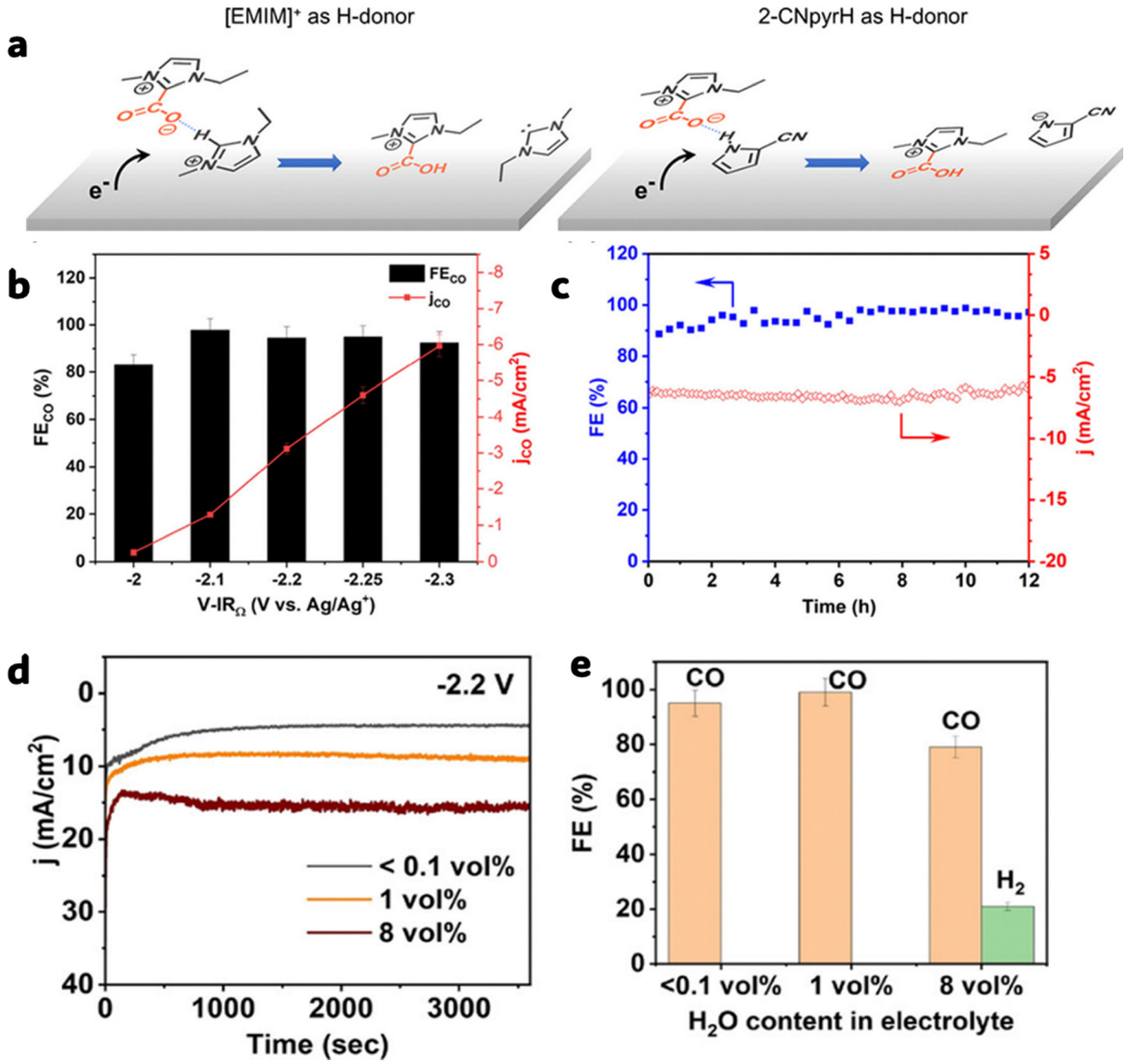


Fig. 63 (a) Illustration of the possible interactions on the electrode surface. (b) Faradaic efficiency (FECO) and partial current density of CO ($j_{CO}$) at different potentials during $CO_2$RR over Ag with 0.1 M [Emim][2-CNpyr] in the supporting electrolyte. (c) FE (filled blue squares) for CO production and total current density (red hollow diamonds) during 12 h of continuous $CO_2$RR with 0.1 M [Emim][2-CNpyr] in the supporting electrolyte on the Ag electrode at −2.2 V *vs.* Ag/$Ag^+$. (d) Faradaic efficiencies measured from chronoamperometry shown in. and (e), Gaseous product composition was determined by GC. Reprinted (adapted) from *ACS Catal.* 2023, **13**(12), 7812–7821. Copyright © 2023, The Authors. Published by American Chemical Society under the terms of CC-BY-NC-ND 4.0 license.

intermediate that interacts with $CO_2$ in an additional step. At the same time, the cation accumulates at the electrode interface, which helps stabilize $CO_2$ adsorbed there and accelerates electron transfer. *Operando* Spectro-electrochemical methods (SERS and EPR) validated the generation of IL–$CO_2$ adducts, surface-bound CO intermediates, and radical species, hence corroborating the


© 2026 The Author(s). Published by the Royal Society of Chemistry

Open Access Article. Published on 12 fevral 2026. Downloaded on 01.06.2026 11:06:26.
This article is licensed under a Creative Commons Attribution-NonCommercial 3.0 Unported Licence.

suggested cooperative mechanism. One of the most interesting factors that affects the selectivity is the water content. By adding up to 1 vol% water, the FE of CO increases up to 98%, while adding too much water makes hydrogen evolution more likely. This tunability underscores the importance of the solvent environment in guiding reaction paths (Fig. 63d and e).

### 3. Future work

Ionic liquids (ILs) are advantageous for $CO_2$ capture and $CO_2$ER due to their high $CO_2$ solubility, tunable structures, and electrochemical stability. Future directions of research should focus on improving the capacity of ILs to absorb $CO_2$, decreasing viscosity through optimizing IL-$CO_2$ interactions, and using supported ILs or hybrid materials such as SIL-coated membranes for enhanced performance. For $CO_2$ER, it will be critical to minimize IL dosage while maintaining catalytic efficacy with particular focus on understanding IL-$CO_2$ complexation, electric double layer structures, and co-catalytic effects. Future work should focus on *in situ* IL-regeneration methods for IO and on investigating machine-learning-optimized IL and electrode combinations. Hybrid architectures (*e.g.*, PIL-coat gas-diffusion electrodes) present an exciting avenue to scale $C_2^+$ production.

Supported ionic liquids (SILs) contribute an additional layer of functionality to IL-modifiers and have the potential to be a scalable and practical approach to eliminating economic and mass-transfer limitations associated with bulk ILs for $CO_2$ capture. SILs also consist of ionic liquids immobilized within porous solids, which is a particularly advantageous sub-approach, where high-surface-area solids such as MCM-41 or $Al_2O_3$ as wise support materials, ILs are capable of significantly higher gas–liquid contact while being able to also significantly decrease the volume of ILs needed to achieve the same level of mass-transport, often by +50% volume depending on the complex! This approach is compelling; SILs delivered a 2–3 times improvement in $CO_2$ with absorption rates compared to neat ILs with extended cyclic stability and retained tunable selectivity with target gases. These characteristics make SILs a desirable platform for the industrial-scale carbon capture and integrated conversion approaches.

The improved performance of SILs is due to multiple synergistic processes. The porous supports physically control IL distribution, specifically anchoring the anions (primarily on $Al_2O_3$ surfaces), which enhances $CO_2$ adsorption by reducing desorption losses. Materials such as MCM-41 greatly expedite mass transfer by exposing a larger interfacial area where both the gas and liquid can interact, more than doubling the $CO_2$ diffusion rate compared with unsupported ILs. At the optimum IL loadings, around 5 wt%, the supports allow the efficient uptake of $CO_2$ by avoiding pore blockage without filling the pores completely and still allowing a favorable economic and operational conditions. Moreover, advances in poly(ionic liquid) (PIL) networks, such as P[[VBTMA][$PF_6$]], have demonstrated even greater performance improvements, as high as 77% $CO_2$ uptake by weight and $CO_2/N_2$ selectivity of 70 : 1, and consistency with no degradation over 100 absorption–desorption cycles.[379,380]

As summarized in (Table 22), recent studies have explored a range of IL-support configurations and functionalizations, revealing important design considerations for future development.

### 4. Challenges and economic analysis

Although ionic liquids (ILs) have notable properties for $CO_2$ capture and conversion (*e.g.*, high ionic conductivity, thermal stability, and tunable structures), their challenges remain significant limiting factors for industrial application and large-scale deployment. ILs are often synthesized through energy-intensive processes that use costly raw materials (*e.g.*, fluorinated anions) and environmentally toxic reagents, creating barriers to scale. It is also essential to consider that concerns over toxicity (such as imidazolium persistence) are compounded by severe transport limitations inherent to the solvent matrix. Unlike aqueous electrolytes, ionic liquids are characterized by high viscosity, typically ranging from 50 to 400 cP at room temperature (*e.g.*, ~300 cP for [Bmim][$PF_6$]), which is two orders of magnitude higher than that of water (~0.89 cP).[321] This high viscosity suppresses mass transfer, restricting the diffusion coefficient of $CO_2$ ($D_{CO_2}$) to approximately 1–8 × $10^{-6}$ $cm^2$ $s^{-1}$, compared to ~2 × $10^{-5}$ $cm^2$ $s^{-1}$ in aqueous media.[330] Furthermore, despite being composed entirely of ions, the ionic conductivity of common ILs is relatively low (~1–10 mS $cm^{-1}$) compared to standard alkaline electrolytes (*e.g.*, >200 mS $cm^{-1}$), leading to significant ohmic losses during electrolysis.[324] Consequently, without the use of elevated temperatures or gas-diffusion electrodes, IL-based systems are often limited to partial current densities below 10–20 mA $cm^{-2}$, significantly lower than industrial benchmarks (Table 23).

These limitations necessitate a transition towards simpler structures or hybrid systems for electrochemical capture and conversion. Despite these physical hurdles, ionic liquids (ILs) still offer potential economic advantages as electrolytes for $CO_2$ electrochemical reduction ($CO_2$R), especially for producing carbon monoxide, which remains the only economically viable carbon C1 product pathway when appropriately optimized. TEAs indicate that CO-production, at a rate of 100 tons/day, reaches a net present value (NPV) of $13.5 million, and the production of formic acid (HCOOH) reaches $39.4 million. The cost of electricity can highly influence the profitability of these products, with a variation of $0.01 per kWh changing the NPV

Table 22 A summary of recent studies on various ionic liquid (IL)-support configurations and functionalizations for future material development

| Research focus | Key findings | Ref. |
|---|---|---|
| Amino-ILs on MCM-41/$Al_2O_3$ | $Al_2O_3$ enhances $CO_2$ adsorption *via* anion anchoring; charge-dependent IL distribution | 381 |
| [$P_{66614}$][2-Op] on MCM-41 | $CO_2$ absorption rate 2× higher than pure Ils | 325 |
| Organic solvents on MCM-41 | Weaker solvent-support interactions increase $CO_2$ absorption synergistically | 382 |
| Poly(IL) P[[VBTMA][PF6]] | 77% $CO_2$ uptake (wt); 70 : 1 $CO_2/N_2$ selectivity; 100-cycle stability | 383 |

Open Access Article. Published on 12 fevral 2026. Downloaded on 01.06.2026 11:06:26.
This article is licensed under a Creative Commons Attribution-NonCommercial 3.0 Unported Licence.

Table 23 Key physical properties of ionic liquids (ILs) compared to aqueous electrolytes relevant for $CO_2$ electrochemical conversion

| Property | Ionic liquids (ILs) | Aqueous electrolytes |
|---|---|---|
| Viscosity (cP) | 50–400 (*e.g.*, ~300 for [Bmim][$PF_6$]) | ~0.89 |
| $CO_2$ diffusion coefficient ($D_{CO_2}$, $cm^2\ s^{-1}$) | ~1–8 × $10^{-6}$ | ~2 × $10^{-5}$ |
| Ionic conductivity (mS $cm^{-1}$) | ~1–10 | >200 |
| Partial current density (mA $cm^{-2}$) | 10–20[a] | >100 |

[a] Measured under standard conditions without elevated temperature or gas-diffusion electrodes; aqueous electrolytes achieve higher current densities due to lower viscosity, faster $CO_2$ diffusion, and higher ionic conductivity.

by ~$40 million for higher value products like *n*-propanol. CO could be economically viable, even at low faradaic efficiencies (<50%), as long as the overpotential does not exceed ~0.4 V. In comparison, for methanol it would require efficiencies greater than 60% and for ethanol, something greater than 90%. For products identified as C1 other (*e.g.*, $CH_4$, syngas), TPC currently exceeds the market prices (*e.g.*, 4.09 € per kg for $CH_4$, market price is 0.18–0.35 € per kg). Scalability in the future must reduce IL synthesis costs, minimize energy-intensive processes, particularly the energy required for the synthesis of fluorinated anions, and improve lifetime stability to reduce high capital expenses.[368,383–388]

## Deep eutectic solvents (DESs)

Deep eutectic solvents (DESs) are a new class of tunable solvating media consisting of a hydrogen-bonding solvent, formed by a hydrogen bond donor (HBD) and a hydrogen bond acceptor (HBA), which forms a eutectic mixture that exhibits a melting point well below that of either individual component. The term "eutectic" is derived from the Greek term that means "easily melted," which designates the unique temperature at which both components crystallize together from the molten liquid; and usually consist of innocuous, bio-based components, such as choline chloride (HBA) and urea, glycerol, or organic acids (HBDs). DESs have been formed by mixing components at mild thermal conditions, typically without cumbersome purification and hazardous reagents[389] as shown in (Fig. 64).

The easy preparation of DESs is in stark contrast to the often energy-intensive, expensive synthesis of ionic liquids (ILs), making them a more eco-efficient and technologically and commercially valuable solvent. DESs represent the next-generation solution to the limitations of ILs, as shown in (Fig. 65):

- Simplified synthesis: combining low-cost hydrogen bond acceptors (HBAs; *e.g.*, choline chloride) and donors (HBDs; *e.g.*, urea) at mild temperatures, avoiding complex purification.[390]
- Eco-efficiency: bio-sourced components (*e.g.*, organic acids) enable biodegradable, non-toxic formulations with minimal environmental impact.
- Cost reduction: raw materials are 10–50× cheaper than ILs, with 80% lower synthesis energy demands.

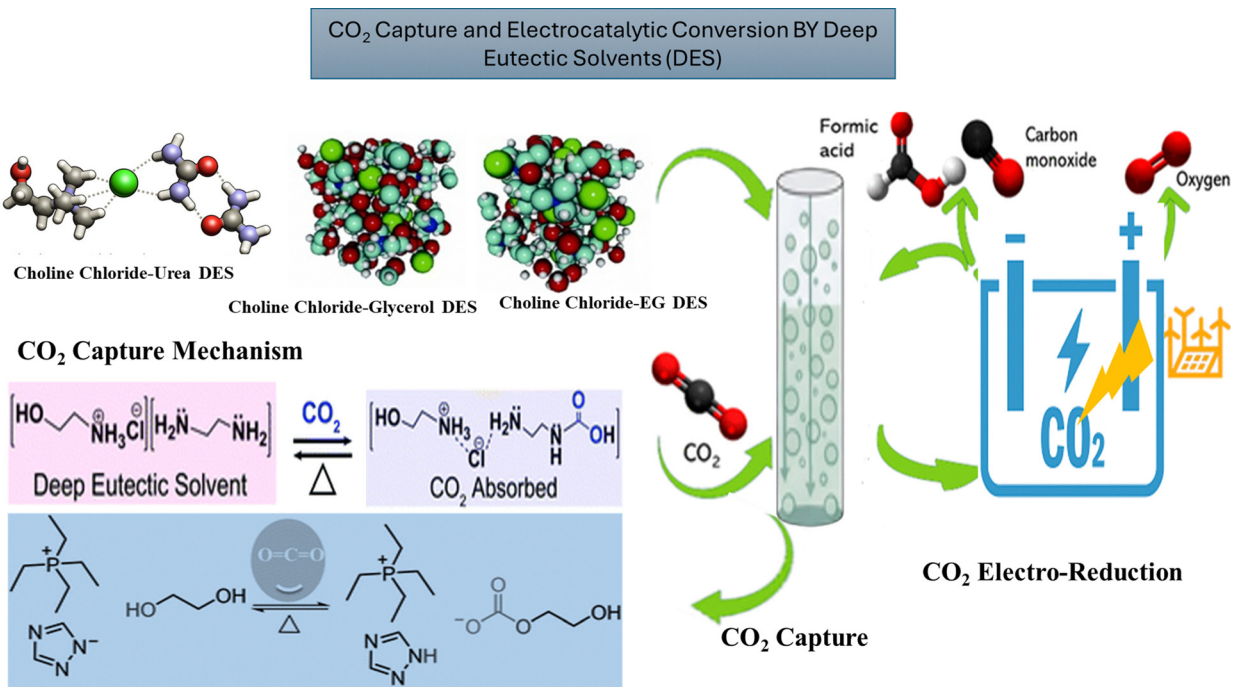


Fig. 64 Detailed schematic of integrated $CO_2$ capture and electrocatalytic conversion using choline chloride – deep eutectic solvents (DESs) in a synergistic ICCC process.


© 2026 The Author(s). Published by the Royal Society of Chemistry

Open Access Article. Published on 12 fevral 2026. Downloaded on 01.06.2026 11:06:26.
This article is licensed under a Creative Commons Attribution-NonCommercial 3.0 Unported Licence.

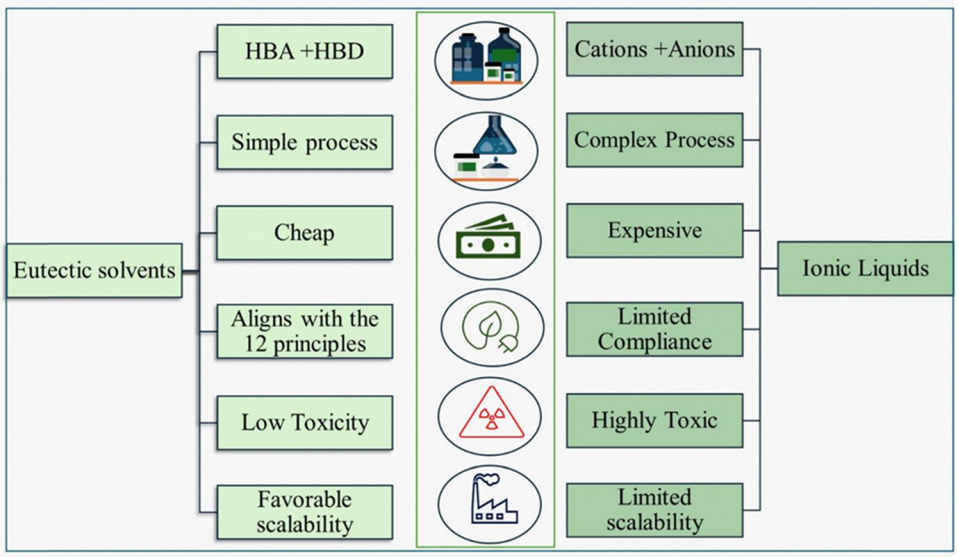


Fig. 65 A comparative analysis of eutectic solvents and ionic liquids.

• Performance parity: DESs match ILs in $CO_2$ solubility (*e.g.*, choline chloride/urea: 0.6 mol $CO_2$ per kg) while enhancing mass transfer *via* lower viscosity (200–500 cP *vs.* 500–1000 cP for ILs).[391,392]

### 1. Deep eutectic solvents: DESs mechanism

The first-generation Eutectic Solvents were produced from Hydrogen Bond donors with a quaternary ammonium. DESs are an adaptable class of green solvents synthesized from the complexation of a hydrogen bond acceptor (HBA), which is most often a quaternary ammonium salt like choline chloride, with a hydrogen bond donor (HBD), which could be urea, ethylene glycol, glycerol, or many organic acids, most often in a defined molar ratio. This interaction establishes an extensive hydrogen-bonding network and a significant lowering of the melting temperature of the resulting mixture when compared to the original components.

Typically, DESs follow a general formula $Cat^+X^-zY$, where $Cat^+$ is a cation (commonly ammonium, phosphonium, or sulfonium), $X^-$ is of course a Lewis base (most commonly a halide), and Y is a Lewis or Brønsted acid (associated with a donor). Depending on the exact donor and acceptor within each DES, they can be subdivided into four categories, each providing different physicochemical properties and applications. The versatility of DESs is due to the fact that there can be a substantial number of HBA's and HBD's that can be combined in a DES, and the ability to carefully control attributes of the DES, including its viscosity, polarity, ionic conductivity, and basicity,[393,394] and the following (Table 24) shows four different DES systems used in the literature.[395–397]

(Table 25) presents key quantitative and qualitative properties of representative DES systems, with a focus on Type III (the most common), and notes on electrochemical activity types.

Mechanistically, DESs interact with $CO_2$ through both physical and chemical interactions. The key role in the overall reaction mechanism is explained by the structuring of the functional groups found in the constituent components of the DES. So, while physical absorption is happening through physical interactions (dipole-quadrupole interactions or van der Waals interactions) that occur with $CO_2$ molecules and the DES matrix, the availability of other properties that can influence the DES (viscosity, polarity, and density) will affect the extent to which $CO_2$ can be absorbed. While the primary focus is the use of DES as electrolyte for capturing and conversion, some other research used the DES in electrodeposition Bohlen *et al.*[404] performed the electrodeposition of indium from 1 : 2 M choline based DES (ChCl : EG–1 : 2), employed them as an electrocatalyst for the electrochemical reduction of $CO_2$ to formate.[405]

(Table 26) demonstrates the way several deep eutectic solvents (DESs) utilize both chemical and physical mechanisms in relation to $CO_2$ capture, with their effectiveness determined by a complex balance of inherent molecular properties and environmental influences. Factors such as viscosity can be critical

Table 24 A summary of the four different DES systems

| Components | Type | Example components | Notes |
|---|---|---|---|
| Quaternary ammonium salt + metal chloride | Type I | Choline chloride + $ZnCl_2$ | Early studied DESs, often used in electrochemistry |
| Quaternary ammonium salt + metal chloride hydrate | Type II | Choline chloride + $CrCl_3{\cdot}6H_2O$ | Like Type I but with hydrated metal salts |
| Quaternary ammonium salt + hydrogen bond donor | Type III | Choline chloride + urea, glycerol, acids | Most common; includes classic DESs and many NADES |
| Metal chloride hydrate + hydrogen bond donor | Type IV | $ZnCl_2{\cdot}6H_2O$ + urea | Metal-based, used for specific applications |

Open Access Article. Published on 12 fevral 2026. Downloaded on 01.06.2026 11:06:26.
This article is licensed under a Creative Commons Attribution-NonCommercial 3.0 Unported Licence.

Table 25 A quantitative and qualitative analysis of the different DES systems

| Formation/ components | Type | HBA/HBD | Meltin point (°C) | Viscosity (mPa s, 25 °C) | Conductivity (mS $cm^{-1}$, 25 °C) | $CO_2$ interaction mechanism | Electrochemical suitability/ activity type |
|---|---|---|---|---|---|---|---|
| Choline chloride + $ZnCl_2$ | I | ChCl/$ZnCl_2$ | ~20[398] | ~750[399] | 1.0–2.0[400] | Limited, depends on metal salt[401] | (Electroplating, batteries)[401] |
| Choline chloride + $CrCl_3 \cdot 6H_2O$ | II | ChCl/$CrCl_3 \cdot 6H_2O$ | ~25[398] | ~800[399] | 0.8–1.5[400] | Limited, hydration effect[401] | (Electroplating, batteries)[401] |
| Choline chloride + urea (1 : 2) | III | ChCl/Urea | 12[398] | 750[399] | 1.2–1.6[399] | Strong H-bonding; van der Waals; interaction energy with $CO_2$: −10.65 kcal $mol^{-1}$,[401] | (Wide electrochemical window, electrocatalysis, batteries)[401] |
| Choline chloride + glycerol (1 : 2) | III | ChCl/Glycerol | −40 to −30[402] | 324[399] | 1.1–1.5[399] | H-bonding, moderate $CO_2$ affinity[403] | (Flow batteries, electrocatalysis)[401] |
| Choline chloride + ethylene glycol (1 : 2) | III | ChCl/EG | −66[401] | 35[399] | 2.0–3.0[399] | H-bonding, moderate $CO_2$ affinity[403] | (Electrocatalysis, sensors)[401] |
| $ZnCl_2 \cdot 6H_2O$ + urea | IV | $ZnCl_2 \cdot 6H_2O$/ urea | ~30[398] | ~900[399] | 0.9–1.3[400] | Partial, less studied[401] | (Metal recovery, catalysis)[401] |

since lower viscosity allows for greater gas diffusion and $CO_2$ solubility, while high viscosity can prevent mass transfer.[406–408] Adjustment of the molar ratio of hydrogen bond donors (HBD) and hydrogen bond acceptors (HBA) may mitigate this source of viscosity limitation.[409,410] Generally, increasing HBD content reduces viscosity and increases $CO_2$ uptake. Addition of co-solvents, including water or alcohols, for example, expands the range of operational conditions, while reducing viscosity and assisting with gas transport, but they also add to the risks of compromising the chemical reactivity of the DES solvent.[411,412] The presence of specific functional groups in the molecular structure of component one and two strongly influence the capture mechanism; amines will chemically bond $CO_2$ *via* the formation of carbamate, hydroxy groups can enhance bicarbonate creation, and basic anionic groups like acetate facilitate acid–base interactions.[370,407,413,414]

The polarity of DES solvents also contributes to solubility and overall absorption strength; higher polarity generally favors physical absorption, while stronger basicity promotes stronger chemical binding. The hydrogen bonding network present in the DES solvents also facilitates stabilization of $CO_2$-derived interaction intermediates, improving both capacity and selectivity.[415,416] Environmental conditions such as moderate temperatures optimize the balance between absorption and desorption, while increased pressure typically enhances $CO_2$ solubility, particularly in DESs that rely more on physical absorption.[417,418] Finally, hydrophobicity and density impact both the solvent's regeneration efficiency and its thermal stability. Together, these factors underscore the tunability of DESs and their promising potential for efficient and selective $CO_2$ capture.[419,420]

## 2. DES in carbon capture and electrochemical conversion

DES have become a recognized class of sustainable solvents for integrated $CO_2$ capture and electrochemical conversion, with unique properties that enable high $CO_2$ solubility and tunable physicochemical properties, as well as broad electrochemical stability. DESs are formed by a complexation of a hydrogen bond acceptor (HBA; *e.g.*, choline chloride) with a hydrogen bond donor (HBD; *e.g.*, urea, ethylene glycol, or proline), which generates an extensive hydrogen-bonding matrix. With complexation, melting points decrease substantially (for example, ChCl:urea has a melting point of over 300 °C, and when complexed, its melting temperature drops to ~12 °C). The fluidity and chemical reactivity exhibited by the DES enhances gas ($CO_2$) diffusion, with increased interaction from $CO_2$ molecules both through physical absorption and chemical binding (*i.e.*, carbamate or bicarbonate formation), directly dependent on the state of the DES (*i.e.*, higher interacting environment when functionalized with amines, hydroxyls, and carboxylic acids). Furthermore, the extensive hydrogen-bonding framework affords stabilization of important reaction intermediates, which yield a better selectivity and lower energy barrier of the electrochemical $CO_2$ reduction ($ECO_2R$) pathways. DESs also have a wide electrochemical window, often exhibiting >3 V, which support multi-electron $CO_2$ conversion reactions at cathodic potentials (*e.g.*, −1.9 V *vs.* SHE) without solvent degradation. The modular nature of DESs permits fine-tuning of viscosity, conductivity, and polarity, thus optimizing mass transfer and charge transfer during electrolysis. The low-cost, biodegradable ingredients used to produce DESs, for example, choline chloride produced from vitamin B4, make DESs cost-effective and environmentally friendly options compared to ionic liquids and traditional electrolytes. DESs offer the functionality of both a $CO_2$ absorbent and electrochemical medium with regard to certain formulations of DESs, including metal salt-based DESs, such as $ZnCl_2$:ethylene glycol. Metal salt-based DESs contain Lewis acid sites that catalysis $CO_2$ through redox chemistry directly at the electrode interface. This has been shown in studies resulting in faradaic efficiencies of 78% for CO (ChCl:urea) and 71% for formate (ChCl:proline), and the addition of the versatility of the product selectivity depending on the electrode material (Ag, Sn, Cu, Bi, Zn) utilized during the electrochemical process. While there are challenges associated with electrode stability over relatively long periods of time, as well as the difficulty associated with $C_2^+$ product formation, continuous advances such as the development of task-specific DESs and formatting targeted functional groups will likely expand applicability.[402,429–434]

A recent study by Halilu *et al.* investigated bifunctional ionic deep eutectic solvents (DESs) made of diethyl ammonium chloride (DEACI) and diethanolamine (DEA).[435] The study found that these solvents could be used as dual-function


© 2026 The Author(s). Published by the Royal Society of Chemistry

Open Access Article. Published on 12 fevral 2026. Downloaded on 01.06.2026 11:06:26.
This article is licensed under a Creative Commons Attribution-NonCommercial 3.0 Unported Licence.



Table 26 A summary of various deep eutectic solvents (DESs) that capture $CO_2$ through a combination of physical and chemical mechanisms

| DES components (HBA:HBD) | DES type* | $CO_2$ capture mechanism | $CO_2$ capacity | Additional factors affecting adsorption | Ref. |
|---|---|---|---|---|---|
| TPAB : formic acid (1 : 2) | Type III (choline chloride analog) | Physical and chemical *via* hydrogen bonding from –OH of formic acid | Higher absorption with 1 : 2 ratio; viscosity at 25 °C: 53.98 mPa s | Viscosity decrease with higher HBD ratio enhances $CO_2$ solubility; temperature-dependent viscosity | 410 |
| DBN : ethylene glycol (varied ratios) | Type III | Chemical absorption *via* carbamate and carbonate formation (amine + hydroxyl synergy) | Max 0.17 g $CO_2$ per g DES at optimal ratio | Molar ratio of HBD critical; FTIR and NMR confirm carbamate and carbonate species | 421 |
| Methyltriphenylphosphonium bromide : ethylene glycol (1 : 4) | Type III | Physical absorption (physisorption) | 0.074 mol $CO_2$ per mol DES at 303 K, 12 bar | Temperature and pressure influence solubility | 391 |
| Methyltriphenylphosphonium bromide : glycerol (1 : 3) | Type III | Physical absorption | 0.075 mol $CO_2$ per mol DES at 303 K, 12 bar | Similar to above; solvent polarity and viscosity matter | 391 |
| Tetraalkylammonium chloride : 3-amino-1-propanol (1 : 4) | Type V (amine-based) | Chemical absorption *via* carbamate formation confirmed by FTIR | Best uptake among studied DESs (exact capacity not specified) | Molar ratio of HBD influences chemisorption efficiency | 422 |
| Choline chloride: proline: ethylene glycol (ternary) | Type V | Chemical absorption *via* carbamate formation with proline anion | Not quantified explicitly | Synergistic effect of amine and hydroxyl groups; thermal stability and viscosity important | 413 |
| Vanillin : 4-oxoisophorone (1 : 3) | Type III (hydrophobic) | Physical absorption | Comparable to selexol solvent (exact capacity not given) | Hydrophobicity, density $>1.0$ g $mL^{-1}$, thermal stability below 420 K | 423 |
| Various IL/DES combinations | Mixed types | Both physical and chemical absorption | Top 10 ILs/DESs ranked by $CO_2$ capture efficiency (specific values vary) | Polarity, viscosity, basicity, and COSMO-RS predicted properties influence performance | 406 |
| MTPB : diethylene glycol (1 : 4) | Type III | Physical absorption | 0.1 mol $CO_2$ per mol DES@303 K, 12 bar | Low viscosity, increased pressure enhances solubility | 424 |
| MTPB : glycerol (1 : 3) | Type III | Physical absorption | 0.075 mol $CO_2$ per mol DES | Hydrogen bonding density affects performance | 424 |
| TPAC : ethanolamine (1 : 4) | Type III | Chemical absorption (enhanced with EA) | 1.4 mol $CO_2$ per kg DES | Functionalization with EA increases solubility to 3.2 mol $kg^{-1}$ | 425 |
| [DBNH][Oxa] : EG (1 : 0.5) | Type III | Chemical absorption (carbamate + carbonate) | 0.17 g $CO_2$ per g DES | Strong synergy of imino and hydroxyl groups | 426 |
| TBAB : 3-amino-1-propanol (1 : 4) | Type III | Chemical absorption | Not specified | Molar ratio significantly affects solubility | 422 |
| [MEAHCl][MDEA] | Type III | Carbamate + carbonate formation | Not specified | Best performance among amine-based DESs tested | 427 |
| [CHO][Arg] | Type III | Chemical absorption | 0.6046 mol $mol^{-1}$@288.15 K, 4 bar | Amino acid-based IL, multiple amine sites increase uptake | 428 |
| TEAC : acetic acid (1 : 1) + GLY/EA | Type III | Physical absorption | Decreased compared to unfunctionalized | Addition of third component can reduce capacity | 425 |
| ChCl:MEA | Type III | Chemical absorption | Highest among tested (*vs.* DEA & MDEA) | High viscosity limits performance despite strong chemisorption | 416 |
| [MEA.Cl]:EDA | Type III | Chemical absorption | 25.2 wt% $CO_2$ @ 0% water | Uptake drops as water content increases (competition for sites) | 414 |

© 2026 The Author(s). Published by the Royal Society of Chemistry

Open Access Article. Published on 12 fevral 2026. Downloaded on 01.06.2026 11:06:26.
This article is licensed under a Creative Commons Attribution-NonCommercial 3.0 Unported Licence.

electrolytes for $CO_2$ capture and electroreduction, with the DEACI-DEA (1 : 3) composition showing the best results (Fig. 66a). This DES had a deep eutectic point of −69.78 °C, good thermal stability, and a long cathodic limit of −1.7 V *versus* Ag/AgCl. This made it possible to reduce $CO_2$ at −1.5 V with a faradaic efficiency (FE) of 94% and a capture capacity of 52.71 mol $L^{-1}$ after 350 s of sparging (Fig. 66b and c). Conventional aqueous electrolytes, on the other hand, usually have $CO_2$ solubilities $< 0.03$ mol $L^{-1}$ at room temperature and only sometimes reach 40–60% FE because the hydrogen evolution process (HER) is more common at negative potentials. Ionic liquids can also have high FE (70–90%), but they usually have low $CO_2$ solubility ($\sim$0.2–0.4 mol $L^{-1}$) and high viscosity, which makes it hard to move mass and scale up (Fig. 66d and e). DEACI–DEA, on the other hand, has a strong $CO_2$ uptake and an efficient conversion while keeping HER low. Electrochemical impedance spectroscopy demonstrated $CO_2$ chemisorption by a decrease in double-layer capacitance from $8.76 \times 10^{-9}$ F to $3.15 \times 10^{-9}$ F. Simultaneously, COSMO-RS analysis indicated bifunctional interactions of both HBA and HBD sites with $CO_2$ through n-orbital overlap in the non-polar region (Fig. 66f). Chronoamperometric studies revealed an initial diffusion-limited regime succeeded by a steady state in which capture, and conversion reached equilibrium, thereby establishing a direct correlation between absorption capacity and electroreduction kinetics. These results collectively demonstrate that, in contrast to aqueous or ionic liquid systems, DEACI-DEA provides a distinctive equilibrium of solubility, stability, and selectivity, thereby establishing bifunctional deep eutectic solvents (DESs) with enhanced cathodic windows as a logical design framework for next-generation $CO_2$ capture and electro conversion technologies.

Based on (Table 27), Deep eutectic solvents (DESs) possess numerous electrochemical advantages over traditional aqueous electrolytes for $CO_2$ reduction applications. As mentioned above, there are some cases when DESs have marginally lower ionic conductivities than aqueous media, the larger electrochemical

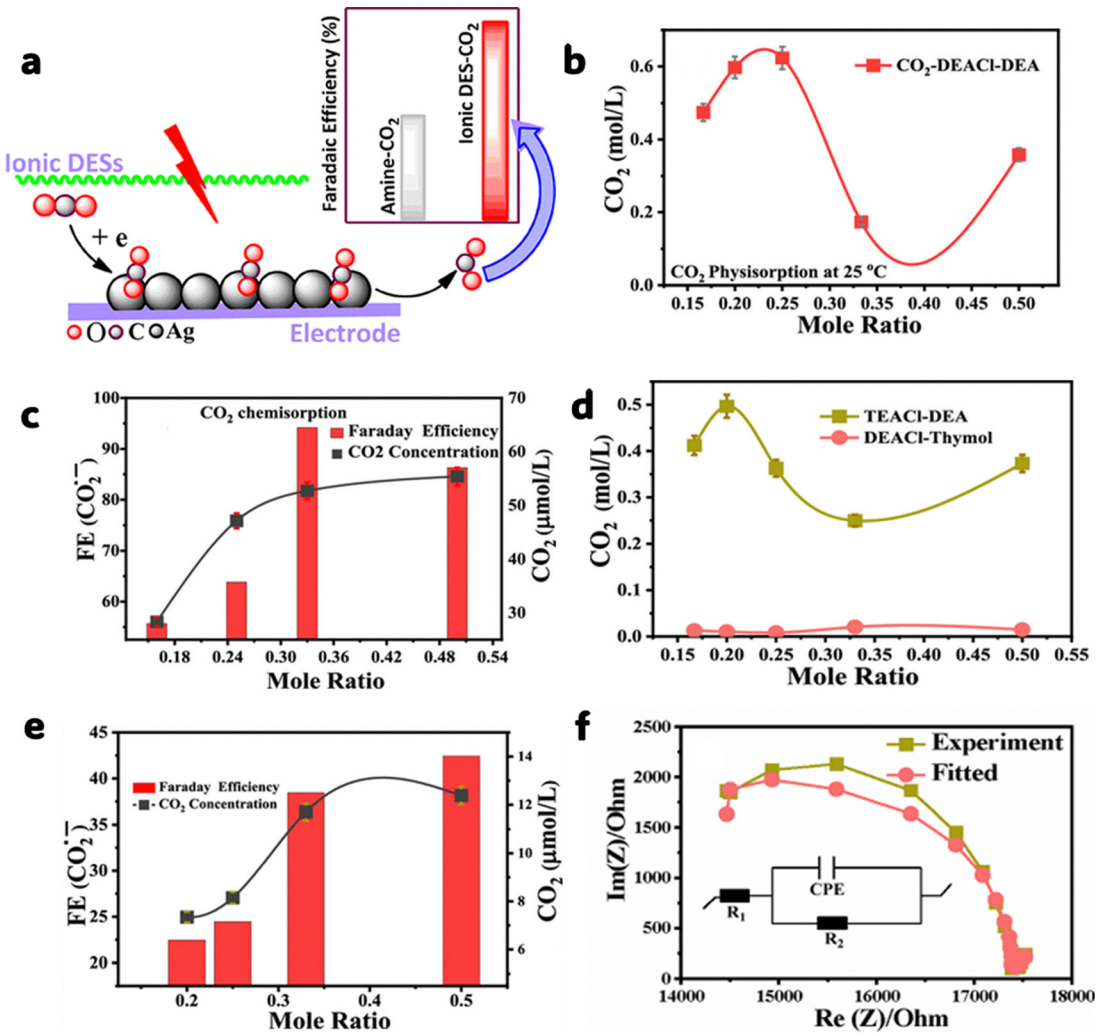


Fig. 66 (a) The graphical representation of $CO_2$ adsorption and electroreduction by DEACl–DEA. (b) Physisorption of $CO_2$ by DEACl–DEA. (c) FE of $CO_2$ electroreduction to $CO_2$. (d) Physisorption of $CO_2$ by DEACl-thymol and TEACl–DEA. (e) FE of $CO_2$ electroreduction to $CO_2$ in TEACl–DEA where the secondary axis shows the amount of $CO_2$ chemisorbed. (f) Nyquist plot for $CO_2$ saturated DEACl–DEA. Reprinted (adapted) from *ACS Omega* 2022, **7**(42), 37764–37773. Copyright © 2022, The Authors. Published by American Chemical Society under the terms of CC-BY-NC-ND 4.0 license.


© 2026 The Author(s). Published by the Royal Society of Chemistry

Open Access Article. Published on 12 fevral 2026. Downloaded on 01.06.2026 11:06:26.
This article is licensed under a Creative Commons Attribution-NonCommercial 3.0 Unported Licence.



Table 27 The performance of various Deep Eutectic Solvents (DESs) used in carbon capture and electrochemical conversion

| DES used (HBA : HBD, ratio) | Electrode | Main product | FE (%) (DES *vs.* aq.) | Current density (mA $cm^{-2}$) | Conductivity (DES/aq.) | Conventional electrolyte (comparison) | Electrochemical advantage | Ref. |
|---|---|---|---|---|---|---|---|---|
| Choline chloride : ethylene glycol (1 : 2) | Au sheet | CO | 81.8% (DES, not compared to aq.) | 1.1 (at −1.6 V) | 6.8 mS $cm^{-1}$ (DES) | 0.1 M $TBAPF_6$/DMF | Lower overpotential, higher $CO_2$ solubility, selective CO production | 436 |
| Choline chloride : urea (1 : 2) | Ag foil | CO | 96% (DES, not compared to aq.) | ∼4.8 (at −0.884 V) | 34.5–131.4 mS $cm^{-1}$ (with KCl) | 0.5 M $KHCO_3$ | High selectivity for CO, HER suppression | 429 |
| Choline chloride : ethylene glycol (1 : 2) | Ag foil | CO | 78–98.8% (in acetonitrile) | 0.4–20 (in acetonitrile) | Not specified | Water, Acetonitrile, Propylene Carbonate | High CO selectivity in aprotic media, tunable viscosity/selectivity | 437 |
| Choline chloride : urea (1 : 2) | Ag NPs/GDE | CO | 94.1% (DES, not compared to aq.) | 11.6 (at −0.83 V) | 34.5–131.4 mS $cm^{-1}$ (with KCl) | 0.5 M $H_2SO_4$ | High selectivity, improved current density with salt | 436 |
| Choline chloride : ethylene glycol (1 : 2), choline chloride : urea (1 : 2) | Au, Ag, Cu, Zn | CO, HCOOH | 15.8–98.8% (varies) | 0.1–20 (varies) | 1.5–1244 cP (viscosity) | Aqueous, acetonitrile, propylene carbonate | Wide potential window, tunable selectivity, high $CO_2$ solubility | 430 |
| Choline chloride : urea (1 : 2) | Roughened Ag foil | CO | 96% | ∼4.8 at −0.884 V *vs.* RHE | 0.1 M $KHCO_3$ | HER suppression, surface restructuring | HER suppression, surface restructuring | 438 |
| Choline chloride : urea (1 : 2) | Ag | CO | 90% | Not specified | 0.5 M $KHCO_3$ | High selectivity, low overpotential | High selectivity, low overpotential | 430 |
| Choline chloride : urea (1 : 2) | Ag | CO | 92% | Not specified | 0.5 M $KHCO_3$ | High selectivity, improved current density | High selectivity, improved current density | |
| Choline chloride : urea (1 : 2), with KCl | Ag-based GDE | CO | Not directly reported; higher $j_{CO}$ with DES/KCl | Not specified (improved with KCl in DES) | Not specified | Aqueous KOH, KCl, Emim Cl | Enhanced $CO_2$ absorption, improved current density | 437 |
| Choline chloride : ethylene glycol (1 : 2), imidazolium chloride:EG | Ag | CO | High FE for CO (exact % not specified) | Not specified | Not specified | RTILs, aqueous | Non-toxic, cost-effective, improved solubility/selectivity | 439 |
| $ZnCl_2$ : EA (1 : 4), $CoCl_2$ : EA (1 : 4); DEACl : DEA (1 : 3) | Single-atom Ag, Ag | $CO_2$ | Up to 94% (DEACl:DEA 1 : 3) | Not specified | Up to 36 200 μS $cm^{-1}$ ($ZnCl_2$/EA) | Not specified | High $CO_2$ absorption, unique interfacial phenomena, bifunctional sorption, wide cathodic window | |
| MEAHCl:MDEA | Ag | CO | 71% | Not reported | Not reported | Not reported | Amine-functionalized DES promoted $CO_2$-to-CO conversion | 429 |
| ChCl : ethylene glycol (1 : 2) | In | Formate | Up to 95% | Not reported | Not reported | Not reported | Selective formate production in DES medium | |
| [Ch][Cl] : urea (1 : 2), 50 wt% in $H_2O$ | Roughened Ag foil | CO | 96% *vs.* lower in aq. $KHCO_3$ | ∼4.8 | 34.5 mS $cm^{-1}$ (DES), 131.4 mS $cm^{-1}$ (DES + KCl) | 0.5 M $KHCO_3$ | Restructures Ag surface, suppresses HER | |
| [MEAH][Cl] : MDEA (1 : 4), 0.4 M in $H_2O$ | Ag foil | CO | 71% *vs.* lower in water | 10.5 | Not explicitly given | Aqueous only | Amine-DES enhances COOH* intermediate stabilization | |
| [Ch][Cl] : EG (1 : 2), 0.1 M in $H_2O$ | Ag foil | CO | Up to 94.1% | 11.6 (w/KCl: 22.1) | 34.5 → 131.4 mS $cm^{-1}$ (w/KCl) | Aqueous $H_2SO_4$ | Addition of KCl doubled current density with same FE | |
| [Ch][Cl] : urea (1 : 2), 2 M in $H_2O$ | Ag NPs/GDE | CO | 94.10% | 11.6 | Not directly reported | Aqueous | KCl enhances conductivity and performance | |
| [Ch][Cl] : EG (1 : 2), 1 M in acetonitrile | Not specified | CO | 98.80% | 20 | Not specified | — | High FE in aprotic solvent system | |
| [Ch][Cl] : EG (1 : 2), neat | Au metal sheet | CO | 81.80% | 1.1 | Not reported | — | High selectivity even without co-solvent | |
| [Ch][Cl] : EG (1 : 2), in propylene carbonate | $Cu_{0.3}Zn_{9.7}$ on Cu foam | CO | 94.90% | ∼16 | Not specified | 0.1 M $H_2SO_4$ | Enhanced CO selectivity on Cu-based alloy | |

© 2026 The Author(s). Published by the Royal Society of Chemistry

Open Access Article. Published on 12 fevral 2026. Downloaded on 01.06.2026 11:06:26.
This article is licensed under a Creative Commons Attribution-NonCommercial 3.0 Unported Licence.

window (often more than 3 V) when using DESs permits the application of higher overpotentials for $CO_2$ reduction without stress from solvent degradation.[430,436]

DESs have consistently produced higher faradaic efficiencies for target products such as CO, formate, and ethylene, due in part to their higher solubility of $CO_2$, as well as providing a more stable medium for intermediates formed throughout the reaction, which benefit from the networks of hydrogen bonding exhibited in these solvents. The DESs have also improved product selectivity and stability when subjected to reaction conditions compared to their aqueous counterparts, leading to less decay of phase separation and electrode damage over cyclic runs while DESs can be prepared readily in a single step from low-cost precursor materials, and do not require a purification step.[429,440]

### 3. Challenges, future outlook, and economic analysis

While the results are promising, several challenges are present. First, there is still limited information about the intermediate species formed during the reduction process. Second, the stability of some DES electrodes appears poor over the long term. Third, multi-carbon product selectivity is difficult to obtain. However, one promising direction in research involving deep-eutectic-solvents (DES) is investigating hybrid or polymer-modified DES systems to improve $CO_2$ capture and electrochemical conversion efficiencies further. The incorporation of polymers in DES matrices presents a valuable avenue to modify physicochemical properties such as viscosity, conductance, and stability, which may even address some of the challenges present in traditional DES. Improvements on mass transfer may be possible, enabling the potential for lower viscosity and the formation of microenvironments that facilitate $CO_2$ diffusion, transport, and interactions with active sites. In addition to manipulating the viscosity of DES, the addition of polymers may also introduce additional functional groups that can interact with the DES to create chemical absorption interactions, improve the stabilization of reactive intermediates during electrochemical reduction, and, due to their modification of the viscosity, also improve the electrochemical stability of DES.

## Polymer-enhanced deep eutectic solvents

Polymer-based eutectic systems, particularly polymerizable deep eutectic solvents (DES), offer distinct advantages over traditional DES by integrating polymerization capabilities directly into the eutectic framework. These systems act as multi-functional platforms serving simultaneously as solvent, monomer, and templating agent, which streamlines synthesis while enhancing material properties. For instance, DES-polymer hybrids achieve superior mechanical strength (*e.g.*, hydrogels with high cross-linking density, reducing swelling) and improved thermal stability compared to non-polymerized DES. They also enable faster polymerization kinetics under milder conditions (*e.g.*, visible-light RAFT polymerization in open air) and facilitate eco-friendly synthesis by eliminating volatile organic solvents. Additionally, polymerizable eutectics expand application versatility, enabling advanced electrochemical performance in batteries (*e.g.*, high ionic conductivity and cycling stability) and precision in nanostructured sensing films. These advantages position polymer-enhanced eutectics as transformative for sustainable material design.[441] In $CO_2$ capturing, based on the search results, only one publication explicitly details the use of polymer-enhanced deep eutectic solvents (DES) for $CO_2$ capture. The study by Nunes (2021) developed Polymeric Deep Eutectic Solvents (PRIDES) hybridized with the bi opolymer chitosan for $CO_2$ capture[442] as illustrated in (Table 28).

The ternary deep eutectic solvent (DES) composed of choline chloride, glycerol, and citric acid, when combined with 1% w/w chitosan, achieved a remarkable $CO_2$ capture capacity of 768.74 mmol $kg^{-1}$ at 10 bar, significantly outperforming the same DES without chitosan, which captured only 110.11 mmol $kg^{-1}$ at atmospheric pressure. This enhancement is attributed to chitosan's amino groups, which facilitate additional chemical adsorption of $CO_2$ under elevated pressure. In comparison, a standalone DES of tetrabutylammonium bromide and polyethylene glycol (PEG 200) captured 120.44 mmol $kg^{-1}$ at ambient conditions. Notably, among available studies, only Nunes (2021) explores a DES-polymer composite system, highlighting the unique role of chitosan in improving $CO_2$ capture performance, whereas most other research focuses on additives such as amines or support materials such as silica, rather than incorporating polymeric matrices.

To boost the kinetics of $CO_2$ electrochemical conversion, we need to optimize the reactor configuration and the operating conditions. Gas diffusion electrodes (GDEs) typically used in flow cells allow direct $CO_2$ to contact the catalyst interface, drastically boosting mass transport while reducing the ubiquitous diffusion limitations found in other liquid-phase reactors, as shown in (Fig. 67).[443] By pressurizing the electrochemical cell, the solubility of $CO_2$ is significantly increased in the reaction medium due to Henry's law, which maximizes the availability of $CO_2$ at the interface and/or reduces the kinetics as detailed in (Table 29).[444] With regards to gas solubility and kinetics, lowering the temperature also has advantages, but greater gains may need to be weighed against lower reaction rates at lower thermal energies.[445] Additionally,

Table 28 A summary of the DES composition, polymer used, and key performance metrics

| DES composition | Polymer used | Polymer concentration | $CO_2$ capture performance | Conditions |
|---|---|---|---|---|
| Choline chloride-glycerol-citric acid | Chitosan | 1% w/w | 768.74 mmol $CO_2$ per kg DES | 10 bar pressure |
| Choline chloride-glycerol-citric acid | — | 0% w/w | 110.11 mmol $CO_2$ per kg DES | Atmospheric pressure, $CO_2$ flow |
| Tetrabutylammonium bromide-PEG 200 | None | N/A | 120.44 mmol $CO_2$ per kg DES | Atmospheric pressure, 25 °C |


© 2026 The Author(s). Published by the Royal Society of Chemistry

Open Access Article. Published on 12 fevral 2026. Downloaded on 01.06.2026 11:06:26.
This article is licensed under a Creative Commons Attribution-NonCommercial 3.0 Unported Licence.

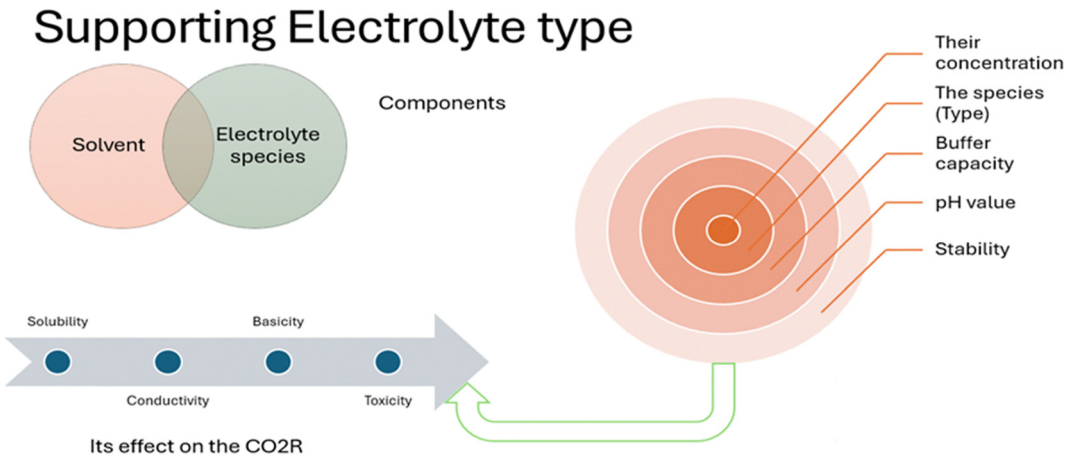


Fig. 67 A schematic overview of a supporting electrolyte, detailing its core components and the key physicochemical properties.

Table 29 Key operational parameters and the kinetic impact on the electrochemical reduction of $CO_2$

| Parameter | Kinetic impact |
|---|---|
| Gas diffusion electrodes (GDEs) | ↑ Mass transport; ↑ Stability (~450 mA $cm^{-2}$ for 200+ hours) |
| Pressure optimization | ↑ $CO_2$ surface coverage; ↑ Formate selectivity (up to 50 bar) |
| Flow rate tuning | ↑ $CO_2$ supply; ↓ Blockage (optimal: 10–20 sccm) |
| Catalyst nanostructuring | ↑ $C_2^+$ selectivity; ↑ Current density (*e.g.*, Cu nanowires: 77.7% FE at 233.2 mA $cm^{-2}$) |
| Reactor configuration | ↓ Ohmic resistance; ↑ Efficiency (*e.g.*, zero-gap cells at 10 bar) |
| Temperature management | Balances $CO_2$ solubility/reaction kinetics (20–40 °C) |

some studies have reported that tuning ionic strength or salinity of the electrolyte will impact the $CO_2$ capture and transport across the two-phase interface, but at times, the results are conflicting or complex.[446] Flow rate, while not specifically noted in the literature, is critical for maintaining the available $CO_2$ supply and removing the gaseous product, in turn affecting kinetics and selectivity. Higher flows will optimize the mass transfer but will decrease the residence times, so greater effort may need to be directed to optimizing flow rate depending on scale and design.[443]

## Molten salts

The Molten salt $CO_2$ electrolysis is an innovative method that integrates $CO_2$ capture and conversion. The method's development commenced in the 1960s and has rapidly proliferated since the 2000s. This technology facilitates the capture of $CO_2$ from elevated-temperature flue gas, enabling the direct conversion of the collected $CO_2$ in the molten salt electrolyte at high temperatures into useful products, including carbon, carbon monoxide, and $O_2$.[447] Due to its higher energy consumption and reduced current efficiency, CO is not an optimal product. Researchers are increasingly focused on the production of high-quality carbon materials and the manipulation of their nanostructures.

Molten salt electrolysis, utilizing an anhydrous electrolyte that focuses on carbon creation, can yield a singular solid carbon product with elevated current efficiency, thereby circumventing intricate byproducts that necessitate challenging or many separations. Moreover, the *in situ* conversion of $CO_2$ into value-added products obviates supplementary expenses following carbon capture, such as $CO_2$ transportation fees, disputed and uncertain storage, and maintenance expenditures, *etc.*[448,449] A molten salt $CO_2$ electrolysis facility is anticipated to generate a net profit of $50 000 per ton of captured $CO_2$ for a power station when the final electrolysis product is carbon nanotubes (CNTs).[450] A common technique for synthesizing carbon nanotubes (CNTs) is chemical vapor deposition (CVD), requiring at least 1440 MJ and producing 28.55 kg of $CO_2$ for the generation of one gram of CNTs.[451,452] Thus, this profit and these advantages can promote the expansion of the molten technique for prospective plants and improve the execution of carbon capture in conventional power plants, surpassing the financial drawbacks linked to the aforementioned technologies, as shown in (Fig. 68).

The method of capturing $CO_2$ using molten salt and electrochemical conversion is efficient and advantageous, as it facilitates the immobilization of $CO_2$ and its transformation into valuable goods. The molten salt electrochemical unit features a straightforward design comprising an insulated electrolyzer, electrolyte, heating unit, cathode, and anode. The absence of additional equipment facilitates ease of usage and management.[453,454] Secondly, the molten salt possesses an extensive electrochemical window, and no side reactions occur during operation.[455,456] Third, electrons serve as the reducing agent for $CO_2$ reduction *via* molten salt. The effective current density during electrolysis can be adjusted to regulate the conversion rate of $CO_2$ into solid carbon compounds.[457,458] The molten salt electrolyte primarily consists of carbonate, which is inexpensive to produce and can be reused, hence minimizing operational costs.[457,459] Ultimately,

Open Access Article. Published on 12 fevral 2026. Downloaded on 01.06.2026 11:06:26.
This article is licensed under a Creative Commons Attribution-NonCommercial 3.0 Unported Licence.

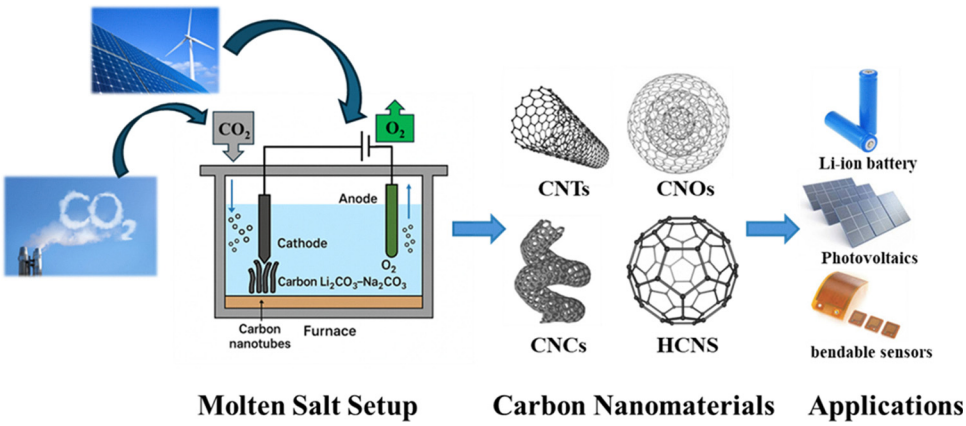


Fig. 68 Process schematic of molten salt electrolysis for integrated $CO_2$ capture, electrocatalytic conversion, and carbon nanomaterial production with rate-matched kinetics.

carbonate electrolyte exhibits high solubility in $CO_2$ and is highly effective in capturing $CO_2$.[460]

### 1. Process of $CO_2$ capture and conversion in molten salt systems

The process of $CO_2$ capture and conversion in molten salt systems is governed by a combination of chemical absorption and electrochemical transformation steps.

**(A) $CO_2$ capture in molten salts.** When $CO_2$ gas is introduced into the molten salt (commonly carbonates or chlorides), it reacts with oxide ions ($O^{2-}$) or directly dissolves to form carbonate ions ($CO_3^{2-}$):[461,462]

$$CO_{2g} + O^{2-} \rightarrow CO_3^{2-} \quad (1)$$

The efficiency of this absorption is highly dependent on the composition of the molten salt, with ternary carbonates (*e.g.*, Li–Na–K) and binary chlorides (*e.g.*, Li–K) showing high solubility for $CO_2$ and favorable absorption kinetics:[462]

**(B) Electrochemical conversion at electrodes**

*(a) Cathode reactions.* The widely accepted cathodic reactions are the 4-electron reaction and the 2-electron reaction processes, which are closely related to the electrolyte reaction temperature.

- The 4-electron reaction (low to moderate temperatures):

$$CO_3^{2-} + 4e^- \rightarrow C_s + 3O^{2-} \quad (2)$$

This reaction leads to the deposition of solid carbon (which can be amorphous carbon, carbon nanotubes, or other nanostructures) on the cathode.[463]

- The 2-electron reaction (higher temperatures):

$$CO_3^{2-} + 2e^- \rightarrow CO_g + 2O^{2-} \quad (3)$$

At elevated temperatures, the formation of CO becomes thermodynamically favored over solid carbon, shifting the selectivity toward CO production.[464]

*(b) Anode reactions.* The oxygen ions generated at the cathode migrate to the anode, where they are oxidized to release oxygen gas:[465]

$$2O^{2-} \rightarrow O_{2g} + 4e^- \quad (4)$$

In some systems, the anode may also participate in the oxidation of other species, depending on the electrode material and cell design.

**(C) Electrolytes.** Researchers have predominantly examined carbonates, chlorides, and oxides containing $Li^+$, $Ca^{2+}$, $Na^+$, and $K^+$ due to their extensive electrochemical windows and high $CO_2$ solubility.[466] Carbonates and chlorides are prevalent in salts, typically containing oxides in concentrations between 1 wt% and 30 wt%. Various types of salts possess distinct advantages and disadvantages, prompting researchers to amalgamate them to get optimal results, such as reduced melting points. However, it is essential to understand the characteristics of the salts prior to their amalgamation.

*(a) Carbonates or chlorides.* Molten chlorides such as LiCl–KCl exhibit inadequate $CO_2$ absorption. Consequently, chlorides must collaborate with oxides or carbonates to enhance carbon absorption and conversion, as shown in (Fig. 69a). In comparison to carbonate electrolytes with oxide additives, chloride electrolytes with oxide additives exhibit accelerated $CO_2$ absorption, achieving equilibrium within 2 hours, hence indicating superior $CO_2$ absorption performance. The reaction of $Li_2O$ and $CO_2$ resulting in $Li_2CO_3$ is responsible for the high absorption capacity. The conversion efficiency of $Li_2O$ to $Li_2CO_3$ nearly doubled in molten chloride electrolyte (about 94%) compared to molten carbonate electrolyte (around 45%), demonstrating that the molten salt composition influences both the thermodynamics and kinetics of $Li_2O$ conversion.[467] Moreover, combined salts often have lower melting points than their pure components.[468] Kanai *et al.* are among the limited research groups examining mass transport in molten carbonates, as illustrated in (Fig. 69b). Increased temperature improved $CO_2$ solubility in both binary (Li–K) and ternary (Li–K–Na) molten carbonates, with solubility values for the two carbonate types being similar.[469]

*(b) Cation selections.* (Table 30) indicates that carbon deposition occurs more readily in Li, Ca, and Ba carbonates compared to Na or K carbonates.[470] At respective melting points, $Li_2CO_3$ has a conductivity of 6 S $cm^{-1}$, which is double that of $Na_2CO_3$


© 2026 The Author(s). Published by the Royal Society of Chemistry

Open Access Article. Published on 12 fevral 2026. Downloaded on 01.06.2026 11:06:26.
This article is licensed under a Creative Commons Attribution-NonCommercial 3.0 Unported Licence.

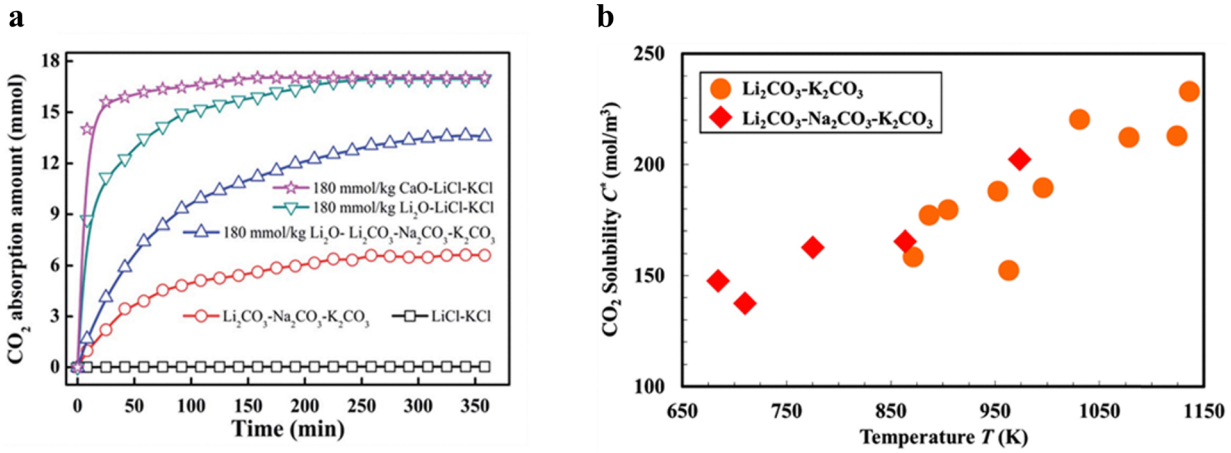


Fig. 69 (a) $CO_2$ absorption curves in different molten salts at 450 °C with the $CO_2$ partial pressure of 50 kPa. (b) $CO_2$ solubility in molten carbonates at different temperatures at 1.01 × $10^5$ Pa. Reprinted (adapted) from *Ind. Chem. Mater.*, 2023, **1**, 595. Copyright © 2023, The Authors. Published by Royal Society of Chemistry under the terms of CC-BY license.

Table 30 Deposition potentials (*vs.* $CO_3^{2-}/CO_2$–$O_2$) of alkali and alkaline earth metals, and carbon in their molten carbonate salts at 600 °C

| Molten salt | Alkali metal (V) | Carbon (V) |
|---|---|---|
| $CaCO_3$ | −3.033 | −1.349 |
| $Li_2CO_3$ | −2.964 | −1.719 |
| $BaCO_3$ | −3.069 | −1.992 |
| $Na_2CO_3$ | −2.546 | −2.551 |
| $K_2CO_3$ | −2.612 | −3.083 |

and triple that of $K_2CO_3$. Increased conductivity reduces ohmic loss, facilitating the movement of electrons or reactants.[471] Furthermore, Li or Ca carbonates exhibit greater stability and utility compared to Na or K carbonates when considering factors such as deposition potentials, thermal decomposition, and the quality of the resultant carbon.

Various cations in carbonates produce distinct carbon nanostructures. $Li^+$ and $Ba^{2+}$ are believed to facilitate the formation of carbon nanotubes, but $K^+$ inhibits the growth of carbon nanostructures.[472] Recent studies indicate that electrolytes containing over 50 wt% Na or more than 30 wt% K carbonates inhibit the growth of carbon nanotubes (CNTs) while accelerating the formation of carbon nano-scaffolds (CNS).[473]

*(c) Additives.* A prominent research area centers on molten salt carbon dioxide capture and electrolysis for the production of carbon nanotubes and other specialized nanostructures. Foreign metal oxides act as essential nucleation sites for the formation of specific carbon nanostructures, particularly carbon nanotubes. Diverse metal oxides have been evaluated and analyzed for carbon nanostructures. Additives of Zn or ZnO were advantageous for the production of carbon nanofibers.[474] $Fe_2O_3$ is a widely utilized additive, too. In certain instances, the electrodes comprise transition metals that may be reduced to metallic elements during electrolysis.[475] These transition metals enabled the formation of the apex and the end of a carbon nanotube (CNT). The incorporation of metal oxides enhances $CO_2$ absorption and triggers subsequent carbon deposition, while concurrently introducing significant defects into the resultant carbon products (*e.g.*, CNT).[476,477]

**(D) Electrodes.** The anode and cathode constitute the primary components of the molten salt $CO_2$ electrolysis systems. During the capture and conversion process, each component has a distinct role. The primary function of the anode is to facilitate oxygen evolution, whereas the cathode's principal role is to retain carbon, enabling the formation of various carbon nanostructure.[478] For optimal performance, the anode must facilitate oxygen production, while the cathode should possess active sites that promote the nucleation and growth of specific carbon materials, such as carbon nanotubes or nanofibers.[479] Both electrodes must exhibit substantial corrosion resistance, despite their distinct functions. This is due to their operation in extremely hostile conditions, such as molten carbonate salts.[480]

*(a) Cathode.* The cathode plays a critical role in molten salt $CO_2$ reduction reactions ($CO_2$RR) as it controls the efficiency and selectivity of $CO_2$ reduction as well as the morphology, purity, and functionality of the carbon products that are generated. Recent years have seen significant advancements in cathode material design, process optimization, and mechanistic understanding. Because of their beneficial catalytic properties, metals like Ni, Fe, Mo, Ti, and their alloys have been the subject of most research. Transition metals, particularly Ni and Fe, are known to catalyze the nucleation and growth of carbon nanostructures.[474] Furthermore, alloys including NiCr, CuNi, and FeNi are specifically engineered to balance catalytic performance with corrosion resistance.[481] For example, NiCr alloys have demonstrated improved durability in molten carbonate environments compared to pure Ni, thus extending electrode lifespan and maintaining process efficiency.[482] In addition to solid metals and alloys, low-melting-point metals such as Sn and Bi have also been studied as liquid cathodes. These materials can dynamically catalyze carbon growth and help form core–shell structures such as Sn@C, in addition to suppressing the Boudouard reaction and increasing current efficiency.[483] Furthermore, metal oxides like

Open Access Article. Published on 12 fevral 2026. Downloaded on 01.06.2026 11:06:26.
This article is licensed under a Creative Commons Attribution-NonCommercial 3.0 Unported Licence.

$TiO_2$, NiO, and $MoO_3$ provide exceptional corrosion resistance and can act as stable scaffolds for catalytic metal nanoparticles. Interestingly, some oxides have the ability to engage in redox cycling, which opens up new channels for the reduction of $CO_2$.[484–486]

*(b) Anode.* The anode material must exhibit exceptional resistance to corrosion and degradation from prolonged usage in an oxidative environment. Prevalent anode materials include metals, alloys, metal oxides, and carbon-based compounds. Researchers frequently select alloys composed of tin dioxide ($SnO_2$), nickel oxide (NiO), platinum (Pt), and nickel (Ni) due to their exceptional durability and superior electrochemical characteristics. This renders them ideal for application in molten salt $CO_2$ electrolysis systems requiring prolonged operation.[475,487–489] Furthermore, carbon-based anodes such as graphite, glassy carbon, and amorphous carbon are highly useful due to their chemical stability.[490,491]

The anode serves a pivotal function in molten salt electrolysis by catalyzing oxygen evolution and ensuring that $O^{2-}$ ions do not accumulate within the electrolyte.[492] Since free $O^{2-}$ ions are not stable in molten salts, they rapidly react with dissolved $CO_2$ or metal ions, forming carbonate ions ($CO_3^{2-}$) and metal oxides.[493,494] To maintain efficient carbon deposition at the cathode, it is essential that $O^{2-}$ ions are removed promptly, which in turn sustains the necessary electrical current for the process as illustrated in (Table 31).

## 2. Morphology and structure of the carbon products

Licht, S. *et al.* successfully synthesized CNTs with a productivity of 80–100% in molten $Li_2CO_3$–$Li_2O$ (4 M $Li_2O$ in $Li_2CO_3$) using a Ni anode and a steel cathode at 750 °C.[505] In this electrolysis system, nickel at the anode is oxidized to form $Ni^{2+}$ ions, which then move to the cathode. There, these ions are reduced back to metallic nickel, providing nucleation sites for carbon nanotube (CNT) growth. Additionally, the presence of $Li_2O$ in the molten mixture converts straight CNTs into tangled ones by introducing extra defects into their structure (Fig. 70a–c).

Peng *et al.* illustrated how the ZnO ratio affects morphology and the percentage of carbon nanotubes (CNTs) in cathodic carbon products.[506] They found that using $Li_2CO_3$ electrolyte with 1% ZnO supports CNT formation. This is likely because ZnO reduces the energy barrier for both nucleation and carbon deposition. The results show that the ZnO content significantly affects CNT growth; with only less than 50% of CNTs observed in $Li_2CO_3$ electrolyte containing 0.5% and 2% ZnO, compared to over 90% in the 1% ZnO setup, as shown in (Fig. 70d–f). Additionally, in a $Li_2CO_3$–$Na_2CO_3$ (1 : 1 weight ratio) system, adding 1% ZnO results in carbon products with more than 80% CNTs. This evidence indicates that it is possible to use more cost-effective electrolytes for CNT production.

Yu, R. *et al.* developed a novel Ge@CNT composite material to address the limitation of carbon-based anodes in lithium-ion batteries (LIBs) regarding charge capacity.[486] The incorporation of germanium and carbon nanotubes significantly enhances the battery's overall performance. The synthesis occurs in a heated mixture of NaCl, $CaCl_2$, and CaO, which additionally contains $GeO_2$. The reaction initiates when $GeO_2$ interacts with ionized $Ca^{2+}$ in the molten salt. This produces a liquid CaGe alloy. This alloy phase facilitates the development of carbon nanotubes by accelerating the process. (Fig. 71a and b) illustrates the completed assembly, featuring several germanium nanoparticles embedded directly into the carbon nanotube matrix. This unique configuration integrates germanium's capacity to retain substantial lithium with the stable, conductive framework of carbon nanotubes. This addresses the common issues associated with carbon. In addition, various M@CNTs, such as Sn@CNTs, Zn@CNTs, and Fe@CNTs, were synthesized, and $CO_2$ was reduced in molten salts.[483] The mechanisms by which these three M@CNTs evolve are fundamentally different from the nucleation process of liquid metals. (Fig. 71c) illustrates the

Table 31 Effect of molten salt and cathode components on the morphology of carbon products

| Electrolyte | $T$ (°C) | Cathode | Anode | Current density | Products | Ref. |
|---|---|---|---|---|---|---|
| $Li_2CO_3$ | 770 | Galvanized steel; Ni–Cr | Ni–Cr; galvanized steel | 1 A | Multi-walled carbon nanotubes (MWCNTs) | 482 |
| $Ta_2O_5$–$CaCl_2$–CaO | 650 | Ni | Graphite | 0.2–1 A $cm^{-2}$ | Carbon particles | 490 |
| $Li_2CO_3$–$Li_2O$ | 770 | Cu | Ir–Pt | 0.2 A $cm^{-2}$ | Carbon nano-onions; CNTs | 495 |
| $Li_2CO_3$–$Li_2O$–CaO–$H_3BO_3$ | 770 | Muntz brass sheet | Nichrome sheet | 0.2 A $cm^{-2}$ | Carbon nanotubes (CNTs) | 496 |
| $Li_2CO_3$–$Na_2CO_3$–$K_2CO_3$–$H_3BO_3$ | 670 | Muntz brass sheet | Inconel | | CNTs | 473 |
| $Li_2CO_3$–$Na_2CO_3$–$K_2CO_3$ | 450–650 | Ni | $SnO_2$ | 0.2–4 A $g^{-1}$ | Activated carbons | 487 |
| $Li_2CO_3$–$Li_2O$ | 770 | Muntz brass as | Inconel 718; Nichrome; Incoloy | 0.5 A | $Fe_3C$; CNTs | 463 |
| LiCl–$Li_2CO_3$–$LiBO_2$ | 550 | Ni | Graphite | 25–100 mA $cm^{-2}$ | CO | 497 |
| LiCl–$Li_2CO_3$–$LiBO_2$ | 550 | Ni | Graphite | | Carbon nanofibers (CNFs); CO | 498 |
| $Li_2CO_3$ | 730 | Galvanized steel | Pt | | Graphene; CNTs | 488 |
| $Li_2CO_3$–$K_2CO_3$–$Na_2CO_3$ | 650 | NiO–$Co_3O_4$ | $Ni_{10}Cu_{11}Fe$ | 10 mA $cm^{-2}$ | NiCo@g-c powder | 485 |
| $Li_2CO_3$–$K_2CO_3$–$Na_2CO_3$ | 650–750 | Ni | Pt | 5–100 mA $cm^{-2}$ | Graphite | 499 |
| $Li_2CO_3$–$Na_2CO_3$ | 750 | Brass | Inconel 718 | 200 mA $cm^{-2}$ | CNTs | 500 |
| $Li_2CO_3$ | 750 | Ni | SS | 7.5 A | Carbon sphere | 501 |
| NaCl-$CaCl_2$-CaO | 750 | $GeO_2$ | Graphite | 2000 mA $g^{-1}$ | Ge@CNTs | 486 |
| $Li_2CO_3$–$Na_2CO_3$–$K_2CO_3$ | 450 | nickel foam | Glassy carbon | 500 mA $g^{-1}$ | Porous carbon | 491 |
| $Li_2CO_3$ | 780 | nickel foam | Glassy carbon | 600 mA $g^{-1}$ | Crystalline nano-graphite | 502 |
| $Li_2CO_3$-K2CO3-Na2CO3 | 500 | Galvanized Fe wire | Ni wire | — | Honeycomb carbon nanostructure | 503 |
| $Na_2CO_3$-$K_2CO_3$ | | FeNi foam | $Ni_{10}Cu_{11}Fe$ alloy | 100 mA $cm^{-2}$ | CO | 504 |


© 2026 The Author(s). Published by the Royal Society of Chemistry

Open Access Article. Published on 12 fevral 2026. Downloaded on 01.06.2026 11:06:26.
This article is licensed under a Creative Commons Attribution-NonCommercial 3.0 Unported Licence.

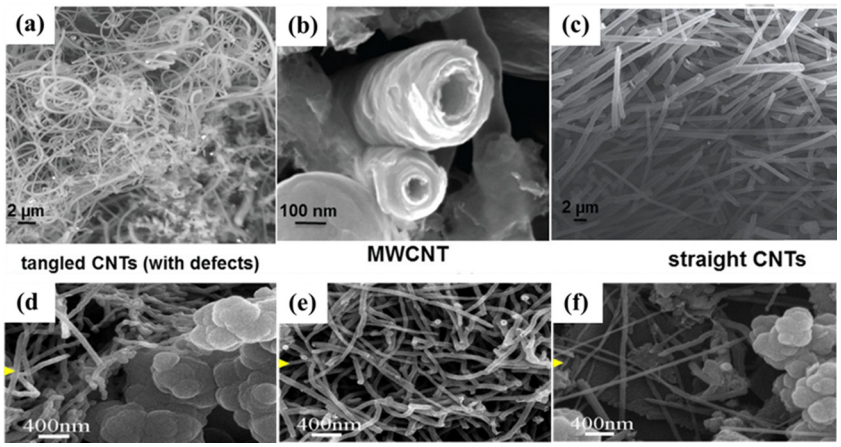


Fig. 70 (a)–(c) SEM images showing the different CNT morphologies formed based on either the addition of $Li_2O$. Reprinted (adapted) from *ACS Cent. Sci.* 2016, **2**(3), 162–168. Copyright © 2016, American Chemical Society under the terms of CC-BY license. (d)–(f) SEM images of the carbon products prepared in $Li_2CO_3$ with (d) 0.5% ZnO, (e) 1% ZnO, (f) 2% ZnO. Reprinted (adapted) from *J. Electrochem. Soc.* **168** 083501. Copyright © 2021, IOP Publishing, Ltd.

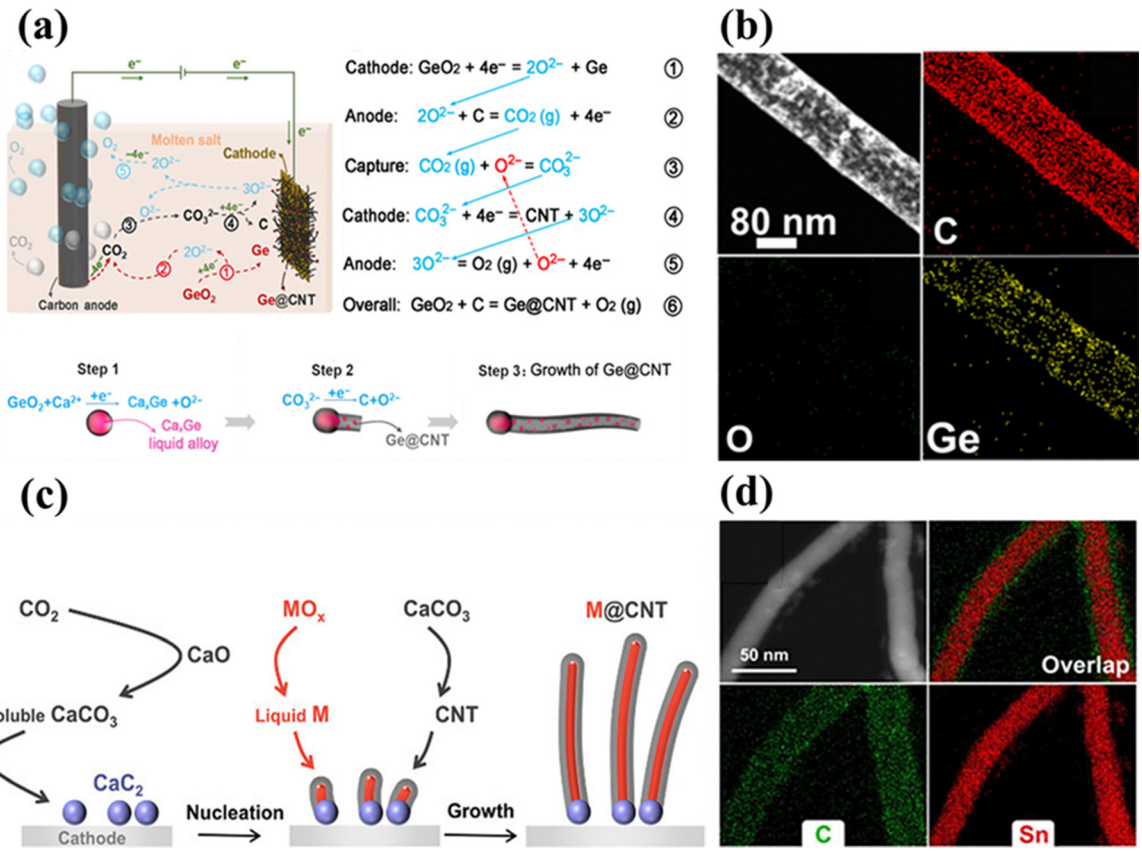


Fig. 71 (a) Schematic illustration of the coelectrolysis of soluble $GeO_2$ and *in situ*–generated $CO_2$ at carbon anode to cathodic Ge@CNTs. (b) HAADF-STEM image, and the corresponding elemental mappings of C, O, and Ge. Reprinted (adapted) from *Sci. Adv.* 2020, **6**, eaay9278. Copyright © 2020, The American Association for the Advancement of Science under the terms of CC BY-NC license. (c) Illustration of the preparation of metal-confining CNT (M@CNT) *via* a $CaC_2$-mediated mechanism. (d) HAADF-STEM image and the corresponding elemental mappings of Sn@CNT. Reprinted (adapted) from *Chem. Int. Ed.* 2023, **62**, e202306877. Copyright © 2023, Wiley-VCH GmbH.

electrochemical reduction of $CO_2$ in an inexpensive, calcium-containing molten salt. This method effectively generates CNTs and M@CNTs *via* a $CaC_2$-mediated process. In the synthesis of metal-free carbon nanotubes, calcium carbonate in the melt is first converted into calcium carbide. Calcium carbide ($CaC_2$) acts as a precursor for the fabrication of carbon nanotubes (CNTs) by the decomposition of calcium carbonate ($CaCO_3$). The CaO and $CO_2$ cycle subsequently replenishes the consumed $CaCO_3$. In the

Open Access Article. Published on 12 fevral 2026. Downloaded on 01.06.2026 11:06:26.
This article is licensed under a Creative Commons Attribution-NonCommercial 3.0 Unported Licence.

production of M@CNTs (Sn@CNTs, Zn@CNTs, and Fe@CNTs), MOx (metal oxides $SnO_2$, ZnO, and FeO) and $CaCO_3$ are reduced to liquid metals and CNTs, respectively. The liquid metals are subsequently introduced into the internal cavities of the CNTs (Fig. 71d). Sn@CNT shows a significant capacity of 510 mAh $g^{-1}$ at a current density of 1000 mA $g^{-1}$ due to the synergistic interaction between the Sn core and the CNT shell. These techniques illustrate the strategic application of molten salt for the sequestration and transformation of $CO_2$. They also promote the advancement of novel CNT composites and highlight the adaptability of this technology for production.

Carbon nano-onions are a special type of carbon nanostructure that is made up of many layers of fullerenes. In the past, these structures were made by putting nanodiamonds through pyrolysis at very high temperatures, often reaching 1700 °C, which made the process use a huge amount of energy. Liu *et al.* demonstrated an alternative approach to capture and electrochemically reduce $CO_2$ in a pure $Li_2CO_3$ electrolyte with six molal $Li_2O$. Their tests showed that using galvanized copper as the cathode and platinum flakes as the anode produced about 97% yield of carbon nano-onions. When a nickel sheet was used as the anode, it facilitated carbon nanotubes forming instead of nano-onions. The results show that the type of carbon nanostructure that is made depends on both the electrode material and the ratio of molten salt. Using electrodes and electrolytes that don't contain nickel and are high in $Li_2O$ generally makes more $sp^3$ defects happen in the solid carbon that forms at the cathode. Adding more $sp^3$ character makes the carbon layers bend more, which enhances the production of carbon nano-onions, as shown in (Fig. 72a and b).[495] Rui *et al.* discovered that the alkalinity of the electrolyte, electrode substrate, and current density play a crucial role in the growth of carbon nanocoils (CNCs) on graphite electrode in $Li_2CO_3$–$Na_2CO_3$–$K_2CO_3$–0.001 wt% $Li_2O$ as a molten salt, and the alkalinity of the molten salt electrolyte induced specific structural defects in carbon, leading to the formation of coiled structures in a controlled manner[507] as shown in (Fig. 72c and d). Interestingly, through scanning electron microscopy, the *in situ* mechanical properties were measured, and it was found

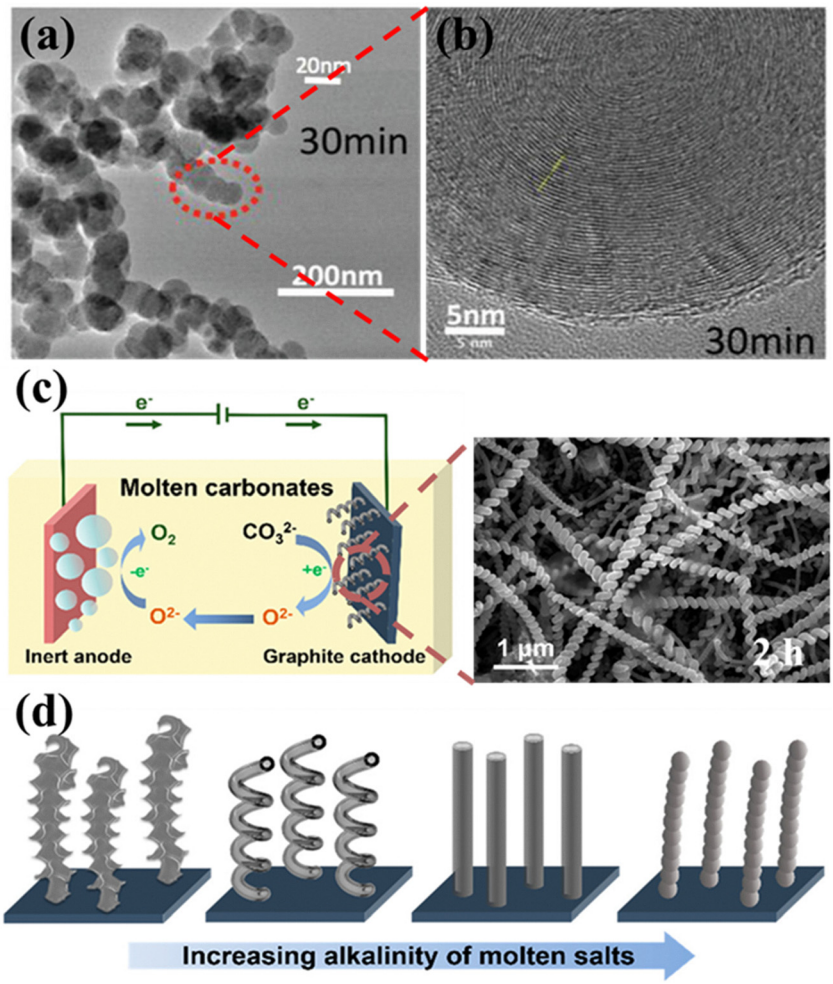


Fig. 72 (a) and (b) TEM of carbon nano-onion synthesis product at 770 °C, without added Ni. Reprinted (adapted) from *Adv. Sustainable Syst.* 2019, **3**, 1900056. Copyright © 2019 Wiley-VCH Verlag GmbH & Co. KGaA, Weinheim. (c) Schematic illustration of the synthesis of carbon nanocoils (CNCs) and SEM images of carbon nanocoils. (d) Schematic illustration of the different carbon structures obtained with the increasing alkalinity of molten carbonate. Reprinted (adapted) from *Nano Lett.* 2022, **22**(1), 97–104. Copyright © 2022, American Chemical Society.


© 2026 The Author(s). Published by the Royal Society of Chemistry

Open Access Article. Published on 12 fevral 2026. Downloaded on 01.06.2026 11:06:26. This article is licensed under a Creative Commons Attribution-NonCommercial 3.0 Unported Licence.

Table 32 Techno-economics of carbon nanotubes produced by different methods.[508–510]

| Parameter | Molten salt electrolysis | CVD | Arc discharge | Laser ablation |
|---|---|---|---|---|
| Production cost | 0.05–0.20 per g SWCNs | $0.366–$1.7 per g SWCNs | $100–$150 per g SWCNs | $100–$1000 per g SWCNs |
| Scalability | High (compatible with industrial-scale reactors) | High (dominant commercial method) | Low (batch process) | Very low (research-scale) |
| Energy consumption | High (750–900 °C, -intensive) | High (900–1000 °C, hydrocarbon cracking) | Very high (arc plasma) | Extremely high (laser systems) |
| Raw material cost | Low (uses $CO_2$ or graphite) | Moderate (hydrocarbons, catalysts) | Moderate (graphite electrodes) | High (graphite targets) |
| Environmental impact | $CO_2$-negative potential | High GHG emissions (methane/ethane use) | Moderate ($CO_2$ from energy) | High (energy-intensive) |
| Market viability | Emerging (profitable at scale) | Mature (dominant market share) | Limited (niche applications) | Rare (specialized uses) |

that the shear modulus and the spring stiffness of the electrolytic CNCs are far larger than those of CVD-derived CNCs and close to the theoretical values. Noting that (Table 32) presents the techno-economics of carbon nanotubes produced by different methods.

## Future outlook of molten salts

The $CO_2$ absorption over molten salts process, cathodic reduction reactions, and the corrosive behavior of inert anodes, as well as the morphologies of electro-deposited carbon. MSCC-ET demonstrates the potential for great applications; on the other hand, there are a lot of unknowns remaining for fundamental investigation and considerable engineering expertise to develop. For example, although different carbon materials were prepared and reported, the detailed reduction mechanism of $CO_2$ and the assembling pathway of the reduced carbon atoms and their controlling principle are not fully covered. In addition, the optimization of molten salt composition and understanding of the molten salt structure and the gas behavior in molten salt and the electrode/electrolyte interface should further be addressed.

## Comprehensive analysis of dual-functional materials (DFMs)

This comprehensive analysis section synthesizes performance, stability, and mechanistic insights to assess the practical viability of DFMs for integrated $CO_2$ capture and electrocatalytic conversion (ICCC). Tables 33–38 collectively benchmark DFM platforms across comparative performance metrics, operating windows, flue-gas tolerance, and technology readiness levels, while explicitly delineating material-specific advantages and limitations. Thermal and oxidative stability under ICCC-relevant conditions is evaluated, with particular attention to porous polymer network platforms, alongside a unifying mechanistic framework that contrasts established reaction pathways with emerging dual-site hypotheses. Finally, kinetic benchmarking links $CO_2$ adsorption–desorption dynamics to catalytic turnover frequencies, enabling a system-level assessment of rate compatibility and identifying kinetic mismatches that currently constrain scalable ICCC deployment.

Table 33 highlights that only a few systems such as Ni–N/CNT@CTF, high-performance CMP/CNT composites, MOF-based gas-diffusion electrodes, and molten carbonates, currently combine high selectivity with industrially relevant current densities, whereas most POP/CTF, COF, amine, ionic-liquid, and DES platforms are limited by conductivity, viscosity, stability, or mass-transport constraints. Robust inorganic frameworks like zeolites, oxides, and molten salts offer excellent thermal and chemical durability but often require conductive scaffolds or high-temperature, corrosion-resistant hardware, while molecular media primarily function as tunable electrolytes rather than stand-alone DFMs. As a result, future ICCC development will likely rely on hybrid architectures that merge stable inorganic backbones with engineered porous polymers and optimized liquid environments to achieve high current densities, long lifetimes, and high selectivity under humid, impurity-rich flue-gas conditions at acceptable cost.

Dual-functional materials (DFMs) must operate within constrained flue-gas conditions (373 K, 0.1 bar, 10–15% $CO_2$, humid/$SO_x$/$NO_x$) while delivering catalytic currents $\geq$200 mA $cm^{-2}$ for industrial viability. Table 34 benchmarks operating windows across platforms: molten carbonates excel at 550–900 °C (>90% FE at 1 A $cm^{-2}$) with complete flue-gas tolerance but high energy costs, zeolites span 25–500 °C with excellent stability yet require nanoconfinement for $CO_2$RR, and room-temperature DES/ILs offer green scalability (94% $FE_{CO}$) but remain current-limited (<20 mA $cm^{-2}$). MOF GDEs achieve breakthrough performance (380 mA $cm^{-2}$ at 15% $CO_2$) despite hydrolysis risks, while POPs/CTFs need hydrophobic engineering for humidity tolerance yet deliver balanced kinetics (12.8 mA $cm^{-2}$ Ni-CTF). Amines provide high capacity but suffer impurity degradation, positioning zeolites/molten salts as most robust and MOF/DES GDEs as highest-rate room-T solutions. Table 35 quantifies DFM performance under these practical constraints, moving beyond descriptive surveys to assess operating-window-ranked ICCC viability.

Table 35 systematically addresses a unified mechanistic taxonomy across ICCC platforms: physisorptive DFMs (POPs/CTFs/CMPs −24 to −45 kJ $mol^{-1}$; COFs −42 kJ $mol^{-1}$; MOFs −30 to −80 kJ $mol^{-1}$; zeolites −30 to −70 kJ $mol^{-1}$) generate *$CO_2$/*COOH at N-sites/OMS *via* weak van der Waals/cation–π interactions, while chemisorptive systems (oxides/DFMs −50 to −90 kJ $mol^{-1}$; amines −80 to −120 kJ $mol^{-1}$; DESs −44 to −209 kJ $mol^{-1}$; molten salts −150 kJ $mol^{-1}$) form covalent carbamate/$CO_3^{2-}$ species at nucleophilic centers. Capture mode dictates RDS coupling, physisorption sustains high *$CO_2$ → *COOH barriers ($\Delta G_{RDS}$ 0.4–0.8 eV) requiring EDL/co-catalysts, chemisorption eliminates adsorption RDS but bottlenecks at carbamate hydrolysis (amines), $R_{ct}$-limited *COOH (DESs), or 4e$^-$

Open Access Article. Published on 12 fevral 2026. Downloaded on 01.06.2026 11:06:26.
This article is licensed under a Creative Commons Attribution-NonCommercial 3.0 Unported Licence.





Table 33 Comparative performance metrics of dual-functional materials (DFMs) for integrated $CO_2$ capture and electrocatalytic conversion (ICCC), highlighting advantages, limitations, and technology readiness levels (TRL)

| Material class | Capture capacity (273–298 K, ∼1 bar) | Textural/binding metrics | $CO_2$RR selectivity (FE) | Current density & kinetics | Stability/TRL insight | Ref. |
|---|---|---|---|---|---|---|
| POPs/CTFs | – PHCTF-1a/-4 : 30–52 $cm^3\ g^{-1}$ $CO_2$ at 273 K<br>– N-rich CTFs (PCBZL, CTF-CSU41): 30–52 $cm^3\ g^{-1}$ at 273 K. | – $S_{BET}$ ≈ 1200–1300 $m^2\ g^{-1}$<br>– $V_{micro}$ = 58–79%<br>– $Q_{st}$ ≈ 24–45 kJ $mol^{-1}$ (favourable for 10–15% $CO_2$) | – Metal-free CTF: $FE_{CO}$ ≈ 82% F-CTF: $FE_{CH_4}$ ≈ 99.3%<br>– Ni-CTF: $FE_{CO}$ ≈ 90%; NiPor-CTF: $FE_{CO}$ ≈ 92.3%<br>– Ni–N/CNT@CTF: $FE_{CO}$ ≈ 98% | – NiPor-CTF: $j_{CO}$ ≈ 12.8 mA $cm^{-2}$<br>– Ni–N/CNT@CTF: $j_{CO}$ ≈ 201 mA $cm^{-2}$<br>– $\Delta G_{*COOH}$ ≈ 0.58–0.59 eV<br>– Tafel ≈ 56–86 mV $dec^{-1}$ (*vs.* ≥0.85 eV and ∼130 mV $dec^{-1}$ for Ni-TPP) | – Good capture at flue-gas $P_{CO_2}$<br>– Ni–N/CNT@CTF approaches industrial *j* but humidity and long-term oxidative stability remain limiting; TRL ≈ 3–4 | 65, 66, 82, 84–86, 88, 90–92, 103 and 105 |
| POPs/CMPs | – Co-CMP: 79.3 mg $g^{-1}$<br>– Al-CMP: 76.5 mg $g^{-1}$<br>– Parent CMP: 71.0 mg $g^{-1}$ at 298 K, 1 bar (similar to MOF-177, NOTT-112) | – Co-CMP: $S_{BET}$ ≈ 965 $m^2\ g^{-1}$, $V_{tot}$ ≈ 2.81 $cm^3\ g^{-1}$<br>– Al-CMP: 798 $m^2\ g^{-1}$, 1.41 $cm^3\ g^{-1}$; capacity tracks $V_{tot}$ and metal–$CO_2$ interactions more than $S_{BET}$ | – CNT@CMP(CoPc–$H_2$Pc): $FE_{CO}$ ≈ 97%<br>– CMPANI-3: $FE_{CO}$ ≈ 97%; CMP-$(bpy)_{20}$–Mn: $FE_{CO}$ ≈ 0.4% (HER-dominated). | – CNT@CMP(CoPc–$H_2$Pc) & CMPANI-3: $j_{CO}$ > 200 mA $cm^{-2}$<br>– TOF up to 9.8 × $10^4$ $h^{-1}$; CMP-$(bpy)_{20}$–Mn: requires −1.6 V for negligible CO. | CMPs can reach industrial *j* and high FE when combined with CNT backbones and proton-relay ligands; stability and flue-gas tolerance still underexplored; TRL ≈ 3 | 113, 114, 117, 128 and 130 |
| COFs | – TPE-COF-II: 118.8 $cm^3\ g^{-1}$ (23.2 wt%) at 273 K<br>– RICE-5 : 50 $cm^3\ g^{-1}$ at 273 K<br>– COF-102/103: up to 27 mmol $g^{-1}$ at 298 K | – RICE-5: porosity 94%, density 0.094 g $cm^{-3}$<br>– HEX-COF-1: $S_{BET}$ 1214 $m^2\ g^{-1}$, $Q_{st}$ ≈ 42 kJ $mol^{-1}$<br>– COF-300-$SO_3$H: 6.23 mmol $g^{-1}$ $CO_2$ and $CO_2/N_2$ selectivity 393 *vs.* 10–31 for other functional groups | – CoPc-PI-COF: $FE_{CO}$ ≈ 96–97%<br>– Co-TTCOF: $FE_{CO}$ ≈ 99.7%; PA-Co-COF: $FE_{CO}$ ≈ 86.97% from 15% $CO_2$<br>– Cu-$COF^+$-Pd: ≈95.5% $FE_{CO+CO_2^-}$ | – CoPc-PI-COF: TOF up to 2.2 $s^{-1}$, TON ≈ 2.8 × $10^5$<br>– Co-TTCOF: TOF ≈ 1.3 $s^{-1}$; PA-Co-COF: TOF 1208.8 $h^{-1}$<br>– Most examples operate at $j \lesssim$ 50–100 mA $cm^{-2}$ | COFs offer high FE and tunable binding, but hydrolytic stability, crystallization yield, and limited *j* at low $P_{CO_2}$ restrict ICCC deployment; GDE integration and robust linkers are required; TRL ≈ 2–3 | 153, 158, 174, 176 and 181 |
| Zeolites | – LEV: 5.81 mmol $g^{-1}$ at 0 °C<br>– LTA: up to 3.7 mmol $g^{-1}$ at 25 °C after Si/Al optimization<br>– $CO_2/N_2$ selectivity up to ≈80–84 | – Low Si/Al and high $Na^+/Ni^{2+}$ densities enhance uptake<br>– Hierarchical LTA reduces adsorption/desorption time by 29–92 s and regeneration *T* by 13 °C | – CdO@Zn@Y: $FE_{CO}$ > 90% at −0.8 V; $SnCu_xO_{2+x}$@MFI: high $FE_{CH_4}/FE_{C_2H_4}$ at elevated *j* | – CdO@Zn@Y stable for 120 h; zeolites generally >1000 h in capture<br>– Electrochemical systems are still mostly lab-scale<br>– Conductivity remains a bottleneck. | Zeolites are capture-mature (TRL 8–9) with excellent stability; as ICCC catalysts, they need conductive, hierarchical GDE designs. | 199–201, 221, 226 and 234 |
| MOFs | – HKUST-1/MOF-74: up to ∼10 mmol $g^{-1}$ at high P<br>– CALF-20 MMM: 3.97 mmol $g^{-1}$ with ≈4.5× selectivity *vs.* $N_2/O_2$ at 298 K | – High $S_{BET}$ and open metal sites<br>– CALF-20 stable under humid DAC-like conditions. | – Ag-MOF-$NH_2$: $FE_{CO}$ 96–97% at 355–380 mA $cm^{-2}$ from 15% $CO_2$<br>– CALF-20-PGDE: CO FE ≈ 95% from 10% $CO_2$<br>– Cu-MOF GDEs: $FE_{C2H4}$ ≈ 49%, $JC_2H_4$ ≈ 220 mA $cm^{-2}$ at 1 A $cm^{-2}$ | – MOF GDEs reach $j \gtrsim$ 200–380 mA $cm^{-2}$<br>– Bi-HHTP gives $FE_{HCOOH}$ ≈ 90–93% with modelled cost ≈0.74 \$ $kg^{-1}$<br>– hydrolysis often limits lifetime to <100 h | MOFs can deliver ICCC-level rates *via* local $CO_2$ enrichment but require robust, hydrophobic/conductive frameworks for long-term operation; TRL ≈ 3–4 | 243, 266–270 and 293 |
| Metal oxides/ hybrids | – Amine-oxide systems capture $CO_2$ as carbamates/bicarbonates (DEA–$SnO_x$/C stable up to 50% $CO_2$) | – Strong chemisorption<br>– Limited physical porosity<br>– Capture capacity defined by amine loading | – DEA– $SnO_x$/C: $FE_{HCOO^-}$ ≈ 84.2%<br>– Solid-state oxide reactors: $C_2$ FEs ≈ 34–68% | – DEA–$SnO_x$/C: $j_{HCOO^-}$ ≈ 6.7–7.9 mA $cm^{-2}$<br>– Solid-state capture *j* up to 440 mA $cm^{-2}$ with costs ≈33–83 \$ $t^{-1}$ $CO_2$ | Oxide-based DFMs clearly reduce capture energy *versus* thermal stripping but amine-based systems have low *j* and degradation; oxide solid-state reactors are closer to TE targets but face poisoning and capital-cost issues; TRL ≈ 3–5 | 294–299 |

© 2026 The Author(s). Published by the Royal Society of Chemistry

Open Access Article. Published on 12 fevral 2026. Downloaded on 01.06.2026 11:06:26.
This article is licensed under a Creative Commons Attribution-NonCommercial 3.0 Unported Licence.



Table 33 (*continued*)

| Material class | Capture capacity (273–298 K, ∼1 bar) | Textural/binding metrics | $CO_2$RR selectivity (FE) | Current density & kinetics | Stability/TRL insight | Ref. |
|---|---|---|---|---|---|---|
| Amines | – Typical 30 wt% MEA: 0.4–0.5 mol $CO_2$ per mol amine<br>– High capacities at 40–60 °C | – Carbamate formation<br>– Regeneration energy ≈3 GJ $t^{-1}$ $CO_2$; oxidative/thermal degradation above ≈100–110 °C | – MEA/Ag: $FE_{CO}$ ≈ 72% at 50 mA $cm^{-2}$<br>– AMP-based systems: $FE_{HCOO^-}$ ≈ 40–50%<br>– Ni–N/C in MEA: $FE_{CO}$ ≈ 65% | – $j$ usually ≤50 mA $cm^{-2}$ in H-cells<br>– Best flow systems approach ≈200 mA $cm^{-2}$<br>– Integrated schemes can save up to ≈44% capture energy *versus* thermal stripping | Amines are capture-mature (TRL4) but electrochemically limited by conductivity, HER, and degradation; useful for energy savings but not yet superior in productivity to gas-fed $CO_2$RR | 312–320 |
| Ionic liquids | – Physical ILs: ≤0.5 mol $CO_2$ $mol^{-1}$ at 1 bar<br>Reactive ILs (*e.g.* $[P_{66614}][AA]$) up to 1.6–2.0 mol $mol^{-1}$ | – Strong, tunable interactions but high viscosities (50–1000 cP) and cost<br>– Non-fluorinated, heterocycle ILs show better viscosity–capacity trade-offs | – Neat imidazolium ILs: $FE_{CO/HCOO^-}$ ≥80–96%<br>– IL additives (0.01–0.5 M $[Emim][BF_4]$/[TFO]): FE ≈ 75–80%<br>– [Emim][2-CNPyrr]: $FE_{CO}$ > 94–98% | – Strong overpotential reduction (≈0.2–0.24 V) but often limited $j$ due to viscosity in neat Ils<br>– Additive/surface-modifier modes maintain aqueous-like $j$ while improving FE | ILs excel as interfacial modifiers/additives rather than bulk electrolytes; cost, viscosity, and toxicity remain barriers for large-scale ICCC; TRL ≈ 3–4 | 321, 330, 337, 338 and 389 |
| DESs | – ChCl:urea/EG: ≈0.6 mol $kg^{-1}$<br>– PRIDES: up to 769 mmol $kg^{-1}$<br>– DEACl:DEA: 52.71 mol $L^{-1}$ equivalent loading | – Viscosity 200–800 cP (lower than many ILs but higher than water)<br>– H-bond network controls $CO_2$ speciation and transport | – DEACl:DEA: $FE_{CO}$ ≈ 94%<br>– ChCl:urea-based systems: $FE_{CO}$ 90–98% at low $j$ | – $j$ typically 4–20 mA $cm^{-2}$<br>– $R_{ct}$ lower than in $KHCO_3$, but still limits high-rate operation<br>– Stability is good over tens of hours | DESs offer green, low-cost, high-FE media but need GDEs/pressure and polymeric hybrids to reach ≥200 mA $cm^{-2}$; TRL ≈ 2–3 | 390, 402, 407, 408, 429–435 and 439 |
| Molten salts | – $Li_2CO_3$/Li–Na–K carbonates: $CO_2$ solubility up to 0.835 mol $CO_2$ per mol Li at 723 K | – Toper 550–900 °C; fully inorganic, excellent stability; strong chemisorption *via* $CO_3^{2-}$ species | – MSCC-ET: current efficiency >80–93% for C or CO; CNT products with near-100% carbon selectivity | – $j$ typically 0.2–1 A $cm^{-2}$; SWCNT cost 0.05–0.20 \$ $g^{-1}$ with effective profit ≈50 k\$ $t^{-1}$ $CO_2$; >100 h operation demonstrated | Molten salts uniquely enable $CO_2$-negative carbon materials at industrial current densities and flue-gas tolerance, but high $T$ and corrosion limit integration with low-T ICCC; TRL ≈ 4–5 for MSCC-ET | 447, 470, 472 and 507 |

© 2026 The Author(s). Published by the Royal Society of Chemistry

Open Access Article. Published on 12 fevral 2026. Downloaded on 01.06.2026 11:06:26. This article is licensed under a Creative Commons Attribution-NonCommercial 3.0 Unported Licence.

Table 34 Operating windows & flue-gas tolerance of DFMs

| Material class | $T$ (°C) | $P$ (bar) | $P_{CO_2}$ range | $H_2O$ tolerance | $SO_x/NO_x$ tolerance | Typical $j_{max}$ (mA cm$^{-2}$) | Ref. |
|---|---|---|---|---|---|---|---|
| POPs/CTFs | 25–100 | 0.1–5 | 0.01–0.15 | Moderate | Low | 10–50 (up to 201 for Ni–N/CNT@CTF) | 62, 82, 91 and 108 |
| COFs | 25–80 | 0.1–10 | 0.01–0.20 | Poor (hydrolysis) | Low | 5–100 | 149, 164 and 175 |
| MOFs | 25–150 | 0.1–40 | 0.01–1.0 | Poor–moderate (framework-dependent) | Variable | 200–380 (GDEs) | 247, 261–263, 266–270 and 273 |
| Zeolites | 25–500 | 0.1–20 | 0.01–0.15 | Excellent | Excellent | 100–440 (in integrated cells) | 183, 185, 199–201, 212 and 213 |
| Metal oxides | 25–400 | 1–10 | 0.10–1.0 | Good | Moderate | 6–200 | 294–299 |
| Amines | 40–120 | 0.1–2 | 0.01–0.15 | Excellent | Poor (degradation) | 20–200 | 305, 309, 312 and 319 |
| ILs | 25–100 | 0.1–93 | 0.01–1.0 | Good (hydrophobic ILs) | Moderate | 10–100 | 322, 323, 325, 356 and 383–388 |
| DES | 25–80 | 0.1–10 | 0.01–0.50 | Excellent | Good | 4–20 | 390, 402, 407, 408 and 429–434 |
| Molten salts | 550–900 | 0.1–5 | 0.01–0.15 | Excellent | Excellent | 200–1000 | 447, 465, 495 and 505 |

C deposition (molten salts), revealing an optimal $\Delta H_{ads}$ "Goldilocks window" (−40 to −60 kJ mol$^{-1}$) for kinetic balance. Synergy manifests quantitatively: Ag-MOF-$NH_2$ retains 93% $j_{CO}$ (355 mA cm$^{-2}$, 15% $CO_2$), DESs/ILs boost $FE_{CO}$ to 94% ($R_{ct}$ 65 Ω *vs.* 120 Ω $KHCO_3$), molten salts achieve 93% CNT selectivity at 1 A cm$^{-2}$, and amines deliver 44% energy savings *versus* thermal stripping, confirming local $P_{CO_2}$ enrichment, overpotential suppression (−240 mV IL onset), and transport optimization as validated ICCC performance drivers.

(Fig. 73) illustrates the distinct capture mechanisms, while Table 35 consolidates the associated intermediates, activation barriers, and their coupling to the rate-determining electrochemical steps across amines, ILs, and DES. While these classes differ in chemical functionality and solvation environments, they all modulate the local thermodynamics of $CO_2$ activation, proton availability, and electron-transfer barriers. Importantly, the comparison illustrates how capture strength (chemisorption *vs.* physisorption) does not simply correlate with performance; rather, it controls whether the apparent RDS shifts toward adsorption/desorption, first-electron transfer, or proton-coupled steps. This mechanistic synthesis provides a framework for rationally selecting capture media based on the desired catalytic pathway rather than solely on bulk absorption capacity.

The synergy between capture media and catalytic turnover is quantified by improvements in product selectivity and kinetic barriers compared to non-integrated systems. For amine-based CTCs, direct conversion of captured $CO_2$ has been demonstrated to bypass the energy-intensive desorption step. In an aqueous monoethanolamine capture solution, amine–$CO_2$ conversion to CO was achieved with a faradaic efficiency (FE) of 72% at 50 mA cm$^{-2}$, confirming that chemisorbed species contribute directly to the reduction pathway rather than acting merely as inert reservoirs.[312] Complementary work by Pérez-Gallent *et al.* reported the direct reduction of captured $CO_2$ to formate with FEs up to 50%, and to CO with efficiencies up to 45% in mixed amine media, significantly outperforming physical absorption baselines.[311] In contrast, synergy in Ionic Liquids (ILs) is primarily driven by selectivity tuning rather than raw reaction rate; functionalized imidazolium ILs have been shown to steer the reaction pathway toward formate with >85% selectivity by stabilizing the specific carboxylate intermediate, although overall turnover frequencies are often limited by viscosity.[321,330] Finally, in Deep Eutectic Solvents (DES), the hydrogen-bond network actively stabilizes the $CO_2$ radical anion intermediate, reducing the overpotential for $CO_2$ reduction by approximately 150–200 mV compared to conventional ILs while maintaining current densities above 10 mA cm$^{-2}$.[347,368] These quantitative results support the existence of distinct synergistic pathways: amines primarily enhance kinetic efficiency, ILs tune product selectivity, and DES networks lower the energetic overpotential.

Table 36 directly fulfills the explicit mechanistic demarcation, distinguishing settled capture paradigms OMS physisorption (MOFs, $\Delta H_{ads}$ −35 kJ mol$^{-1}$), zwitterion → carbamate (amines, FTIR/NMR-validated), carbonate chemisorption (molten salts), H-bonding networks (DESs), and ultramicropore confinement (COFs/CTFs/zeolites), from emerging dual-site hypotheses like Ag-cluster *COOH stabilization (amine-MOFs), DEA-$SnO_x$ *OCHO coupling (oxides), [Emim][2-CNPyrr] carbene-anion cooperativity (ILs), and N-site/CNT *$CO_2$ activation (POPs). Each hypothesis is rigorously qualified by quantitative performance gaps and TRL realities: Ag-MOF-$NH_2$ delivers 355 mA cm$^{-2}$ (93% retention, 15% $CO_2$) but hydrolyzes 80% capacity in humid cycles (TRL 3); DES HBA/HBD interfaces cut $R_{ct}$ to 65 Ω ($FE_{CO}$ 94%) yet cap $j$ at 20 mA cm$^{-2}$ due to 800 cP viscosity (TRL 2–3); molten $Ni^{2+}$/ZnO CNT nucleation achieves 93% carbon selectivity at 1 A cm$^{-2}$ but demands 900 °C Ni-Cr hardware (<5000 h, TRL 4–5). Critical verdict: while capture mechanisms stand on decades of equilibrium/spectroscopic data, dual-site $CO_2$RR claims remain system-specific, short-term (<100 h), and sub-industrial ($j$ < 200 mA cm$^{-2}$), necessitating GDE validation under impure feeds before scale-up confidence.

Porous organic polymers (POPs) exhibit structural diversity but face critical stability limitations under ICCC-relevant conditions (373 K flue gas, humid/$SO_x/NO_x$, oxidative potentials ±1.0 V *vs.* RHE). Table 37 quantifies thermal/oxidative resilience: CTFs demonstrate superior stability ($T_{decomp}$ > 500 °C, stable to −1.0 V *vs.* RHE over 10 h at 201 mA cm$^{-2}$) due to aromatic triazine linkages, while COFs suffer hydrolysis (>50% crystallinity loss after 100 h at 80% RH). Amorphous CMPs/PIMs oxidize rapidly under anodic potentials (+0.8 V), losing 60–70% surface area


© 2026 The Author(s). Published by the Royal Society of Chemistry

Open Access Article. Published on 12 fevral 2026. Downloaded on 01.06.2026 11:06:26.
This article is licensed under a Creative Commons Attribution-NonCommercial 3.0 Unported Licence.



Table 35 Comparative mechanistic framework across DFMs classes

| Material class | Adsorption route | $\Delta H_{ads}$ (kJ mol$^{-1}$) | Key intermediates | Active sites | Coupling between capture mode and RDS | RDS ($\Delta G_{RDS}$) | Synergy metric | Ref. |
|---|---|---|---|---|---|---|---|---|
| POPs/CTFs/CMPs | Physisorption in N-rich ultramicropores | −24 to −45 | *$CO_2$, *COOH | Triazine N, NiPor, CNT | Hydrophobic micropore confinement increases local $CO_2$ fugacity near catalytic sites, shifting the RDS to proton-coupled electron transfer | *COOH (0.58–0.59 eV) | Ni–N/CNT@CTF: $j_{CO}$ 201 mA cm$^{-2}$, $FE_{CO}$ 98% | 62, 88 and 90–92 |
| COFs | Pore confinement + imine/azine N-sites | −42 | *$CO_2$, *COOH | CoPc, imine N, $Cu^{2+}$ | Ordered 1D channels align $CO_2$ with functionalized linkers, lowering the entropic penalty of *COOH formation *via* cooperative host–guest interactions | *COOH (0.4–0.6 eV) | CoPc-PI-4COF: TOF 2.2 s$^{-1}$, $FE_{CO}$ 97% | 153 and 155 |
| MOFs | OMS coordination + amine physisorption | −30 to −80 | Metal-$CO_2$, *COOH | $Cu^{2+}$ OMS, Ag-$NH_2$ | $CO_2$ binds at open metal sites, lowering activation barriers, but overall ICCC rates are often limited by charge-transport resistance across non-conductive linkers | *COOH (0.4–0.6 eV) | Ag-MOF-$NH_2$: $j_{CO}$ 355 mA cm$^{-2}$ (93% retention, 15% $CO_2$) | 243 and 293 |
| Zeolites | Cation–π quadrupole + framework sites | −30 to −70 | Formates, *COOH | $Na^+$/$Ni^{2+}$, Brønsted acid | Extra-framework cations stabilize adsorbed $CO_2$ and transition states, while rigid pores and intracrystalline diffusion limit the overall ICCC rate | *$CO_2$ activation | CdO@Zn@Y: $FE_{CO}$ > 90% (120 h stable) | 199–201 and 234 |
| Metal Oxides/DFMs | Lewis acid–base + amine chemisorption | −50 to −90 | *OCHO, carbonates | $SnO_x$, Ni/Co NPs | Strong surface carbonate formation facilitates capture but imposes a high energy penalty on regeneration, coupling carbonate activation with catalytic turnover | *$CO_2$ → *COOH (0.8 eV) | DEA-$SnO_x$: $FE_{HCOO^-}$ 84% (6.7 mA cm$^{-2}$) | 294–299 |
| Amines | Chemisorption *via* zwitterion → carbamate/bicarbonate formation ($RNH_2 + CO_2 \rightleftharpoons RNHCOO^- + RNH_3^+$) | ∼20–40 kJ mol$^{-1}$ (typically lower for sterically hindered amines) | Zwitterion, carbamate, bicarbonate | Amine N atoms (primary/secondary) | Chemisorption increases local $CO_2$ activity and can lower the barrier for the first electron-transfer/desorption steps; however, overly strong binding may shift the apparent RDS toward regeneration | Carbamate hydrolysis | MEA/Ag: $FE_{CO}$ 72% (50 mA cm$^{-2}$, 44% energy savings) | 305, 308, 310 and 312–320 |
| ILs | Anion coordination/weak chemisorption or task-specific nucleophilic binding | ∼10–30 kJ mol$^{-1}$ (physisorption) and 40–60 kJ mol$^{-1}$ (chemisorption) | $CO_2$–anion complexes, carbene-like species | Anionic functional groups; imidazolium C2–H | Strong solvation stabilizes $CO_2^-$ and CO-forming pathways; viscosity and mass-transfer effects can shift the apparent RDS from electron transfer to diffusion control | *$CO_2$ (↓0.3 eV) | [Emim][2-CNPyrr]: $FE_{CO}$ 94% (onset −240 mV) | 321, 325, 330, 339, 340 and 389 |
| DES | H-bond network stabilization leading to bicarbonate/carbonate species | ∼15–35 kJ mol$^{-1}$ (H-bond networks reduce the barrier *vs.* neat IL analogues) | H-bonded $CO_2$, $HCO_3^-$/$CO_3^{2-}$ | HBD/HBA hydrogen-bond network (*e.g.*, urea–ChCl, glycerol–ChCl) | Hybrid chemisorption–physisorption environment promotes proton-coupled steps and often reduces overpotential (∼100–200 mV reported), without excessively penalizing desorption | *COOH ($R_{ct}$ 65 Ω) | DEACl:DEA: $FE_{CO}$ 94% (53 mol L$^{-1}$) | 347–349, 368, 390 and 439 |
| Molten salts | $O^{2-}$ nucleophilic → $CO_3^{2-}$ | −150 | $CO_3^{2-}$, C* | $Li^+$/Ni nuclei | Extra-framework cations stabilize adsorbed $CO_2$ and transition states, yet rigid pores and intracrystalline diffusion often govern the overall ICCC rate | C deposition ($4e^-$) | 93% CNT efficiency (j 0.2–1 A cm$^{-2}$) | 447 and 507 |

© 2026 The Author(s). Published by the Royal Society of Chemistry

Open Access Article. Published on 12 fevral 2026. Downloaded on 01.06.2026 11:06:26.
This article is licensed under a Creative Commons Attribution-NonCommercial 3.0 Unported Licence.

Table 36 Settled mechanisms *vs.* emerging dual-site hypotheses across ICCC materials

| Materials | Settled mechanistic understanding | Emerging dual-site/$CO_2$-activation hypothesis | Quantitative performance & failure mode | Ref. |
|---|---|---|---|---|
| MOFs | OMS-driven physisorption governs $CO_2$ uptake (*e.g.* HKUST-1 Type I isotherm, MOF-74 low-*P* capture; CALF-20 physisorbs $CO_2$ with $\Delta H_{ads} \approx -35$ kJ mol$^{-1}$ and retains capacity under humid gas) | Amine-enriched MOFs (Ag-MOF-$NH_2$) proposed to couple high $CO_2/N_2$ selectivity with *Ag-cluster COOH stabilization for dual capture–conversion; saturation of strong sites risks *$CO_2$/*COOH blocking | Ag-MOF-$NH_2$: $CO_2/N_2 \approx 280$ and $j_{CO} \approx 355$ mA cm$^{-2}$ from 15% $CO_2$; CALF-20–PGDE reaches ≈95% $FE_{CO}$ but requires weak physisorption to avoid product trapping; typical hydrolytically sensitive MOFs lose up to 80% capacity in a few humid cycles, and many systems stay <100 mA cm$^{-2}$, below ≥200 mA cm$^{-2}$ industrial target | 62, 65, 66, 90–92 and 243 |
| Metal oxides | Lewis acid–base capture: surface M–O sites and grafted amines form bicarbonate/carbamate pools; capture step is well described by chemisorption and $CO_2$ hydration equilibria | Dual-site view: local DEA enrichment at $SnO_x$ combines with *Sn–OCHO stabilization (lowering $\Delta G$ for formate pathway) to enable bifunctional capture–reduction | DEA–$SnO_x$/C: hydration doubles uptake; $FE_{HCOO^-} \approx 84\%$ at modest $j \approx 6$–8 mA cm$^{-2}$; viscosity rise and amine degradation during operation limit lifetime; membrane-type oxide BGDE designs still far from ≥200 mA cm$^{-2}$ and rarely tested *vs.* $O_2$/impurities | 294–299 |
| Amines | Zwitterion → carbamate mechanism is classical: $CO_2 + 2RNH_2 \rightarrow RNHCOO^- + RNH_3^+$; kinetics and speciation confirmed by FTIR/NMR and widely used in process models | Dual-site electrochemical hypothesis: amine EDL compression plus metal (Ag, Sn, *etc.*) centers create coupled capture–conversion micro-environments for *in situ* reduction of carbamate/bicarbonate | Ag/MEA and AMP/PC systems achieve ≈72–100% $FE_{CO}$ at ≈50 mA cm$^{-2}$, and AMP/PC boosts formate rates ~10×; however, viscosity, HER competition, oxidative degradation and 3–5 V cell voltages prevent reaching stable ≥200 mA cm$^{-2}$ and yield higher LCOE than gas-fed $CO_2$RR | 312–320 |
| ILs | Settled picture: physical solubility and specific anion–$CO_2$ interactions control capture; $CO_2$ loading and viscosity trends *vs.* anion/cation family are well mapped; bifunctional ILs like [Emim][2-CNPyrr] form carbamate adducts and shift onset by ≈ +240 mV | Dual-site hypothesis: $[Emim]^+$ carbene/$[2\text{-CNPyrr}]^-$ nucleophilic attack pre-activate $CO_2$ (*$CO_2$–IL adduct) and lower *$CO_2$ activation barrier *via* EDL compression | [Emim][2-CNPyrr] shifts $CO_2$RR onset by ≈240 mV and enables $FE_{CO}$ > 90–95% for ≥10–12 h, but viscosity explosion and proton transport disruption at high IL loading limit *j* and require dilution/mixtures; fluorinated ILs remain expensive and poorly tested under flue impurities | 330, 337, 338 and 389 |
| DESs | Settled: H-bonding networks between HBA/HBD components provide bifunctional capture and conductivity; DEACl:DEA DES shows strong $CO_2$ affinity and supports $ECO_2R$ with $FE_{CO} \approx 94\%$ at −1.5 V | Dual-site view: HBA/HBD cooperative binding plus interfacial structuring at the electrode create enriched $CO_2$ layers and tuned EDL, lowering $R_{ct}$ and facilitating *$CO_2$/*COOH formation | DEACl:DEA: $FE_{CO} \approx 94\%$, $R_{ct} \approx 65\ \Omega$ *vs.* 120 Ω in $KHCO_3$, but viscosity 200–800 cP cuts $D_{CO_2}$ and caps *j* at ≈10–20 mA cm$^{-2}$; $H_2O$ > 40 wt% disrupts DES structure and halves capacity | 390, 407, 408 and 439 |
| Molten salts | Settled: carbonate chemisorption ($CO_2 + O^{2-} \rightarrow CO_3^{2-}$) and high-*T* electrolysis to C or CO; molten $Li_2CO_3$–based systems make CNTs or carbon nano-onions directly from $CO_2$ with high selectivity | Dual-site hypothesis: $Ni^{2+}$/ZnO or other nucleation sites steer CNT *vs.* other carbon morphologies (*e.g.* onions *vs.* sheets) *via* local carbon supersaturation and metal–C interactions | Near-quantitative CNO or CNT yields (>90%) and industrial-level *j* (0.2–1 A cm$^{-2}$); however, 750–900 °C operation, Ni–Cr corrosion (<5000 h), and poor $SO_x$ tolerance raise energy and materials costs *vs.* low-*T* systems | 447, 470, 472 and 507 |
| COFs/ CTFs/ CMPs/ Zeolites | Settled: pore chemistry and ultramicroporosity dictate $CO_2$ uptake and selectivity (*e.g.* TPE-COF-II 118.8 cm$^3$ g$^{-1}$ at 273 K; N-rich CTFs and zeolite cation sites deliver high $CO_2/N_2$ selectivity) | Dual-site claims: coupling Lewis basic N sites or cation sites with confinement and conductive backbones (*e.g.* MWCNTs, π-systems) to facilitate *$CO_2$/*COOH activation in addition to capture | COFs/CTFs/CMPs deliver excellent low-P capture and $FE_{CO}$ up to ≈80–90% in some hybrid electrodes, but imine hydrolysis, N-site oxidation, and $H_2O$ competition in zeolites halve capacity under humid gas; most systems operate at $j$ < 100 mA cm$^{-2}$ and TRL remains low | 62, 130, 153 and 234 |

Table 37 Thermal/oxidative stability of porous polymer network platforms in ICCC conditions

| Material class | $T_{decomp}$ (°C) | Oxidative limit (V *vs.* RHE) | Stability in $CO_2$RR (h@$j_{max}$ | Ref. |
|---|---|---|---|---|
| CTFs | >500 | −1.0 to +0.8 | ≈20 h@201 mA cm$^{-2}$ (Ni–N/CNT@CTF) | 82, 86, 90–92, 104 and 108 |
| COFs | 300–400 | down to ≈−0.8 | ≈24 h@100 mA cm$^{-2}$ (best cases) | 149 and 162–164 |
| CMPs | 350–450 | up to ≈ + 0.5 (60–70% SSA loss in 24 h) | <12 h@50 mA cm$^{-2}$ | 62 and 164 |
| Zeolites (benchmark) | >800 | −1.2 to +1.5 | >1000 h@440 mA cm$^{-2}$ (integrated cells) | 183, 185, 199–201, 212, 213 and 233 |
| Molten salts (benchmark) | >1000 | Wide electrochemical window | >100 h@1 A cm$^{-2}$ ($CO_2$-to-C/CO) | 447, 465, 495 and 505 |

within 24 h, whereas HCPs maintain microporosity but swell irreversibly in water vapor (20% $V_{micro}$ loss). NiPor-CTF achieves 92.3% FECO stability over 20 h at 12.8 mA cm$^{-2}$ with $NiN_4$ sites intact, but F-CTFs lose 30% activity after 50 cycles due to C-F hydrolysis. Compared to zeolites (>1000 h stability at 440 mA cm$^{-2}$) and molten salts (>90% efficiency at 1000 °C), POPs require protective strategies: fluorination (FCTF-1: hydrophobic, $Q_{st}$ 24 → 40 kJ mol$^{-1}$), conductive backbones


© 2026 The Author(s). Published by the Royal Society of Chemistry

Open Access Article. Published on 12 fevral 2026. Downloaded on 01.06.2026 11:06:26.
This article is licensed under a Creative Commons Attribution-NonCommercial 3.0 Unported Licence.

Table 38 Kinetic benchmarking of dual-functional materials (DFMs), relating $CO_2$ adsorption/desorption dynamics to catalytic turnover frequencies to assess ICCC viability

| Material | Adsorption kinetics | Desorption kinetics | Catalytic TOF ($s^{-1}$) | Rate mismatch | Ref. |
|---|---|---|---|---|---|
| CTFs (PHCTF-1a/4) | Fast physisorption (<1 nm pores) | Moderate $Q_{st}$ 24–45 kJ $mol^{-1}$ | Ni-CTF: ~1–2 $s^{-1}$ (12.8 mA $cm^{-2}$) | Desorption > catalytic at low $P_{CO_2}$ | 82, 90–92 and 108 |
| MEA (amines) | Carbamate formation ~40 °C (fast) | Thermal stripping 1.5–2.5 GJ $t^{-1}CO_2$ (slow) | Ag: 72% FE at 50 mA $cm^{-2}$ | Stripping ≫ catalytic | 312 |
| MOFs (HKUST-1) | OMS binding ~30 kJ $mol^{-1}$ (fast) | Regeneration 100–150 °C (moderate) | Ag-MOF-$NH_2$: 355 mA $cm^{-2}$ | Well-matched in GDEs | 273 |
| Molten carbonates | $O^{2-} \rightarrow CO_3^{2-}$ equilibrium ~2 h | Instantaneous at 723 K | C deposition >90% at 1 A $cm^{-2}$ | Well-matched (high $T$) | 447 |

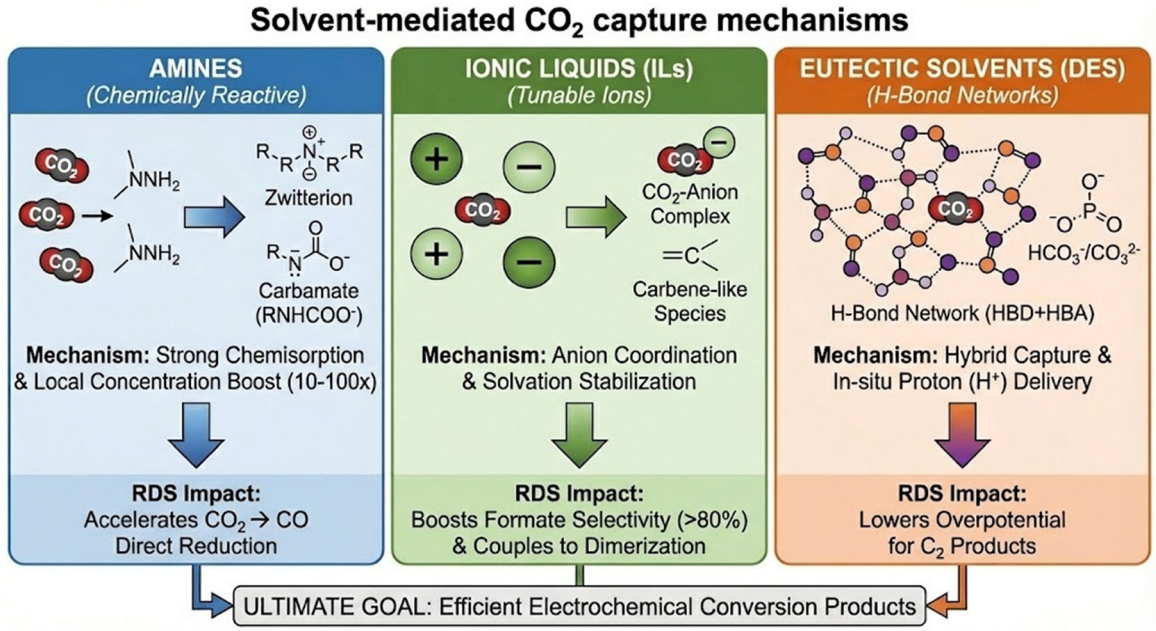


Fig. 73 Comparative mechanisms of solvent-mediated $CO_2$ capture and their impact on electrochemical reduction.

(Ni–N/CNT@CTF: 98% FECO, 201 mA $cm^{-2}$), and GDE encapsulation to shield against oxidative degradation and flue-gas impurities.

Integrated Carbon Capture and Conversion (ICCC) demand precise rate-matching between capture kinetics and electrocatalytic turnover frequencies (TOFs) to eliminate bottlenecks that plague decoupled systems. As shown in Table 38, while CTFs like PHCTF-4 exhibit rapid physisorption (52 $cm^3$ $g^{-1}$ at 273 K/1 bar in minutes) with moderate desorption energies ($Q_{st}$ 24–45 kJ $mol^{-1}$), Ni-CTF electrocatalysts deliver TOFs of ~1–2 $s^{-1}$ (12.8 mA $cm^{-2}$), requiring continuous $CO_2$ supply >10× faster than flue gas delivers (0.03 mmol $h^{-1}$ $cm^{-2}$ at 10% $CO_2$). Amine systems face the opposite problem: MEA carbamate formation occurs rapidly (~40 °C), but thermal stripping demands 1.5–2.5 GJ $t^{-1}CO_2$ over hours, creating >$10^3$-fold mismatch *versus* Ag cathodes operating at 50 mA $cm^{-2}$ turnover. Gas-diffusion electrode (GDE) architectures with MOF/DES interlayers elevate local $P_{CO_2}$ >1 atm, harmonizing rates to support industrial currents ≥200 mA $cm^{-2}$, while molten carbonates achieve natural synchronization at 723 K (>90% efficiency, 1 A $cm^{-2}$). Hierarchical porosity (micropores for binding, mesopores for diffusion) further reduces LTA zeolite kinetics by 29–92 s.[82,83,90–92,273,312]

Integrated carbon capture and conversion (ICCC) case studies consistently identify adsorption thermodynamics, catalytic kinetics, and operating temperature as the dominant, tightly coupled parameters governing system cost through their combined effects on regeneration energy, reactor sizing, and heat integration. The adsorption enthalpy ($\Delta H_{ads}$) of $CO_2$ defines a central thermodynamic trade-off: stronger binding enhances capture efficiency and single-pass utilization but increases regeneration or reactive release energy, whereas weaker binding lowers thermal demand at the expense of larger sorbent inventories. Process modeling and TEA of amine-based and dual-function material (DFM) ICCC systems show that variations in $\Delta H_{ads}$ of ~20–30 kJ $mol^{-1}$ can shift total $CO_2$ avoidance costs by ~25–40%, depending on cycle design and heat integration, making $\Delta H_{ads}$ one of the most economically sensitive thermodynamic parameters.[511] Furthermore, catalytic turnover frequency (TOF) is a primary kinetic cost lever, as it directly determines reactor volume and catalyst loading; ICCC case studies of DFM-assisted methanation demonstrate that order-of-magnitude increases in TOF can reduce reactor-related CAPEX by ~30–50%, with limited impact on operating costs.[512] Moreover, operating temperature as mentioned in (Table 34) further couples' kinetics, adsorption

Open Access Article. Published on 12 fevral 2026. Downloaded on 01.06.2026 11:06:26.
This article is licensed under a Creative Commons Attribution-NonCommercial 3.0 Unported Licence.

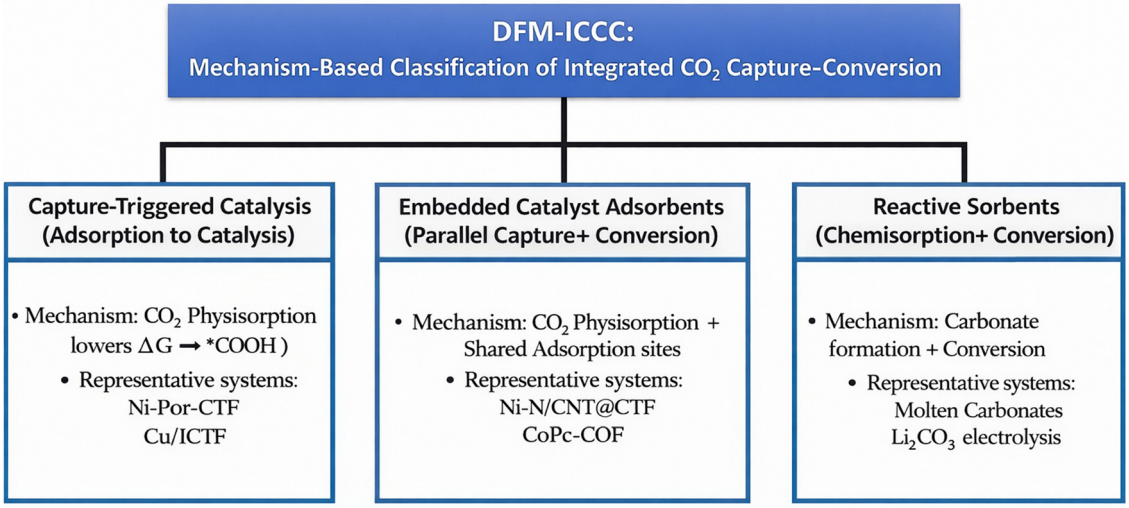


Fig. 74 Categorization of dual function materials. A breakdown of ICCC systems into three primary classes based on capture-conversion synergy.

equilibria, and heat recovery, with TEA of Ca-looping- and DFM-based ICCC systems showing that deviation from the optimal temperature window increases total system cost by ~20–35% due to inefficient heat integration and higher utility demand.[513] Collectively, these studies highlight that ICCC economics are governed by co-optimization of adsorption thermodynamics, catalytic activity, and operating temperature, underscoring the need for integrated material–process design.

The proposed classification framework in Fig. 74 categorizes DFM-ICCC platforms into three distinct strategies based on the synergy between the capture and conversion steps. Capture-Triggered Catalysis operates *via* a physisorption mechanism where the physical binding of $CO_2$ thermodynamically lowers the Gibbs free energy barrier ($\Delta G$) for the critical activation step ($*CO_2$ → *COOH), a pathway exemplified by systems such as Ni-Por-CTF. In contrast, Embedded Catalyst Adsorbents utilize the spatial integration of catalytic centers within porous frameworks (*e.g.*, CoPc-COF) to enable parallel capture and conversion at shared adsorption sites. Finally, Reactive Sorbents are distinguished by a chemisorption-driven mechanism; in these systems, such as molten carbonates or $Li_2CO_3$ electrolysis configurations, $CO_2$ is chemically fixed into stable carbonate intermediates which subsequently undergo conversion. This distinction highlights the progression from physical adsorption-assisted catalysis to chemical fixation-dependent transformation.

## Techno-economic analysis of ICCC

A techno-economic analysis (TEA) can assess the feasibility of ICCC, identify economically viable products, and determine the performance metrics necessary for achieving economic viability. In terms of technological evaluation, a reference process simulation is needed to estimate the mass and energy balance, which relies on thermodynamics properties and kinetic factors for producing reliable simulation results. Regarding economic evaluation, it comprises calculating the levelized cost of $CO_2$ capture, power price, separation cost, product selling price, and the $CO_2$ electrolyzers' CAPEX and OPEX. Consequently, it is crucial to conduct a discounted and undiscounted cash flow analysis, a sensitivity analysis of different process metrics, and an uncertainty analysis to determine which factors affect the project's environmental and economic feasibility. To illustrate the practical potential of integrated $CO_2$ capture and conversion technologies, several case studies and techno-economic assessments (TEAs) are discussed.

Regarding the ICCC system's efficiency, Xia *et al.* conducted a techno-economic analysis (TEA) for three different electrochemical $CO_2$ capture and reduction processes: independent $CO_2$ capture and electrochemical conversion, integrated $CO_2$ capture and conversion in a dual electrochemical cell, and integrated $CO_2$ capture and conversion in a single electrochemical cell.[514] And, they concluded that the independent system has the lowest energy efficiency as it involves multiple procedures of $CO_2$ capture, compression, and storage; about 55.56 GJ of energy was needed to produce 1 ton of CO. However, the dual electrolytic cell system, which consists of two electrolytic cells for both capturing and reduction processes under mild conditions without a $CO_2$ compression process, needs 44.38 GJ of energy to produce 1 ton of CO, compared to 27.41 GJ of energy for the single electrolytic cell system (Fig. 75a). Also, both independent and dual electrolytic systems show similar cost distributions, with capture and conversion together make up nearly 60% of the total cost while electrochemical conversion exceeds 70% in single-cell system despite its overall lowest total cost, highlighting the importance of energy efficiency in both stages (Fig. 75b). Furthermore, they highlighted that under optimistic conditions, producing 1 ton of CO from the single electrolytic cell system can cost $224 with a low cell voltage of 2.1 V, while reaching $342 per 1 ton of CO with a 60% conversion rate in the dual electrolytic cell system (Fig. 75c and d).

Compared to conventional decoupled Carbon Capture and Utilization (CCU), Li *et al.*[515] Integrated Carbon Capture and Utilization (ICCU) demonstrate superior thermodynamic


© 2026 The Author(s). Published by the Royal Society of Chemistry

Open Access Article. Published on 12 fevral 2026. Downloaded on 01.06.2026 11:06:26.
This article is licensed under a Creative Commons Attribution-NonCommercial 3.0 Unported Licence.

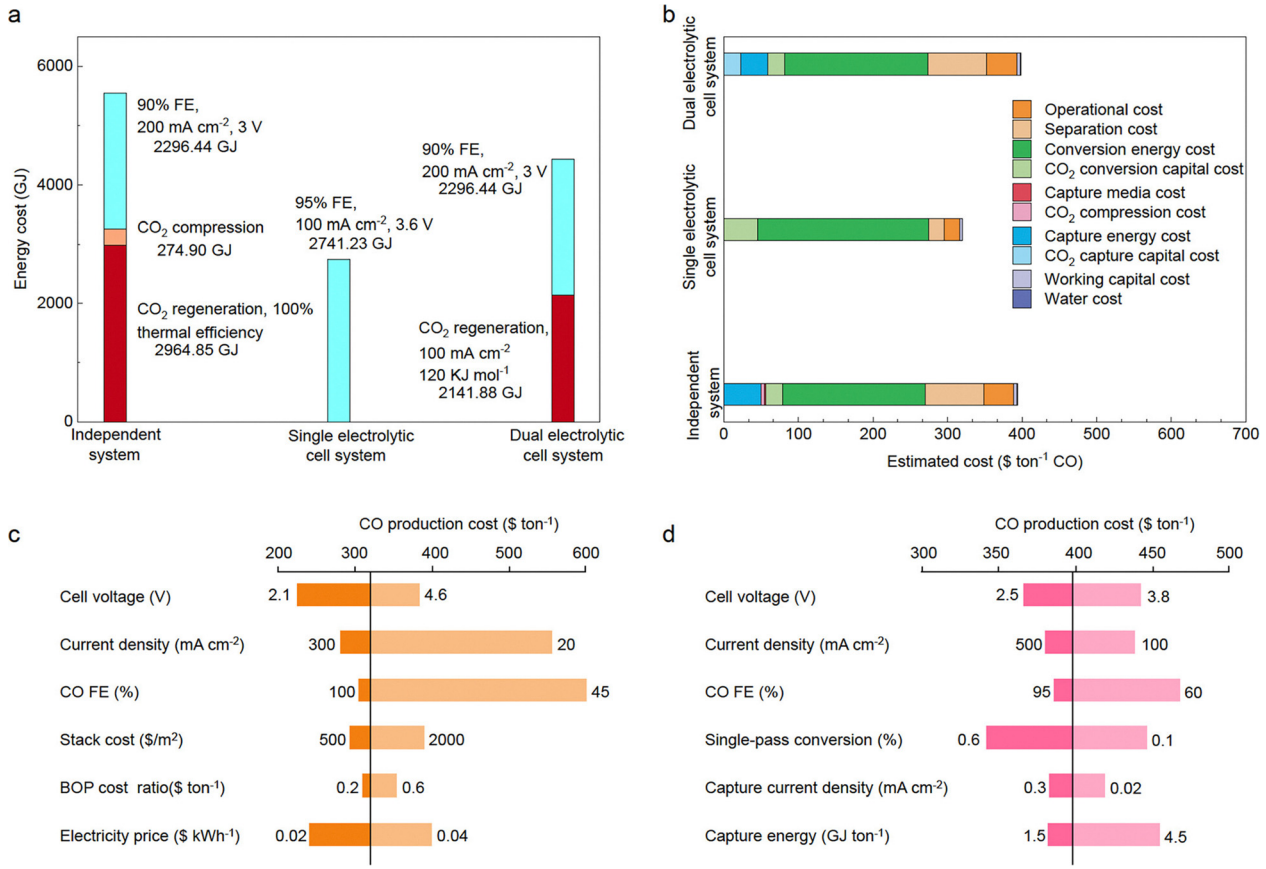


Fig. 75 (a) Comparative schematic of energy consumption for the production of 100 tons of CO across various systems. (b) Techno-economic assessment (TEA)-based estimation of CO production costs. (c) and (d). Sensitivity analysis of CO production costs for a single electrolytic cell system and a dual electrolytic cell system, respectively, based on optimistic and pessimistic parameter assumptions. Reprinted (adapted) with permission from *ACS Energy Lett.* 2023, **8**(6), 2840–2857. Copyright © 2023 American Chemical Society.

and economic performance. (Fig. 76) provides a comprehensive techno-economic and exergy comparison of four DRM-based configurations, conventional CCU, ICCU, and solar-driven direct and indirect ICCU (D-ICCU and ID-ICCU), highlighting the systemic benefits of integration and renewable energy coupling. The energy balance shows that all ICCU systems require lower reactor energy input than CCU because $CO_2$ capture and conversion occur in a single unit, eliminating transport-related penalties, although D-ICCU exhibits the lowest syngas output due to partial substitution of methane-derived energy with solar input as seen in (Fig. 76a). Economically in (Fig. 76b), *in situ* DRM reduces variable O&M costs from 389.03 M$ $year^{-1}$ in CCU to 322.49 M$ $year^{-1}$ in ICCU, while solar integration further lowers this value to approximately 268.7 M$ $year^{-1}$ in D/ID-ICCU, with methane feedstock remaining the dominant cost contributor (~70%), reflecting the strongly endothermic nature of $CaCO_3$ decomposition and DRM. In (Fig. 76c), exergy analysis indicates a progressive improvement from CCU (83.59%) to ICCU and solar-driven systems, with D-ICCU achieving the highest exergy efficiency (89.24%) and reducing exergy losses for $CO_2$ avoidance by more than 80%, while all ICCU configurations simultaneously generate high-value syngas (0.67–0.68 MWh $t^{-1}$). Correspondingly, $CO_2$ avoiding costs decrease sharply from 1464.22 $ $t^{-1}$ in CCU to 689.32 $ $t^{-1}$ in ICCU and further to 333–346 $ $t^{-1}$ in solar-driven ICCU, approaching MEA-based capture benchmarks; when electricity and carbon tax benefits are included, D-ICCU and ID-ICCU achieve costs as low as 208–216 $ $t^{-1}$, representing nearly a 79% reduction relative to CCU as proven in (Fig. 76d). Sensitivity analysis reveals that syngas cost is most sensitive to methane price in CCU and ICCU, whereas D/ID-ICCU exhibit enhanced resilience to fuel price volatility (Fig. 76e); catalyst cost has only a marginal effect across all systems (Fig. 76f), while increasing electricity prices and carbon taxes consistently improve the competitiveness of integrated configurations, with the strongest impact observed for solar-driven ICCU owing to greater $CO_2$ abatement (Fig. 76g and h). Notably, although ICCU alone reduces indirect $CO_2$ emissions by only 17.23% relative to CCU due to the unavoidable energy demand of $CaCO_3$ decomposition and DRM, solar-driven ICCU replaces approximately half of the fossil fuel input, lowering total $CO_2$ emissions to 24.10 and 24.83 kg $s^{-1}$ for D-ICCU and ID-ICCU, respectively, thereby positioning solar-assisted ICCU as a particularly promising pathway for scalable, low-carbon syngas production.

Moreover, Spurgeon *et al.* explored four different approaches for the synthesis of methyl formate ($HCOOCH_3$): a dual $CH_3OH$/$H_2O$ electrolyzer equipped with a $CO_2$ capture unit, a dual

Open Access Article. Published on 12 fevral 2026. Downloaded on 01.06.2026 11:06:26.
This article is licensed under a Creative Commons Attribution-NonCommercial 3.0 Unported Licence.

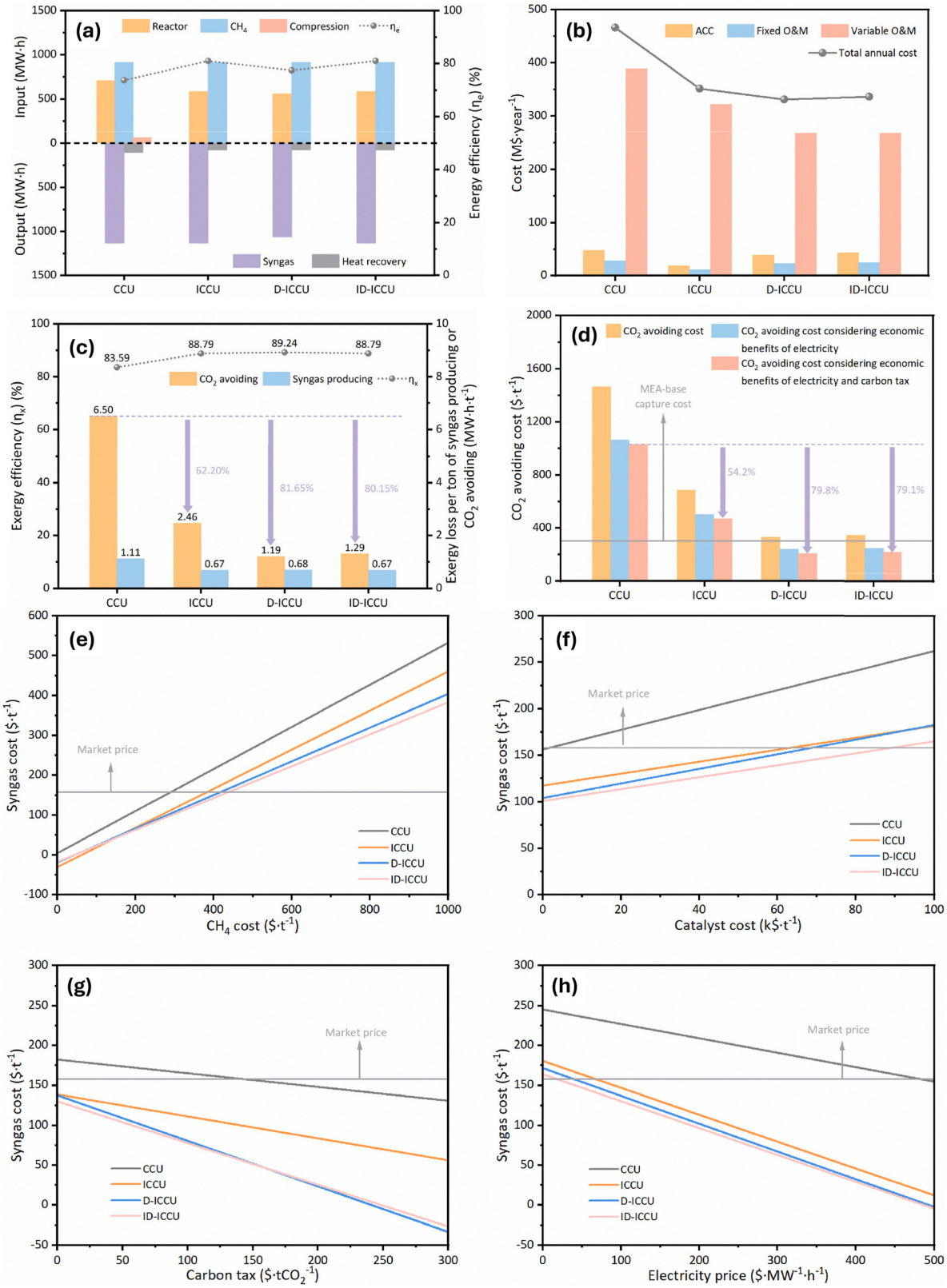


Fig. 76 Techno-economic and thermodynamic assessment of CCU, ICCU, D-ICCU, and ID-ICCU systems. (a) Total energy flows (input and output) and overall energy efficiency ($\eta_e$). (b) Economic evaluation breakdown including Annual Capital Cost (ACC), fixed and variable Operation & Maintenance (O&M) costs, and total annual cost. (c) Exergy efficiency ($\eta_x$) and exergy loss per ton of syngas produced or $CO_2$ avoided. (d) $CO_2$ avoiding cost. (e)–(h) Sensitivity analysis of syngas production cost with respect to variations in: (e) $CH_4$ cost, (f) Catalyst cost, (g) Electricity price, and (h) Carbon tax. The grey horizontal line in plots (e)–(h) indicates the market price. Reprinted (adapted) with permission from *Energy*, 2025, **316**, 134516. Copyright © 2025 Elsevier Ltd.


© 2026 The Author(s). Published by the Royal Society of Chemistry

Open Access Article. Published on 12 fevral 2026. Downloaded on 01.06.2026 11:06:26.
This article is licensed under a Creative Commons Attribution-NonCommercial 3.0 Unported Licence.

$CH_3OH/H_2O$ electrolyzer directly fed with flue gas, a $CH_3OH/CH_3OH$ electrolyzer with a $CO_2$ capture unit, and a $H_2O/H_2O$ electrolyzer producing HCOOH with a downstream HCOOH/$CH_3OH$ nonelectrochemical reactor.[516] And, their economic assessment revealed that the direct flue gas-fed dual $CH_3OH/H_2O$ electrolyzer exhibited the lowest production cost at \$1.37 per kilogram (Fig. 77c), followed by the $CH_3OH/CH_3OH$ electrolyzer with $CO_2$ capture at \$1.42 per kilogram (Fig. 77a), in comparison to the conventional commercial production cost of methyl formate at \$1.60 per kilogram. Then, they revealed that faradaic efficiency and the price of electricity significantly influence the production expenses of $HCOOCH_3$ while type of electrolyzers, flow rate, and current density exhibit modest impacts.

Furthermore, Nabil *et al.*[295] performed a comprehensive techno-economic analysis (TEA) for two scenarios: the conventional decoupled process and integrated/*in situ* separation and electrochemical conversion of $CO_2$ to ethylene from dilute streams (Fig. 78a). And, they stated that the integrated process can reduce the minimum selling price of ethylene by 20% as compared to the decoupled process by eliminating the energy-intensive capture, regeneration, compression and transportation steps. However, when they adopted stretch-target performance metrics by applying the optimistic integrated scenario of cell voltage = 1.60 V, current density = 500 mA $cm^{-2}$, and FE $C_2H_4$ = 65%, compared to the base scenario of cell voltage = 2.30 V, current density = 100 mA $cm^{-2}$, and FE $C_2H_4$ = 45%, the minimum selling price of ethylene significantly decreased by 79% compared to the decoupled process as it costed \$1.1 $kg^{-1}$ $C_2H_4$, which was lower than the market price, about \$1.3 $kg^{-1}$ $C_2H_4$ (Fig. 78b).

Additionally, Li *et al.* assessed the energy performance of sequential and integrated $CO_2$ capture and electrochemical conversion for CO generation.[511] In detail, sequential systems employ advanced gas-fed electrolyzers with either 50% or projected 100% $CO_2$ utilization, whereas integrated systems explore electrolysis performance under optimistic (3 V, 90% CO FE), baseline (4 V, 70% CO FE), and pessimistic (5 V, 40% CO FE) scenarios, emphasizing comparative energy demand and economic viability (Fig. 79a). In the optimistic case, where the integrated electrolyzer fully regenerates the amine, energy consumption dropped by 44% and energy costs by 22% compared to a sequential process (Fig. 79b and c). However, this energy benefit narrows to 26% if gas-fed electrolyzers without $CO_2$ losses to (bi)carbonate at high current densities. Under the pessimistic scenario, the integrated systems required far higher energy (2412 kJ $mol^{-1}$ $CO_2$) to drive the integrated conversion.

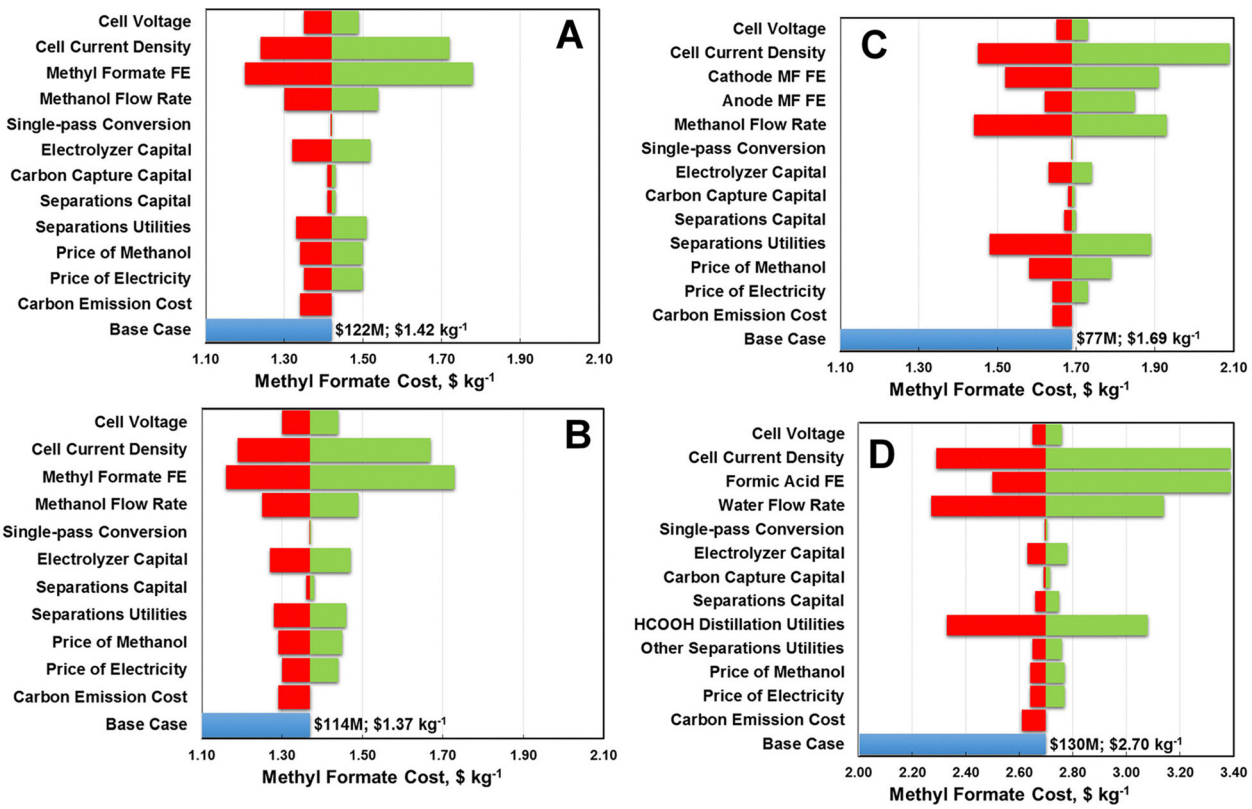


Fig. 77 Sensitivity analysis of four electrochemical systems for methyl formate production *via* $CO_2$ reduction, showing the impact of ±25% variation in key parameters on levelized cost (LC MF) and capital expense, with blue bars indicating base case estimates under a carbon emission cost of \$100 per tonne $CO_2$. (A) Electroreduction of captured $CO_2$ in a dual CH3OH/$H_2O$ electrolyzer. (B) Direct electroreduction of flue gas $CO_2$ in a dual $CH_3OH/H_2O$ electrolyzer. (C) Electroreduction of captured $CO_2$ in a $CH_3OH/CH_3OH$ electrolyzer. (D) Electroreduction of captured $CO_2$ in a $H_2O/H_2O$ electrolyzer with a downstream $CH_3OH$ reactor. Reprinted (adapted) with permission from *ACS Sustainable Chem. Eng.* 2022, **10**, 38, 12882–12894. Copyright © 2022 American Chemical Society.

Open Access Article. Published on 12 fevral 2026. Downloaded on 01.06.2026 11:06:26.
This article is licensed under a Creative Commons Attribution-NonCommercial 3.0 Unported Licence.

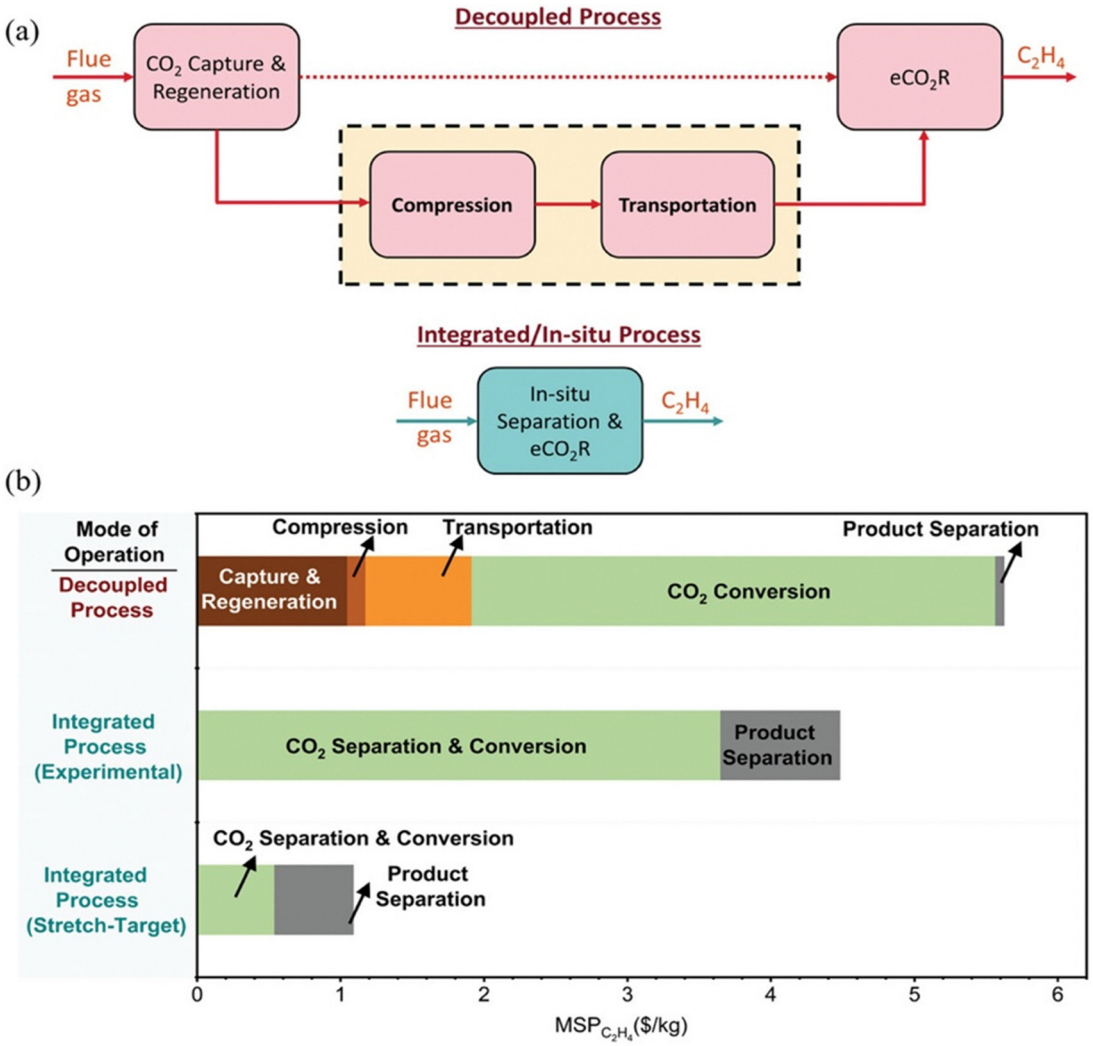


Fig. 78 (a) Comparative schematic and cost analysis of traditional decoupled *vs.* integrated $CO_2$ conversion processes to $C_2H_4$. (b) Cost analysis minimum selling price (MSP($C_2H_4$)) contributors for both approaches, showing lower costs in the integrated approach. Reprinted (adapted) from *Adv. Mater.* 2023, **35**(24), 2300389. Copyrights © 2023 The Authors. Published by Wiley-VCH GmbH under the terms of CC-BY license.

Thus, they pointed out further improvement on faradaic efficiency and cell voltage at industrial current densities is essential to reduce energy consumption at least similar to the gas-fed electrolyzer performance, otherwise, the sequential method remains effective.

Moreover, Pinto *et al.* performed a techno-economic and life-cycle assessment of formate production from blast-furnace gas using either an electrocatalytic route (ER) or a biocatalytic route (BR).[517] With faradaic efficiency 81% and current density 100 mA $cm^{-2}$, ENaF70% and ENaF60% had a production cost between \$1.07 and \$0.71 per kg which was lower than for biocatalysis (BNaF70% and BNaF50%), about \$0.93–\$1.39 per kg, considering uncertainty analysis of electricity/power cost and H2 purchase cost which varied between 0.07 and 0.10 USD per kWh and 0.60–1.0 USD per kg respectively (Fig. 80). Life-cycle assessment reveals that biocatalysis achieved lower product carbon footprints, achieving a net-emissions reduction below petrochemical formate in 58% of simulations, compared to just 2% for electrocatalysis. Although, electrolysis can offset up to 77% of its emissions through carbon-negative credits from blast-furnace-gas valorization, its overall global warming potential (GWP) remains higher.

Kim *et al.* conducted a comprehensive technoeconomic assessment demonstrating the feasibility of an integrated ''reactive carbon capture'' system, which simultaneously captures atmospheric $CO_2$ and directly converts it into carbon monoxide (CO) within a single closed-loop process using a bicarbonate electrolyzer.[518] They addressed the challenge between the high pH required for efficient $CO_2$ capture and the lower pH preferred for electrolysis by employing chemical promoters such as piperazine to accelerate capture kinetics, enabling a cost-effective capture unit. Based on a mass-balance model of the optimized setup, the analysis estimated a break-even CO production cost of \$0.72 $kg_{CO}^{-1}$ without separations, \$0.94 $kg_{CO}^{-1}$ with separations, and \$0.86 $kg_{CO}^{-1}$ with separations and a promoter (Fig. 81), thereby reinforcing the potential


© 2026 The Author(s). Published by the Royal Society of Chemistry

Open Access Article. Published on 12 fevral 2026. Downloaded on 01.06.2026 11:06:26.
This article is licensed under a Creative Commons Attribution-NonCommercial 3.0 Unported Licence.

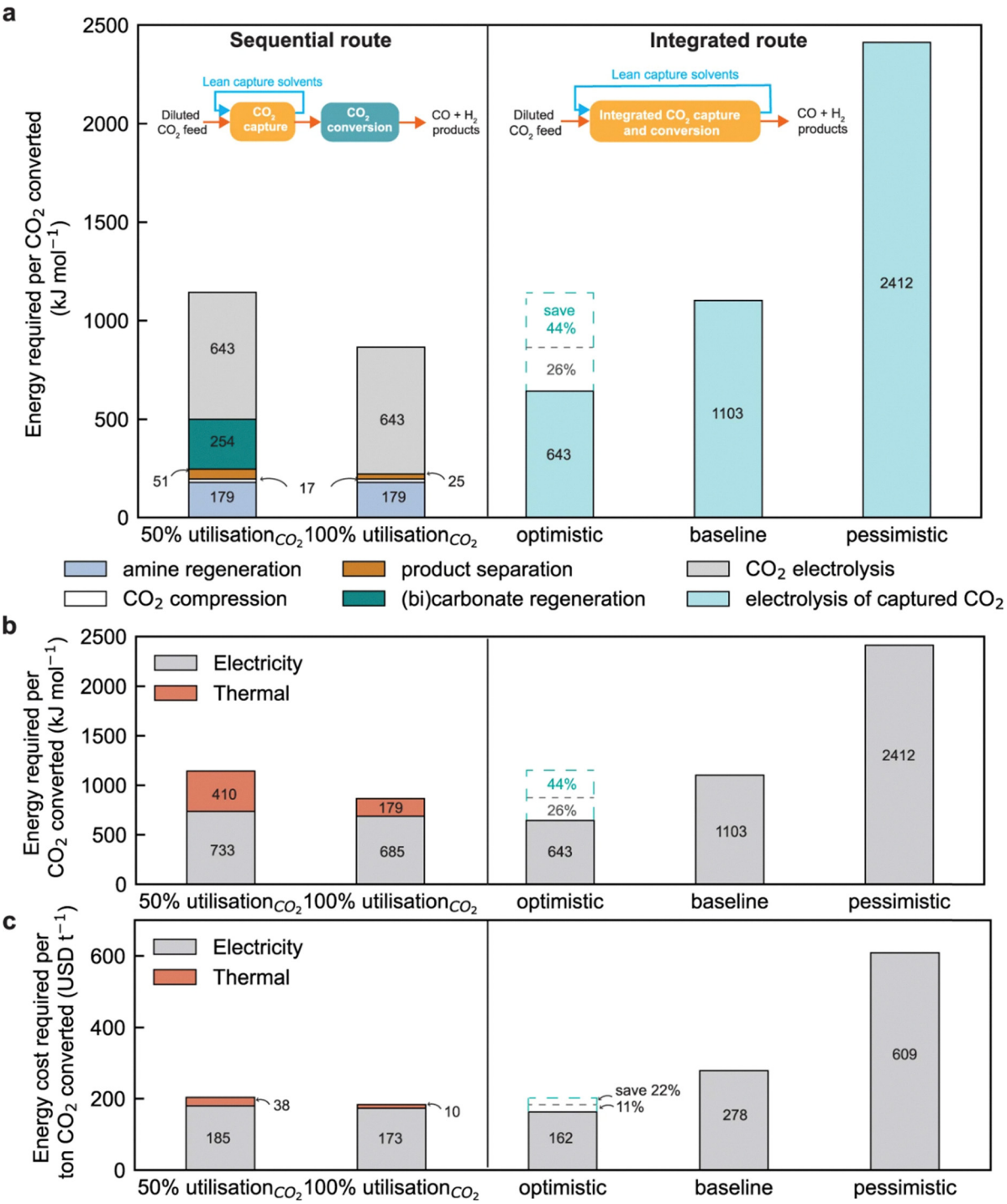


Fig. 79 Scenario analysis of (a), overall energy consumption for sequential and integrated routes. (b) Thermal energy and electricity consumption. (c) Energy cost. Reprinted (adapted) from *Nat Commun* 2022 **13**, 5398. © 2022 The Authors. Published by Springer Nature under the terms of CC-BY license.

of reactive carbon capture as a scalable and viable route for carbon utilization.

Regarding carbon capture and utilization (CCU) *versus* Carbon capture and storage (CCS), Rathore *et al.*[519] assessed the role of both pilot-scale technologies in mitigating $CO_2$ emissions from the highly carbon-intensive steel sector, highlighting both their technical potential and the economic and operational challenges associated with large-scale deployment. In the Blast Furnace–Basic Oxygen Furnace (BF-BOF) route, as shown in (Fig. 82a), the base production cost is INR 28 979 per tcs (~USD 350 per tcs) at an emission intensity of ~2.4 $tCO_2$ per tcs. When CCS is applied at USD 92 per $tCO_2$, costs rise to about INR 38 000 per tcs (~USD 460 per tcs) at ~0.6 $tCO_2$ per tcs, while near-zero steel enabled by CCU at USD 468 per $tCO_2$ increases costs

Open Access Article. Published on 12 fevral 2026. Downloaded on 01.06.2026 11:06:26.
This article is licensed under a Creative Commons Attribution-NonCommercial 3.0 Unported Licence.

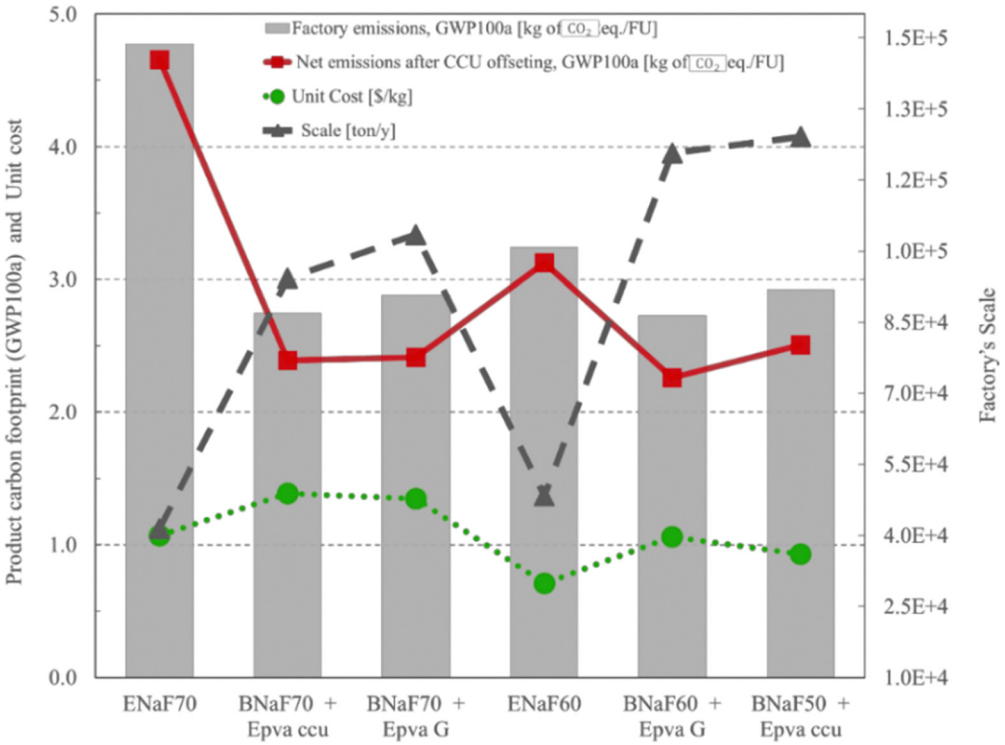


Fig. 80 Summary of TEA and LCA for formate production. Reprinted (adapted) from *ACS Sustainable Resour. Manage.* 2025, **2**(5), 733–743. Copyrights © 2025 The Authors. Published by American Chemical Society under the terms of CC-BY license.

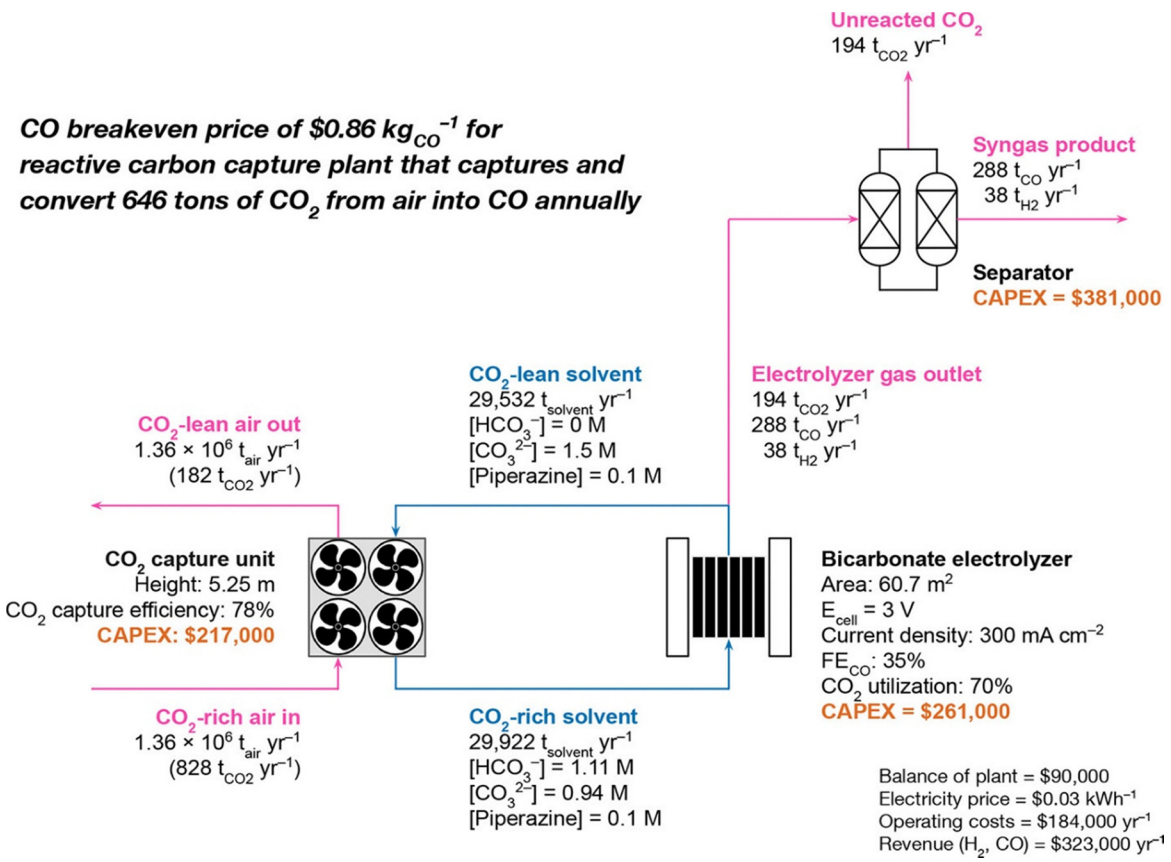


Fig. 81 Process flow diagram and techno-economic analysis of an integrated reactive carbon capture system. Reprinted (adapted) from *ACS Energy Lett.* 2025, **10**(1), 403–409. Copyright © 2025, American Chemical Society.

 © 2026 The Author(s). Published by the Royal Society of Chemistry

Open Access Article. Published on 12 fevral 2026. Downloaded on 01.06.2026 11:06:26.
This article is licensed under a Creative Commons Attribution-NonCommercial 3.0 Unported Licence.

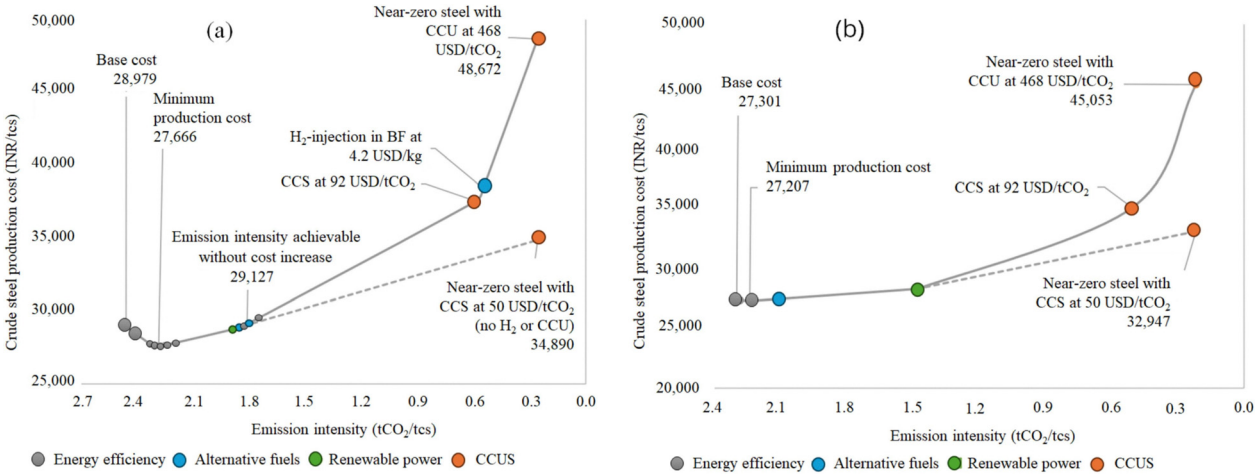


Fig. 82 Economic feasibility of steel decarbonization, highlighting initial emission reduction potentials of (a) 25% (BF-BOF) and (b) 8% (coal DRI-IF) at zero marginal cost. Reprinted (adapted) from *Energy Sustain. Dev.* 2025, **89**, 101866. Copyrights © 2025 by International Energy Initiative. Published by Elsevier Inc.

sharply to INR 48 672 per tcs (~USD 585 per tcs) at ~0.3 $tCO_2$ per tcs. In comparison, the Coal-based Direct Reduced Iron–Electric Arc Furnace (DRI–IF) route, as shown in (Fig. 82b), starts from a slightly lower base cost of INR 27 301 per tcs (~USD 330 per tcs) at ~2.3 $tCO_2$ per tcs. With CCS at USD 92 per $tCO_2$, costs rise to around INR 35 000 per tcs (~USD 420 per tcs) at ~0.6 $tCO_2$ per tcs, while near-zero steel enabled by CCU at USD 468 per $tCO_2$ reaches INR 45 053 per tcs (~USD 540 per tcs). Overall, although both routes exhibit strong cost sensitivity to CCS and CCU, the DRI–IF pathway consistently maintains a modest cost advantage at comparable emission intensities. They have also emphasised that, despite encouraging results from pilot-scale CCU projects such as Tata Steel India, ArcelorMittal Belgium, and HIsarna Netherlands, which report capture efficiencies of 80–90% and partial GHG reductions of 30–50%, progress is still limited by the lack of standardized monitoring, reporting, and verification (MRV) frameworks. This restricts the comparability of outcomes across different sites and technologies. CCU systems, particularly solvent-based capture, remain highly energy-intensive, requiring 3–4 GJ per ton of $CO_2$ captured, and face integration challenges with existing steelmaking operations, including solvent degradation, impurity management, and limited utilization of waste heat. Economic evaluations highlight that high capital expenditures ($100–300 per ton of $CO_2$) and operational costs ($20–50 per ton of $CO_2$) result in long payback periods, making the deployment of CCU heavily dependent on supportive policies such as carbon pricing, tax incentives, or subsidies. Furthermore, scale-up and replicability remain uncertain, as most pilots are tailored to site-specific conditions and lack standardized modular designs, while limited $CO_2$ transport and storage infrastructure further constrains widespread adoption. Finally, life-cycle assessments indicate potential environmental benefits but show wide variability due to differences in system boundaries, assumptions on energy sources, and product lifespans, underscoring the need for harmonized LCA methodologies to quantify net climate impacts reliably.

Regarding the usage of flue gas in comparison with pure $CO_2$, Tian *et al.* developed a 2D steady-state multi-physics model to compare $Cu_xO$-catalyzed $CO_2$ electrolysis fed with purified $CO_2$ to a direct-flue-gas feed containing 20% $CO_2$, 4% $O_2$, 0.5% $SO_2$ and balance $N_2$.[520] At atmospheric pressure and room temperature, the hydrogen evolution reaction (HER) dominated the electrochemical reduction of flue gas, reaching a faradaic efficiency of 91.5% at −1.17 V *vs.* RHE due to the low $CO_2$ partial pressure and competitive oxygen reduction. To overcome these limitations, the study proposed an effective optimization strategy by increasing the operating pressure to 20 atm and reducing the catholyte inlet temperature to 273 K, which significantly enhanced the $CO_2$ reduction reaction with a faradaic efficiency of 71%, compared to pure $CO_2$ electrolysis under standard conditions with a faradaic efficiency of 56% (Fig. 83a). Notably, the yield of valuable $C_1$ products from optimized flue gas became more than 2.3 times greater than pure $CO_2$ electrolysis, which may simplify downstream separation and improve system efficiency (Fig. 83b). The study also explained that this optimization strategy homogenized the dissolved $CO_2$ concentration and mitigated the high temperature in the catalyst layer caused by the increased current density and $SO_2$ partial pressure in the flue gas. Economically, the flue gas electrolysis system required 2 years to reach its break-even point, while the purified $CO_2$ system took 4 years (Fig. 83c). Also, over a 20-year lifecycle, the flue gas electrolysis had a net present value 1.5 times higher than that of purified $CO_2$ electrolysis, making it a more profitable and scalable solution.

To enhance the economic viability of electrochemical $CO_2$ reduction ($eCO_2R$), it can be coupled with anodic oxidation reactions that have lower thermodynamic cell potentials than the oxygen evolution reaction (OER) and yield other value-added byproducts, but it is needed to effectively design the electrolysis system, including optimized flow fields, reactant feeding rates, and integrated systems for industrial applications for efficient conversion.[521] To illustrate, Verma *et al.* stated that coupling $eCO_2R$ with glycerol electro-oxidation reduces energy consumption

Open Access Article. Published on 12 fevral 2026. Downloaded on 01.06.2026 11:06:26.
This article is licensed under a Creative Commons Attribution-NonCommercial 3.0 Unported Licence.

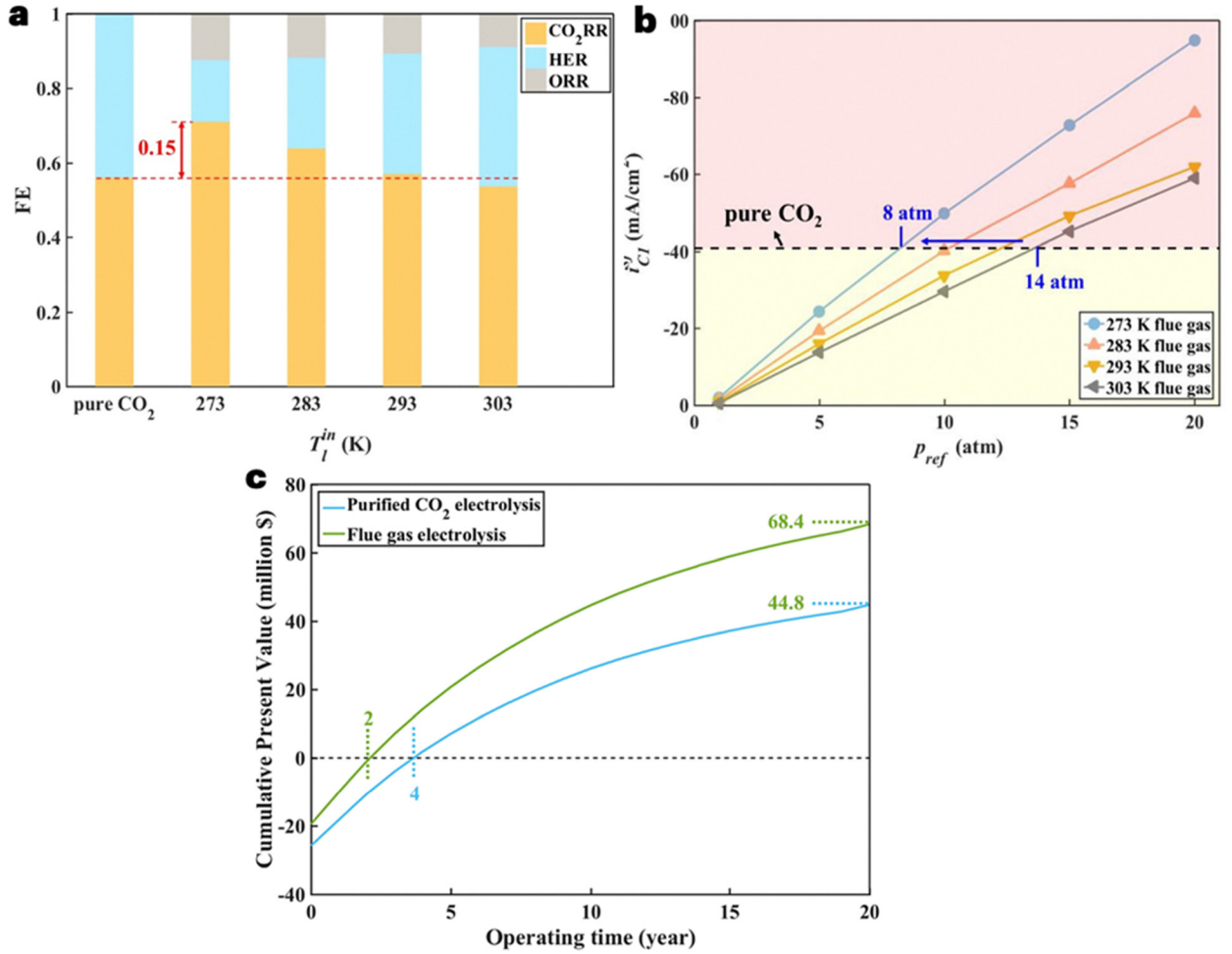


Fig. 83 (a) Effect of electrolyte inlet temperature on FE for flue gas electrolysis at $P_{ref}$ = 20 atm, $V_{app}$ = −1.17 *vs.* RHE. (b) Variation of current density of C1 products in flue gas electrolysis with temperature and pressure at −1.17 *vs.* RHE. (c) Cumulative present value analysis for flue gas electrolysis and purified $CO_2$ electrolysis. Reprinted (adapted) from *Applied Energy*, 2023 **351**, 121787. Copyrights © 2023 The Authors, Published by Elsevier Ltd.

by 37–53% compared to using OER,[522] while reducing the onset cell potentials for the production of HCOOH, $C_2H_4$, and $C_2H_5OH$ to −0.9 V, −0.95 V, and −1.3 V, compared to −1.75 V, −1.8 V, and −2.1 V, respectively, when applying OER (Fig. 84a–c). Also, the onset cell potentials for CO formation reduced to −0.75 V with glycerol and −0.95 V with glucose, *versus* −1.6 V under OER conditions (Fig. 84d). Thus, these reductions in cell potential enhance both $CO_2$ utilization efficiency and technoeconomic viability of the process.

Additionally, Jiang *et al.* developed an $H_2$-integrated $CO_2$ reduction ($CO_2RR$) system that couples $CO_2$ electrolysis with the hydrogen oxidation reaction (HOR) in a single cell, mediated by a $Ni(OH)_2$/NiOOH redox layer that blocks carbon crossover and catalyst poisoning (Fig. 85a).[523] At a current density of 50 mA $cm^{-2}$, the $H_2$-integrated $CO_2$ electrolysis cell delivers CO or formate with up to 95.3% faradaic selectivity at voltages below 0.9 V and remains stable for more than 100 h. They concluded that this approach reduced the total polarization loss by up to 22% and the overall energy consumption by up to 42% compared to conventional $CO_2$ electrolysis, offering a scalable route to integrate $CO_2$ electrolysis with the hydrogen economy (Fig. 85b and c).

Besides that, Wang *et al.* paired acidic $CO_2$-to-CO electroreduction with allyl alcohol oxidation reaction to acrolein, achieving a faradaic efficiency of 96% for $CO_2$-to-CO on the cathode and 85% for allyl alcohol-to-acrolein on the anode (Fig. 86a and b).[524] And, they observed a reduction in the system's full-cell voltage by 0.7 V (Fig. 86c), leading to 1.6 times less energy usage than the most efficient $CO_2$-to-CO $eCO_2R$ process (Fig. 86d). Also, the cell reached 84% single-pass $CO_2$ utilization with a 6 times improvement in atom efficiency by operating in acid and suppressing carbonate formation.

Regarding the feasibility assessment for the $eCO_2R$ products, Gao *et al.* conducted a techno-economic analysis (TEA) of four main products: HCOOH, CO, $C_2H_5OH$ and $C_2H_6$ while assuming $CO_2$ capture cost is $40 per ton of $CO_2$, using the post-combustion method due to its current level of maturity and technological capability.[525] And, they highlighted that, in the base scenario, formic acid at $0.468 per kg and CO at $0.449 per kg are cost-competitive, whereas ethanol at $1.872 per kg and ethylene at $2.907 per kg are not yet economically viable because FE of ethanol and ethylene (60%) is lower than that of formic acid and carbon monoxide, about 80%. For sensitivity analysis, a 25% increase in


© 2026 The Author(s). Published by the Royal Society of Chemistry

Open Access Article. Published on 12 fevral 2026. Downloaded on 01.06.2026 11:06:26.
This article is licensed under a Creative Commons Attribution-NonCommercial 3.0 Unported Licence.

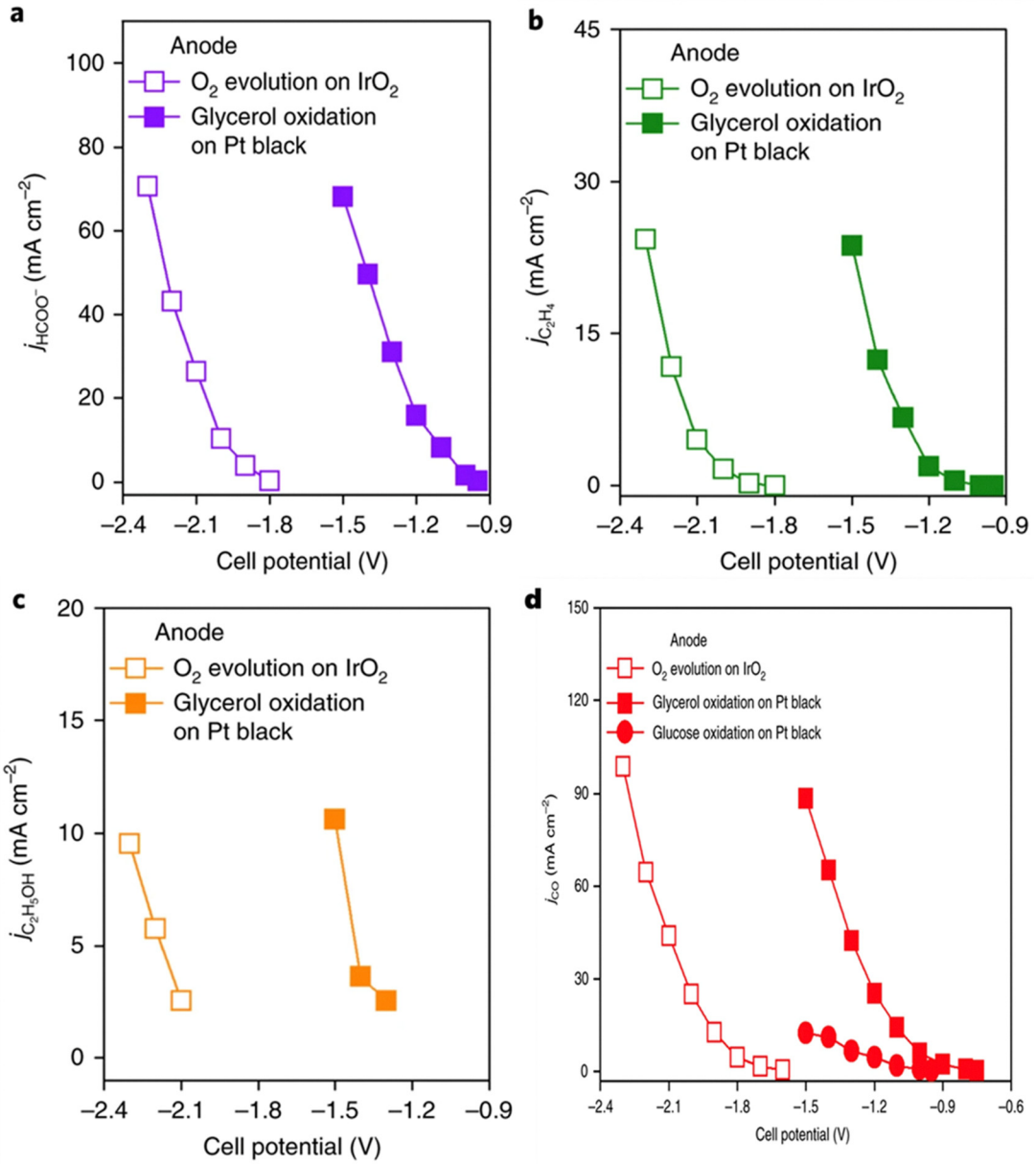


Fig. 84 Electrochemical performance for the electroreduction of $CO_2$, coupled to $O_2$ evolution, glycerol electro-oxidation or glucose electro-oxidation at the anode: Partial current densities plotted against applied cell potential for (a) formate ($HCOO^-$). (b) Ethylene ($C_2H_4$). (c) Ethanol ($C_2H_5OH$) under oxygen evolution (OER) and glycerol oxidation at the anode. (d) Carbon monoxide (CO) under OER, glycerol, and glucose oxidation at the anode. Reprinted (adapted) from *Nat Energy* 2019, **4**, 466–474. Copyrights © 2019, The Author(s), under exclusive license to Springer Nature Limited.

selectivity lowers the levelized cost by ~10.8% (HCOOH), ~16% (CO), ~18% ($C_2H_5OH$), and ~19% ($C_2H_6$), while a 25% reduction in cell voltage cuts costs by ~10.2%, ~18%, ~34%, and ~13%, respectively (Fig. 87a–d). Also, after performing a net present value (NPV) study, they found out that formic acid and CO generate positive NPVs of $89.86 million and $52.11 million, respectively, by the 20th year, while ethanol and ethylene consistently show negative NPVs, reaching −$134.88 million and −$537.79 million, which validates the advantage of C1 chemical production *via* $CO_2$ electrolysis (Fig. 87e). Furthermore, formic acid and carbon monoxide achieved energy conversion efficiencies (EE) values of 35.1% and 39.3%, respectively, while ethanol and ethylene recorded substantially lower efficiencies of 23.7% and 24.3%, reinforcing the viability of $C_1$ product formation in $CO_2$ electrolysis systems (Fig. 87f). Finally, they found out that as all assessed renewable energy could generate a carbon-negative effect, hydroelectricity displayed the most negative value at −1.89 kg of $CO_2$ equiv., followed by −1.75 kg of $CO_2$ equiv. for wind energy. Whereas, concentrated solar power (CSP) technology is a highly desirable renewable energy supply with −1.69 kg of $CO_2$ equiv. over −1.57 kg of $CO_2$ equiv. for PV due to CSP's direct steam generation for the electrolysis plant's downstream separation process.

In terms of solar-driven electrochemical $CO_2$ reduction, Chae *et al.* performed TEA study for PV-Chae *et al.* developed

Open Access Article. Published on 12 fevral 2026. Downloaded on 01.06.2026 11:06:26.
This article is licensed under a Creative Commons Attribution-NonCommercial 3.0 Unported Licence.

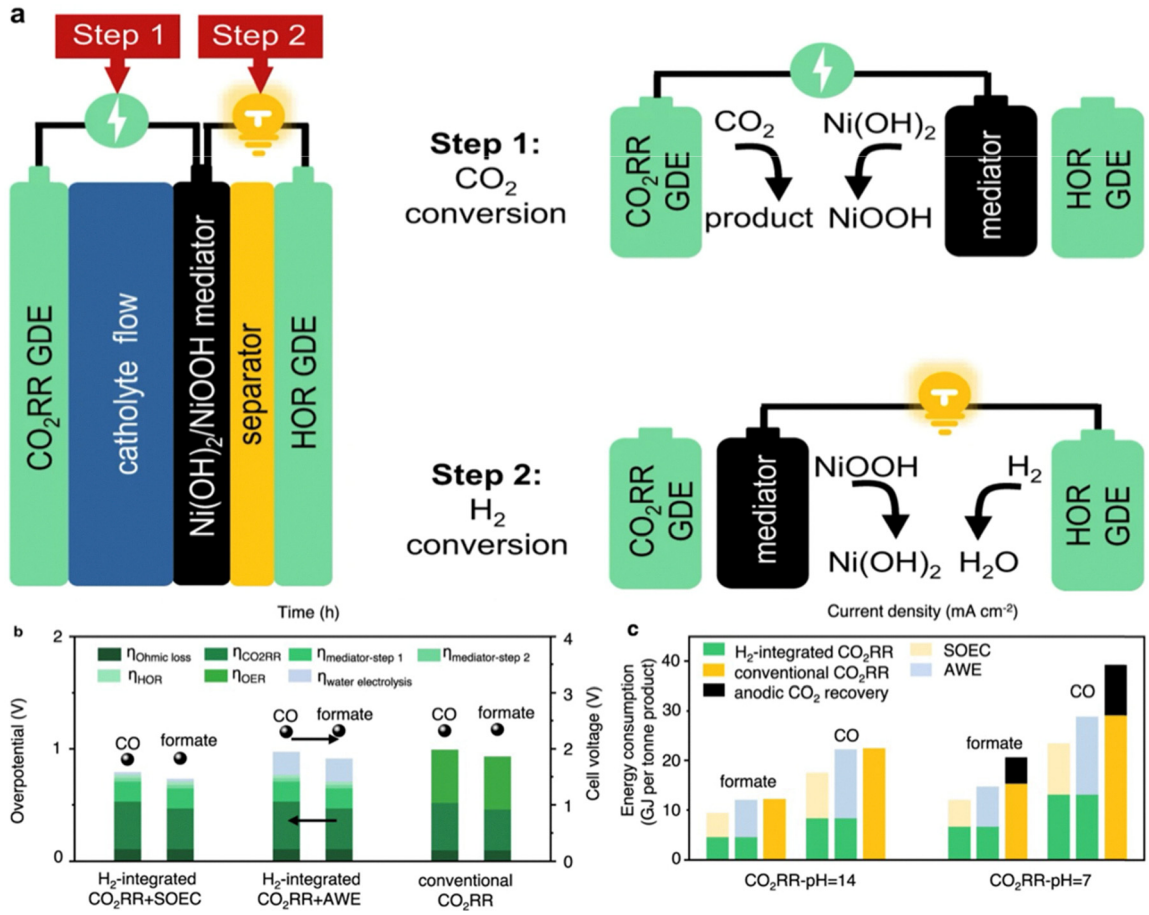


Fig. 85 (a), Schematic of the $H_2$-integrated $CO_2$ electrolysis cell architecture. (b) Polarization loss analysis for $H_2$-integrated $CO_2$ electrolysis. (c) Energy consumption analysis. Reprinted (adapted) from *Nat Commun*, 2024 **15**, 1427. Copyrights © 2024 The Authors. Published by Springer Nature under the terms of CC-BY license.

a solar-powered device for $CO_2$-to-CO conversion, achieving 8.03% solar-to-CO efficiency and estimating a base-case production cost of $10.94 per kg CO at a 4 MW scale (Fig. 88a and b).[526] To compete with the traditional CO price of $0.6 per kg, a sensitivity analysis revealed that the current density must be improved to $>80$ mA $cm^{-2}$ and the $CO_2$ one-path conversion must reach 22% or boosting solar-to-CO efficiency to 20% while halving the membrane cost (Fig. 88c and d). Finally, the study estimated a required carbon tax of $6.6/kg $CO_2$ to bridge the gap with fossil-derived CO pricing.

Furthermore, Agliuzza *et al.* demonstrated that solar-driven $CO_2$ electroreduction to CO, powered by dye-sensitized solar cells (DSSCs), achieved a faradaic efficiency of 73.85% at a current density of 3.35 mA $cm^{-2}$ under 1 sun illumination (Fig. 89a). These results were validated by a mathematical model and sustained efficiencies of 68.5% and 64.1% under reduced light intensities of 0.8 and 0.6 suns, respectively (Fig. 89b), which reproduced by the experimental chronoamperometry and simulated data (Fig. 89c and d). The study highlights the need to address the performance decline of $CO_2$RR under lower incident power for effective PV-EC optimization systems for real-world deployment.[527]

While techno-economic assessments provide valuable initial insights, it is crucial to recognize that most of these analyses are typically conducted under idealized laboratory conditions, presenting best-case scenarios that may not fully account for the complexities of industrial application. Although laboratory prototypes may perform well, demonstrating durability over thousands of hours and scaling from small single cells (1–25 $cm^2$) to industrial stacks (0.01–1 $m^2$) introduces major challenges such as catalyst degradation, mass transport limitations, Ohmic losses, and more. And, addressing these barriers requires multidisciplinary approaches, so the following section will provide a detailed analysis of the key Performance Indicators, challenges, opportunities, and future prospects for ICCC.

## Key performance indicators for ICCC

The key performance indicators for $CO_2$ capture and electrochemical conversion to consider in the TEA study when developing electrocatalysts for the final product are stability, cell voltage, faradaic efficiency, and current density, with carbon efficiency, product purity, productivity, capacity, and more for both industrial


© 2026 The Author(s). Published by the Royal Society of Chemistry

Open Access Article. Published on 12 fevral 2026. Downloaded on 01.06.2026 11:06:26.
This article is licensed under a Creative Commons Attribution-NonCommercial 3.0 Unported Licence.

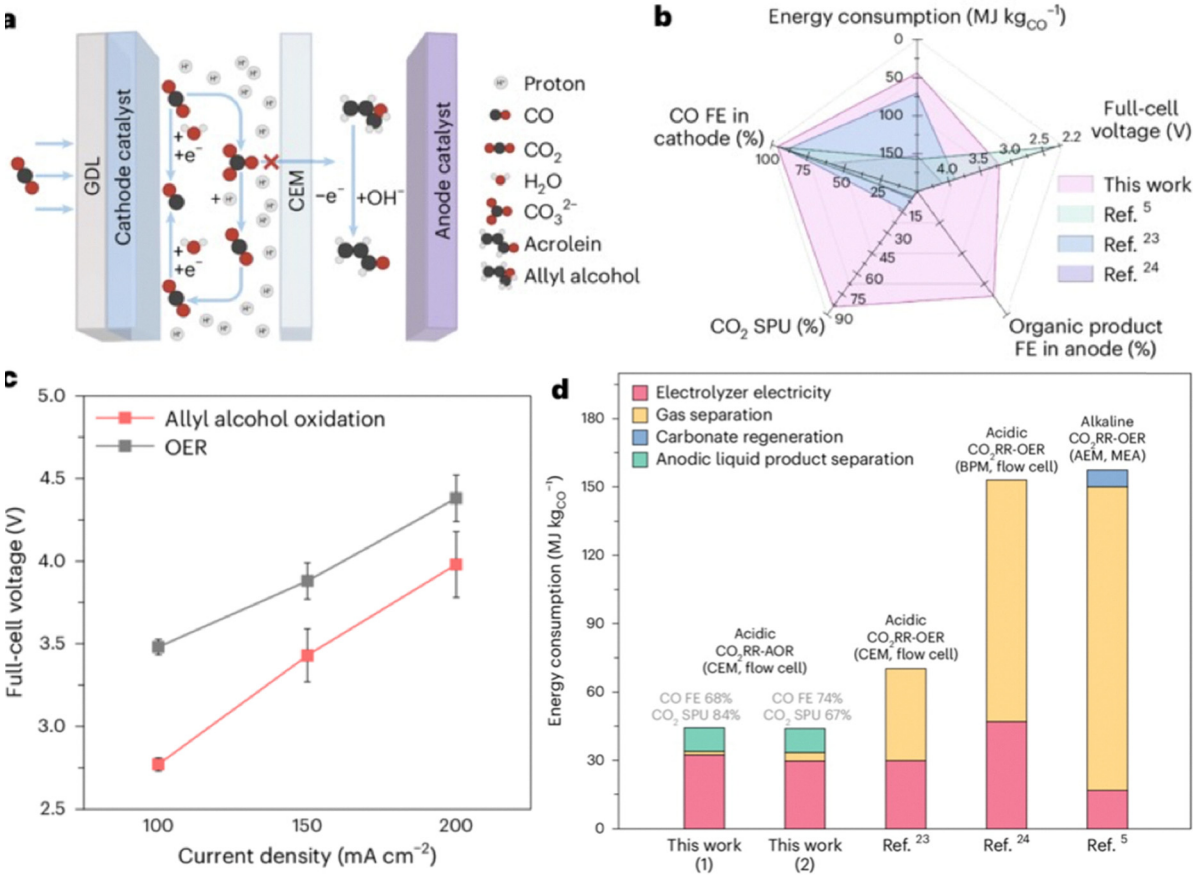


Fig. 86 (a) Schematic of the paired electrolysis system coupling acidic $CO_2$ reduction with alkaline allyl alcohol oxidation. (b) Performance benchmark comparing paired electrolysis to state-of-the-art systems. (c) Full-cell voltage comparison for $CO_2$RR-AOR and $CO_2$RR-OER systems across current densities. (d) Energy consumption analysis across different $CO_2$ electrolysis systems. Reprinted (adapted) from *Nat Sustain*, 2024, **7**, 931–937. Copyrights © 2024 The Authors, under exclusive license to Springer Nature Limited.

and laboratory settings, as detailed in (Table 39). For instance, Segets *et al.* pointed out that some key operational criteria that need to be met for e$CO_2$R-derived products to become economically viable include current densities over 300 mA $cm^{-2}$, cell voltages under 2.5 V, faradaic efficiencies over 80%, and system lifetimes over 50 000 hours.[528]

Furthermore, (Table 40) critically analyzes the four requested industrial feasibility factors, explicitly linking DFM structural features to quantitative performance limitations and mitigation strategies across all material classes. Diffusional resistances arise from microporous architectures (MOFs HKUST-1 PLD > 8 Å halves $D_{eff}$, COFs PLD 4.5–6 Å limit $j < 100$ mA $cm^{-2}$,[153,182,243,293] requiring meso/macropore hierarchies and monolithic shaping to optimize Thiele modulus under industrial GHSV. Competitive adsorption reflects sorbent chemistry where hydrophilic amines/carbonates risk pore flooding (HKUST-1 $H_2O$ blocks OMS) while hydrophobic CALF-20 retains 4 mmol $g^{-1}$ at 80% RH, demanding site-specific tuning for humid flue tolerance.[294] Temperature-pressure constraints emerge from $\Delta H_{ads}$-catalytic kinetics mismatch—strong chemisorption (CaO/amines) favors low-*T*/high-*P* capture but demands severe regeneration conflicting with methanation kinetics, whereas weaker physisorption reduces flue capacity, necessitating heat-conductive supports for *T*–*P* overlap. Cyclic deactivation is structure-intrinsic: COF imine hydrolysis causes 80% capacity loss in 5 humid cycles,[153,158] molten salt Ni-Cr corrosion limits lifetimes <5000 h,[447,507] and amine oxidative degradation above 110 °C requires basic supports/tethered motifs targeting >1000 cycles, confirming robust structure-function design must integrate all four factors for industrial viability.

## Challenges and opportunities of ICCC

Despite clear conceptual advantages and encouraging case studies, ICCC technologies are still at early to mid-technology readiness levels (typically TRL 3–5), with demonstrations largely confined to laboratory or small pilot reactors processing gram- to kilogram-scale sorbent inventories. Thus, as the ICCC process is a new emerging technology, many considerable gaps must be addressed for its industrial applications such as material degradation under realistic flue-gas impurities ($SO_x$, $NO_x$, $H_2O$, $O_2$) and understanding the synergies between catalysts and adsorbents in addition to reaction intermediates, and comprehensive considerations from an engineering perspective such as process design, especially for ICCC-Met, ICCC-RWGS,

Open Access Article. Published on 12 fevral 2026. Downloaded on 01.06.2026 11:06:26.
This article is licensed under a Creative Commons Attribution-NonCommercial 3.0 Unported Licence.

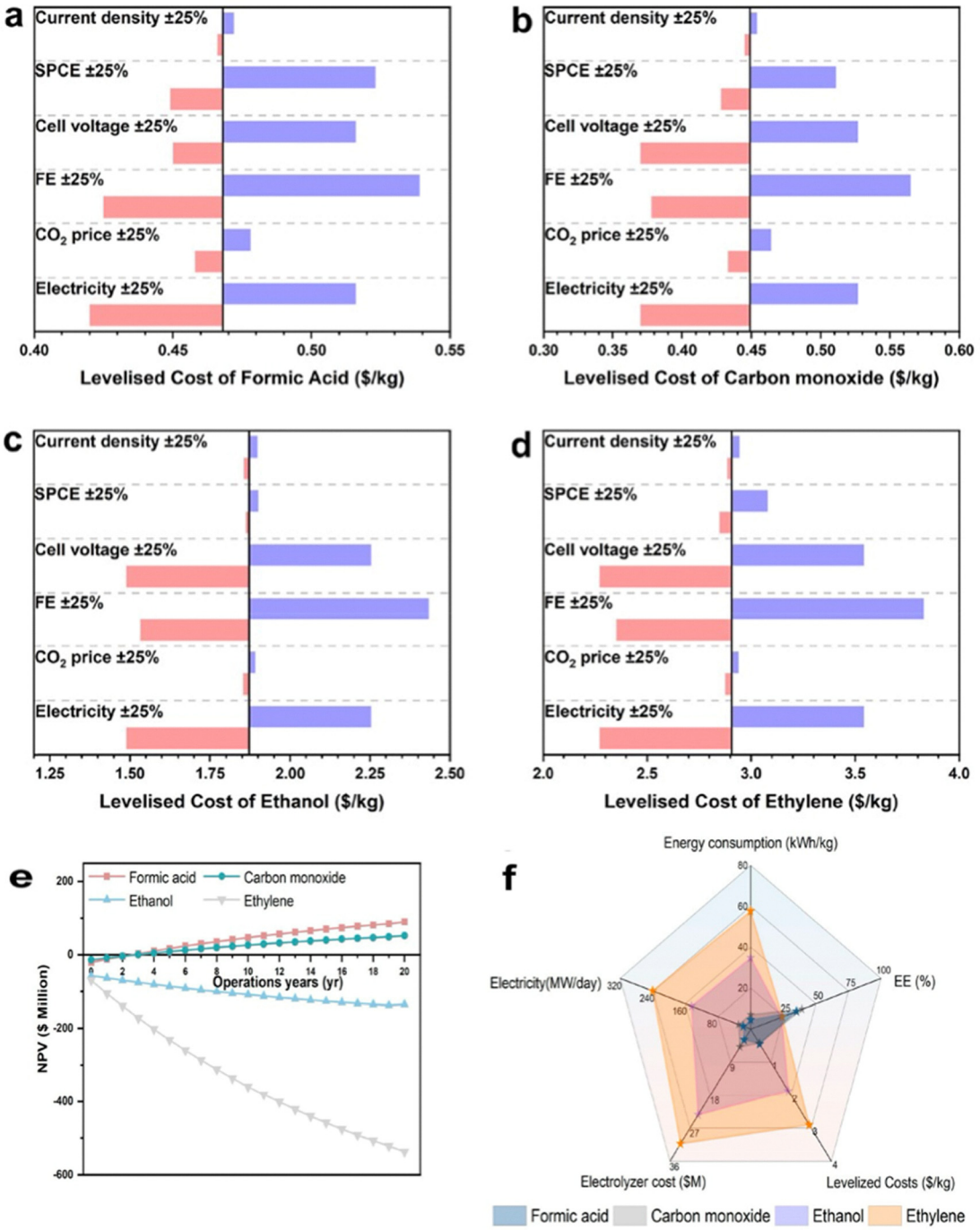


Fig. 87 Sensitivity analysis of the levelized cost for $eCO_2RR$ products: (a) formic acid. (b) Carbon monoxide. (c) Ethanol. (d) Ethylene as a function of cell voltage, selectivity, current density, prices of $CO_2$ and electricity, and SPCE. (e) Net Present Value (NPV) analysis over a 20-year horizon, revealing economic feasibility of formic acid and CO but persistent deficits for ethanol and ethylene. (f) Key energy conversion indicators. Reprinted (adapted) with permission from *Energy Fuels* 2023, **37**, 23, 17997–18008. Copyright © 2023 American Chemical Society.

and ICCC-DR.[14] While ICCC presents promising opportunities, there are ongoing challenges:[530,531]

• Although $CO_2$ can be captured from flue gas streams, its use in producing energy and synthesizing materials is still relatively underdeveloped due to the high expected costs and the efficiency constraints of current techniques as well as the technological immaturity of green hydrogen production which is inevitably used in the ICCC-Met and ICCC-RWGS processes.

• It is challenging to match the operation conditions of both $CO_2$ capture and conversion reactions such as reaction rates, temperatures, duration, heat management, and continuous operation close to industrially relevant conditions which


© 2026 The Author(s). Published by the Royal Society of Chemistry

Open Access Article. Published on 12 fevral 2026. Downloaded on 01.06.2026 11:06:26.
This article is licensed under a Creative Commons Attribution-NonCommercial 3.0 Unported Licence.

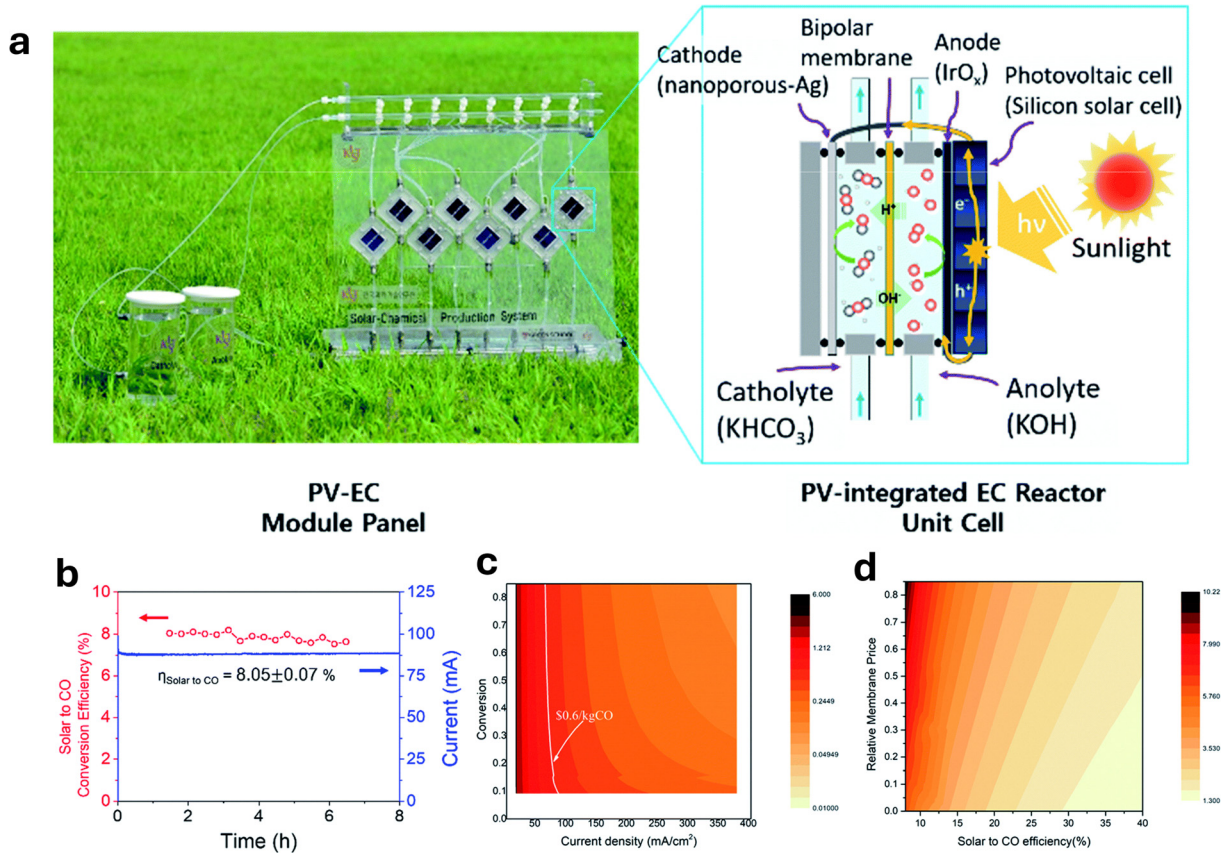


Fig. 88 (a) PV-EC device and schematic of the unit cell structure. (b) Solar to chemical conversion efficiency during PV-EC device operation. (c) and (d) Contour plots of CO cost *vs.* current density, $CO_2$ conversion, relative membrane price, and solar-to-CO efficiency. Reprinted (adapted) from *Sustainable Energy Fuels*, 2020, **4**, 199. Copyrights © 2020 The Authors. Published by Royal Society of Chemistry (RSC).

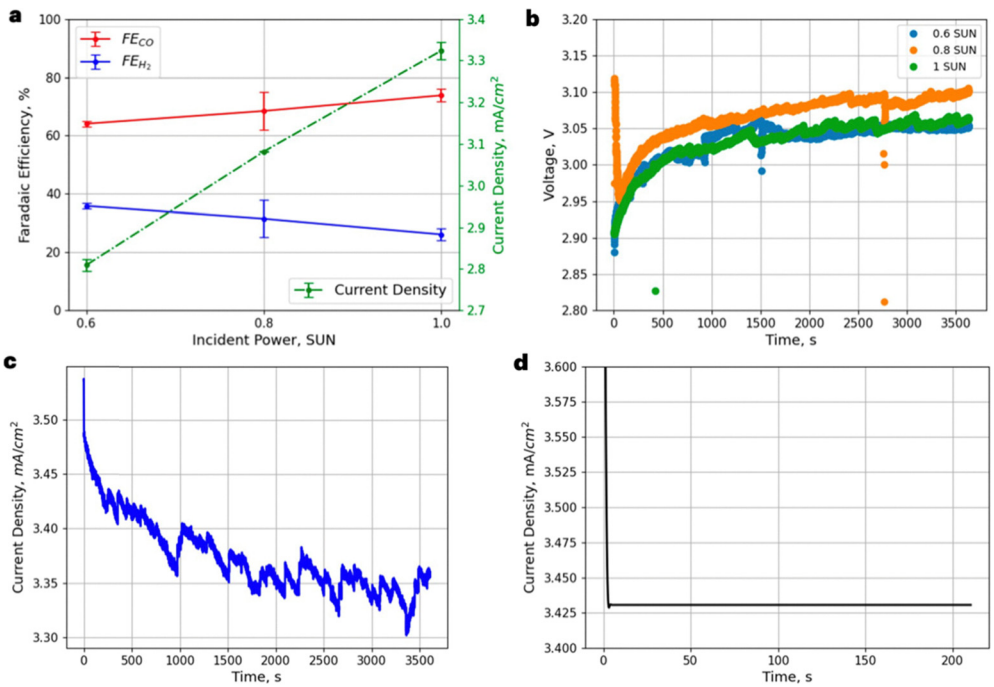


Fig. 89 (a) The performance of the integrated solar-powered $CO_2$ reduction device under different levels of solar irradiance. (b) Cell-voltage stabilization under different light intensities. (c) Experimental chronoamperometry at 1 sun. (d) Modelled current-density response at 1 sun. Reprinted (adapted) from *Appl. Sci.* 2025, **15**(2), 549. Copyrights © 2025 by the Authors. Published by MDPI under the terms of CC-BY license.

Open Access Article. Published on 12 fevral 2026. Downloaded on 01.06.2026 11:06:26.
This article is licensed under a Creative Commons Attribution-NonCommercial 3.0 Unported Licence.





Table 39 Key performance indicators for $CO_2$ electrochemical conversion[277,529]

| Indicators | Definition | Impact |
|---|---|---|
| Faradaic efficiency | A measure of the selectivity in an electrochemical process<br>FE = $(I \times t/z \times F \times n) \times 100$, where:<br>$I$ is the current (in amperes)<br>$t$ is the time (in seconds)<br>$z$ is the number of required electrons to produce the given product.<br>$F$ is Faraday's constant<br>$n$ is the number of moles of the product theoretically produced | High faradaic efficiency (FE) is advantageous for reducing both the capital and operating costs of the system, because it is directly proportional to the energy efficiency and inversely proportional to the electrode area of the electrolyzers, which should exceed 80% for most products |
| Energy efficiency | The energy input per unit mass product<br>EE = $(\Delta E^{\circ}/\Delta E_{applied}) \times$ FE, where:<br>$\Delta E^{\circ}$ is the equilibrium full cell potential<br>$\Delta E_{applied}$ is the applied full cell voltage<br>FE is the average faradaic efficiency | High energy efficiency leads to lower energy losses, better process performance, and hence lower operating costs of the system |
| Partial current density | The fraction of the total current density is specifically used for forming that particular product<br>$J_x = (I/A) \times$ FE, where:<br>$I$ is the current passed by the electrode<br>$A$ is the area of the electrode<br>FE is faradaic efficiency | High partial current density is essential for a higher production rate, resulting in the requirement of a smaller electrode area for the $CO_2$ electrolyzers, which reduces the capital costs of the system |
| Cell voltage | The total applied voltage to a $CO_2$ electrolyzer<br>$P_x = j \times A \times E_{cell}$, where:<br>$P_x$ is the power required to produce component $x$<br>$J$ is the partial current density of component $x$ $\sum$<br>$A$ is the electrode area<br>$E_{cell}$ is the cell voltage | Low cell voltage means less energy consumption to drive the electrochemical reaction by reducing internal resistances and overpotentials for a more energy-efficient and cost-effective system |
| Stability | The time retention of a performance metric (*e.g.*, FE, partial current, or voltage) within an interval while the system's deterioration must be below 10 μV per hour or exceed 10 000 hours | Low catalyst stability means more frequent replacements over the plant's operational lifetime, thereby increasing the capital costs of the system |
| Cycling stability (Capture) | Number of adsorption/desorption cycles without >10% capacity loss | >100 cycles |
| Catalyst durability (Electrolysis) | Continuous operation time without >10% drop in FE or activity | >100 h |
| Carbon efficiency | The ratio of $CO_2$ concentrations in the pre- and post-e$CO_2$R process.<br>carbon eff. = $(\sum C_x \times n_x)/nCO_2$, where:<br>$C_x$ is the number of carbons in product $x$<br>$n_x$ is the number of moles of product $x$ produced<br>$nCO_2$ is the number of moles of $CO_2$ that entered the system | For successful commercialization of the e$CO_2$R process, carbon eff > 50% is recommended to optimize process efficiency and minimize costs |
| $CO_2$ uptake capacity | The amount of $CO_2$ a material can adsorb per unit mass under specified conditions, reflects total capacity | Up to 7–8 mmol $g^{-1}$ at 273 K, 1 bar |
| Internal $CO_2$ utilization rate | Captured $CO_2$ converted *vs.* total captured | >85% |
| Mass transport limitation index | Measure of $CO_2$ diffusion efficiency (*e.g.*, *via* limiting current or impedance) | Minimal diffusion loss; >90% active site accessibility |
| Pressure/flow compatibility | Operates under typical flue gas or DAC conditions | 1–2 atm (flue gas); 400 ppm (air) |
| Resistance to impurities ($SO_x$, $NO_x$) | Tolerance to flue gas contaminants | Minimal loss of capacity (<10%) |
| Scalability index | Scalability of synthesis method and electrode fabrication | >10 g batch synthesis; compatibility with commercial supports |
| Energy consumption per mol $CO_2$ converted | Includes electrolysis energy and capture regeneration | <200 kJ $mol^{-1}$ |
| Carbon intensity (LCA) | Net $CO_2$ avoided per kg of product | Positive $CO_2$ balance (>90%) |
| Product purity | The percentage of purity of a substance, indicating the absence of impurities or contaminants.<br>Purity = (specific product '$n_x$'/$(\sum C_x \times n_x)$) × 100% | High product purity means better conversion, lower separation costs, less energy required, and fewer risks associated with impurities |
| Capacity/productivity | Capacity refers to a system's maximum production (t per day), whereas productivity assesses resource efficiency (MWh $t^{-1}$) | Higher productivity and properly scaled capacity result in higher economic viability, accelerated return on investment, and a cheaper cost per unit |

© 2026 The Author(s). Published by the Royal Society of Chemistry

Open Access Article. Published on 12 fevral 2026. Downloaded on 01.06.2026 11:06:26.
This article is licensed under a Creative Commons Attribution-NonCommercial 3.0 Unported Licence.

Table 40 Critical analysis of industrial feasibility factors limiting dual-functional materials (DFMs) in ICCC

| Feasibility factor | Structural determinants | Quantitative metrics & limitations | Mitigation strategies | Material examples | Ref. |
|---|---|---|---|---|---|
| Diffusional resistances | Pore hierarchy (micro/meso/macropores) tortuosity, particle size shaping (pellets/monoliths/foams) | Thiele modulus ($\varphi$), effectiveness factor ($\eta$) Microporous DFMs: slow intraparticle diffusion at high GHSV CALF-20 GDE: 355–380 mA $cm^{-2}$ *vs.* HKUST-1 half-$D_{eff}$ | Meso/macropore networks Short diffusion paths Hierarchical architectures | MOFs (HKUST-1 PLD $>8$ Å), Zeolites (LTA 3.8 Å), COFs (PLD 4.5–6 Å) | 243, 293 |
| Competitive adsorption | Sorbent site chemistry (amine/carbonate/oxide/carbon) surface hydrophilicity functionalization density | $CO_2/H_2O$ co-adsorption isotherms hydrophilic: pore flooding *vs.* cooperative binding CALF-20 : 4 mmol $g^{-1}$ (RH 80%) *vs.* HKUST-1 blocking | Hydrophobic tuning Site-specific functionalization Humid flue-gas testing | Hydrophilic amines/carbonates *vs.* hydrophobic CALF-20/POPs | |
| *T–P* operating window | Binding strength ($\Delta H_{ads}$) catalyst-support thermal overlap heat conduction | $\Delta H_{ads}$ 40–80 kJ $mol^{-1}$ optimal strong chemisorption: severe regeneration *T* weak physisorption: low flue capacity | Heat-conductive supports Proximal sorbent-catalyst *T–P* overlap optimization | Amines (40–60 °C), Zeolites (25–200 °C), Molten salts (550–900 °C) | 312–320 |
| Cyclic deactivation | Pore architecture, metal dispersion support acidity/basicity phase stability | Coking (Ni/Cu), amine degradation COF imine hydrolysis (80% loss/5 cycles) Molten Ni-Cr corrosion $<5$ kh | Basic supports (anti-coking) tethered amines corrosion-resistant alloys | COFs (imine fragility), Molten salts (Ni-Cr), Amines (oxidative) | 153–158 |

should be considered in further studies as performance tests and process simulation.

• Some challenges with electrochemical conversion are its energy-intensive fuel production process, making it unfeasible, and the need for a comprehensive understanding of highly efficient and selective catalysts, including their mechanisms, degradation, morphological variations, and active site characteristics.

• The absence of a global, consistent carbon pricing system makes it challenging to predict potential revenues from ICCC's projects which prevents developers and investors from accurately assessing the long-term financial assessments due to the lack of economies of scale coupled with high-risk perception while other low-carbon technologies like renewable energy become more affordable.

• The adoption of ICCC technologies is influenced by policy and regulatory challenges including the lack of financial incentives such as grants, tax credits, or feed-in tariffs, the absence of consistent regulations, and public concerns about safety, environmental impact, and long-term viability.

## Recent advances and future prospects

The future development of ICCC technologies will be shaped by efficiently addressing these challenges and leveraging opportunities. Nonetheless, to make ICCC technologies more economically viable and attractive from a sustainable point of view, the following factors should be considered:[11,532,533]

• Reducing the energy costs associated with large-scale $CO_2$ capture through adopting more efficient, innovative $CO_2$ capture technologies and improving process energy efficiency could enhance the economic viability of $CO_2$ capture and conversion.

• Integrating $CO_2$ conversion systems with other clean energy sources like nuclear, solar, wind, and geothermal can address both $CO_2$ emissions and energy supply challenges while enhancing the economic feasibility of the ICCC process, which is challenging and requires significant global governmental support for large-scale and widespread adoption.

• Enhancing material stability and activity, optimizing reactor designs and exploring innovative reactor types are crucial for improving performance. In the context of electrochemical processes, adopting novel solid oxide cell (SOC) configurations can reduce ohmic and polarization resistances, thereby boosting the power densities of SOC stacks.

• To enhance $CO_2$ conversion efficiency, product selectivity, and stability, it is vitally important to address the $CO_2$ conversion process at intermediate temperatures (300–700 °C) as a promising trend where materials such as catalysts, electrodes, and electrolyte materials need to be developed to fulfill the requirements for the conversion process.

• The implementation of emission-based carbon taxes could play a crucial role in accelerating the development of $CO_2$ capture and conversion technologies, given their proven effectiveness in curbing greenhouse gas emissions. And, converting a fraction of the captured $CO_2$ into marketable products would create additional economic value, thereby further supporting the financial sustainability and economic feasibility of the ICCC process.

• ICCC's potential applications across multiple sectors are vast, providing a flexible solution to meet energy demands sustainably and open up new opportunities beyond traditional carbon capture and storage approaches. However, the variety of products and processes from ICCC technologies emphasizes the importance of conducting thorough life cycle assessments, including techno-economic, social, and market evaluations, when considering industrial-scale implementation and the commercial future of $CO_2$-derived products.

• Despite growing interest in the research and development efforts required to assess the technical and economic viability of Integrated Carbon Capture and Conversion (ICCC) in scientific and industrial contexts, there has been little field-based research exploring the public's understanding and perceptions

Open Access Article. Published on 12 fevral 2026. Downloaded on 01.06.2026 11:06:26.
This article is licensed under a Creative Commons Attribution-NonCommercial 3.0 Unported Licence.

of the ICCC technology. Thus, there should be communication strategies that prioritize the practical applications of ICCC products, rather than focusing exclusively on Carbon Capture and Storage (CCS).

• Future progress in ICCC will depend on tightly coupled computational–experimental co-design, where multiscale modeling (DFT, microkinetics, and process simulations) is used not only to screen adsorbents and catalysts but to co-optimize capture thermodynamics, reaction pathways, and reactor operating windows.[534] Integrating these models with high-throughput synthesis and automated testing will enable rational tuning of binding energies, site proximity, and transport properties specifically for integrated capture–conversion rather than standalone capture or catalysis.[12]

• There is an urgent need for in-*operando* spectroscopy and microscopy (*e.g.*, DRIFTS, ambient-pressure XPS, XAS, Raman/IR under flow, *operando* TEM) to resolve $CO_2$ speciation, intermediate formation, and active-site evolution under realistic flue-gas and cycling conditions.[535] Such tools are essential to disentangle adsorption, activation, and deactivation ($SO_x$/$NO_x$/$H_2O$/$O_2$ poisoning) in ICCC materials and to validate mechanistic hypotheses that currently rely heavily on *ex situ* characterization and DFT alone.[26]

• Reactor engineering and heat/mass management remain major bottlenecks for scale-up: exothermic hydrogenation and carbonate formation must be balanced against endothermic desorption and pre-heating, while minimizing temperature gradients, hot spots, and diffusion limitations in packed or structured beds.[27]

• Future work should focus on intensified reactor concepts (*e.g.*, structured monoliths, microchannel and rotating beds, periodic reactors) and robust thermal integration strategies that allow rate-matched capture and conversion under cyclic operation at industrial scales.[536]

## Summary

The integrated carbon capture and conversion (ICCC) process is rapidly emerging as a pivotal research focus in both academia and industry, driven by its potential to provide a promising economic incentive for $CO_2$ mitigation, enhanced energy security, and industrial growth. This review paper discusses the latest ICCC developments, focusing on electrochemical conversion coupled with solvent-based and sorbent-based $CO_2$ capture approaches for flue gas. The review primarily highlights key adsorbent and absorbent materials used in this context, including Porous Organic Polymers (POPs), Covalent Organic Frameworks (COFs), Metal–Organic Frameworks (MOFs), Zeolites, Carbon Materials, Amines, Ionic liquids, Eutectics, and Molten Salts, as concluded below.

• In terms of Porous Organic Polymers (POPs), especially covalent triazine frameworks (CTFs) and conjugated microporous polymers (CMPs), they are a flexible group of crystalline or amorphous organic materials that have long chain of π-conjugation, a large specific surface area, and adjustable heteroatom functionalities. This makes them very useful for capturing $CO_2$ and converting it to electricity. CTFs are prepared *via* different methods such as iono-thermal or acid-catalyzed trimerization of nitrile monomers. They have stiff, nitrogen-rich structures that allow $CO_2$ to be strongly physiosorbed through Lewis's base–acid interactions and provide coordination sites for anchoring metal centers that are catalytically active. CMPs, which are synthesized by cross-coupling approach, have intrinsic characteristics represented in semiconductivity and hierarchical porosity. This makes it suitable materials for charge and mass transfer in electrochemical systems. CTFs can be modified by molecular catalysts, metal nanoparticles, or single-atom sites to these frameworks makes them even better at electrocatalysis by encouraging selective $CO_2$ activation and multi-electron transfer processes. CTFs and CMPs work together to create a flexible platform for producing new materials that combine selective $CO_2$ adsorption with effective, long-lasting electrocatalytic $CO_2$ reduction ($CO_2$RR) activity.

• With respect to Covalent Organic Frameworks (COFs), they are distinguished as promising materials for integrated $CO_2$ capture and conversion owing to their adjustable porosity, structural adaptability, and chemical stability. Their design enables precise functionalization, improving selectivity and catalytic efficacy. COFs, capable of hosting metal centers and conductive units, effectively facilitate electrocatalytic $CO_2$ reduction, rendering them suitable for sustainable carbon utilization strategies and prospective clean energy applications.

• Considering Zeolites for ICCC, they are shown to be a good and dependable substitute for integrated carbon capture and utilization systems when metal-loaded or nanoconfined zeolites are used to make electrochemical reduction more efficient due to their crystalline microporous structures and adjustable acidity. Also, Zeolites are good at separating and activating $CO_2$ molecules because they are very thermally stable, have a high ion-exchange capacity, and can selectively adsorb certain shapes.

• In the context of Metal–Organic Frameworks (MOFs), they have emerged as a highly promising category of materials for the simultaneous collection and electrochemical reduction of $CO_2$. Their modular structures, which integrate adjustable porosity, elevated surface area, and functionalizable metal–organic linkers, enable the simultaneous enrichment of $CO_2$ and the provision of catalytic conditions for selective conversion. Essential tactics encompass the creation of metal–organic framework (MOF)-based gas diffusion electrodes to augment local $CO_2$ concentration, the design of permselective membranes for targeted $CO_2$ transport, and the incorporation of functional groups, such as amines, to boost capture from dilute gas streams. Moreover, metal–organic frameworks (MOFs) can be engineered to influence product selectivity, such as methane, ethylene, or formate, by altering pore chemistry, metal centers, or interfacial environments. The advancement of conductive MOFs or MOF-derived composites mitigates inherent conductivity constraints, facilitating effective electron transfer and stability in electrochemical environments. These advancements collectively illustrate the adaptability of MOFs as dual-function adsorbent-catalyst systems, establishing a basis for sustainable and scalable carbon usage. Their versatility renders them crucial to contemporary initiatives


© 2026 The Author(s). Published by the Royal Society of Chemistry

Open Access Article. Published on 12 fevral 2026. Downloaded on 01.06.2026 11:06:26.
This article is licensed under a Creative Commons Attribution-NonCommercial 3.0 Unported Licence.

in merging $CO_2$ collection with $CO_2$RR, providing significant insights for the design of next-generation electrocatalysts.

Regarding Metal Oxides, they have garnered considerable interest as multifunctional materials that can combine $CO_2$ collection with electrochemical $CO_2$ reduction ($CO_2$RR). Their plentifulness, robust basicity, and structural adaptability facilitate excellent $CO_2$ adsorption, especially when altered with amine groups or integrated into porous substrates. In addition to capture, metal oxides are essential in catalysis by activating $CO_2$ molecules, stabilizing critical intermediates, and inhibiting competing hydrogen evolution. Modifying oxide composition and nanostructure has enhanced selectivity for formate (*e.g.*, $SnO_2$, $Bi_2O_3$, $In_2O_3$) or multi-carbon compounds (oxide-derived Cu). Recent integrated techniques, including amine-functionalized oxides, bifunctional gas diffusion electrodes, and hybrid oxide-metal systems, illustrate the capability of oxides to combine capture and conversion in a singular process, even in dilute flue gas environments. Notwithstanding limitations such as restricted adsorption capacity, stability of functional groups, and the attainment of industrially pertinent current densities, the versatility and scalability of oxide-based systems render them formidable contenders for practical $CO_2$ usage. These advancements collectively underscore the potential of metal oxides as effective, economical materials for enhancing integrated $CO_2$ capture and conversion technologies.

• Regarding Amines electrolytes, Amine electrolytes have served as the pillars of post-combustion $CO_2$ capture (PCC) and early integrated capture-conversion systems because of their cost advantages and chemical reactivity. Nevertheless, their inherent disadvantages, like low ionic conductivity, hydrogen evolution reaction (HER) interference, solvent degradation, and moderate current densities, are significant barriers to long-term sustainability and efficiency. Accordingly, there is a growing tendency toward novel next-generation solvents such as ionic liquids (ILs) and deep eutectic solvents (DESs), with higher $CO_2$ solubility, better electrochemical stability, and tunable physicochemical properties. Such novel solvent systems have promise to enable more efficient, sustainable, and scalable integrated $CO_2$ capture and electrochemical valorization under low-temperature processes such as direct air capture (DAC). Therefore, while amines remain best suited for mature, large-scale systems where cost and reactivity are most important, the future of carbon management is becoming more directed towards ILs, DESs, and hybrid approaches better suited for future generations of carbon capture and conversion technology.

• For Ionic Liquid, Due to their distinct structural features, high $CO_2$ solubility, large ionic conductivity, and broad electrochemical windows, ionic liquids (ILs) are quickly becoming a promising class of solvents for $CO_2$ capture and electrochemical reduction ($CO_2$ER). Researchers can adjust the properties of ILs to achieve the best $CO_2$ capture and conversion performance because of their great diversity, which results from the ability to customize both cations and anions. Recent developments have demonstrated that important limitations of previous IL designs can be addressed by modifying the interactions between ILs and $CO_2$ to further increase absorption capacities and decrease viscosities. While supported ILs, in which ILs are immobilized on solid substrates, offer high capacities, faster adsorption rates, and lower costs, making them appealing for industrial applications, conventional ILs, amino-functionalized ILs, and non-amino functionalized ILs each offer unique mechanisms and performance profiles for $CO_2$ capture. As electrolytes, additives, and electrode modifiers in $CO_2$ER, ILs' potent interactions with $CO_2$ facilitate effective dissolution, activation, and catalytic conversion, frequently improving process efficiency and product selectivity. Future studies should concentrate on methods to maintain the catalytic advantages of ILs while reducing dosage, as this is crucial for industrial scalability due to their comparatively high cost. A deeper mechanistic understanding of IL–$CO_2$ interactions, electric double-layer structures, and co-catalytic effects remains required despite tremendous advancements. This can be accomplished through *in situ* characterization, molecular simulations, and quantum chemical calculations. Furthermore, machine learning is a promising approach for screening and designing high-performance ILs for $CO_2$ capture and conversion. Overall, ILs offer a versatile and potent platform for sustainable carbon management, and their full potential in useful, large-scale applications will depend on continued innovation in material design, mechanistic understanding, and process integration.

• Referring to deep eutectic solvents (DESs), due to their high $CO_2$ solubility, low toxicity, and environmental friendliness, deep eutectic solvents (DESs) are quickly gaining attention as effective, sustainable alternatives for $CO_2$ capture and conversion. DESs are simple to create from low-cost, bio-based ingredients and have adjustable characteristics that can be tailored for chemical and physical $CO_2$ absorption as well as for incorporation into electrochemical reactions. Recent developments, such as the use of co-solvents, immobilization techniques, and functionalized DESs, are improving performance and scalability, even though issues like high viscosity and limited conductivity still exist. DESs are positioned as a promising platform for upcoming carbon capture and utilization technologies due to their adaptability and environmental credentials.

• In the context of Molten Salts, it combines capturing $CO_2$ and converting it into functional carbon nanomaterials. This process uses carbonate-based electrolytes to directly reduce $CO_2$ at the cathode, producing carbon structures such as nano-tubes, nano-onions, and nano-coils. It has high current efficiency, minimizes byproducts, and offers long-lasting economy. The composition of the electrodes, the chemistry of the electrolyte, and the additives all have a significant impact on the morphology and yield of the product. This makes this method a scalable, $CO_2$-negative way to use carbon and make advanced materials.

Besides that, this comprehensive review consolidates literature to assess the techno-economic analysis and key performance indicators of the ICCC process. Despite recent progress in improving ICCC technologies, there are still considerable challenges: technical limitations such as energy consumption and system efficiency, and non-technical barriers such as high capital costs, lack of economic incentives, public awareness, and inadequate government regulations. Thus, scaling up ICCC from laboratory settings to industrial deployment necessitates

Open Access Article. Published on 12 fevral 2026. Downloaded on 01.06.2026 11:06:26.
This article is licensed under a Creative Commons Attribution-NonCommercial 3.0 Unported Licence.

further research into cost-effective syntheses of dual-function materials, the development of reactor and separation apparatus design, and holistic evaluations through integrated system-level modeling, life cycle assessment, and techno-economic analysis for performance optimization and economic feasibility.

## Author contributions

Mohamed A. Elokl: writing – original draft, data curation, visualization, writing – review & editing, investigation, validation, and methodology. Ahmed G. Ali: writing – original draft, investigation, data curation, and visualization. Abdelrahman Mohsen: writing – original draft, investigation, data curation, and visualization. Ahmed Taha: writing – original draft, investigation, data curation, and visualization. Abdelrahman Ashor: writing – original draft, investigation; data curation, and visualization. Salma Elshabrawy: writing – original draft, investigation, data curation; and visualization. Nageh K. Allam: conceptualization, investigation, validation, writing – review & editing, supervision, and funding acquisition.

## Conflicts of interest

The authors declare that they have no conflict of interest.

## Abbreviations

| | |
|---|---|
| AEM | Anion-exchange membrane |
| AFIL | Amino-functionalized Ionic Liquid |
| BET | Brunauer–Emmett–Teller (method for surface area measurement) |
| BGDE | Bifunctional gas diffusion electrode |
| CCUS | Carbon capture, utilization, and storage |
| CMP | Conjugated microporous polymer |
| CNC | Carbon nanocoil |
| DFT | Density functional theory |
| DFM | Dual functional material |
| $eCO_2R$ | Electrochemical $CO_2$ reduction |
| EDS | Energy-dispersive X-ray spectroscopy |
| EGR | Enhanced gas recovery |
| EMAR | Electrochemically mediated amine regeneration |
| EOR | Enhanced oil recovery |
| EPRI | Electric power research institute |
| EXAFS | Extended X-ray absorption fine structure |
| FE | Faradaic efficiency |
| GDE | Gas diffusion electrode |
| GPU | Gas permeation unit |
| GWP | Global warming potential |
| HAADF-STEM | High-angle annular dark-field scanning transmission electron microscopy |
| HBA | Hydrogen bond acceptor |
| HBD | Hydrogen bond donor |
| HCP | Hyper-cross linked polymer |
| HER | Hydrogen evolution reaction |
| HOR | Hydrogen oxidation reaction |
| HPC | High-density polyethylene-derived porous carbon |
| HRTEM | High-resolution transmission electron microscopy |
| ICCC | Integrated $CO_2$ capture and conversion |
| ICCU | Integrated carbon capture and utilization |
| ICP | Inductively coupled plasma |
| IEA | International energy agency |
| SBU | Secondary building unit |
| SMR | Steam methane reforming |
| SOC | Solid oxide cell |
| SWCNT | Single-walled carbon nanotube |
| TEA | Techno-economic analysis |
| TOF | Turnover frequency |
| TON | Turnover number |
| TPP | Tetraphenyl porphyrin |
| TRL | Technology readiness level |
| US GAO | US Government Accountability Office |
| $NO_x$ | Nitrogen oxides |
| CNS | Carbon nano-scaffold |
| CNT | Carbon nanotube |
| COF | Covalent organic framework |
| $CO_2RR$ | $CO_2$ reduction reaction |
| CTF | Covalent triazine framework |
| CVD | Chemical vapor deposition |
| DEA | Diethanolamine |
| DES | Deep eutectic solvent |
| IGCC | Integrated gasification combined cycle |
| IL | Ionic liquid |
| IPCC | Intergovernmental panel on climate change |
| LCA | Life cycle assessment |
| LIB | Lithium-ion battery |
| MDEA | Methyl diethanolamine |
| MFI | Mobil composition of matter no. five (zeolite framework type) |
| MMM | Mixed matrix membrane |
| MOF | Metal–organic framework |
| NPV | Net present value |
| OER | Oxygen evolution reaction |
| OMS | Open metal site |
| ORR | Oxygen reduction reaction |
| PAF | Porous aromatic framework |
| PCP | Porous coordination polymer |
| PEM | Polymer electrolyte membrane |
| PGDE | Permselective gas diffusion electrode |
| PIM | Polymer of intrinsic microporosity |
| POP | Porous organic polymer |
| PTFE | Polytetrafluoroethylene |
| PV | Photovoltaic |
| RCC | Reactive capture of $CO_2$ |
| RDF | Radial distribution function |
| RWGS | Reverse water–gas shift reaction |
| WGSR | Water–gas shift reaction |
| XPS | X-ray Photoelectron Spectroscopy |
| $C_2H_4$ | Ethylene |
| $CH_4$ | Methane |


© 2026 The Author(s). Published by the Royal Society of Chemistry

Open Access Article. Published on 12 fevral 2026. Downloaded on 01.06.2026 11:06:26.
This article is licensed under a Creative Commons Attribution-NonCommercial 3.0 Unported Licence.

| | |
|---|---|
| CO | Carbon monoxide |
| $CO_2$ | Carbon dioxide |
| $H_2$ | Hydrogen |
| $H_2O$ | Water |
| $HCOO^-$ | Formate |
| $N_2$ | Nitrogen |
| $SO_x$ | Sulfur oxides |

## Data availability

The data supporting this article have been included in the manuscript.

## Acknowledgements

This work is supported by the American University in Cairo.

## References

1 W. Gao, S. Liang, R. Wang, Q. Jiang, Y. Zhang, Q. Zheng, B. Xie, C. Y. Toe, X. Zhu, J. Wang, L. Huang, Y. Gao, Z. Wang, C. Jo, Q. Wang, L. Wang, Y. Liu, B. Louis, J. Scott, A. C. Roger, R. Amal, H. He and S. E. Park, *Chem. Soc. Rev.*, 2020, **49**, 8584–8686.
2 D. Sallam, B. S. Shaheen and N. K. Allam, *Green Chemistry*, 2026, **28**, 1286–1315.
3 IEA, *Global Energy Review 2025*, IEA, Paris, 2025.
4 M. Pathak, R. Slade, P. R. Shukla, J. Skea, R. Pichs-Madruga and D. Ürge-Vorsatz, in *Climate Change 2022: Mitigation of Climate Change. Contribution of Working Group III to the Sixth Assessment Report of the Intergovernmental Panel on Climate Change*, ed. P. R. Shukla, J. Skea, R. Slade, A. Al Khourdajie, R. van Diemen, D. McCollum, M. Pathak, S. Some, P. Vyas, R. Fradera, M. Belkacemi, A. Hasija, G. Lisboa, S. Luz and J. Malley, Cambridge University Press, Cambridge, UK and New York, NY, USA, 2022.
5 M. Abdallah and R. Farrauto, *Catal. Today*, 2023, **423**, 113923.
6 S. Chen, J. Liu, Q. Zhang, F. Teng and B. C. McLellan, *Renewable Sustainable Energy Rev.*, 2022, **167**, 112537.
7 IEA, *Net Zero Roadmap: A Global Pathway to Keep the 1.5 °C Goal in Reach*, IEA, Paris, 2023.
8 F. Marocco Stuardi, F. MacPherson and J. Leclaire, *Green Sustainable Chem.*, 2019, **16**, 71–76.
9 K. T. de campos Roseno, R. M. de b. Alves, R. Giudici and M. Schmal, Syngas Production Using Natural Gas from the Environmental Point of View, in *Biofuels – State of Development*, InTech, 2018.
10 G. Leonzio and N. Shah, *Green Sustainable Chem.*, 2024, **46**, 100895.
11 M. A. Sabri, S. Al Jitan, D. Bahamon, L. F. Vega and G. Palmisano, *Sci. Total Environ.*, 2021, **790**, 148081.
12 R. E. Siegel, S. Pattanayak and L. A. Berben, *ACS Catal.*, 2023, **13**, 766–784.
13 M. Bhattacharya, S. Sebghati, R. T. Vanderlinden and C. T. Saouma, *J. Am. Chem. Soc.*, 2020, **142**, 17589–17597.
14 S. Sun, H. Sun, P. T. Williams and C. Wu, *Sustainable Energy Fuels*, 2021, **5**, 4546–4559.
15 Y. Qiao, W. Liu, R. Guo, S. Sun, S. Zhang, J. J. Bailey, M. Fang and C. Wu, *Fuel*, 2023, **332**, 125972.
16 Z. Lv, H. Du, S. Xu, T. Deng, J. Ruan and C. Qin, *Appl. Energy*, 2024, **355**, 122242.
17 H. Wang, Z. Yu, J. Zhou, C. Li, A. Jayanarasimhan, X. Zhao and H. Zhang, *Energies.*, 2023, **16**, 616.
18 M. M. F. Hasan, R. C. Baliban, J. A. Elia and C. A. Floudas, *Ind. Eng. Chem. Res.*, 2012, **51**, 15665–15682.
19 M. Bui, I. Gunawan, T. V. Verheyen and E. Meuleman, in *Absorption-Based Post-Combustion Capture of Carbon Dioxide*, Elsevier Inc., 2016, pp. 589–621.
20 J. Z. Y. Tan, J. M. Uratani, S. Griffiths, J. M. Andresen and M. M. Maroto-Valer, *Nat. Rev. Chem.*, 2025, **9**, 656–671.
21 Z. Kapetaki, O. Eulaerts, A. Georgakaki, M. D. R. Gonzalez Sanchez, M. Grabowska, E. Ince, G. Joanny Ordonez, A. Kuokkanen, S. Letout, A. Mountraki and D. Shtjefni, Clean Energy Technology Observatory: Carbon Capture Utilisation and Storage in the European Union – 2022 Status Report on Technology Development, Trends, Value Chains and Markets, Publications Office of the European Union, 2022.
22 S. Hughes, A. Zoelle, M. Woods, S. Henry, S. Homsy, S. Pidaparti, N. Kuehn, H. Hoffman, K. Forrest, A. Sheriff, T. Fout, W. Summers and S. Herron, *Cost of Capturing CO2 from Industrial Sources*, 2022.
23 J. Gao, S. Choo Sze Shiong and Y. Liu, *Chem. Eng. J.*, 2023, **472**, 145033.
24 A. P. Hallenbeck and J. R. Kitchin, *Ind. Eng. Chem. Res.*, 2013, **52**, 10788–10794.
25 B. H. Ko, B. Hasa and H. Shin, *et al.*, *Nat. Commun.*, 2020, **11**, 5856.
26 M. Sardo, R. Afonso, J. Juźków, M. Pacheco, M. Bordonhos, M. L. Pinto, J. R. B. Gomes and L. Mafra, *J. Mater. Chem. A.*, 2021, **9**, 5542–5555.
27 A. Porta, R. Matarrese, C. G. Visconti, L. Castoldi and L. Lietti, *Ind. Eng. Chem. Res.*, 2021, **60**, 6706–6718.
28 M. Namdari, Y. Kim, D. J. D. Pimlott, A. M. L. Jewlal and C. P. Berlinguette, *Chem. Soc. Rev.*, 2025, **54**, 590–600.
29 D. Bhattacharyya and D. C. Miller, *Chem. Eng*, 2017, **17**, 78–92.
30 D. Jansen, M. Gazzani, G. Manzolini, E. Van Dijk and M. Carbo, *Int. J. Greenhouse Gas Control*, 2015, **40**, 167–187.
31 R. Stanger, T. Wall, R. Spörl, M. Paneru, S. Grathwohl, M. Weidmann, G. Scheffknecht, D. McDonald, K. Myöhänen, J. Ritvanen, S. Rahiala, T. Hyppänen, J. Mletzko, A. Kather and S. Santos, *Int. J. Greenhouse Gas Control*, 2015, **40**, 55–125.
32 B. Dziejarski, R. Krzyżyńska and K. Andersson, *Fuel*, 2023, **342**, 127776.
33 W. Y. Hong, *Carbon Capture Sci. Technol*, 2022, **3**, 100044.
34 J. C. Abanades, B. Arias, A. Lyngfelt, T. Mattisson, D. E. Wiley, H. Li, M. T. Ho, E. Mangano and S. Brandani, *Int. J. Greenhouse Gas Control*, 2015, **40**, 126–166.
35 J. Serafin and B. Dziejarski, *Microporous Mesoporous Mater.*, 2023, **354**, 112513.

© 2026 The Author(s). Published by the Royal Society of Chemistry

Open Access Article. Published on 12 fevral 2026. Downloaded on 01.06.2026 11:06:26.
This article is licensed under a Creative Commons Attribution-NonCommercial 3.0 Unported Licence.

36 Y. Chang, S. Gao, Q. Ma, Y. Wei and G. Li, *Renewable Sustainable Energy Rev.*, 2024, **199**, 114550.
37 E. De Lena, M. Spinelli, M. Gatti, R. Scaccabarozzi, S. Campanari, S. Consonni, G. Cinti and M. C. Romano, *Int. J. Greenhouse Gas Control.*, 2019, **82**, 244–260.
38 G. M. Castilla, D. C. Guío-Pérez, S. Papadokonstantakis, F. Johnsson and D. Pallarès, *Energies*, 2021, **14**, 3211.
39 A. Akinmoladun and O. S. Tomomewo, *Carbon Capture Sci. Technol*, 2025, **16**, 100461.
40 A. Karayil, A. Elseragy and A. M. Aliyu, *Energies.*, 2024, **17**, 1460.
41 H. Hekmatmehr, A. Esmaeili, M. Pourmahdi, S. Atashrouz, A. Abedi, M. Ali Abuswer, D. Nedeljkovic, M. Latifi, S. Farag and A. Mohaddespour, *Fuel*, 2024, **363**, 130898.
42 IEA, *CCUS in Clean Energy Transitions*, IEA, Paris, 2020.
43 D. Kearns, H. Liu and C. Consoli, *Technology Readiness and Costs of CCS, Global CCS Institute*, 2021.
44 C. Font-Palma, D. Cann and C. Udemu, *C—J. Carbon Res.*, 2021, **7**, 58.
45 Y. Zhang, H. Han, N. Zhu, Y. Che, X. Zhang, Y. Xue, J. Deng, C. Wu, H. Wang, Y. Chen and S. Yi, *Ind. Eng. Chem. Res*, 2025, **64**(4), 1933–1967.
46 B. Arias, Y. Alvarez Criado, A. Méndez, P. Marqués, I. Finca and J. C. Abanades, *Energy Fuels*, 2024, **38**, 14757–14764.
47 A. A. Ashour, A. M. Abdelmohsen, G. E. Khedr, K. E. Salem, I. M. Badawy and N. K. Allam, *ACS Appl. Mater. Interfaces*, 2025, **17**, 64687–64698.
48 F. Wang, Y. Dai, Y. Zhang, S. Ren, Y. Hou and W. Wu, *Sep. Purif. Technol.*, 2025, **359**, 130462.
49 C. I. Melo, D. Rente, M. Nunes Da Ponte, E. Bogel-Łukasik and L. C. Branco, *ACS Sustainable Chem. Eng.*, 2019, **7**, 11963–11969.
50 A. Dhakshinamoorthy, S. Navalón, A. Primo and H. García, *Angew. Chem., Int. Ed.*, 2024, **63**, e202311241.
51 I. M. Badawy, G. E. Khedr, A. Hafez, E. A. Ashour and N. K. Allam, *Chem. Commun.*, 2023, **59**, 7974–7977.
52 Y. Lei, Z. Wang, A. Bao, X. Tang, X. Huang, H. Yi, S. Zhao, T. Sun, J. Wang and F. Gao, *Chem. Eng. J.*, 2023, **453**, 139663.
53 S. Kumar De, D. Il Won, J. Kim and D. H. Kim, *Chem. Soc. Rev.*, 2023, **52**, 5744–5802.
54 Z. Liu, J. Qian, G. Zhang, B. Zhang and Y. He, *Sep. Purif. Technol*, 2024, **330**, 125177.
55 X. M. Hu, H. Q. Liang, A. Rosas-Hernández and K. Daasbjerg, *Chem. Soc. Rev.*, 2025, **54**, 1216–1250.
56 R. Küngas, *J. Electrochem. Soc.*, 2020, **167**, 044508.
57 M. Songolzadeh, M. Soleimani, M. Takht Ravanchi and R. Songolzadeh, *Sci. World J.*, 2014, **2014**, 828131.
58 U. Khan, C. C. Ogbaga, O. A. O. Abiodun, A. A. Adeleke, P. P. Ikubanni, P. U. Okoye and J. A. Okolie, *Carbon Capture Sci. Technol*, 2023, **8**, 100125.
59 P. A. Saenz Cavazos, E. Hunter-Sellars, P. Iacomi, S. R. McIntyre, D. Danaci and D. R. Williams, *Front. Energy Res*, 2023, **11**, 1167043.
60 D. Panda, E. A. Kumar and S. K. Singh, *J. CO2 Util.*, 2020, **40**, 101223.
61 Z. Zhang, Z. P. Cano, D. Luo, H. Dou, A. Yu and Z. Chen, *J. Mater. Chem. A.*, 2019, **7**, 20985–21003.
62 D.-H. Yang, Y. Tao, X. Ding and B.-H. Han, *Chem. Soc. Rev.*, 2022, **51**, 761–791.
63 H. Wang, G. Wang, L. Hu, B. Ge, X. Yu and J. Deng, *Materials*, 1630, **2023**, 16.
64 G. Singh, J. Lee, A. Karakoti, R. Bahadur, J. Yi, D. Zhao, K. AlBahily and A. Vinu, *Chem. Soc. Rev.*, 2020, **49**, 4360–4404.
65 W. Song, Y. Tang, B. Y. Moon, Q. Liao, H. Xu, Q. Hou, H. Zhang, D.-G. Yu, Y. Liao and I. Kim, *Green Chem*, 2024, **26**, 2476–2504.
66 K. Cai, P. Liu, Z. Chen, P. Chen, F. Liu, T. Zhao and D.-J. Tao, *Chem. Eng. J.*, 2023, **451**, 138946.
67 C. Chakravarty, B. Mandal and P. Sarkar, *J. Phys. Chem. C*, 2018, **122**, 3245–3255.
68 T. Sick, A. G. Hufnagel, J. Kampmann, I. Kondofersky, M. Calik, J. M. Rotter, A. Evans, M. Döblinger, S. Herbert, K. Peters, D. Böhm, P. Knochel, D. D. Medina, D. Fattakhova-Rohlfing and T. Bein, *J. Am. Chem. Soc.*, 2018, **140**, 2085–2092.
69 H. Vardhan, A. Nafady, A. M. Al-Enizi and S. Ma, *Nanoscale*, 2019, **11**, 21679–21708.
70 L. P. Tang, S. Yang, D. Liu, C. Wang, Y. Ge, L. M. Tang, R. L. Zhou and H. Zhang, *J. Mater. Chem. A.*, 2020, **8**, 14356–14383.
71 Y. Xin, D. Wang, W. Zhang, F. Su, Y. Liu, Y. Lu, W. Fan, D. Yao and Y. Zheng, *Ind. Eng. Chem. Res.*, 2025, **64**(13), 7044–7055.
72 A. Mehtab and T. Ahmad, *ACS Catal.*, 2024, **14**, 691–702.
73 B. Chen, M. Dong, S. Liu, Z. Xie, J. Yang, S. Li, Y. Wang, J. Du, H. Liu and B. Han, *ACS Catal.*, 2020, **10**, 8557–8566.
74 J. K. Tang, C. Y. Zhu, T. W. Jiang, L. Wei, H. Wang, K. Yu, C. L. Yang, Y. B. Zhang, C. Chen, Z. T. Li, D. W. Zhang and L. M. Zhang, *J. Mater. Chem. A.*, 2020, **8**, 18677–18686.
75 J. Li, D. Jia, Z. Guo, Y. Liu, Y. Lyu, Y. Zhou and J. Wang, *Green Chem.*, 2017, **19**, 2675–2686.
76 Z. Zhong, X. Wang and B. Tan, *Chem. Eur. J.*, 2025, **31**, e202404089.
77 T. Ben and S. Qiu, *CrystEngComm*, 2013, **15**, 17–26.
78 N. B. McKeown and P. M. Budd, *Chem. Soc. Rev.*, 2006, **35**, 675–683.
79 Y. Xu, S. Jin, H. Xu, A. Nagai and D. Jiang, *Chem. Soc. Rev.*, 2013, **42**, 8012–8031.
80 T. Ben, H. Ren, M. Shengqian, D. Cao, J. Lan, X. Jing, W. Wang, J. Xu, F. Deng, J. M. Simmons, S. Qiu and G. Zhu, *Angew. Chem., Int. Ed.*, 2009, **48**, 9457–9460.
81 T. X. Wang, H. P. Liang, D. A. Anito, X. Ding and B. H. Han, *J. Mater. Chem. A.*, 2020, **8**, 7003–7034.
82 P. Puthiaraj, Y. R. Lee, S. Zhang and W. S. Ahn, *J. Mater. Chem. A.*, 2016, **4**, 16288–16311.
83 C. Krishnaraj, H. S. Jena, K. Leus and P. Van Der Voort, *Green Chem.*, 2020, **22**, 1038–1071.
84 J. Artz, *ChemCatChem*, 2018, **10**, 1753–1771.
85 N. Tahir, C. Krishnaraj, K. Leus and P. Van Der Voort, *Polymers*, 2019, **11**, 1326.
86 P. Kuhn, M. Antonietti and A. Thomas, *Angew. Chem., Int. Ed.*, 2008, **47**, 3450–3453.


© 2026 The Author(s). Published by the Royal Society of Chemistry

Open Access Article. Published on 12 fevral 2026. Downloaded on 01.06.2026 11:06:26.
This article is licensed under a Creative Commons Attribution-NonCommercial 3.0 Unported Licence.

87 R. Luo, W. Xu, M. Chen, X. Liu, Y. Fang and H. Ji, *ChemSusChem*, 2020, **13**, 6509.
88 P. Su, K. Iwase, T. Harada, K. Kamiya and S. Nakanishi, *Chem. Sci.*, 2018, **9**, 3941–3947.
89 L. Shao, Y. Li, J. Huang and Y. N. Liu, *Ind. Eng. Chem. Res.*, 2018, **57**, 2856–2865.
90 G. Liu, S. Liu, C. Lai, L. Qin, M. Zhang, Y. Li, M. Xu, D. Ma, F. Xu, S. Liu, M. Dai and Q. Chen, *Small*, 2024, **20**, 2307853.
91 C. Lu, J. Yang, S. Wei, S. Bi, Y. Xia, M. Chen, Y. Hou, M. Qiu, C. Yuan, Y. Su, F. Zhang, H. Liang and X. Zhuang, *Adv. Funct. Mater.*, 2019, **29**, 1806884.
92 H. Wang, D. Jiang, D. Huang, G. Zeng, P. Xu, C. Lai, M. Chen, M. Cheng, C. Zhang and Z. Wang, *J. Mater. Chem. A.*, 2019, **7**, 22848–22870.
93 Y. Fu, Z. Wang, S. Li, X. He, C. Pan, J. Yan and G. Yu, *ACS Appl. Mater. Interfaces*, 2018, **10**, 36002–36009.
94 Y. Xiong, Y. Qin, L. Su and F. Ye, *Chem. Eur. J.*, 2017, **23**, 11037–11045.
95 T. Liu, X. Hu, Y. Wang, L. Meng, Y. Zhou, J. Zhang, M. Chen and X. Zhang, *J. Photochem. Photobiol. B*, 2017, **175**, 156–162.
96 K. Scanda, Y. Avila, L. Sánchez, R. Mojica, B. Portales-Martínez, M. González, M. Ávila and E. Reguera, *J. Phys. Chem. C*, 2023, **127**, 21777–21787.
97 J. Wei, D. Zhou, Z. Sun, Y. Deng, Y. Xia and D. Zhao, *Adv. Funct. Mater.*, 2013, **23**, 2322–2328.
98 B. Guo, C. Wu, Q. Su, Z. Liu, X. Li, G. Li and Q. Wu, *Mater. Lett.*, 2018, **221**, 236–239.
99 K. Yuan, C. Liu, L. Zong, G. Yu, S. Cheng, J. Wang, Z. Weng and X. Jian, *ACS Appl. Mater. Interfaces*, 2017, **9**, 13201–13212.
100 D. M. D'Alessandro, B. Smit and J. R. Long, *Angew. Chem., Int. Ed.*, 2010, **49**, 6058–6082.
101 C. Hu, Y. Xiao, Y. Zou and L. Dai, *Electrochem. Energy Rev.*, 2018, **1**, 84–112.
102 K. P. Kuhl, T. Hatsukade, E. R. Cave, D. N. Abram, J. Kibsgaard and T. F. Jaramillo, *J. Am. Chem. Soc.*, 2014, **136**, 14107–14113.
103 X. Zhu, C. Tian, H. Wu, Y. He, L. He, H. Wang, X. Zhuang, H. Liu, C. Xia and S. Dai, *ACS Appl. Mater. Interfaces*, 2018, **10**, 43588–43594.
104 Y. Wang, J. Chen, G. Wang, Y. Li and Z. Wen, *Angew. Chem., Int. Ed*, 2018, **57**, 13120–13124.
105 A. Laemont, S. Abednatanzi, P. G. Derakshandeh, F. Verbruggen, E. Fiset, Q. Qin, K. Van Daele, M. Meledina, J. Schmidt, M. Oschatz, P. Van Der Voort, K. Rabaey, M. Antonietti, T. Breugelmans and K. Leus, *Green Chem.*, 2020, **22**, 3095–3103.
106 S. Kato, T. Hashimoto, K. Iwase, T. Harada, S. Nakanishi and K. Kamiya, *Chem. Sci.*, 2023, **14**, 613–620.
107 L. Gong, X. Wang, T. Zheng, J. Liu, J. Wang, Y. C. Yang, J. Zhang, X. Han, L. Zhang and Z. Xia, *J. Mater. Chem. A.*, 2021, **9**, 3555–3566.
108 K. Ao, P. Zhao, Q. Zhang, X. Fan, Q. Fang, G. Wang and Y. Zhu, *Small Struct.*, 2024, **5**, 2300500.
109 S. Feng, W. Zheng, J. Zhu, Z. Li, B. Yang, Z. Wen, J. Lu, L. Lei, S. Wang and Y. Hou, *Appl. Catal., B*, 2020, **270**, 118908.
110 A. Jana, A. Maity, A. Sarkar, B. Show, P. A. Bhobe and A. Bhunia, *J. Mater. Chem. A.*, 2024, **12**, 5244–5253.
111 M. J. Mao, M. Di Zhang, D. L. Meng, J. X. Chen, C. He, Y. B. Huang and R. Cao, *ChemCatChem*, 2020, **12**, 3530–3536.
112 J. X. Jiang, F. Su, A. Trewin, C. D. Wood, N. L. Campbell, H. Niu, C. Dickinson, A. Y. Ganin, M. J. Rosseinsky, Y. Z. Khimyak and A. I. Cooper, *Angew. Chem., Int. Ed.*, 2007, **46**, 8574–8578.
113 A. Giri, Y. Khakre, G. Shreeraj, T. K. Dutta, S. Kundu and A. Patra, *J. Mater. Chem. A.*, 2022, **10**, 17077–17121.
114 M. Rose, *ChemCatChem*, 2014, **6**, 1166–1182.
115 T. D. Hoang, S. A. Bandh, F. A. Malla, I. Qayoom, S. Bashir, S. B. Peer and A. Halog, *Recycling*, 2023, **8**, 53.
116 S. L. Hou, J. Dong, X. Y. Zhao, X. S. Li, F. Y. Ren, J. Zhao and B. Zhao, *Angew. Chem., Int. Ed.*, 2023, **62**, e202305213.
117 Y. Xie, T. T. Wang, X. H. Liu, K. Zou and W. Q. Deng, *Nat. Commun.*, 2013, **4**, 1960.
118 R. Wang, X. Wang, W. Weng, Y. Yao, P. Kidkhunthod, C. Wang, Y. Hou and J. Guo, *Angew. Chem., Int. Ed.*, 2022, **61**, e202115503.
119 C. Zhang, X. Yang, W. Ren, Y. Wang, F. Su and J. X. Jiang, *J. Power Sources*, 2016, **317**, 49–56.
120 F. Qiu, C. Li, X. Xuan, S. Huang, C. Lu, H. Lin, S. Han, X. Zhuang and W. Y. Wong, *J. Mater. Chem. A.*, 2024, **12**, 33572–33580.
121 C. L. Smith, R. Clowes, R. S. Sprick, A. I. Cooper and A. J. Cowan, *Sustainable Energy Fuels*, 2019, **3**, 2990–2994.
122 X. M. Hu, Z. Salmi, M. Lillethorup, E. B. Pedersen, M. Robert, S. U. Pedersen, T. Skrydstrup and K. Daasbjerg, *Chem. Commun.*, 2016, **52**, 5864–5867.
123 A. B. Soliman, R. R. Haikal, Y. S. Hassan and M. H. Alkordi, *Chem. Commun.*, 2016, **52**, 12032–12035.
124 U. Karatayeva, S. A. Al Siyabi, B. Brahma Narzary, B. C. Baker and C. F. J. Faul, *Adv. Sci.*, 2024, **11**, 2308228.
125 Y. Song, J. J. Zhang, Z. Zhu, X. Chen, L. Huang, J. Su, Z. Xu, T. H. Ly, C. S. Lee, B. I. Yakobson, B. Z. Tang and R. Ye, *Appl. Catal., B*, 2021, **284**, 119750.
126 C. Ampelli, C. Genovese, M. Errahali, G. Gatti, L. Marchese, S. Perathoner and G. Centi, *J. Appl. Electrochem.*, 2015, **45**, 701–713.
127 D. Jiang, R. Bu, W. Xia, Y. Hu, M. Zhou, E. Gao, T. Asahi, Y. Yamauchi and J. Tang, *Materials Reports: Energy*, 2023, **3**, 100176.
128 B. B. Narzary, B. C. Baker and C. F. J. Faul, *Adv. Mater.*, 2023, **35**, 2211795.
129 B. B. Narzary, U. Karatayeva, J. Mintah, M. Villeda-Hernandez and C. F. J. Faul, *Mater. Chem. Front.*, 2023, **7**, 4473–4481.
130 K. S. Song, P. W. Fritz and A. Coskun, *Chem. Soc. Rev.*, 2022, **51**, 9831–9852.
131 G. Ji, Y. Zhao and Z. Liu, *Green Chem. Eng.*, 2022, **3**, 96–110.
132 S. Bin Ren, P. X. Li, A. Stephenson, L. Chen, M. E. Briggs, R. Clowes, A. Alahmed, K. K. Li, W. P. Jia and D. M. Han, *Ind. Eng. Chem. Res.*, 2018, **57**, 9254–9260.
133 I. Khan, A. Altaf, S. Sadiq, S. Khan, A. Khan, S. Khan, M. Humayun, A. Khan, R. A. Abumousa and M. Bououdina, *Chem. Eng. J. Adv.*, 2025, **21**, 100691.

Open Access Article. Published on 12 fevral 2026. Downloaded on 01.06.2026 11:06:26.
This article is licensed under a Creative Commons Attribution-NonCommercial 3.0 Unported Licence.

134 K. Wang, H. Huang, D. Liu, C. Wang, J. Li and C. Zhong, *Environ. Sci. Technol.*, 2016, **50**, 4869–4876.
135 S. Hug, M. B. Mesch, H. Oh, N. Popp, M. Hirscher, J. Senker and B. V. Lotsch, *J. Mater. Chem. A.*, 2014, **2**, 5928–5936.
136 S. Raja, G. T. S. T. da Silva, E. A. Reis, J. C. da Cruz, A. Brunca Silva, M. B. Andrade, G. Periyasami, P. Karthikeyan, I. F. Perepichka, L. H. Mascaro and C. Ribeiro, *Energy Fuels*, 2023, **37**, 19113–19123.
137 X. Feng, X. Ding and D. Jiang, *Chem. Soc. Rev.*, 2012, **41**, 6010–6022.
138 P. W. Anderson, W. F. Brinkman and D. A. Huse, *Science.*, 2005, **310**, 1164–1166.
139 A. P. Cote, A. I. Benin, N. W. Ockwig, M. O'Keeffe, A. J. Matzger and O. M. Yaghi, *Science.*, 2005, **310**, 1166–1170.
140 W. T. Chung, I. M. A. Mekhemer, M. G. Mohamed, A. M. Elewa, A. F. M. EL-Mahdy, H. H. Chou, S. W. Kuo and K. C. W. Wu, *Coord. Chem. Rev.*, 2023, **483**, 215066.
141 W. K. Fan and M. Tahir, *Energy Convers. Manag*, 2022, **253**, 115180.
142 U. Shahzad, H. M. Marwani, M. Saeed, A. M. Asiri, M. R. Repon, R. H. Althomali and M. M. Rahman, *Chem. Rec.*, 2024, **24**, e202300285.
143 M. H. Alenazi, A. Helal, M. Y. Khan, A. Khalil, A. Khan, M. Usman and M. H. Zahir, *Carbon Capture Sci. Technol.*, 2025, **14**, 100365.
144 X. Cui, S. Lei, A. C. Wang, L. Gao, Q. Zhang, Y. Yang and Z. Lin, *Nano Energy*, 2020, **70**, 104525.
145 F. J. Uribe-Romo, J. R. Hunt, H. Furukawa, C. Klöck, M. O'Keeffe and O. M. Yaghi, *J. Am. Chem. Soc.*, 2009, **131**, 4570–4571.
146 Y. Fan, M. Chen, N. Xu, K. Wang, Q. Gao, J. Liang and Y. Liu, *Front.chem.*, 2022, **10**, 942492.
147 H. Dong, M. Lu, Y. Wang, H. L. Tang, D. Wu, X. Sun and F. M. Zhang, *Appl. Catal., B*, 2022, **303**, 120897.
148 B. Han, X. Ding, B. Yu, H. Wu, W. Zhou, W. Liu, C. Wei, B. Chen, D. Qi, H. Wang, K. Wang, Y. Chen, B. Chen and J. Jiang, *J. Am. Chem. Soc.*, 2021, **143**, 7104–7113.
149 M. Dogru and T. Bein, *Chem. Commun.*, 2014, **50**, 5531–5546.
150 C. Y. Lin, D. Zhang, Z. Zhao and Z. Xia, *Adv. Mater.*, 2018, **30**, 1703646.
151 L. Ma, W. Hu, B. Mei, H. Liu, B. Yuan, J. Zang, T. Chen, L. Zou, Z. Zou, B. Yang, Y. Yu, J. Ma, Z. Jiang, K. Wen and H. Yang, *ACS Catal.*, 2020, **10**, 4534–4542.
152 C. P. Wan, J. D. Yi, R. Cao and Y. B. Huang, *Chin. J. Struct. Chem.*, 2022, **41**, 2205001–2205014.
153 H. M. El-Kaderi, J. R. Hunt, J. L. Mendoza-Cortés, A. P. Côté, R. E. Taylor, M. O'Keeffe and O. M. Yaghi, *Science.*, 2007, **316**, 268–272.
154 M. Lu, M. Zhang, J. Liu, Y. Chen, J. Liao, M. Yang, Y. Cai, S. Li and Y. Lan, *Angew. Chem.*, 2022, **134**, e202200003.
155 J. F. Kurisingal, H. Kim, J. H. Choe and C. S. Hong, *Coord. Chem. Rev.*, 2022, **473**, 214835.
156 G. Singh and C. M. Nagaraja, *J. CO2 Util.*, 2021, **53**, 101716.
157 K. Xu, Y. Dai, B. Ye and H. Wang, *Dalton Trans.*, 2017, **46**, 10780–10785.
158 Q. Gao, X. Li, G.-H. Ning, H.-S. Xu, C. Liu, B. Tian, W. Tang and K. P. Loh, *Chem. Mater.*, 2018, **30**, 1762–1768.
159 Y. B. Zhang, J. Su, H. Furukawa, Y. Yun, F. Gándara, A. Duong, X. Zou and O. M. Yaghi, *J. Am. Chem. Soc.*, 2013, **135**, 16336–16339.
160 R. Wang, J. Zhao, Q. Fang and S. Qiu, *Chem. Synth.*, 2024, **4**, 29.
161 D. Zhu, Y. Zhu, Y. Chen, Q. Yan, H. Wu, C. Y. Liu, X. Wang, L. B. Alemany, G. Gao, T. P. Senftle, Y. Peng, X. Wu and R. Verduzco, *Nat. Commun.*, 2023, **14**, 2865.
162 X. Huang, C. Sun and X. Feng, *Sci. China Chem.*, 2020, **63**, 1367–1390.
163 T. Saeed, A. Naeem, B. Ahmad, S. Ahmad, S. Afridi, F. Khan, I. U. Din and N. H. Khan, *J. Porous Mater.*, 2024, **31**, 33–48.
164 H. A. Patel, J. Byun and C. T. Yavuz, *ChemSusChem*, 2017, **10**, 1303–1317.
165 G. Kumar, M. Singh, R. Goswami and S. Neogi, *ACS Appl. Mater. Interfaces*, 2020, **12**, 48642–48653.
166 H. Furukawa and O. M. Yaghi, *J. Am. Chem. Soc.*, 2009, **131**, 8875–8883.
167 S. B. Alahakoon, C. M. Thompson, A. X. Nguyen, G. Occhialini, G. T. McCandless and R. A. Smaldone, *Chem. Commun.*, 2016, **52**, 2843–2845.
168 S. Wei, H. Xin, M. Wang, S. Xu, W. Zhai, S. Liu, L. Wang, S. Liu, Z. Wang and X. Lu, *Adv. Theory Simul.*, 2022, **5**, 2200588.
169 G. Lin, H. Ding, R. Chen, Z. Peng, B. Wang and C. Wang, *J. Am. Chem. Soc.*, 2017, **139**, 8705–8709.
170 A. Paparo and J. Okuda, *Coord. Chem. Rev.*, 2017, **334**, 136–149.
171 S. Vijay, W. Ju, S. Brückner, S.-C. Tsang, P. Strasser and K. Chan, *Nat. Catal.*, 2021, **4**, 1024–1031.
172 S. Lin, C. S. Diercks, Y.-B. Zhang, N. Kornienko, E. M. Nichols, Y. Zhao, A. R. Paris, D. Kim, P. Yang and O. M. Yaghi, *Science.*, 2015, **349**, 1208–1213.
173 D. Wu, J. Wu, P. Lv, H. Li, K. Chu and D. Ma, *Small Struct*, 2023, **4**, 2200358.
174 F. W. Dagnaw, K. Harrath, T. Zheng, X. D. Wu, Y. Z. Liu, R. Q. Li, L. H. Xie, Z. Li, X. He, Q. X. Tong and J. X. Jian, *Adv. Sci.*, 2024, **11**, 2408152.
175 H.-J. Zhu, M. Lu, Y.-R. Wang, S.-J. Yao, M. Zhang, Y.-H. Kan, J. Liu, Y. Chen, S.-L. Li and Y.-Q. Lan, *Nat. Commun.*, 2020, **11**, 497.
176 G. Liu, X. Li, M. Liu, S. Yang, X. Yang, X. Chen, W. Wei, Q. Xu and G. Zeng, *ACS Catal.*, 2024, **14**, 11076–11086.
177 X. Yang, X. Li, M. Liu, S. Yang, Q. Xu and G. Zeng, *Angew. Chem., Int. Ed.*, 2024, **63**, e202317785.
178 X. Wang, X. Ding, T. Wang, K. Wang, Y. Jin, Y. Han, P. Zhang, N. Li, H. Wang and J. Jiang, *ACS Appl. Mater. Interfaces*, 2022, **14**, 41122–41130.
179 Y. Wang, H. Ding, X. Ma, M. Liu, Y. Yang, Y. Chen, S. Li and Y. Lan, *Angew. Chem., Int. Ed.*, 2022, **61**, e202114648.
180 P. Guan, J. Qiu, Y. Zhao, H. Wang, Z. Li, Y. Shi and J. Wang, *Chem. Commun.*, 2019, **55**, 12459–12462.
181 S. An, T. Xu, C. Peng, J. Hu and H. Liu, *RSC Adv.*, 2019, **9**, 21438–21443.


© 2026 The Author(s). Published by the Royal Society of Chemistry

Open Access Article. Published on 12 fevral 2026. Downloaded on 01.06.2026 11:06:26.
This article is licensed under a Creative Commons Attribution-NonCommercial 3.0 Unported Licence.

182 W. Zhou, Q. W. Deng, G. Q. Ren, L. Sun, L. Yang, Y. M. Li, D. Zhai, Y. H. Zhou and W. Q. Deng, *Nat. Commun.*, 2020, **11**, 4481.
183 Q. Zhang, S. Gao and J. Yu, *Chem. Rev.*, 2022, **123**, 6039–6106.
184 B. Yue, S. Liu, Y. Chai, G. Wu, N. Guan and L. Li, *J. Energy Chem.*, 2022, **71**, 288–303.
185 Y. Li and J. Yu, *Nat. Rev. Mater.*, 2021, **6**, 1156–1174.
186 X. Deng, R. Bai, Y. Chai, Z. Hu, N. Guan and L. Li, *CCS Chemistry*, 2022, **4**, 949–962.
187 Y. Li and J. Yu, *Chem. Rev.*, 2014, **114**, 7268–7316.
188 C. S. Cundy and P. A. Cox, *Chem. Rev.*, 2003, **103**, 663–702.
189 G. T. M. Kadja, M. D. Rukmana, R. R. Mukti, M. H. Mahyuddin, A. G. Saputro and T. D. K. Wungu, *Mater. Lett.*, 2021, **290**, 129501.
190 M. A. Keane, *Colloids Surf. A Physicochem. Eng. Asp.*, 1998, **138**, 11–20.
191 W. W. Lestari, L. Yunita, T. E. Saraswati, E. Heraldy, M. A. Khafidhin, Y. K. Krisnandi, U. S. F. Arrozi and G. T. M. Kadja, *Chem. Pap.*, 2021, **75**, 3253–3263.
192 J. Gao, C. Jia and B. Liu, *Catal. Sci. Technol.*, 2017, **7**, 5602–5607.
193 J. Wei, Q. Ge, R. Yao, Z. Wen, C. Fang, L. Guo, H. Xu and J. Sun, *Nat. Commun.*, 2017, **8**, 15174.
194 S. Bhatia, *Zeolite Catalysts: Principles and Applications*, 1st edn, CRC Press, 1989.
195 R. P. Townsend and E. N. Coker, in *Studies in surface science and catalysis*, Elsevier, 2001, vol. 137, pp. 467–524.
196 N. J. Azhari, N. Nurdini, S. Mardiana, T. Ilmi, A. T. N. Fajar, I. G. B. N. Makertihartha, S. Subagjo and G. T. M. Kadja, *J. CO2 Util.*, 2022, **59**, 101969.
197 B. Dziejarski, J. Serafin, K. Andersson and R. Krzyżyńska, *Mater. Today Sustain.*, 2023, **24**, 100483.
198 M. W. Ackley, S. U. Rege and H. Saxena, *Microporous Mesoporous Mater.*, 2003, **61**, 25–42.
199 D. G. Boer, J. Langerak and P. P. Pescarmona, *ACS Appl. Energy Mater*, 2023, **6**(5), 2634–2656.
200 Q. Zhang, J. Li, L. Li and J. Yu, *Sci. China Chem*, 2025, **68**, 1703–1716.
201 H. J. Choi, D. Jo, J. G. Min and S. B. Hong, *Angew. Chem., Int. Ed.*, 2021, **60**, 4307–4314.
202 Q. Jiang, J. Rentschler, G. Sethia, S. Weinman, R. Perrone and K. Liu, *Chem. Eng. J.*, 2013, **230**, 380–388.
203 M. R. Hudson, W. L. Queen, J. A. Mason, D. W. Fickel, R. F. Lobo and C. M. Brown, *J. Am. Chem. Soc.*, 2012, **134**, 1970–1973.
204 M. Mofarahi and F. Gholipour, *Microporous Mesoporous Mater.*, 2014, **200**, 1–10.
205 M. M. Lozinska, E. Mangano, J. P. S. Mowat, A. M. Shepherd, R. F. Howe, S. P. Thompson, J. E. Parker, S. Brandani and P. A. Wright, *J. Am. Chem. Soc.*, 2012, **134**, 17628–17642.
206 J. Shang, G. Li, R. Singh, Q. Gu, K. M. Nairn, T. J. Bastow, N. Medhekar, C. M. Doherty, A. J. Hill and J. Z. Liu, *J. Am. Chem. Soc.*, 2012, **134**, 19246–19253.
207 M. P. S. Santos, C. A. Grande and A. E. Rodrigues, *Ind. Eng. Chem. Res.*, 2011, **50**, 974–985.
208 Z. Song, Y. Huang, W. L. Xu, L. Wang, Y. Bao, S. Li and M. Yu, *Sci. Rep.*, 2015, **5**, 13981.
209 Database of Zeolite Structures, International Zeolite Association, https://www.iza-structure.org/databases/, accessed July 2025.
210 R. Krishna, *Chem. Soc. Rev.*, 2012, **41**, 3099–3118.
211 E. Beerdsen, D. Dubbeldam and B. Smit, *Phys. Rev. Lett.*, 2006, **96**, 044501.
212 M. C. Verbraeken, R. Mennitto, V. M. Georgieva, E. L. Bruce, A. G. Greenaway, P. A. Cox, J. G. Min, S. B. Hong, P. A. Wright and S. Brandani, *Sep. Purif. Technol.*, 2021, **256**, 117846.
213 B. Ilić and S. G. Wettstein, *Microporous Mesoporous Mater.*, 2017, **239**, 221–234.
214 V. M. Georgieva, E. L. Bruce, R. G. Chitac, M. M. Lozinska, A. M. Hall, C. A. Murray, R. I. Smith, A. Turrina and P. A. Wright, *Chem. Mater.*, 2021, **33**, 1157–1173.
215 O. Cheung and N. Hedin, *RSC Adv.*, 2014, **4**, 14480–14494.
216 G. Calleja, J. Pau and J. A. Calles, *J. Chem. Eng. Data*, 1998, **43**, 994–1003.
217 H. Chen, W. Wang, J. Ding, X. Wei and J. Lu, *Energy Procedia*, 2017, **105**, 4370–4376.
218 R. A. Schoonheydt, P. Geerlings, E. A. Pidko and R. A. Van Santen, *J. Mater. Chem.*, 2012, **22**, 18705–18717.
219 D. Barthomeuf, *J. Phys. Chem.*, 1984, **88**, 42–45.
220 M. Palomino, A. Corma, F. Rey and S. Valencia, *Langmuir*, 2010, **26**, 1910–1917.
221 D. Newsome, S. Gunawan, G. Baron, J. Denayer and M.-O. Coppens, *Adsorption*, 2014, **20**, 157–171.
222 H. J. Choi and S. B. Hong, *Chem. Eng. J.*, 2022, **433**, 133800.
223 D. Barthomeuf, *Microporous Mesoporous Mater.*, 2003, **66**, 1–14.
224 J. C. Lavalley, *Catal. Today*, 1996, **27**, 377–401.
225 Z. Tao, Y. Tian, S. Y. Ou, Q. Gu and J. Shang, *AIChE J.*, 2023, **69**, e18139.
226 E. B. Clatworthy, S. Ghojavand, R. Guillet-Nicolas, J.-P. Gilson, P. L. Llewellyn, N. Nesterenko and S. Mintova, *Chem. Eng. J.*, 2023, **471**, 144557.
227 A. A. Dabbawala, I. Ismail, B. V. Vaithilingam, K. Polychronopoulou, G. Singaravel, S. Morin, M. Berthod and Y. Al Wahedi, *Microporous Mesoporous Mater.*, 2020, **303**, 110261.
228 J. Shen, Q. Sun, J. Cao, P. Wang, W. Jia, S. Wang, P. Zhao and Z. Wang, *New J. Chem.*, 2022, **46**, 6720–6728.
229 J. Al Atrach, A. Aitblal, A. Amedlous, E. B. Clatworthy, D. Honorato Piva, Y. Xiong, R. Guillet-Nicolas and V. Valtchev, *ACS Appl. Mater. Interfaces*, 2025, **17**, 7119–7130.
230 L. Xu, Y. Xiu, F. Liu, Y. Liang and S. Wang, *Molecules*, 2020, **25**, 3653.
231 M. Usman, A. S. Ghanem, S. Niaz Ali Shah, M. D. Garba, M. Yusuf Khan, S. Khan, M. Humayun and A. Laeeq Khan, *Chem. Rec.*, 2022, **22**, e202200039.
232 M. Zhu, Q. Ge and X. Zhu, *Trans. Tianjin Univ.*, 2020, **26**, 172–187.
233 Z. Zhang, M. Li, R. Gao, S. Yang, Q. Ma, R. Feng, H. Dou, J. Dang, G. Wen, Z. Bai, D. Liu, M. Feng and Z. Chen, *J. Am. Chem. Soc.*, 2024, **146**, 6397–6407.

Open Access Article. Published on 12 fevral 2026. Downloaded on 01.06.2026 11:06:26.
This article is licensed under a Creative Commons Attribution-NonCommercial 3.0 Unported Licence.

234 Y. Zhu, P. Li, X. Yang, M. Wang, Y. Zhang, P. Gao, Q. Huang, Y. Wei, X. Yang, D. Wang, Y. Shen and M. Wang, *Adv. Energy Mater.*, 2023, **13**, 2204143.
235 L. Li, H. S. Jung, J. W. Lee and Y. T. Kang, *Renewable Sustainable Energy Rev.*, 2022, **162**, 112441.
236 X. Lin, S. Wang, W. Tu, Z. Hu, Z. Ding, Y. Hou, R. Xu and W. Dai, *Catal. Sci. Technol.*, 2019, **9**, 731–738.
237 T. Qiu, S. Gao, Z. Liang, D. Wang, H. Tabassum, R. Zhong and R. Zou, *Angew. Chem.*, 2021, **133**, 17455–17477.
238 V. A. Tran, H. H. Do, V. T. Le, Y. Vasseghian, V. Vo, S. H. Ahn, S. Y. Kim and S. W. Lee, *Int. J. Hydrogen Energy*, 2022, **47**, 19590–19608.
239 M. A. Nazir, N. A. Khan, C. Cheng, S. S. A. Shah, T. Najam, M. Arshad, A. Sharif, S. Akhtar and A. ur Rehman, *Appl. Clay Sci.*, 2020, **190**, 105564.
240 H. Zhang, X. Liu, Y. Wu, C. Guan, A. K. Cheetham and J. Wang, *Chem. Commun.*, 2018, **54**, 5268–5288.
241 S. S. A. Shah, T. Najam, M. K. Aslam, M. Ashfaq, M. M. Rahman, K. Wang, P. Tsiakaras, S. Song and Y. Wang, *Appl. Catal., B*, 2020, **268**, 118570.
242 Z. Zeng, X. Fang, W. Miao, Y. Liu, T. Maiyalagan and S. Mao, *ACS Sens*, 2019, **4**, 1934–1941.
243 H. Zhang, J. Li, Q. Tan, L. Lu, Z. Wang and G. Wu, *Chem. Eur. J.*, 2018, **24**, 18137.
244 S. Bose, D. Sengupta, T. M. Rayder, X. Wang, K. O. Kirlikovali, A. K. Sekizkardes, T. Islamoglu and O. K. Farha, *Adv. Funct. Mater.*, 2024, **34**, 2307478.
245 S. Mahajan and M. Lahtinen, *J. Environ. Chem. Eng.*, 2022, **10**, 108930.
246 J. Wang, Z. Jiang, S. Wen, Y. Wei, P. Ning and Y. Zhang, *J. Mater. Chem. A.*, 2025, **13**, 11185–11209.
247 A. R. Millward and O. M. Yaghi, *J. Am. Chem. Soc.*, 2005, **127**, 17998–17999.
248 C. A. Trickett, A. Helal, B. A. Al-Maythalony, Z. H. Yamani, K. E. Cordova and O. M. Yaghi, *Nat. Rev. Mater.*, 2017, **2**, 17045.
249 S. Gao, Y. Lin, X. Jiao, Y. Sun, Q. Luo, W. Zhang, D. Li, J. Yang and Y. Xie, *Nature*, 2016, **529**, 68–71.
250 F. Li, H. Yang, W. Li and L. Sun, *Joule*, 2018, **2**, 36–60.
251 A. Banerjee and C. G. Morales-Guio, *EES Catal*, 2025, **3**, 205–234.
252 X. Zhang, Z. Wu, X. Zhang, L. Li, Y. Li, H. Xu, X. Li, X. Yu, Z. Zhang, Y. Liang and H. Wang, *Nat. Commun.*, 2017, **8**, 1.
253 L. Zhang, Z. J. Zhao and J. Gong, *Angew. Chem., Int. Ed.*, 2017, **56**, 11326–11353.
254 R. Hinogami, S. Yotsuhashi, M. Deguchi, Y. Zenitani, H. Hashiba and Y. Yamada, *ECS Electrochem. Lett.*, 2012, **1**, H17.
255 R. Senthil Kumar, S. Senthil Kumar and M. Anbu Kulandainathan, *Electrochem. Commun.*, 2012, **25**, 70–73.
256 M. Cheng, X. Zheng, F. Ma, Z. Zhu and Q. Xu, *ChemCatChem*, 2024, **16**, e202400438.
257 R. Chen, L. Cheng, J. Liu, Y. Wang, W. Ge, C. Xiao, H. Jiang, Y. Li and C. Li, *Small*, 2022, **18**, 2200720.
258 C. P. Wan, H. Guo, D. H. Si, S. Y. Gao, R. Cao and Y. B. Huang, *JACS Au*, 2024, **4**, 2514–2522.
259 H. Li, R. Li, J. Niu, K. Gan and X. He, *Front. Chem.*, 2022, **10**, 1067327.
260 C. Li, Y. Ji, Y. Wang, C. Liu, Z. Chen, J. Tang, Y. Hong, X. Li, T. Zheng, Q. Jiang and C. Xia, *Nano-Micro Lett.*, 2023, **15**, 1–44.
261 C. Li, H. Yan and H. Yang, *et al.*, *Sci. China Mater.*, 2025, **68**, 21–38.
262 M. Ding, R. W. Flaig, H. L. Jiang and O. M. Yaghi, *Chem. Soc. Rev.*, 2019, **48**, 2783–2828.
263 J. M. Huang, X. Da Zhang, J. Y. Huang, D. S. Zheng, M. Xu and Z. Y. Gu, *Coord. Chem. Rev.*, 2023, **494**, 215333.
264 D. Kim, W. Choi, H. W. Lee, S. Y. Lee, Y. Choi, D. K. Lee, W. Kim, J. Na, U. Lee, Y. J. Hwang and D. H. Won, *ACS Energy Lett.*, 2021, **6**, 3488–3495.
265 J. Wang, Y. Zhang, Y. Ma, J. Yin, Y. Wang and Z. Fan, *ACS Mater. Lett.*, 2022, **4**, 2058–2079.
266 Y. Belmabkhout, V. Guillerm and M. Eddaoudi, *Chem. Eng. J.*, 2016, **296**, 386–397.
267 Q. Yang, C. Xue, C. Zhong and J. F. Chen, *AIChE J.*, 2007, **53**, 2832–2840.
268 H. M. Polat, S. Kavak, H. Kulak, A. Uzun and S. Keskin, *Chem. Eng. J.*, 2020, **394**, 124916.
269 W. Liang, P. M. Bhatt, A. Shkurenko, K. Adil, G. Mouchaham, H. Aggarwal, A. Mallick, A. Jamal, Y. Belmabkhout and M. Eddaoudi, *Chem*, 2019, **5**, 950–963.
270 C. Y. Gao, J. Ai, H. R. Tian, D. Wu and Z. M. Sun, *Chem. Commun.*, 2017, **53**, 1293–1296.
271 J. S. Yan, R. T. Guo, L. Q. Yu, H. Liu, S. H. Guo and W. G. Pan, *Energy Fuels*, 2023, **37**, 15453–15475.
272 Y.-Y. Liu, J.-R. Huang, H.-L. Zhu, P.-Q. Liao and X.-M. Chen, *Angew. Chem.*, 2023, **135**, e202311265.
273 T. Al-Attas, S. K. Nabil, A. S. Zeraati, H. S. Shiran, T. Alkayyali, M. Zargartalebi, T. Tran, N. N. Marei, M. A. Al Bari, H. Lin, S. Roy, P. M. Ajayan, D. Sinton, G. Shimizu and M. G. Kibria, *ACS Energy Lett.*, 2023, **8**, 107–115.
274 Y. L. Qiu, H. X. Zhong, T. T. Zhang, W. Bin Xu, P. P. Su, X. F. Li and H. M. Zhang, *ACS Appl. Mater. Interfaces*, 2018, **10**, 2480–2489.
275 S. Nitopi, E. Bertheussen, S. B. Scott, X. Liu, A. K. Engstfeld, S. Horch, B. Seger, I. E. L. Stephens, K. Chan, C. Hahn, J. K. Nørskov, T. F. Jaramillo and I. Chorkendorff, *Chem. Rev.*, 2019, **119**, 7610–7672.
276 D.-H. Nam, O. Shekhah, A. Ozden, C. McCallum, F. Li, X. Wang, Y. Lum, T. Lee, J. Li, J. Wicks, A. Johnston, D. Sinton, M. Eddaoudi and E. H. Sargent, *Adv. Mater.*, 2022, **34**, 2207088.
277 B. Kumar, B. Muchharla, M. Dikshit, S. Dongare, K. Kumar, B. Gurkan and J. M. Spurgeon, *Environ. Sci. Technol. Lett.*, 2024, **11**(11), 1161–1174.
278 Z. H. Zhao, J. R. Huang, D. S. Huang, H. L. Zhu, P. Q. Liao and X. M. Chen, *J. Am. Chem. Soc.*, 2024, **146**, 14349–14356.
279 E. M. Johnson, S. Ilic and A. J. Morris, *ACS Cent. Sci.*, 2021, **7**, 445–453.
280 C. Cammarere, J. Cortés, T. G. Glover, R. Q. Snurr, J. T. Hupp and J. Liu, *Front. Chem.*, 2025, **13**, 1634637.
281 D. Bohra, J. H. Chaudhry, T. Burdyny, E. A. Pidko and W. A. Smith, *Energy Environ. Sci.*, 2019, **12**, 3380–3389.
282 X. Zhang, D. Xue, S. Jiang, H. Xia, Y. Yang, W. Yan, J. Hu and J. Zhang, *InfoMat*, 2022, **4**, e12257.


© 2026 The Author(s). Published by the Royal Society of Chemistry

Open Access Article. Published on 12 fevral 2026. Downloaded on 01.06.2026 11:06:26.
This article is licensed under a Creative Commons Attribution-NonCommercial 3.0 Unported Licence.

283 K. Yang, M. Li, T. Gao, G. Xu, D. Li, Y. Zheng, Q. Li and J. Duan, *Nat. Commun.*, 2024, **15**, 7060.
284 D. Bůžek, S. Adamec, K. Lang and J. Demel, *Inorg. Chem. Front.*, 2021, **8**, 720–734.
285 X. Zhao, C. Y. Zhu, J. S. Qin, H. Rao, D. Y. Du, M. Zhang, P. She, L. Li and Z. M. Su, *Mater. Chem. Front.*, 2024, **8**, 2439–2446.
286 W. Wang, H. Yan, U. Anand and U. Mirsaidov, *J. Am. Chem. Soc.*, 2021, **143**, 1854–1862.
287 B. Han, K. A. Stoerzinger, V. Tileli, A. D. Gamalski, E. A. Stach and Y. Shao-Horn, *Nat. Mater.*, 2017, **16**, 121–126.
288 N. Gholampour, C. I. Ezugwu, H. A. Younus, D. P. Debecker, M. Al Abri, R. Alhajri, C. M. Kao and F. Verpoort, *J. Mater. Chem. A.*, 2024, **12**, 27825–27854.
289 S. Yuan, L. Feng, K. Wang, J. Pang, M. Bosch, C. Lollar, Y. Sun, J. Qin, X. Yang, P. Zhang, Q. Wang, L. Zou, Y. Zhang, L. Zhang, Y. Fang, J. Li and H. C. Zhou, *Adv. Mater.*, 2018, **30**, 1704303.
290 S. Yuan, J. S. Qin, C. T. Lollar and H. C. Zhou, *ACS Cent. Sci.*, 2018, **4**, 440–450.
291 S. Dou, X. Li and X. Wang, *ACS Mater. Lett.*, 2020, **2**, 1251–1267.
292 M. Ding, X. Cai and H.-L. Jiang, *Chem. Sci.*, 2019, **10**, 10209–10230.
293 M. A. Abdelkareem, Q. Abbas, E. T. Sayed, N. Shehata, J. B. M. Parambath, A. H. Alami and A. G. Olabi, *Energy*, 2024, **299**, 131127.
294 Y. Cheng, J. Hou and P. Kang, *ACS Energy Lett.*, 2021, **6**, 3352–3358.
295 S. K. Nabil, S. Roy, W. A. Algozeeb, T. Al-Attas, M. A. Al Bari, A. S. Zeraati, K. Kannimuthu, P. G. Demingos, A. Rao, T. N. Tran, X. Wu, P. Bollini, H. Lin, C. V. Singh, J. M. Tour, P. M. Ajayan and M. G. Kibria, *Adv. Mater.*, 2023, **35**, 2300389.
296 T. Yan, S. Liu, Z. Liu, J. Sun and P. Kang, *Adv. Funct. Mater.*, 2024, **34**, 1–8.
297 Y. Xu, J. P. Edwards, J. Zhong, C. P. O'Brien, C. M. Gabardo, C. McCallum, J. Li, C. T. Dinh, E. H. Sargent and D. Sinton, *Energy Environ. Sci.*, 2020, **13**, 554–561.
298 P. Zhu, Z. Y. Wu, A. Elgazzar, C. Dong, T. U. Wi, F. Y. Chen, Y. Xia, Y. Feng, M. Shakouri, J. Y. (Timothy) Kim, Z. Fang, T. A. Hatton and H. Wang, *Nature*, 2023, **618**, 959–966.
299 M. B. Li, M. Li, F. Luo, L. Zhou and H. Li, *Energy Fuels*, 2024, **38**, 10390–10393.
300 X. Y. D. Soo, J. J. C. Lee, W. Y. Wu, L. Tao, C. Wang, Q. Zhu and J. Bu, *J. CO2 Util.*, 2024, **81**, 102727.
301 G. Zhang, J. Liu, J. Qian, X. Zhang and Z. Liu, *J. Ind. Eng. Chem.*, 2024, **134**, 28–50.
302 J. Hack, N. Maeda and D. M. Meier, *ACS Omega*, 2022, **7**(44), 39520–39530.
303 S. Hafizi Yazdabadi, D. Mihrin, K. L. Feilberg and R. Wugt Larsen, *Molecules*, 2024, **29**, 5521.
304 K. Gottschling, L. Stegbauer, G. Savasci, N. A. Prisco, Z. J. Berkson, C. Ochsenfeld, B. F. Chmelka and B. V. Lotsch, *Chem. Mater.*, 2019, **31**, 1946–1955.
305 X. Yang, R. J. Rees, W. Conway, G. Puxty, Q. Yang and D. A. Winkler, *Chem. Rev.*, 2017, **117**(14), 9524–9593.
306 B. Yoon and G. A. Voth, *J. Am. Chem. Soc.*, 2023, **145**, 15663–15667.
307 D. Loachamin, J. Casierra, V. Calva, A. Palma-Cando, E. E. Ávila and M. Ricaurte, *Chem. Eng.*, 2024, **8**, 129.
308 H. Yu and P. H. M. Feron, in *Absorption-Based Post-Combustion Capture of Carbon Dioxide*, Elsevier Inc., 2016, pp. 283–301.
309 B. K. Choi, S. M. Kim, K. M. Kim, U. Lee, J. H. Choi, J. S. Lee, I. H. Baek, S. C. Nam and J. H. Moon, *Chem. Eng. J.*, 2021, **419**, 129517.
310 M. Caplow, *J. Am. Chem. Soc.*, 1968, **90**, 6795–6803.
311 E. Pérez-Gallent, C. Vankani, C. Sánchez-Martínez, A. Anastasopol and E. Goetheer, *Ind. Eng. Chem. Res.*, 2021, **60**, 4269–4278.
312 G. Lee, Y. C. Li, J. Y. Kim, T. Peng, D. H. Nam, A. Sedighian Rasouli, F. Li, M. Luo, A. H. Ip, Y. C. Joo and E. H. Sargent, *Nat. Energy*, 2021, **6**, 46–53.
313 M. Abdinejad, Z. Mirza, X. A. Zhang and H. B. Kraatz, *ACS Sustainable Chem. Eng.*, 2020, **8**, 1715–1720.
314 L. Chen, F. Li, Y. Zhang, C. L. Bentley, M. Horne, A. M. Bond and J. Zhang, *ChemSusChem*, 2017, **10**, 4109–4118.
315 N. Ahmad, Y. Chen, X. Wang, P. Sun, Y. Bao and X. Xu, *Renew. Energy*, 2022, **189**, 444–453.
316 J. H. Kim, H. Jang, G. Bak, W. Choi, H. Yun, E. Lee, D. Kim, J. Kim, S. Y. Lee and Y. J. Hwang, *Energy Environ. Sci.*, 2022, **15**, 4301–4312.
317 M. N. Hossain, S. Ahmad, I. S. da Silva and H. B. Kraatz, *Chem. Eur. J.*, 2021, **27**, 1346–1355.
318 S. Akhter, T. Palai, L. M. Aeshala and A. M. Kannan, *Carbon Capture Sci. Technol*, 2024, **13**, 100289.
319 J. Lin, Y. Zhang, P. Xu and L. Chen, *Materials Reports: Energy.*, 2023, **3**, 100194.
320 X. Zhu, Z. Chen and H. Ai, *J. Mol. Model.*, 2020, **26**, 345.
321 J. P. Hallett and T. Welton, *Chem. Rev*, 2011, **111**(5), 3508–3576.
322 L. Sun, H. Xia, O. Morales-Collazo and J. F. Brennecke, *ECS Trans.*, 2016, **75**, 469–487.
323 S. Hussain, A. Ali, S. Foorginezhad, Y. Chen and X. Ji, *Sep. Purif. Technol.*, 2025, **360**, 130997.
324 B. E. Gurkan, T. R. Gohndrone, M. J. McCready and J. F. Brennecke, *Phys. Chem. Chem. Phys.*, 2013, **15**, 7796–7811.
325 J. Cheng, Y. Li, L. Hu, J. Zhou and K. Cen, *Energy Fuels*, 2016, **30**, 3251–3256.
326 S. Seo, M. A. Desilva, H. Xia and J. F. Brennecke, *J. Phys. Chem. B*, 2015, **119**, 11807–11814.
327 L. A. Blanchard, Z. Gu and J. F. Brennecke, *J. Phys. Chem. B*, 2001, **105**, 2437–2444.
328 A. Shariati and C. J. Peters, *J. Supercrit. Fluids*, 2005, **34**, 171–176.
329 S. G. Kazarian, B. J. Briscoe and T. Welton, *Chem. Commun.*, 2000, 2047–2048.
330 C. Cadena, J. L. Anthony, J. K. Shah, T. I. Morrow, J. F. Brennecke and E. J. Maginn, *J. Am. Chem. Soc.*, 2004, **126**, 5300–5308.
331 J. L. Anthony, J. L. Anderson, E. J. Maginn and J. F. Brennecke, *J. Phys. Chem. B*, 2005, **109**, 6366–6374.

Open Access Article. Published on 12 fevral 2026. Downloaded on 01.06.2026 11:06:26.
This article is licensed under a Creative Commons Attribution-NonCommercial 3.0 Unported Licence.

332 X. Zhang, K. Jiang, Z. Liu, X. Yao, X. Liu, S. Zeng, K. Dong and S. Zhang, *Ind. Eng. Chem. Res.*, 2019, **58**, 1443–1453.
333 R. Zhang, Q. Ke, Z. Zhang, B. Zhou, G. Cui and H. Lu, *Int. J. Mol. Sci.*, 2022, **23**, 11401.
334 S. K. Shukla, S. G. Khokarale, T. Q. Bui and J. P. T. Mikkola, *Front. Mater*, 2019, **6**, 42.
335 S. Onofri and E. Bodo, *J. Phys. Chem. B*, 2021, **125**, 5611–5619.
336 S. Saravanamurugan, A. J. Kunov-Kruse, R. Fehrmann and A. Riisager, *ChemSusChem*, 2014, **7**, 897–902.
337 J. Ma, Y. Du, M. Liu, Y. Zhou, X. Wang, B. Wang, J. Zhu and M. Zhu, *J. Phys. Chem. B*, 2025, **129**, 372–384.
338 J. Ma, Y. Zhou, M. Liu, Y. Du, X. Wang, B. Wang, M. Zhu and J. Zhu, *Carbon Capture Sci. Technol.*, 2024, **12**, 100222.
339 H. Huang, R. Peters, R. C. Samsun, D. Stolten, C. He and X. Zhou, *Energy*, 2024, **301**, 131670.
340 E. D. Bates, R. D. Mayton, I. Ntai and J. H. Davis, *J. Am. Chem. Soc.*, 2002, **124**, 926–927.
341 W. Faisal Elmobarak, F. Almomani, M. Tawalbeh, A. Al-Othman, R. Martis and K. Rasool, *Fuel*, 2023, **344**, 128102.
342 H. Zhao and G. A. Baker, *Green Chem. Lett. Rev.*, 2023, **16**, 1.
343 H. Ohno and K. Fukumoto, *Acc. Chem. Res.*, 2007, **40**, 1122–1129.
344 G. Yu, D. Zhao, L. Wen, S. Yang and X. Chen, *AIChE J.*, 2012, **58**, 2885–2899.
345 R. Macchieraldo, L. Esser, R. Elfgen, P. Voepel, S. Zahn, B. M. Smarsly and B. Kirchner, *ACS Omega*, 2018, **3**, 8567–8582.
346 T. Numpilai, L. K. H. Pham and T. Witoon, *Ind. Eng. Chem. Res.*, 2024, **63**(46), 19865–19915.
347 S. J. Grabowski, *Crystals.*, 2020, **10**, 460.
348 T. B. Lee, S. Oh, T. R. Gohndrone, O. Morales-Collazo, S. Seo, J. F. Brennecke and W. F. Schneider, *J. Phys. Chem. B*, 2016, **120**, 1509–1517.
349 S. F. R. Taylor, C. McCrellis, C. McStay, J. Jacquemin, C. Hardacre, M. Mercy, R. G. Bell and N. H. De Leeuw, *J. Solution Chem.*, 2015, **44**, 511–527.
350 Q. R. Sheridan, W. F. Schneider and E. J. Maginn, *J. Phys. Chem. B*, 2016, **120**, 12679–12686.
351 O. Palumbo, A. Cimini, F. Trequattrini, J. B. Brubach, P. Roy and A. Paolone, *Int. J. Mol. Sci.*, 2021, **22**, 6155.
352 T. Koishi, *J. Phys. Chem. B*, 2018, **122**, 12342–12350.
353 F. Ju, J. Zhang and W. Lu, *Catalysts*, 2020, **10**, 1–14.
354 A. Senocrate and C. Battaglia, *J. Energy Storage*, 2021, **36**, 102373.
355 B. A. Rosen, A. Salehi-Khojin, M. R. Thorson, W. Zhu, D. T. Whipple, P. J. A. Kenis and R. I. Masel, *Science.*, 2011, **334**, 643–644.
356 B. Kumar, M. Asadi, D. Pisasale, S. Sinha-Ray, B. A. Rosen, R. Haasch, J. Abiade, A. L. Yarin and A. Salehi-Khojin, *Nat. Commun.*, 2013, **4**, 2819.
357 E. E. L. Tanner, C. Batchelor-McAuley and R. G. Compton, *J. Phys. Chem. C*, 2016, **120**, 26442–26447.
358 S. Yu and P. K. Jain, *Nat. Commun.*, 2019, **10**, 2022.
359 A. Kemna, N. García Rey and B. Braunschweig, *ACS Catal.*, 2019, **9**, 6284–6292.
360 Y. Wang, M. Hatakeyama, K. Ogata, M. Wakabayashi, F. Jin and S. Nakamura, *Phys. Chem. Chem. Phys.*, 2015, **17**, 23521–23531.
361 L. Yuan, L. Zhang, J. Feng, C. Jiang, J. Feng, C. Li, S. Zeng and X. Zhang, *Chem. Eng. J.*, 2022, **450**, 138378.
362 S. S. Neubauer, R. K. Krause, B. Schmid, D. M. Guldi and G. Schmid, *Adv. Energy Mater.*, 2016, **6**, 1502231.
363 T. N. Huan, P. Simon, G. Rousse, I. Génois, V. Artero and M. Fontecave, *Chem. Sci.*, 2016, **8**, 742–747.
364 J. L. Dimeglio and J. Rosenthal, *J. Am. Chem. Soc.*, 2013, **135**, 8798–8801.
365 H. K. Lim, Y. Kwon, H. S. Kim, J. Jeon, Y. H. Kim, J. A. Lim, B. S. Kim, J. Choi and H. Kim, *ACS Catal.*, 2018, **8**, 2420–2427.
366 A. Leal-Duaso, Y. Adjez and C. M. Sánchez-Sánchez, *ChemElectroChem*, 2024, **11**, e202300771.
367 Y. Li, F. Li, A. Laaksonen, C. Wang, P. Cobden, P. Boden, Y. Liu, X. Zhang and X. Ji, *Ind. Chem. Mater.*, 2023, **1**, 410–430.
368 X. Tan, X. Sun and B. Han, *Natl. Sci. Rev.*, 2022, **9**, nwab022.
369 A. Verma, J. P. Stoppelman and J. G. McDaniel, *Int. J. Mol. Sci.*, 2020, **21**, 403.
370 X. Li, W. Han, S. Yu and F. Zou, *Chem. Eng. Trans.*, 2018, **66**, 223–228.
371 W. A. Parada, D. V. Vasilyev, K. J. J. Mayrhofer and I. Katsounaros, *ACS Appl. Mater. Interfaces*, 2022, **14**(12), 14193–14201.
372 Y. Sha, J. Zhang, X. Cheng, M. Xu, Z. Su, Y. Wang, J. Hu, B. Han and L. Zheng, *Angew. Chem., Int. Ed.*, 2022, **61**, e202200039.
373 G. Iijima, T. Kitagawa, A. Katayama, T. Inomata, H. Yamaguchi, K. Suzuki, K. Hirata, Y. Hijikata, M. Ito and H. Masuda, *ACS Catal*, 2018, **8**, 1990–2000.
374 J. Tamura, A. Ono, Y. Sugano, C. Huang, H. Nishizawa and S. Mikoshiba, *Phys. Chem. Chem. Phys.*, 2015, **17**, 26072–26078.
375 P. Tamilarasan and S. Ramaprabhu, *J. Mater. Chem. A.*, 2015, **3**, 797–804.
376 S. Kamalakannan, K. Rudharachari Maiyelvaganan, K. Palanisamy, A. Thomas, R. Ben Said, M. Prakash and M. Hochlaf, *Chemosphere*, 2022, **286**, 131612.
377 D. Faggion, W. D. G. Gonçalves and J. Dupont, *Front. Chem.*, 2019, **7**, 102.
378 S. Dongare, O. K. Coskun, E. Cagli, K. Y. C. Lee, G. Rao, R. D. Britt, L. A. Berben and B. Gurkan, *ACS Catal.*, 2023, **13**, 7812–7821.
379 Y. Zhao, X. Wang, Z. Li, H. Wang, Y. Zhao and J. Qiu, *J. Phys. Chem. B*, 2024, **128**, 1079–1090.
380 X. An, P. Wang, X. Ma, X. Du, X. Hao, Z. Yang and G. Guan, *Carbon Resources Conversion*, 2023, **6**, 85–97.
381 M. M. Wan, H. Y. Zhu, Y. Y. Li, J. Ma, S. Liu and J. H. Zhu, *ACS Appl. Mater. Interfaces*, 2014, **6**, 12947–12955.
382 N. L. Ho, J. Perez-Pellitero, F. Porcheron and R. J. M. Pellenq, *J. Phys. Chem. C*, 2012, **116**, 3600–3607.
383 S. Supasitmongkol and P. Styring, *Energy Environ. Sci.*, 2010, **3**, 1961–1972.
384 D. Yang, Q. Zhu, C. Chen, H. Liu, Z. Liu, Z. Zhao, X. Zhang, S. Liu and B. Han, *Nat. Commun.*, 2019, **10**, 677.


© 2026 The Author(s). Published by the Royal Society of Chemistry

Open Access Article. Published on 12 fevral 2026. Downloaded on 01.06.2026 11:06:26.
This article is licensed under a Creative Commons Attribution-NonCommercial 3.0 Unported Licence.

385 M. H. Barecka, J. W. Ager and A. A. Lapkin, *Energy Environ. Sci.*, 2021, **14**, 1530–1543.
386 M. Rumayor, A. Dominguez-Ramos, P. Perez and A. Irabien, *J. CO2 Util.*, 2019, **34**, 490–499.
387 J. Baier, G. Schneider and A. Heel, *Front. Energy Res.*, 2018, **6**, 5.
388 Y. Li, $CO_2$ electrochemical reduction to CO with ionic liquids: evaluation and technology exploration, *Luleå University of Technology*, 2025, ISBN: 978-91-8048-831-0.
389 B. B. Hansen, S. Spittle, B. Chen, D. Poe, Y. Zhang, J. M. Klein, A. Horton, L. Adhikari, T. Zelovich, B. W. Doherty, B. Gurkan, E. J. Maginn, A. Ragauskas, M. Dadmun, T. A. Zawodzinski, G. A. Baker, M. E. Tuckerman, R. F. Savinell and J. R. Sangoro, *Chem. Rev.*, 2021, **121**(3), 1232–1285.
390 Q. Zhang, K. De Oliveira Vigier, S. Royer and F. Jérôme, *Chem. Soc. Rev.*, 2012, **41**, 7108–7146.
391 M. F. H. Ismail, A. N. Masri, N. Mohd Rashid, I. M. Ibrahim, S. A. S. Mohammed and W. Z. N. Yahya, *J. Mol. Liq.*, 2024, **4**, 100114.
392 A. Paiva, R. Craveiro, I. Aroso, M. Martins, R. L. Reis and A. R. C. Duarte, *ACS Sustainable Chem. Eng*, 2014, **2**(5), 1063–1071.
393 L. I. N. Tomé, V. Baião, W. da Silva and C. M. A. Brett, *Appl. Mater. Today*, 2018, **10**, 30–50.
394 A. P. Abbott, D. Boothby, G. Capper, D. L. Davies and R. K. Rasheed, *J. Am. Chem. Soc.*, 2004, **126**, 9142–9147.
395 O. E. Plastiras and V. Samanidou, *Molecules*, 2022, **27**, 7699.
396 R. Urvika and R. Kataria, Deep Eutectic Solvents, in *ACS Symposium Series*, vol. 1504, American Chemical Society, 2025, pp. 1–29.
397 S. P. Ijardar, V. Singh and R. L. Gardas, *Molecules*, 2022, **27**, 1368.
398 M. Freemantle, *Chem. Eng. News*, 2005, **83**(37), 33–38.
399 V. Agieienko and R. Buchner, *J. Chem. Eng. Data*, 2021, **66**, 780–792.
400 A. Umar, M. Munir, M. Murtaza, R. Sultana, M. A. Riaz, G. R. Srinivasan, A. Firdous and M. Saeed, *Egypt. J. Chem.*, 2020, **63**, 59–69.
401 H. Wang, X. Kang and B. Han, *Chem. Sci.*, 2024, **15**, 9949–9976.
402 X. Meng, K. Ballerat-Busserolles, P. Husson and J. M. Andanson, *New J. Chem.*, 2016, **40**, 4492–4499.
403 V. Alizadeh, L. Esser and B. Kirchner, *J. Chem. Phys.*, 2021, **154**, 094503.
404 B. Bohlen, D. Wastl, J. Radomski, V. Sieber and L. Vieira, *Electrochem. commun.*, 2020, **110**, 106597.
405 T. J. Trivedi, J. H. Lee, H. J. Lee, Y. K. Jeong and J. W. Choi, *Green Chem.*, 2016, **18**, 2834–2842.
406 S. Foorginezhad and X. Ji, *Results Eng.*, 2025, **26**, 105162.
407 Q. Shi, K. Jia, X. Zhang, C. Wang, P. Cobden, A.-M. B. Amnéus, D. Muren and X. Ji, *Chem. Eng. J.*, 2025, **522**, 167866.
408 Z. Coin, S. Dangwal, M. H. Irwin, T. Knight, R. Bhave, G. Rother, R. Sacci, M. Arifuzzaman, V. Bocharova, I. Ivanov, D. S. Sholl and S. Z. Islam, *ACS Omega*, 2025, **10**, 3407–3417.
409 S. Sarmad, Y. Xie, J. P. Mikkola and X. Ji, *New J. Chem.*, 2016, **41**, 290–301.
410 A. A. Manafpour, F. Feyzi and M. Rezaee, *Sci. Rep.*, 2024, **14**, 19744.
411 H. Wibowo, L. Zhong, Q. Huan, Q. Hu, D. A. Rahim and M. Yan, *Biomass Convers. Biorefin.*, 2022, **12**, 61–71.
412 S. Bhattacharjee and R. Getman, Effect of Water On Deep Eutectic Solvents: Structural Properties and Interactions with CO2, *ChemRxiv*, 2023, DOI: 10.26434/chemrxiv-2023-bqj91.
413 M. Chen and J. Xu, *Molecules*, 2023, **28**, 5461.
414 S. K. Shukla and J. P. Mikkola, *Phys. Chem. Chem. Phys.*, 2018, **20**, 24591–24601.
415 T. Umecky, A. Goto, N. Hayashi and K. Eguchi, *ACS Omega*, 2023, **8**, 14694–14698.
416 X. Liu, Q. Ao, S. Shi and S. Li, *Mater. Res. Express*, 2022, **9**, 015504.
417 Q. Shi, Z. Zuo and X. Ji, *Sep. Purif. Technol.*, 2025, **367**, 132877.
418 L. L. Bezerra, A. N. Correia, P. de Lima-Neto, N. de and K. V. Monteiro, *J. Mol. Graphics Modell.*, 2024, **126**, 108649.
419 A. Al-Bodour, N. Alomari, S. K. Liew, S. Aparicio, J. Springstead and M. Atilhan, *ACS Omega*, 2025, **10**, 24675–24696.
420 M. Heydari Dokoohaki and A. R. Zolghadr, *J. Phys. Chem. B*, 2021, **125**, 10035–10046.
421 B. Jiang, C. Zhang, Q. Zhou, L. Zhang, J. Li, X. Tantai, Y. Sun and L. Zhang, *ACS Sustainable Chem. Eng.*, 2024, **12**, 14109–14118.
422 I. Cichowska-Kopczyńska, D. Warmińska and B. Nowosielski, *Materials*, 2021, **14**, 1–14.
423 K. Xin, F. Gallucci and M. Van Sint Annaland, *ACS Sustainable Chem. Eng.*, 2022, **10**, 15284–15296.
424 M. B. Haider, P. Maheshwari and R. Kumar, *J. Environ. Chem. Eng.*, 2021, **9**, 106727.
425 C. Ma, S. Sarmad, J. P. Mikkola and X. Ji, in *Energy Procedia*, Elsevier Ltd, 2017, vol. 142, pp. 3320–3325.
426 H. Sang, L. Su, W. Han, F. Si, W. Yue, X. Zhou, Z. Peng and H. Fu, *J. CO2 Util.*, 2022, **65**, 102201.
427 N. Ahmad, X. Lin, X. Wang, J. Xu and X. Xu, *Fuel*, 2021, **293**, 120466.
428 N. Noorani and A. Mehrdad, *J. Mol. Liq.*, 2022, **357**, 119078.
429 A. Alnajjar and S. A. Onaizi, *J. Mol. Liq.*, 2025, **421**, 126832.
430 S. Dongare, M. Zeeshan, A. S. Aydogdu, R. Dikki, S. F. Kurtoglu-Oztulum, O. K. Coskun, M. Munoz, A. Banerjee, M. Gautam, R. D. Ross, J. S. Stanley, R. S. Brower, B. Muchharla, R. L. Sacci, J. M. Velazquez, B. Kumar, J. Y. Yang, C. Hahn, S. Keskin, C. G. Morales-Guio, A. Uzun, J. M. Spurgeon and B. Gurkan, *Chem. Soc. Rev*, 2024, **53**, 8563–8631.
431 K. K. Maniam and S. Paul, *Materials*, 2021, **14**, 4519.
432 M. Gilmore, M. Swadzba-Kwasny and J. D. Holbrey, *J. Chem. Eng. Data*, 2019, **64**, 5248–5255.
433 F. Li and X. Ji, *Sci. Talks*, 2025, **16**, 100495.
434 P. J. Smith, C. B. Arroyo, F. Lopez Hernandez and J. C. Goeltz, *J. Phys. Chem. B*, 2019, **123**, 5302–5306.

Open Access Article. Published on 12 fevral 2026. Downloaded on 01.06.2026 11:06:26.
This article is licensed under a Creative Commons Attribution-NonCommercial 3.0 Unported Licence.

435 A. Halilu, M. K. Hadj-Kali, M. A. Hashim, R. Yusoff and M. K. Aroua, *ACS Omega*, 2022, **7**, 37764–37773.
436 S. Imteyaz, C. M. Suresh, T. Kausar and P. P. Ingole, *J. CO2 Util.*, 2023, **68**, 102349.
437 S. Verma, X. Lu, S. Ma, R. I. Masel and P. J. A. Kenis, *Phys. Chem. Chem. Phys.*, 2016, **18**, 7075–7084.
438 S. Garg, M. Li, Y. Wu, M. Nazmi Idros, H. Wang, A. J. Yago, L. Ge, G. G. X. Wang and T. E. Rufford, *ChemSusChem*, 2021, **14**, 2601–2611.
439 D. V. Vasilyev, A. V. Rudnev, P. Broekmann and P. J. Dyson, *ChemSusChem*, 2019, **12**, 1635–1639.
440 V. Bušić, S. Roca and D. Gašo-Sokač, *Separations*, 2023, **10**, 551.
441 D. Yu, Z. Xue and T. Mu, *Cell Rep. Phys. Sci.*, 2022, **3**, 100809.
442 D. C. Nunes, *Development of PRIDES – PolymeRIc Deep Eutectic Solvents – for $CO_2$ capture, NOVA School of Science and Technology (FCT NOVA), 2021.*
443 F. P. García de Arquer, C. T. Dinh, A. Ozden, J. Wicks, C. McCallum, A. R. Kirmani, D. H. Nam, C. Gabardo, A. Seifitokaldani, X. Wang, Y. C. Li, F. Li, J. Edwards, L. J. Richter, S. J. Thorpe, D. Sinton and E. H. Sargent, *Science*, 2020, **367**, 661–666.
444 C. T. Dinh, T. Burdyny, M. G. Kibria, A. Seifitokaldani, C. M. Gabardo, F. P. García de Arquer, A. Kiani, J. P. Edwards, P. De Luna, O. S. Bushuyev, C. Zou, R. Quintero-Bermudez, Y. Pang, D. Sinton and E. H. Sargent, *Science*, 2018, **360**, 783–787.
445 S. Zong, A. Chen, M. Wiśniewski, L. Macheli, L. L. Jewell, D. Hildebrandt and X. Liu, *Carbon Capture Sci. Technol*, 2023, **8**, 100133.
446 J. Resasco, L. D. Chen, E. Clark, C. Tsai, C. Hahn, T. F. Jaramillo, K. Chan and A. T. Bell, *J. Am. Chem. Soc.*, 2017, **139**, 11277–11287.
447 H. Yin, X. Mao, D. Tang, W. Xiao, L. Xing, H. Zhu, D. Wang and D. R. Sadoway, *Energy Environ. Sci.*, 2013, **6**, 1538–1545.
448 H. Yamada, *Polym. J.*, 2021, **53**, 93–102.
449 E. S. Rubin, J. E. Davison and H. J. Herzog, *Int. J. Greenhouse Gas Control.*, 2015, **40**, 378–400.
450 S. Licht, *J. CO2 Util.*, 2017, **18**, 378–389.
451 V. Khanna, B. R. Bakshi and L. J. Lee, *J. Ind. Ecol.*, 2008, **12**, 394–410.
452 H. Y. Teah, T. Sato, K. Namiki, M. Asaka, K. Feng and S. Noda, *ACS Sustainable Chem. Eng.*, 2020, **8**, 1730–1740.
453 M. Yin, X. Bai, D. Wu, F. Li, K. Jiang, N. Ma, Z. Chen, X. Zhang and L. Fang, *Chem. Eng. J.*, 2022, **433**, 134441.
454 Q. Yu, J. Liu, Y. Liang, T. Liu, Y. Zheng, Z. Lai, X. Liu, J. Chen, Q. Zhang and X. Li, *Electrochim. Acta*, 2022, **422**, 140515.
455 I.-N. Tano, E. Rasouli, T. Ziev, Z. Wu, N. Lamprinakos, J. Seo, L. S. Balhorn, P. Vaishnav, A. Rollett and V. Narayanan, *Solar Energy*, 2022, **234**, 152–169.
456 Y. Zuo, Y. Li and H. Zhou, *Energy*, 2022, **251**, 123893.
457 Z. Xie, X. Tang, J. Shi, Y. Wang, G. Yuan and J.-M. Liu, *Nano Energy*, 2022, **98**, 107247.
458 H. Hua, K. Yasuda and T. Nohira, *ACS Sustainable Chem. Eng.*, 2022, **10**, 9225–9231.
459 Z. Wang, J. Ban, K. Su, H. Cheng, Q. Geng, H. Wang, J. Shen, Q. Jia, Z. Zhang and X. Liu, *Ceram. Int.*, 2022, **48**, 12342–12349.
460 F. Yuan, Y.-L. He, M.-J. Li and X.-Y. Li, *Sol. Energy Mater. Sol. Cells*, 2022, **238**, 111631.
461 A. Yu, G. Ma, J. Ren, P. Peng and F. Li, *ChemSusChem*, 2020, **13**, 6229–6245.
462 A. Yu, S. Liu, W. Zhang and Y. Yang, *ACS Appl. Nano Mater.*, 2024, **7**, 27960–27978.
463 X. Wang, F. Sharif, X. Liu, G. Licht, M. Lefler and S. Licht, *J. $CO_2$* Util., 2020, **40**, 101218.
464 I. A. Novoselova, N. F. Oliinyk, S. V. Volkov, A. A. Konchits, I. B. Yanchuk, V. S. Yefanov, S. P. Kolesnik and M. V. Karpets, *Phys. E*, 2008, **40**, 2231–2237.
465 S. Licht, *J. Phys. Chem. C*, 2009, **113**, 16283–16292.
466 R. Jiang, M. Gao, X. Mao and D. Wang, *Curr. Opin. Electrochem.*, 2019, **17**, 38–46.
467 B. Deng, Z. Chen, M. Gao, Y. Song, K. Zheng, J. Tang, W. Xiao, X. Mao and D. Wang, *Faraday Discuss.*, 2016, **190**, 241–258.
468 E. Sada, S. Katoh, H. Yoshii, I. Takemoto and N. Shiomi, *J. Chem. Eng. Data*, 1981, **26**, 279–281.
469 Y. Kanai, K. Fukunaga, K. Terasaka and S. Fujioka, *Chem. Eng. Sci.*, 2013, **100**, 153–159.
470 X. Chen, Z. Zhao, J. Qu, B. Zhang, X. Ding, Y. Geng, H. Xie, D. Wang and H. Yin, *ACS Sustainable Chem. Eng.*, 2021, **9**, 4167–4174.
471 S. Licht, B. Wang, S. Ghosh, H. Ayub, D. Jiang and J. Ganley, *J. Phys. Chem. Lett.*, 2010, **1**, 2363–2368.
472 H. Wu, Z. Li, D. Ji, Y. Liu, L. Li, D. Yuan, Z. Zhang, J. Ren, M. Lefler and B. Wang, *Carbon*, 2016, **106**, 208–217.
473 X. Wang, G. Licht, X. Liu and S. Licht, *Sci. Rep.*, 2020, **10**, 21518.
474 J. Ren, F.-F. Li, J. Lau, L. González-Urbina and S. Licht, *Nano Lett.*, 2015, **15**, 6142–6148.
475 X. Liu, G. Licht, X. Wang and S. Licht, *Catalysts*, 2022, **12**, 137.
476 X. Wang, G. Licht, X. Liu and S. Licht, *Adv. Sustain. Syst.*, 2022, **6**, 2100481.
477 G. A. Mutch, L. Qu, G. Triantafyllou, W. Xing, M.-L. Fontaine and I. S. Metcalfe, *J. Mater. Chem. A.*, 2019, **7**, 12951–12973.
478 N. Prasongthum, A. Suemanotham, Y. Thanmongkhon, P. Khowattana, P. Butniam, N. Khoduangklang, C. Samart and L. Attanatho, in *Journal of Physics: Conference Series*, IOP Publishing, 2023, vol. 2602, p. 012002.
479 H. V. Ijije, R. C. Lawrence and G. Z. Chen, *RSC Adv.*, 2014, **4**, 35808–35817.
480 H. Yin and D. Wang, in *Electrochemical Society Meeting Abstracts 243*, The Electrochemical Society, Inc., 2023, p. 2737.
481 L. Zhang, B. Geng, Y. Gao, H. Kang, P. Wang, C. Liu, H. Xiao, M. Zhao, J. Jia and H. Wu, *Chem. Eng. J.*, 2024, **481**, 148086.
482 S. Arcaro, F. A. Berutti, A. K. Alves and C. P. Bergmann, *Appl. Surf. Sci.*, 2019, **466**, 367–374.


© 2026 The Author(s). Published by the Royal Society of Chemistry

Open Access Article. Published on 12 fevral 2026. Downloaded on 01.06.2026 11:06:26.
This article is licensed under a Creative Commons Attribution-NonCommercial 3.0 Unported Licence.

483 J. Cao, S. Jing, H. Wang, W. Xu, M. Zhang, J. Xiao, Y. Peng, X. Ning, Z. Wang and W. Xiao, *Angew. Chem., Int. Ed.*, 2023, **62**, e202306877.
484 V. Kaplan, E. Wachtel, K. Gartsman, Y. Feldman and I. Lubomirsky, *J. Electrochem. Soc.*, 2010, **157**, B552.
485 R. Yu, B. Deng, K. Zheng, X. Wang, K. Du and D. Wang, *Composites Communications*, 2020, **22**, 100464.
486 W. Weng, B. Jiang, Z. Wang and W. Xiao, *Sci. Adv.*, 2020, **6**, eaay9278.
487 D. Tang, Y. Dou, H. Yin, X. Mao, W. Xiao and D. Wang, *J. Energy Chem.*, 2020, **51**, 418–424.
488 X. Liu, X. Wang, G. Licht and S. Licht, *J. CO2 Util.*, 2020, **36**, 288–294.
489 D. Ji, Q. Jia, C. Zhu, W. Dong, H. Wu and G. Wang, *Appl. Sci.*, 2022, **12**, 8874.
490 X. Chen, H. Zhao, H. Xie, J. Qu, X. Ding, Y. Geng, D. Wang and H. Yin, *Electrochim. Acta*, 2019, **324**, 134852.
491 B. P. Thapaliya, A. S. Ivanov, H.-Y. Chao, M. Lamm, H. M. Meyer III, M. Chi, X.-G. Sun, T. Aytug, S. Dai and S. M. Mahurin, *ACS Appl. Mater. Interfaces*, 2024, **16**, 2251–2262.
492 K. Otake, H. Kinoshita, T. Kikuchi and R. O. Suzuki, *Electrochim. Acta*, 2013, **100**, 293–299.
493 M. Gao, B. Deng, Z. Chen, M. Tao and D. Wang, *Electrochem. Commun.*, 2019, **100**, 81–84.
494 B. Deng, M. Gao, R. Yu, X. Mao, R. Jiang and D. Wang, *Appl. Energy*, 2019, **255**, 113862.
495 X. Liu, J. Ren, G. Licht, X. Wang and S. Licht, *Adv. Sustain. Syst.*, 2019, **3**, 1900056.
496 X. Wang, X. Liu, G. Licht and S. Licht, *Sci. Rep.*, 2020, **10**, 15146.
497 L. Hu, B. Deng, Z. Yang and D. Wang, *Electrochem. commun.*, 2020, **121**, 106864.
498 L. Hu, B. Deng, K. Du, R. Jiang, Y. Dou and D. Wang, *iScience.*, 2020, **23**, 101607.
499 R. Yu, B. Deng, K. Du, D. Chen, M. Gao and D. Wang, *Carbon*, 2021, **184**, 426–436.
500 X. Wang, G. Licht and S. Licht, *Sep. Purif. Technol.*, 2021, **255**, 117719.
501 E. Laasonen, V. Ruuskanen, M. Niemelä, T. Koiranen and J. Ahola, *J. Environ. Chem. Eng.*, 2022, **10**, 106933.
502 B. P. Thapaliya, A. S. Ivanov, H.-Y. Chao, M. Lamm, M. Chi, H. M. Meyer III, X.-G. Sun, T. Aytug, S. Dai and S. M. Mahurin, *Carbon*, 2023, **212**, 118151.
503 T. Giannakopoulou, N. Todorova, E. Sakellis, N. Plakantonaki and C. Trapalis, *Carbon*, 2025, **238**, 120179.
504 H. Shi, M. Cai, W. Li, X. Chen, K. Du, L. Guo, P. Wang, P. Li, B. Deng and H. Yin, *Chem. Eng. J.*, 2023, **462**, 142240.
505 S. Licht, A. Douglas, J. Ren, R. Carter, M. Lefler and C. L. Pint, *ACS Cent. Sci.*, 2016, **2**, 162–168.
506 P. Wang, Y. Liu, Z. Li, D. Ji, Z. Qiao, J. Zhang, Q. Jia and H. Wu, *J. Electrochem. Soc.*, 2021, **168**, 083501.
507 R. Yu, J. Xiang, K. Du, B. Deng, D. Chen, H. Yin, Z. Liu and D. Wang, *Nano Lett.*, 2021, **22**, 97–104.
508 M. M. A. Rafique and J. Iqbal, *J. Encapsulation Adsorpt. Sci.*, 2011, **1**, 29–34.
509 A. Rezaei and A. R. Kamali, *Diam. Relat. Mater.*, 2018, **83**, 146–161.
510 I. D. Rahatwan, P. P. D. K. Wulan and M. Solahudin, in *AIP Conference Proceedings*, AIP Publishing, 2020, vol. 2230.
511 M. Li, E. Irtem, H. P. Iglesias van Montfort, M. Abdinejad and T. Burdyny, *Nat. Commun.*, 2022, **13**, 5398.
512 M. A. Arellano-Treviño, N. Kanani, C. W. Jeong-Potter and R. J. Farrauto, *Chem. Eng. J.*, 2019, **375**, 121953.
513 D. P. Hanak, E. J. Anthony and V. Manovic, *Energy Environ. Sci.*, 2015, **8**, 2199–2249.
514 Q. Xia, K. Zhang, T. Zheng, L. An, C. Xia and X. Zhang, *ACS Energy Lett.*, 2023, **8**(6), 2840–2857.
515 J. Li, C. Qin, Z. Lv, C. Gao, L. Chen and S. Xu, *Energy*, 2025, **316**, 134516.
516 J. M. Spurgeon, N. Theaker, C. A. Phipps, S. S. Uttarwar and C. A. Grapperhaus, *ACS Sustainable Chem. Eng.*, 2022, **10**, 12882–12894.
517 A. Silveira Sbrice Pinto, N. Gulpinar, F. Liu, E. Gibson, L. Fuller and P. Souter, *ACS Sustainable Resour. Manage.*, 2025, **2**, 733–743.
518 Y. Kim, M. Namdari, A. M. L. Jewlal, Y. Chen, D. J. D. Pimlott, M. Stolar and C. P. Berlinguette, *ACS Energy Lett.*, 2025, **10**, 403–409.
519 D. Rathore, *Energy Sustain. Dev.*, 2025, **89**, 101866.
520 D. Tian, Z. Qu and J. Zhang, *Appl. Energy*, 2023, **351**, 121787.
521 Y. Li and T. B. Lu, *Mater. Chem. Front*, 2024, **8**, 341–353.
522 S. Verma, S. Lu and P. J. A. Kenis, *Nat. Energy*, 2019, **4**, 466–474.
523 X. Jiang, L. Ke, K. Zhao, X. Yan, H. Wang, X. Cao, Y. Liu, L. Li, Y. Sun, Z. Wang, D. Dang and N. Yan, *Nat. Commun*, 2024, **15**, 1427.
524 X. Wang, P. Li, J. Tam, J. Y. Howe, C. P. O'Brien, A. Sedighian Rasouli, R. K. Miao, Y. Liu, A. Ozden, K. Xie, J. Wu, D. Sinton and E. H. Sargent, *Nat. Sustainable*, 2024, **7**, 931–937.
525 T. Gao, B. Xia, K. Yang, D. Li, T. Shao, S. Chen, Q. Li and J. Duan, *Energy Fuels*, 2023, **37**, 17997–18008.
526 S. Y. Chae, S. Y. Lee, S. G. Han, H. Kim, J. Ko, S. Park, O. S. Joo, D. Kim, Y. Kang, U. Lee, Y. J. Hwang and B. K. Min, *Sustainable Energy Fuels*, 2019, **4**, 199–212.
527 M. Agliuzza, R. Speranza, A. Lamberti, C. F. Pirri and A. Sacco, *Appl. Sci.*, 2025, **15**, 549.
528 D. Segets, C. Andronescu and U. P. Apfel, *Nat. Commun.*, 2023, **14**, 7950.
529 B. Belsa, L. Xia and F. P. García de Arquer, *ACS Energy Lett*, 2024, **9**, 4293–4305.
530 K. Zhao, C. Jia, Z. Li, X. Du, Y. Wang, J. Li, Z. Yao and J. Yao, *Fuel*, 2023, **351**, 128913.
531 J. Chen, Y. Xu, P. Liao, H. Wang and H. Zhou, *Carbon Capture Sci. Technol*, 2022, **4**, 100052.
532 K. Armstrong, *Carbon Dioxide Utilisation: Closing the Carbon Cycle*, Elsevier, 2015, pp. 237–251, ISBN: 9780444627469.
533 Y. Zheng, W. Zhang, Y. Li, J. Chen, B. Yu, J. Wang, L. Zhang and J. Zhang, *Nano Energy*, 2017, **40**, 512–539.
534 I. S. Omodolor, H. O. Otor, J. A. Andonegui, B. J. Allen and A. C. Alba-Rubio, *Ind. Eng. Chem. Res.*, 2020, **59**, 17612–17631.
535 Y. Zhang, S. Zhao, L. Li, J. Feng, K. Li, Z. Huang and H. Lin, *Catal. Sci. Technol.*, 2024, **14**, 790–819.
536 S. Sarmad, D. Lu, S. Gao, Z. Sun, Z. Zhou, A. Ali and L. Duan, *J. Environ. Chem. Eng.*, 2024, **12**, 114562.